CRANFIELD UNIVERSITY

HSIEN-CHUN CHUNG

THE DEVELOPMENT OF A PIEZOELECTRIC FAN SYSTEM FOR THE FLAPPING WING MICRO-AIR-VEHCILE APPLICATION

SCHOOL OF APPLIED SCIENCES

PhD THESIS

CRANFIELD UNIVERSITY

SCHOOL OF APPLIED SCIENCES

PhD THESIS

Academic Year 2007-2008

HSIEN-CHUN CHUNG

THE DEVELOPMENT OF A PIEZOELECTRIC FAN SYSTEM FOR THE FLAPPING WING MICRO-AIR-VEHCILE APPLICATION

Supervisor: Zhaorong Huang

October 2008

This thesis is submitted in partial fulfilment of the requirements for the degree of PhD of Science

ACKNOWLEDGEMENTS

First, I would like to express my deepest appreciation to my supervisor, Dr. Zhaorong Huang for his guidance, instruction and supervision of this study. Without his support, encouragement and tolerating my mistakes, I would not have been able to finish this research work successfully.

Second, I would like to thank Professor Roger Whatmore sincerely for his mentoring during the early stage of my research, which truly enlightened me.

My appreciation goes to Dr. Nicholas Lawson and Dr. Shijun Guo for their support and help to accomplish this research work. I am also grateful to my colleagues Kranti Lal Kummari, Simon Croucher and Evandro Liani for their help in this study.

I would like to thank all my family for their support and encouragement, especially to my wife Chia-Chin for her steady love, patience and cheering up when I was weary; the deepest thanks are due to my two lovely children Te-Jung and Te-Kang for their company, which gave me a lot of support. Finally, I would like to present this thesis to my parents, especially to my father, to comfort his soul in heaven and express my deepest missing of him.

ABSTRACT

A micro air vehicle (MAV) is a semiautonomous airborne vehicle which measures less than 15 cm in any dimension. It can be used to access situations too dangerous for direct human intervention, e.g., explosive devices planted in buildings and video reconnaissance and surveillance, etc. As demonstrated by flying birds and insects, flapping flight is advantageous for its superior manoeuvrability and much more aerodynamically efficient at small size than the conventional steady-state aerodynamics. Piezoelectric actuators are easy to control, have high power density and can produce high output force but usually the displacement is small. With appropriate stroke amplification mechanisms piezoelectric actuators can be used to drive the flapping wings of MAV.

This research aims to develop a piezoelectric fan system with 2 degrees of freedom of motion for flapping wing MAV applications. In this project, piezoelectric fans consisting of a piezoelectric layer and an elastic metal layer were prepared by epoxy bonding. A flexible wing formed by carbon fibre reinforced plastic wing spars and polymer skin was attached to two separate piezoelectric fans to make them coupled. Two sinusoidal voltages signals of different phase were then used to drive the coupled piezoelectric fans. High speed camera photography was used to characterize the two degrees of freedom motion of the wing. Theoretical equations were derived to analyse the performance of the piezoelectric fans in both quasi-static and dynamic operations, and the calculated results agreed well with the finite element analysis (FEA) modelling results. It has been observed that the phase delay between the driving voltages applied to the coupled piezoelectric fans plays an important role in the control of the flapping

and twisting motions of the wing. Selected factors such as the gap between the two piezoelectric fans which can affect the performances of the wing have been investigated and the experimental results were compared with the FEA modelling results.

CONTENTS

LIST OF TABLES

LIST OF FIGURES

Glossary of Terms

Δ	Dimensionless factor
α	Bending angle
δ	Tip deflection
ε_0	Dielectric constant of vacuum
ε_{33}^{T}	The permittivity at constant stress
ε_r	Relative dielectric constant of the dielectric material
ρ_m	Density of passive elastic layer (metal)
ρ_p	Density of piezoelectric layer
τ_m	Bond failure stresses
τ_u	Shear strength
ω	Frequency in radians
A	Young's modulus ratio of metal layer and piezoelectric layer
A_b	Cross section area of the substrate layer
A_p	Cross section area of the piezoelectric layer
B	Thickness ratio of metal layer and piezoelectric layer
C	Density ratio of metal layer and piezoelectric layer
C	Capacitance
D_n,	Dielectric displacement
E_m	Electric field

E_m	Young's modulus of passive elastic layer
E_p	Young's modulus of piezoelectric layer
E_3	Electric field in the z-axis.
F^{el}	The compresional force in the elastic layer
F^{p}	Tensional force in piezo layer
F_{bl}	Blocking force
I	Current
I_{bn}	Moment of inertia relative to the neutral axis for the substrate layer
I_p	Moment of inertia for the piezo layer
I_{pn}	Moment of inertia relative to the neutral axis for the piezo layer
L	Length of the unimorph actuator
M^{el}	Bending moments of the elastic layer
M^{p}	Bending moments of the piezo layer
Q	Electrical charge
S^E	The strain due to the electric field in the piezo layer
S^{el}	The total strain for the elastic layer
S^{p}	The total strain for the piezo material
S_{el}^{F}	The strain due to the force F^{el} in the elastic layer
S_{p}^{F}	The strain due to the tensional force F^{p} in piezo layer
T_{kl}	Stress tensor

U^{p}	Internal energy
V	Voltage
d_{nkl}	Piezoelectric coefficient tensor
d_{31}	Transverse piezoelectric coefficient
f_r	Fundamental bending resonance
h_{el}	The thickness of metal layer
h_p	the thickness of piezo layer
k_{31}	Transverse coupling factor
n	Stress concentration factor
s_{ijkl}^{E}	Compliance tensor at constant electric field
s_{11}^{el}	compliance of the elastic layer
s_{11}^{p}	Compliance of the piezo layer.
t	Total thickness of the unimorph cantilever
t_N	Neutral axis position
t_m	Thickness of passive elastic layer
t_p	Thickness of piezoelectric layer

CHAPTER 1

INTRODUCTION

The interest in the flapping micro air vehicle (MAV) has grown significantly in recent years (Shyy et al., 1999; Raney et. al., 2003; Ellington, 1999). A micro air vehicle is defined as a semiautonomous airborne vehicle, which measures less than 15 cm in any dimension, weighs no more than 50 grams, and flies up to a range of 10 km (McMichael and Francis, 1997). A MAV can be used to access situations too dangerous for direct human intervention, e.g., explosive devices planted in buildings, damage assessment, video reconnaissance and surveillance, search for disaster survivors, etc (Shyy et al., 1999). As demonstrated by flying birds and insects, flapping flight is advantageous for its superior manoeuvrability and is much more aerodynamically efficient at small size than conventional steady-state aerodynamics (Ellington, 1999; Ellington et al., 1996). Dickinson et al. (1999) identified the three key unsteady aerodynamic mechanisms used by insects: delayed stall, wake capture and rotational circulation. Different mechanisms such as pneumatic and motor-driven actuators have been applied to mimic the complex motion pattern of an insect flying, but these mechanisms often suffer from heavy weight and system complexity (Dickinson et al., 1999).

Piezoelectric materials especially lead zircornate titanate (PZT) are widely used in smart structures as sensors (e.g. accelerometers, microphones, etc) and actuators (e.g. micropumps, micromotors, etc) due to their high bandwidth, high force output, compact size, and high power density (Niezrecki et al., 2001). However, the piezoelectric effect is intrinsically very small, only a small deflection can be expected directly from the bending of a piezoelectric unimorph/bimorph; therefore, some kind of motion amplification mechanism is required to achieve a large deflection. Fearing et al. (2000) developed piezoelectrically actuated four-bar mechanisms for a micromechanical flying insect thorax (Fearing et al., 2000; Sitti, 2001; Yan et al., 2001). Cox et al. (2002) reported three piezoelectrically activated four bar and five bar linkage systems for the electromechanical emulation of mesoscale flapping flight. Park et al. (2004) developed a four bar linkage system driven by a lightweight piezo-composite actuator to mimic the

flapping wing system of birds.

A simpler motion amplification mechanism is a piezoelectric fan (piezofan) which couples a piezoelectric unimorph to an attached flexible blade and is able to produce large deflections especially at resonance. Piezofans were first investigated in the late seventies (Toda et al., 1981). In the last few years, the surge of the portable electronic devices has brought interest in the use of piezofans as compact, low power, noiseless air cooling technology for applications such as in laptop computers, mobile phones, DVD players etc. (Yoo et al., 2000; Wu et al., 2003). Piezoelectric unimorph/bimorph structures have also been extensively studied for static and dynamic operations (Smits et al., 1991; Smits et al., 1997; Smits et al., 1991; Wang and Cross, 1998; Gibbs and Fuller, 1992; Crawley and de Luis, 1987; Brennan et al., 1997). Dynamic and topological optimization of piezofan structures without load for cooling applications have been reported recently (Yao and Uchino, 2001; Burman et al., 2002; Basak et al., 2005). As far as the author is aware, there are no reports on using piezofan structures as actuators for loaded applications.

To mimic the complex motion pattern of an insect flying, three degrees of freedom (DOF) movements are needed to be realised. One piezoelectric fan can provide one DOF to large amplitude; multi-piezoelectric actuators are needed to produce two or more DOF motion. For example, two piezoelectric unimorphs in parallel connected to a wing should be able to provide flapping and rotating motion by controlling their phase and amplitude difference. To obtain complex wing motions it should be possible to drive multiple piezoactuators with signals of different amplitudes and phases. This may also permit adjustment and control of the phase between flapping and rotational motion~ a key for flapping flight control. The development of this basic concept, as part of an EPSRC supported project (EP/C511190/1: Development and Aeroelastic Optimisation of a Piezoelectric Powered Flapping Wing Micro Air Vehicle)**,** is the main topic of this research project. We will develop simple piezoelectric actuators like piezofan or a system of piezofans to provide two degrees of freedom motion for the wing of a flapping MAV.

1.1. Overview of the thesis

1.1.1. Research aim and objects

The aim of this research is to develop a piezoelectric fans system with 2 degrees of freedom motion for flapping wing MAV application.

The objectives of this research can be divided into two parts:

1. The design and fabrication of PZT unimorph actuators for the application of piezoelectric fans.
2. The control of a coupled piezoelectric fans system with a phase difference for the flapping wing MAV application.

1.1.2. Structure of the thesis

This thesis is divided into several chapters described as following:

Chapter 1: a brief introduction on the concept of flapping MAV and its potential applications; the aims and objectives of the current project.

In chapter 2, a literature review is given. This includes the basic concepts of piezoelectricity and a brief general review on piezoelectric actuators. Also reviewed is the development of MAV; from the initial concept to different types of MAV devices developed, including the fixed wing and flapping wing MAVs. Piezoelectric fans and their applications are also discussed in this chapter. Basics on the fabrication of the laminar devices such as the bonded piezofan and the bonding mechanisms are also reviewed.

Chapter 3 discusses the methodology used in this project. This includes: the adhesive selection for fabricating the piezofan and measurement of the bonding strength; the analytic and finite element modelling (FEM or FEA) study of cantilever actuators; the FEA modelling and fabrication of piezofans; the evaluation of the piezofan and the

control of the coupled piezofan system. Relevant electrical driving system and measuring instrumentation are also discussed in this chapter. Generally speaking, analytical calculation is used as a benchmark for the validation of the FEM. Analytical calculation and FEM are used to optimise the design parameters for the unimorph and piezofan actuators and then these devices are prepared and characterised by experiments. Piezoelectric unimorph cantilevers where the piezoelectric and the elastic layers have the same length are investigated at first. For this simple structure analytical solutions are readily available for the calculation of the tip displacement, blocking force and the resonate frequencies. Then the piezofan structure where the piezoelectric and the elastic layers have different lengths is investigated. For this structure there are no readily available equations to calculate the tip displacement and blocking force, and the resonant frequencies could only be obtained by complex matrix calculation. FEM programme are developed for both the cantilever and piezofan structures and their results were compared with their respective analytical solutions and experimental measurement results. For the coupled piezofans structure, not even the matrix analytical approach is possible, so only the FEM and measurement are discussed.

In Chapter 4, a theoretical analysis is presented. These include: the analysis for the quasi-static operation of unimorph actuators based on the piezoelectric constitutive equations and force balance conditions at equilibrium; the derivation for the equation of motion for the unimorph piezoelectric cantilever actuators based on the Lagrangian variation method; and finally the analysis to the dynamic operation of piezofans used in this project.

Chapter 5 presents and discusses all the analytic, FEM and experimental results of the project. At first, the lap shear strengths of the epoxy bondings, prepared under different conditions, are reported this lead to the optimised conditions for the preparation of the piezoelectric actuators. Then the optimisation of the thickness, width and length for the cantilever and piezofan structures for MAV applications are discussed. At quasi-static operation, the main characterisation parameters are the tip displacement and the blocking force. The first resonant frequency and the tip displacement are the main parameters to characterise the dynamic operation. The first resonant frequency, the

flapping and twisting motion amplitudes of the wing attached to the coupled piezofans are the main indicators to characterise the coupled piezofan systems. Conclusions and suggested future works are described in Chapter 6 and Chapter 7 respectively. The references and appendix relevant to this research are included in Chapter 8 and 9 respectively.

CHAPTER 2

LITERATURE REVIEW

2.1. Piezoelectricity

In 1880, Pierre and Jacque Curie discovered that some crystalline materials, when they are compressed, produce a voltage proportional to the applied pressure and when an electric field is applied across the material, there is a corresponding change of shape, this characteristic is called piezoelectricity (Ikeda, 1990). Piezoelectricity stems from the Greek word piezein, meaning to press or to squeeze.

A material is said to possess piezoelectric properties if an electrical charge is produced when a mechanical stress is applied. This is commonly referred as the “Direct piezoelectric effect”. Conversely, an applied electric field will produce a mechanical strain in the material. This is commonly referred as the “Converse piezoelectric effect”. The piezoelectric (shorted as piezo thereafter) effect occurs in all materials for which the crystal structure is “non-centrosymmetric”. Since piezo effect exhibited by natural materials such as quartz, tourmaline, Rochelle salt, etc. is very small, polycrystalline ferroelectric ceramic materials such as barium titanate and lead zirconate titanate (PZT) with improved properties have been developed. These ferroelectric ceramics become piezoelectric when poled. Most commercially available ceramics (such as barium titanate and PZT) are based on the perovskite structure (Figure 2.1) (Rosen et al., 1992). The structure of PZT is often described by using the ideal cubic perovskite structure ABO_3, in which BO_6 octahedral units are centred on the cube corners (B-site) and linked by sharing of the oxygen ions while the A-site is located at the centre of the cube. In PZT the A-sites are occupied by Pb^{2+} cations while the B-sites are occupied in equal measure by Zr^{4+} and Ti^{4+} cations. To date, PZT is the most widely used piezoelectric materials for actuator applications.

PZT crystals exhibit tetragonal or rhombohedra structure at the temperatures below its

Curie temperature. Due to their permanent electrical and mechanical asymmetry, these types of unit cells exhibit spontaneous polarization and deformation. The asymmetric arrangement of the positive and negative ions imparts permanent electric dipole behaviour to the crystals.

Groups of unit cells with the same polarization and deformation orientation are called domains. Because of the random distribution of the domain orientations in the ceramic material, a ferroelectric poling process is required to obtain any macroscopic anisotropy and the associated piezoelectric properties. The poling field can be applied so the ceramic exhibits piezoelectric responses in various directions or combination of directions. When the field is removed, the electric dipoles stay in alignment (Figure 2.2) (Rosen et al., 1992). The material now has a remnant polarization (which can be degraded by exceeding the mechanical, thermal and electrical limits of the material). Subsequently, when a voltage is applied to the poled piezoelectric material, the ions in the unit cells are shifted and, additionally, the domains change their degree of alignment. The result is a corresponding change of the dimensions (expansion, contraction). Above the Curie temperature, PZT unit cells take on cubic centrosymmetric (isotropic) structure. When cooled, domains form, but with randomized orientations, and the material does not regain its piezoelectric properties. The piezoelectric effect for a given item depends on the type of piezoelectric material and the mechanical and electrical axes of operation. These axes are set during poling. The orientation of the dc poling field determines the orientation of the mechanical and electrical axes.

The direct piezoelectric effects are usually used in the sensor applications and the converse piezoelectric effects are generally used in the actuators applications. The latter is the focus of this study.

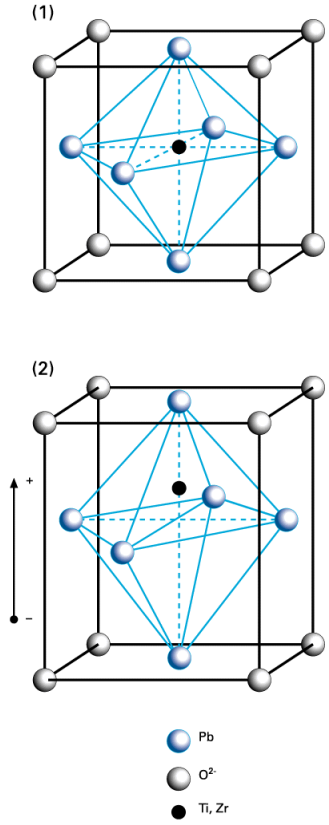

Figure 2.1 PZT unit cell: (1) Perovskite-type lead zirconate titanate (PZT) unit cell in the symmetric cubic state above the Curie temperature. (2) Tetragonal distorted unit cell below the Curie temperature

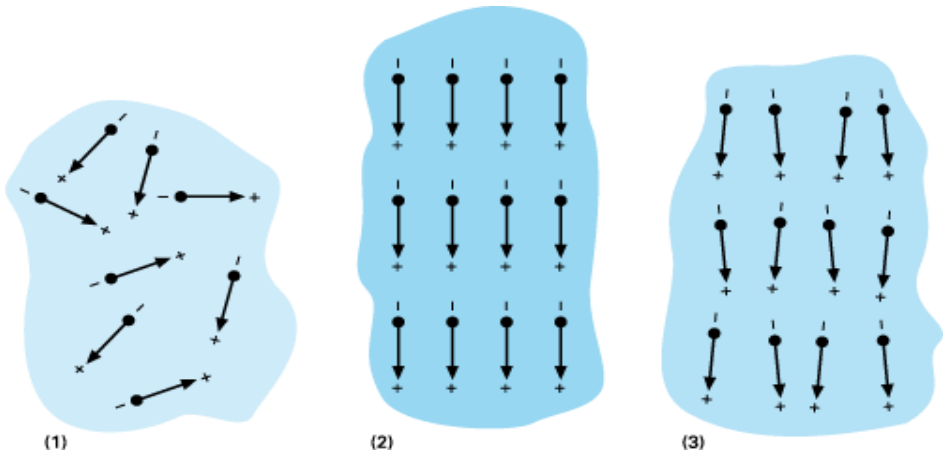

Figure 2.2 Electric dipoles; (1) unpoled ferroelectric ceramic, (2) during and (3) after poling

2.2. Piezoelectric actuators

Piezoelectric actuators exploit the converse piezoelectric effect to transform electrical energy into mechanical work and have been widely researched in the past decades (Herakovic, 1996). Piezoelectric actuators are the most widely used smart material actuators because of their wide operating frequency range. Detailed review of piezoelectric actuators can be found in Smits et al. (1991), Giurgiutiu, (2000) and Niezrecki et al. (2001).

Niezrecki et al. (2001) divided piezoelectric actuators into three main categories based on the mechanisms amplifying the deflection, one is internally leveraged actuators which amplify deflection by an internal structure, including stacks, bender, unimorph and building-block types of actuators; another category is externally leveraged actuators which need an external mechanical structure for their actuating ability, including lever arm, hydraulic amplification and flex tensional types of actuators, and the last category is frequency leveraged actuators which require a control signal to generate motion. All the categories could be summarized as in Figure 2.3

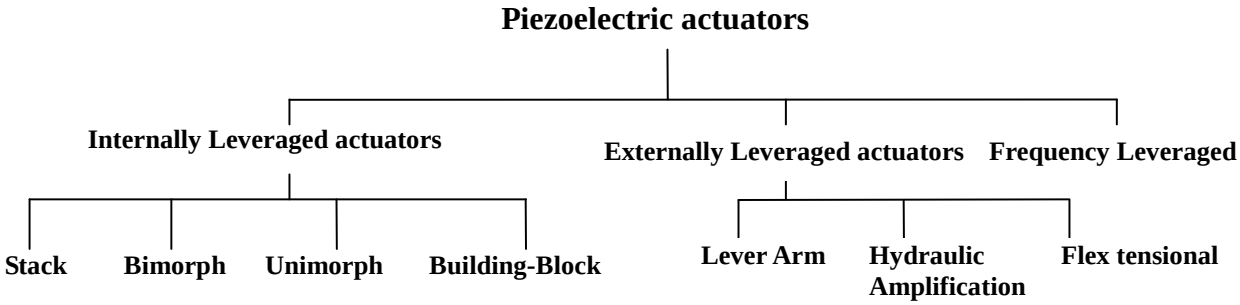

Figure 2.3 The category of the piezoelectric actuators

2.2.1. Internally Leveraged Actuators

2.2.1.1. Stack actuators

Stacks actuators consist of thin piezoceramic patches piled together to increase their total deflection linearly whilst keeping a low voltage expanse, the deflection and out put force of a stack actuator are proportional directly to the length and cross-sectional area of the actuator respectively.

The applications of the stacks actuators have be shown to include the following:

- Control of vibrations (Redmond and Barney, 1997).
- The trailing edge of a helicopter rotor blade (Chandra and Chopra, 1999; Lee and Chopra, 1999; Straub et al., 1999).
- Suspension control (Fukami et al., 1994)
- Vibration damping in machine tools (Martinez et al., 1996).
- Control of missile fins (August and Joshi, 1996)
- Micropositioning (Yang et al., 1996),
- Drum brake actuation (Gogola and Goldfarb, 1999).

2.2.1.2. Bimorph bender actuators

The bimorph actuators use the internal piezoelectric strain to induce actuator motion. A bimorph actuator consists of two or more layers of piezoelectric material, which are poled on opposite sides of the neutral axis. The opposing strain from the piezoelectric layers creates an internal bending moment that causes the entire actuator to flex. Most bimorph actuators have piezoelectric material extending the full length of the beam, and the inactive substrates may be used to increase the structural stability

Bimorph benders were first developed bender actuator in the early 1930s by Sawyer (1931) at the Brush Development Company. However, the performance of these actuators was not understood in great detail until the research on smart structures became more popular (Steel et al., 1978; Tzou, 1989). Tapered bender is another example of bender actuators which decreased the thickness of the material, with the thickest part at the root, to provide more efficient usage of the material for bending (Prechtl and Hall, 1997).

The applications of the bender actuators included:

- Robotic applications when large displacements are required (Chonan et al., 1996).
- Spoilers on missile fins (August and Joshi, 1996).
- Actuation for a quick-focusing lens (Kaneko et al., 1998).
- Vibration control of a helicopter rotor blade (Fulton and Ormiston, 1998; Koratkar and Chopra, 1999).
- Vibration control on the vertical tail of an fight jet airframe (Hopkins et al., 1998; McGowan et al., 1998)

2.2.1.3. Unimorph actuators

An unimorph actuator is a special case of the bender actuator structure. An unimorph is a plate, beam, or disk compositing with one active layer and one inactive substrate. RAINBOW, CERAMBOW, Crescent, and THUNDER actuators are some typical unimorph actuators.

RAINBOW (Reduced And Internally Biased Oxide Wafer) actuator was invented by Haertling (Haertling, 1994a, 1994b), and have been investigated by other researchers (Elissalde and Cross, 1995; Chandran et al., 1996; Hooker, 1997). A RAINBOW actuator consists of a piezoelectric wafer reduced on one side by chemical acid. A piezoelectric layer is placed on the other side in compression to form a dome. A 100 mm diameter RAINBOW actuator could produce a displacement up to 3 mm. (Haertling, 1994a). RAINBOW actuators were manufactured previously by Aura Ceramics Inc., but are no longer commercially available now.

CERAMBOW (CERAMic Biased Oxide Wafer, Barron et al., 1996) and Crescent actuators (Chandran et al., 1997) are stressed-biased unimorph actuators, which are fabricated by bonding a metal and an electroded ceramic plate together at an elevated temperature. As the actuator cooling down to the room temperature, a pre-stress is induced in the active material due to the difference in thermal expansion coefficients between the metal and the ceramics. This causes these unimorph actuators to adopt curved shapes (Kugel et al., 1997; Chandran et al., 1997).

THUNDER (THin layer UNimorph ferroelectric DrivER) actuator is another pre-stressed actuator, which are manufactured by Face International Corporation now and was developed originally by the NASA Langley Research Center in 1994. This sort of actuator consists of a piezoceramic layer bonded with a metal using a polymide adhesive material (LaRC-SI). Because of the high temperature and high pressure used in the manufacturing process, it can stand high electrical and mechanical loading (Capozzoli et al., 1999; Shakeri et al., 1999). The significant advantage of THUNDER actuators is they have extremely robust structure, which allows them to be used more in the commercial applications, such as synthetic jets (Smith et al., 1999).

2.2.1.4. Building-Block actuators

A building-block actuator consists of lots of small actuation building blocks, to form a larger actuation system with an improved performance.

The C-block actuator is one example of the building-block actuators; comparing with the traditional straight bender actuator, the C-block actuator could generate 8% more work (Moskalik and Brei, 1997).

The applications of the C-block actuators include:

- A rotor blade smart flap test (Clement et al., 1998).
- Noise cancellation (Fuller et al., 1994; Fuller et al., 1996)
- Sound generation (Bailo et al., 1998a, 1998b).

Recurve actuator (Ervin and Brei, 1998) is another example of a building-block actuator, which causes the first half of the length, has a displacement opposite to the second half. This makes the Recurve actuator an ideal actuation unit to be built up into arrayed actuators to increase overall displacement. They have been investigated for use in the active rotor blades (Ervin, 1999) and synthetic jets (Jacot and Calkins, 2000).

2.2.2. Externally Leveraged Actuators

Externally leveraged actuators use an external structure which could be a mechanical, hydraulic or kinematical mechanism to increase the output deflection at the expense of the force output.

2.2.2.1. Lever arm actuators

A lever arm actuator is a simple device to increase the displacement of a stack actuator. A typical method to fabricate this sort of actuator is to use a flexure-hinged mechanism and a stack actuator. Due to the lever arm structure, this type of device increases the output displacement; however, the output force is decreased. The applications of these types of actuators include the control the trailing edge flap of helicopter rotor blades and the micropositioning (Samak and Chopra, 1996, Chandra and Chopra, 1999). Lever arm actuators are manufactured currently by Dynamic Structures, Materials LLC, Marco Systemanalyse and Entwicklung GmbH.

2.2.2.2. Hydraulic amplification actuators

Researchers had investigated piezoelectric pumps to create an actuator to overcome the displacement limitations of traditional piezoelectric stack actuators (Mauck and Lynch, 1999; Nasser et al., 2000). A typical hydraulic amplification actuator consists of a stack actuator, an input and output piston, and some hydraulic fluid. This actuator could improve the displacement of piezoelectric actuators.

2.2.2.3. Flextensional actuators

Flextensional actuators use a stack actuator and an external amplification mechanism to convert the displacement generated by the stack actuator to an output displacement in the transverse direction.

Flextensional devices were first developed in 1967 and were applied mainly in acoustic applications (Royster, 1970). One type of this flextensional actuator is called the Moonie (Sugawara et al., 1992). A Moonie actuator consists of two caps with cavities and a stack actuator sandwiched between them. Displacement of the stack causes flexes the end caps, producing an increased deflection. The displacement output of the actuator increases with the cavity diameter and depth.

Cymbal actuator is another example of flextensional actuator which is similar to the Moonie actuator. (Dogan et al., 1996). The Cymbal actuator consists of a stack actuator with an external structure which could create both the flexural and rotational motions. The advantages of Cymbal actuator are easier to manufacture than the Moonie and the displacement can be increased by a factor of two whereas the force output can be increased by a factor of five comparing with the Moonie actuator (Dogan et al., 1997).

Another actuator similar to a Cymbal actuator is called Bimorph-Based Double-Amplifier actuator which uses a bimorph bender instead a stack actuator as the active component. This structure combines both bending and flextensional features to produce the displacement. The displacement of Bimorph-Based Double-Amplifier actuator is

close to 10 times as the one of a bimorph bender alone (Xu, et al., 1996). The applications of the flextensional actuators include micropositioning (Le Letty et al., 1997, Pokines and Garcia, 1998), and active/passive vibration control (Bruneau et al., 1999). Flextensional actuators are currently being manufactured by Dynamic Structures and Materials LLC, EDO Corporation, and Cedrat (Meylan, France).

2.2.3. Frequency Leveraged Actuators

Frequency leveraged actuators are those actuators using the frequency performance of the piezoelectric material to produce output strain to rapidly move the actuator in one direction in series of small steps.

The first frequency leveraged actuator is known as Inchworm, developed by Burleigh Instruments in the 1970s (Richard, 1975). The Inchworm consists of three stack actuators connected together that operate in sequence to move the actuator down a rod. Initially, the leading stack actuator unclamps from the rod, then the Inchworm extends, and the leading stack actuator re-clamps to the rod. Next, the trailing actuator unclamps, the Inchworm contracts, and the actuator re-clamps to the rod. After a full cycle sequence, the actuator is in a position down the rod.

Frequency-leveraged actuators have been applied in lots of applications, including alignment of fiber optic components (Houde-Walter, 1985), shape control of wings (Austin and Van Nostrand, 1995), and positioning of wire electrical discharge machining (Mohri et al., 1997). Some of the companies that manufacture frequency-leveraged piezoceramic linear actuators include Burleigh Instruments, Polytec PI Inc., Cedrat, and EDO Corporation.

2.3. Piezoelectric Fans

Piezoelectric fans are piezoelectric bimorph and unimoph cantilever actuators using piezoelectric excitation to drive a thin blade into resonance to create a fluid flow (Figure 2.4). Piezoelectric fans were first discussed in the seventies (Toda, 1981). The surge of portable electronics devices in the past decades has generated renewed interest in the use of piezoelectric fans as a very compact, low power, noiseless air cooling technology for applications as varied as mobile phones, laptop computers, DVD player and automobile multimedia boxes etc. (Yoo et al., 2000, Wu et al., 2003)

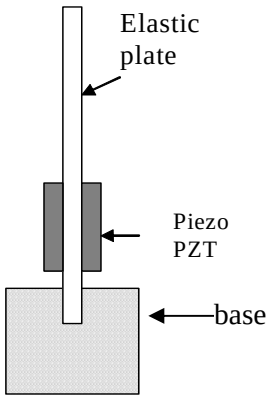

Figure 2.4 Schematic configurations of a piezoelectric fan

A number of researches on piezofans have been reported in the literature; almost of them are focused on the thermal performance for the cooling application. Toda (Toda, 1979, 1981) and found by placing a piezoelectric fan on the side of a power transistor panel of a television receiver it could decrease the temperature by 17 °C on the panel surface. Schmidt studied the local and average transfer coefficients on a vertical surface cooled by two piezoelectric fans resonating out of phase and found changing the distance between the fans and the surface, or the distance between these two fans would significantly change the transfer coefficients (Schmidt, 1994). Ihara and Watanabe (1994) investigated the flows around the tips of an oscillating piezoelectric fan, and the discrete vortex method was used to numerically simulate the flow field. Yoo et al. (2000)

used PZT to develop a few types of piezoelectric fans, one of these fans could generate a 3.55 cm tip deflection and 3.1 m/s air velocity , measured 0.1 cm away from the fan tip. Loh et al. (2002) investigated the cooling effects of the acoustic streaming from an ultrasonically vibrating beam. Acikalin et al. (2003) developed a closed-form analytical solution to predict the two-dimensional streaming flow from an infinite vibrating beam. The structure optimization of piezoelectric fans was studied by Buermann et al. (2002) and Basak et al. (2005) who investigated fans with two symmetrically bonded piezoelectric patches and a piezoelectric patch only on one side respectively, and the optimization of the electromechanical coupling factor (EMCF) of the fans was investigated.

Using piezofans in small-scale electronics for cooling applications were investigated by Acikalin et al. (2004) and Wait et al. (2004).The thermal performance of piezoelectric fans was investigated by experiments on the cooling of mobile phones and laptops. Acikalin et al. (2007) investigated the thermal management of low-power electronics components experimentally and numerically for the piezoelectric fans for the cooling applications. Different parameters including the vibration amplitude, the distance between the fan and the heat source, the fan length, resonant frequencies, and the fan offset from the centre of the heat source are considered in the investigation on the effects of the heat transfer from a small heat source.

Although piezoelectric fans as a cooling application are a novel technology, the basic design rules for applying these fans into practical thermal solutions are not yet established. Complicated thermal phenomenon coupling with the three-dimensional, unsteady temperature and flow fields involved in such a small-scale device would be a significant challenge to the integration of piezofans into portable commercial electronic devices.

2.4. Adhesive Bonding

For piezoelectric actuators or piezoelectric fans, the bond between the metal and the piezoelectric material affects their performance. However, there are few papers referring

to the detailed bonding materials and methods. Xiaoping Li et al. (1999) described a conductive epoxy (GC Electrics, Rockford, IL) to glue the PZT ceramic to brass to produce an unimorph under a pressure of ~0.03 MPa for one day curing, the thickness of the epoxy layer was ~10μm. Wang et al. (1999) mentioned they used epoxy resin to bond two PZT ceramic plates (500μm in thickness for one plate) to produce a bimorph, and bond one PZT ceramic plate and one stainless steel (380μm in thickness) to produce an unimorph. However, they did not specify the epoxy used, their curing temperature was 80 degree Celsius and the curing time was 24 hrs. The thickness of the bonding layer was about 20 μm or less, measured by a micrometer and an optical microscopy. Steel et al. (1978) suggested using a commercial adhesive produced by 'Araldite' to bond PZT ceramic (150μm in thickness) and BeCu metal (150μm in thickness) layer, the adhesive layer was < 0.1 mm, and their curing temperature was about 50 degree Celsius.

The literatures above show that the adhesive bonding is an effective way for joining the piezoelectric ceramics and metal substrate. It is therefore necessary to understand the mechanism of adhesive bonding.

2.4.1. Mechanisms of adhesive bonding

A few theories have been developed to explain the process of bonding in adhesive structures. Individually, each of these theories is inadequate to describe the complete process of bonding in most situations. However, each contributes an understanding of the overall process of bonding and therefore is important. Figure 2.5 illustrates the four predominant mechanisms of adhesion.

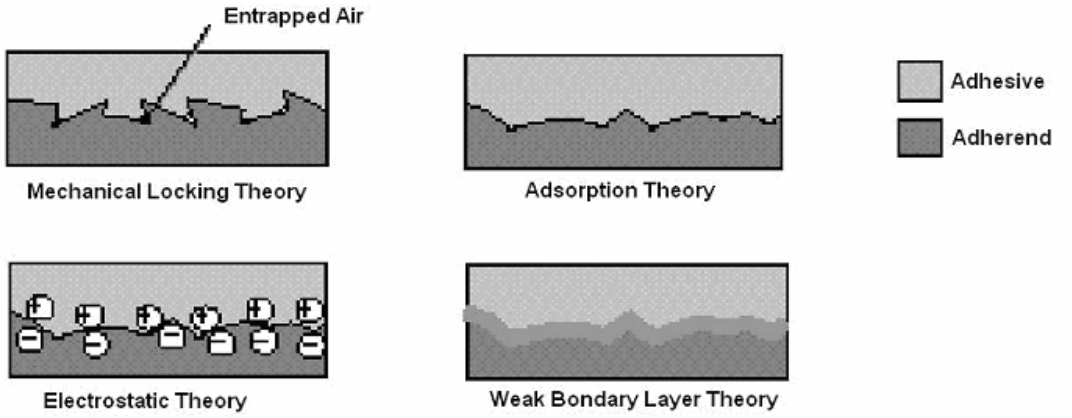

Figure 2.5 Dominant mechanisms of bonding (Messler, 1993)

● Mechanical Locking Theory

According to the mechanical locking theory, an adhesive must fill the valleys of each adherend (body to be bonded) and displace trapped air to work well. Adhesion is the mechanical interlocking of the adhesive and the adherend together, and the overall strength of the bond is dependent upon the quality of this interlocking interface. Chemical or physical abrading is highly recommended for optimum bonding.

● Adsorption Theory

The adsorption theory suggests that bonding is the process of intermolecular attraction (van der Waals bonding or permanent dipole, for example) between the adhesive and the adherend at the interface. An important factor in the strength of the bond according to this theory is the wetting of the adherend by the adhesive. Wetting is the process in which a liquid spreads onto a solid surface and is controlled by the surface energy of the liquid-solid interface versus the liquid-vapour and the solid-vapour interfaces. In a practical sense, to wet a solid surface, the adhesive should have a lower surface tension than the adherend.

● Electrostatic Theory

Electrostatic forces may also be a factor in the bonding of an adhesive to an adherend. These forces arise from the creation of an electrical double layer of separated charges at the interface and are believed to be a factor in the resistance to separation of the adhesive and the adherend. Adhesives and adherends that contain polar molecules or

permanent dipoles are most likely to form electrostatic bonding according to this theory.

● Weak Boundary Layer Theory

This theory has been developed to explain the curious behaviour of the failure of bonded materials. Upon failure, many adhesive bonds break not at the adhesion interface, but slightly within the adherend or the adhesive, adjacent to the interface. This suggests that a boundary layer of weak material is formed around the interface between the two media. Impurities in the bond and adverse chemical reactions are common causes of weak boundary layers.

2.4.2. Mechanisms of failure in bonded joints

The two predominant mechanisms of failure in adhesively bonded joints are adhesive failure and cohesive failure. Adhesive failure is the interfacial failure between the adhesive and one of the adherends. It indicates a weak-boundary layer often from improper surface preparation or adhesive choice. Cohesive failure is the internal failure of either the adhesive or, rarely, one of the adherends. Ideally, the bond will fail within one of the adherends or the adhesive. This indicates that the maximum strength of the bonded materials is less than the strength of the adhesive strength between them. Usually, the failure of joints is neither completely cohesive nor completely adhesive. Measurement of the success of a particular joint is based on the relative percentage of cohesive failure to adhesive failure.

2.5. Micro-air-vehicle (MAV)

DARPA (Defence Advanced Research Projects Agency), the research and development organization for the Ministry of Defense (MoD) of America, reported the concept of an insect like miniature vehicle for the military application in 1997 (McMichael, and Francis, 1997), defined a MAV to be sized less than 15 centimetres in length or width or height, weight less of 50 grams and must be capable of staying aloft for 20 to 60 minutes for a distance of 10 kilometres. The MAVs could be applied to assess environments which are too dangerous for direct human intervention, for instances,

searching for disaster survivors, detecting explosive devices planted in buildings or hostage locations; Video reconnaissance and surveillances for urban combat applications and counter terrorist operations etc., this would require a highly manoeuvrable capability of avoiding obstacle to access the targets.

MAVs fly at a very low Reynolds number (100,000 or below for MAV against over 100 million for fast-flying commercial aircraft) as compared to the conventional aircrafts due to their small size and low speed, there are a number of aerodynamic challenges for designing a MAV to achieve enough lift and low drag.

Recent studies in the understanding of aerodynamics of flapping wing flight or insect /birds flight have led to new approaches to achieve the flapping wing flight; a critical challenge in construction of bird/insect-mimicking flapping device is to select a driving force or actuator which could generate enough wing movement. In the following sections, three types of MAV, including the fixed wing, rotary wing, and flapping wing MAVs are described.

2.5.1. Fixed Wing MAVs

Most of the MAV have fixed wings. One reported by Oh, P. Y. (2004) could cruise at the speed of 65 km/hour at Reynolds number of about 130,000. However, as the size of a MAV decrease, the Reynolds number of the flow surrounding the MAV also reduces. The challenge to the fixed wing aircraft is that at low Reynolds number, the aircraft lacks of manoeuvrability and needs a large turning radius to navigate and avoid obstacles in a tight space (Michelson, et al., 2003.). The fixed-wing designs rely on conventional scaled-down aerodynamics and flight control approaches, and do not possess the flight agility that would enable missions to be conducted within the confines of a building.

One of the most famous fixed wing MAVs is Black Widow MAV reported by Grasmeyer and Keennon (2001), which has a wing span of 15.2 cm and can achieve a flight speed of 48.2 km/hour, a maximum range of 1.8 km and the maximum altitude of

769 feet, and the endurance of 30 minutes. Black Widow can be used for missions such as target tracking and video monitoring over its operational range. The Lockheed Martin MicroSTAR is another MAV (Ifju et al., 2002) can be used in the same applications, this vehicle has a wing span of about 15.2 cm and weighs less than one third of a pound. It has a range of 5 km and can reach altitudes of 50 to 300 feet at speeds of 55.5 km/hr with an endurance of 20 minutes. The UF 6” MAV (Ifju et al., 2002) is another MAV with a 15.2 cm length, and weighing 52 grams, it can reach the speeds of 20 to 48 km/hour.

These three models are based on a disc shape structure as shown in Figure 2.6, and many other MAVs have been developed with subtle modification using this similar shape structural concept. Honeywell International Inc. reported a commercially MAV system which can be used for military surveillances. The system consists of two MAVs with the capability of vertical take-off and landing, one ground station and other support equipments. The total weight of the complete system is less than 18 kg and the endurance of each MAV of the system is 40 minutes at 5,500 feet.

Figure 2.6 The 'Black Widow', 'MicroSTAR' and the 'UF 6" MAV' respectively (from left)

2.5.2. Rotary Wing MAVs

The main purpose to develop MAVs is for the military surveillance applications; hence an agile MAV would be more beneficial. If the MAV could hover or fly slowly, then it could explore and relay clear images back to the control centre. This function can be achieved with the rotary wing MAV. The "Micro Flying Robot FR-I" (Figure 2.7) is a rotary wing MAV developed by Seiko Epson (2003), which weighs 8.9 gram, contains a 2.5 gram heavy control module with 2 CPUs, a 1.3 gram Bluetooth module and a CCTV video camera module.

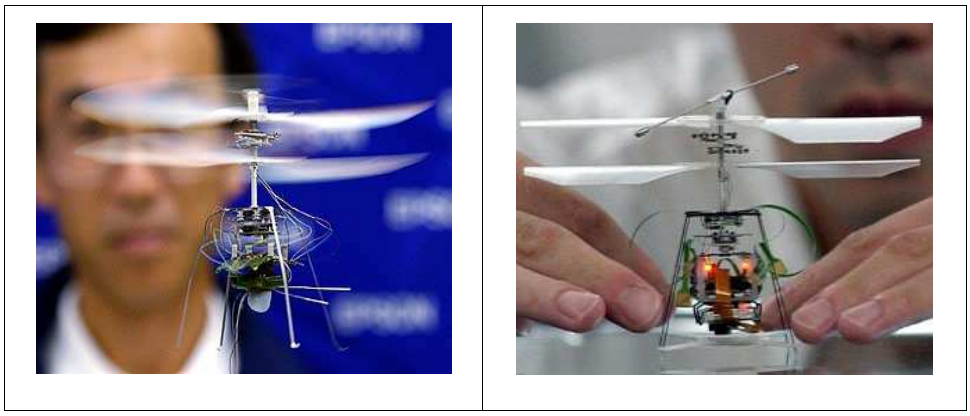

Figure 2.7 The Micro Flying Robot “FR-I”

The Pixel and Proxyflyer Micron are other types of rotary wing MAVs (Figure 2.8) which can hover and fly in any direction. The Pixel weighs 6.9 grams and uses a small motor and a gear train with a 45mAh LiPo battery. It is a fully functional helicopter controlled by an infrared signal with four channels. The Proxyflyer has the same weight of 6.9 grams as the Pixel, but developed under a different concept with two control channels instead of four channels applied by the Pixel.

The MAVs described above are scaled down versions of helicopters. The smallest scaled down version of the helicopter is the “small flying helicopter” (Figure 2.8), developed by Microtechnology in Mainz, Germany with the size of 24 x 8 x 0.4 mm and weight of 0.4 grams. It is powered by a motor with 5 mm length and a diameter of 2.4 mm. This

small flying helicopter could take off at 40,000 revolutions per minute, but without remote control capability.

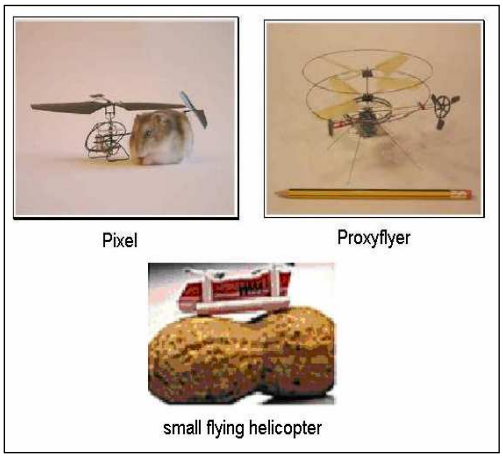

Figure 2.8 The Pixel, Proxyflyer and Small flying helicopter compared to a hamster, pencil and peanut respectively

2.5.3. Flapping Wing MAVs

In nature, flight has been achieved by birds and insects by the flapping motion of their wings which makes them more manoeuvrable and versatile. Flapping is much more aerodynamically efficient than the conventional steady-state aerodynamics at small size (Ellington, 1999).

Taking an example of a fruit fly; it can beat its wings 200 times a second, flapping and rotating them in a complicated action that relies on three separate mechanisms to provide lift. Drosophila has a wing stroke of 160 degrees combined with wing rotations of more than 90 degrees. Over 100,000 fold flying insects size range from the smallest ones weighing 20-30 μg to the largest ones approximately 2-3 g have been studied, the scaling rule is close to isometric, wing area is proportional to $m^{2/3}$ on average, where m is body mass, wing beat frequency increases as size decreases, scaling as $m^{-1/4}$, a relatively small wing area can be compensated by a higher frequency. The small size and the relatively small Reynolds Numbers of MAVs correspond to very small birds or insects.

It has been reported that the mass of the system has a large influence on the performance of the flapping wing MAV. Singh et al. (2005) reported that when the mass of the flapping wing MAV increases, the maximum frequency of the mechanism need to increase as well due to high inertial power requirements. Also, wing tests showed a decrease in thrust at high frequencies. The order of the weight to endurance for the existing MAVs and the desired order can be seen in Figure 2.9. The desired MAV should weigh about 100 grams and should be capable of flying for 60 minutes.

It is worthwhile to point out that an insect based biomimetic flight may be a solution for hover capable MAVs. However, merely copying biological morphology, kinematics, or behaviours could not lead to an optimum system, as reported by Michelson and Naqvi (2003). Because, even if such an optimum system could be achieved; it may not be practical due to external constraints such as availability of suitable material or non-existent manufacturing techniques.

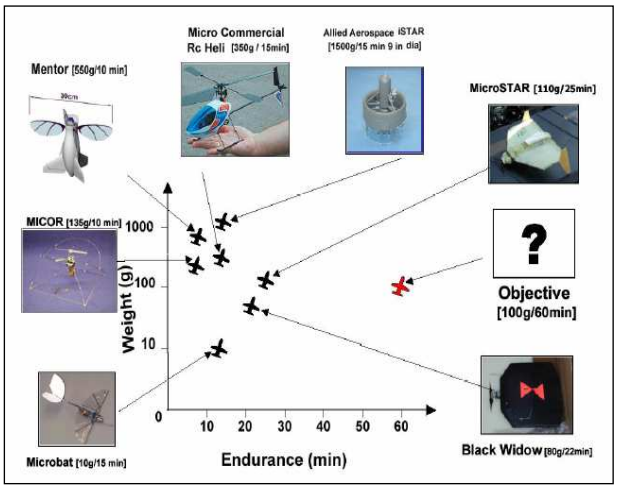

Figure 2.9 Weight to endurance order of existing and desired MAVs (Michelson and Naqvi, 2003)

Most of the recent flapping wing MAV projects have adopted a battery powered electrical motor as an actuator. The rotary motion of the electrical motor is converted to a linear or flapping motion by a mechanism. The most common mechanism that can convert rotary motion to linear or flapping motion is a slider crank type four-bar

mechanism. A recent work on flapping wing MAV adopted a stepper motor as an actuator along with a robotic-flapper mechanism to achieve the required flapping motion (Madangopal et al., 2004), where the robotic-flapper mechanism they used is basically a crank type four-bar mechanism.

The Microbat is another flapping wing MAV which applied a super capacitor powered electric motor. Pornsin-sirriak et al. (2003) devised this model which is 10.6 grams, and can fly for 18 seconds. They used a 1 volt NiCd battery in combination with a DC-to-DC converter to produce the required 4 to 6 volt operating voltage and used a low-weight, low-friction transmission mechanism (Figure 2.10) to convert rotary motion to flapping wing motion. Another similar model developed by Madangopal et al. (2005) has a weight of 15 grams; they also used a motor and a combination of a 5-bar and a 4-bar mechanism to acquire the required flapping and twisting motions. Both of the models mentioned above were developed to replicate birds or insect flights and used a battery powered electrical motor as the actuator.

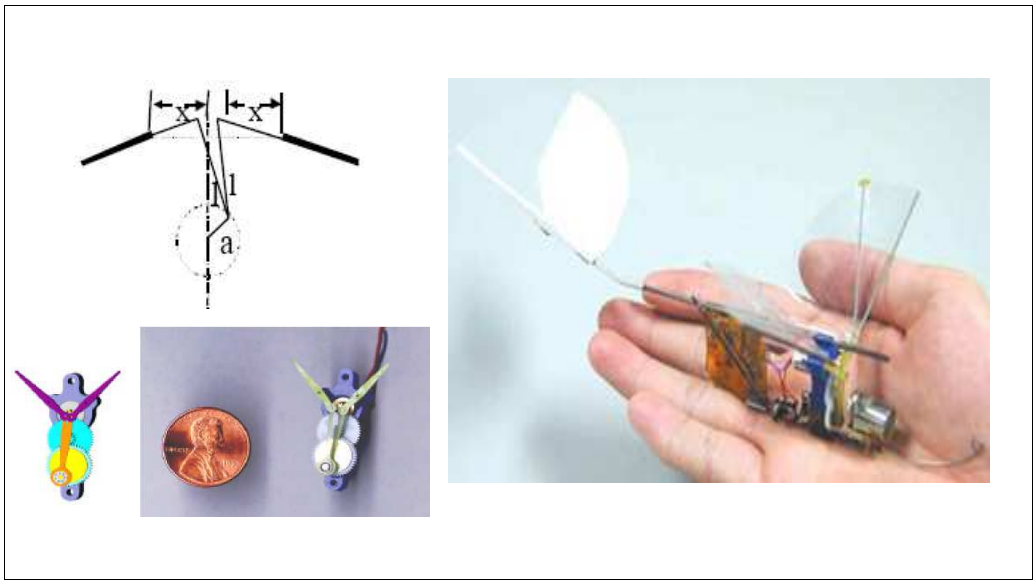

Figure2.10 Transmission mechanism of Microbat & the Microbat respectively (Pornsin-sirriak et al. (2003))

2.6. Piezoelectric fans for the application of the flapping Wing Micro air vehicle (MAV)

A serious limitation to the development of flapping wing MAV is the lack of a compact, high energy density propulsion system. Current mechanical designs present significant challenges at small scales where conventional joints and bearings are heavy and can give inefficient actuation. Control of these mechanical vehicles with mechanical systems also presents major challenges. Piezoelectric materials, particularly lead zirconate titanate (PZT), offer the potential for a flapping wing propulsion system with integrated electronics and simplified control systems.

There has been limited work on flapping wing MAV systems using piezoelectric fans/actuators. Cox et al. (2002) reported development of a system to emulate the flapping flight in mesoscale, which consisted of one piezoelectric unimorph actuator and three flextual-based mechanisms to transform the linear output of the actuator into single-degree-of freedom flapping motion (Figure 2.11). University of California, Berkeley has done considerable work on a piezoelectrically actuated flapping wing MAV and used a pair of piezoelectric unimorph actuators and four bar mechanisms (Fearing, et al. 2000; Sitti, M., 2001; Sitti et al., 2001; Yan et al., 2001; Yan et al., 2003)

The current study is to investigate the feasibility of an efficient and compact PZT flapping-wing system with an MAV sized propulsion mechanism. To mimic the three DOF's complex motion pattern of an insect flapping, multi-piezoelectric actuators are required. For example, two piezoelectric unimorph fans in parallel connected to a wingspan should be able to provide flapping and twisting motions by controlling their phase and amplitude difference. Figure 2.12 shows two piezoelectric unimorph fans in

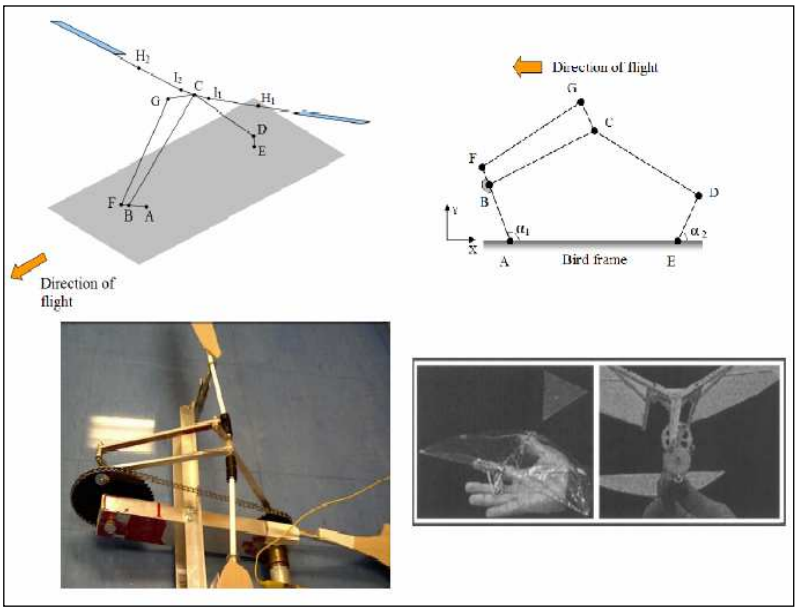

Figure 2.11 University of Delaware Flapping Wing Vehicle & The Mechanism Adopted

anti-phase which will enable the wing to rotate. The wing will be flapping when the two fans are in-phase. To obtain complex wing motions it should be possible to drive multi piezoelectric actuators with signals of different amplitudes and phases. This design will also enable the adjustment and control of the phase between the flapping and twisting motions which is a key for flapping flight control.

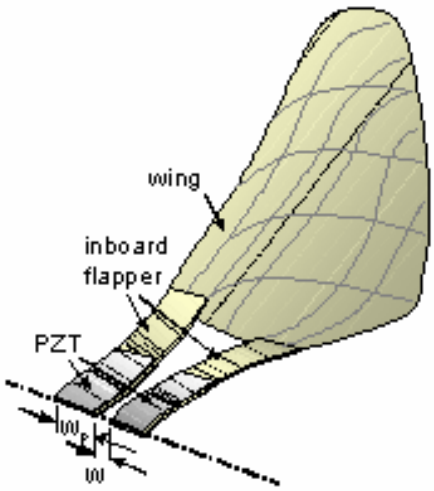

Figure2.12 Schematic of the coupled piezoelectric fans for MAV applications

CHAPTER 3

METHODOLOGY AND EXPERIMENTAL

The methodology used in this research is shown as a flowchart in Figure 3.1.

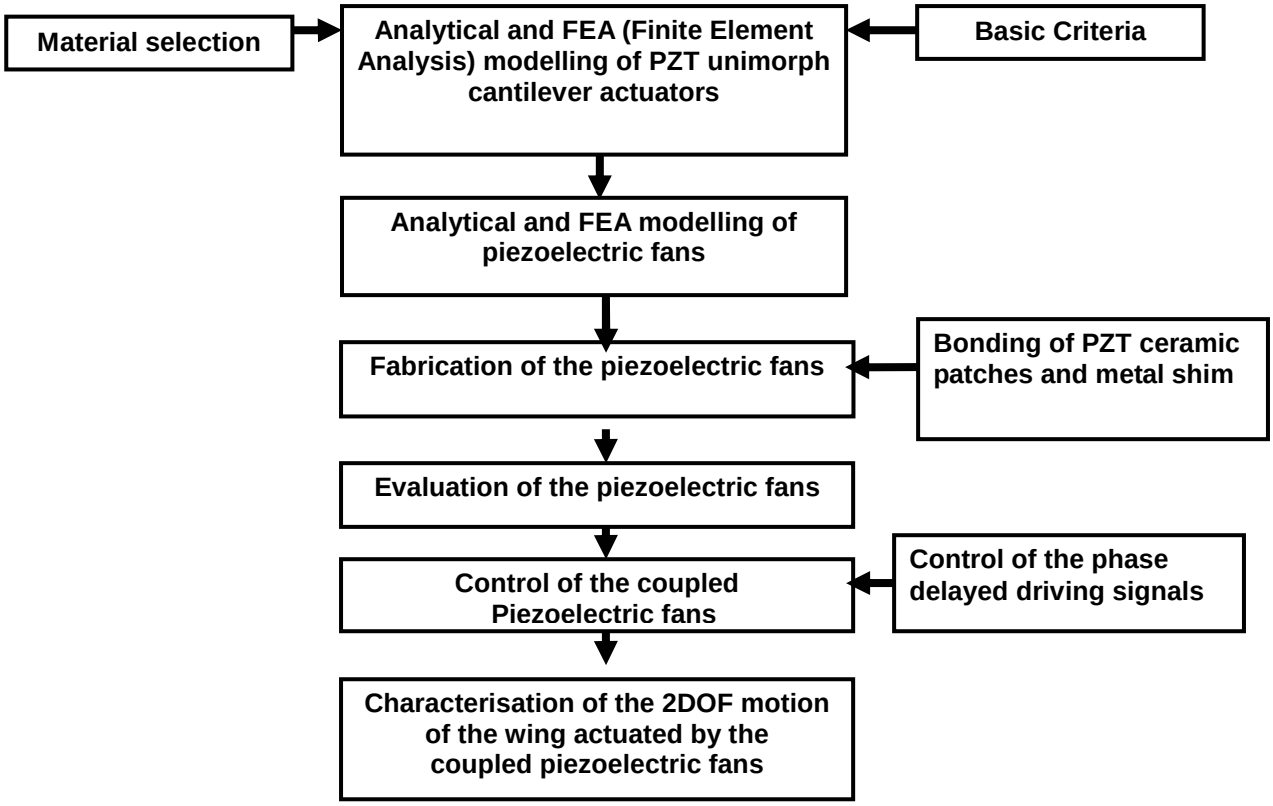

Figure 3.1 The flowchart of the methodology

At first, the analytical and finite element analysis (FEA) modelling of the cantilever piezoelectric unimorph actuators was investigated. In the meantime, basic criteria were drawn by referring to the requirements of MAV, and the basic principles for material selection were obtained in order to achieve the maximum displacement and work output.

Once a reliable FEA model of the cantilever piezoelectric actuators was achieved, it was used to model the behaviours of piezoefans in which the piezoelectric and the elastic layers do not have the same lengths, and then the design of the piezofan can be achieved. Afterwards, how to bond the piezoelectric layer and the substrate firmly was

investigated. Once the optimized bonding conditions, which can produce the maximum bonding strength, have been obtained, piezofans were fabricated. The appropriate facilities such as the driving system, measurement equipments and phase delay control system were investigated and been set up before evaluating the performance of the piezofans. After the performance of the piezofans was characterized, the two degree of freedom (DOF) motion of the coupled piezofans was investigated and its application on the control of the flapping and twisting motion of a flapping wing MAV evaluated.

3.1. Basic criteria and material selection

As stated before, a MAV is a semiautonomous airborne vehicle, which measures less than 15 cm in any dimension, weighs no more than 50 grams, and flies up to a range of 10 km. According to the survey of different flight species the wing beating frequencies when they are flying are often less than 100 Hz (Dickinson et al., 1999), so some criteria can be set accordingly. These are:

- The Length of the wing (wing span + Piezo fan) $\leq$15cm
- The range of working frequency f: $0 \leq f \leq 100$ (Hz)
- The total weight of the system <50g

The basic performance criteria are the maximum tip displacement and blocking force. As can be shown in Chapter 4 Theoretical Analysis, both of these are linearly proportional to the transverse piezoelectric coefficient d_{31}. Another criterion is the maximum electrical mechanical energy transformation, which is proportional to the k_{31} (Wang et al., 1999). Accordingly, a few piezoelectric materials including a few PZT ceramics (PSI-5H4E and 5A4E of the Piezo Systems, Inc), PZN-PT, PMN-PT single crystals (PZT-PT, TRS Ceramic Inc.) have been surveyed. Although the PZT-PT, PMN-PT single crystals have the highest d_{31} and k_{31} value, $950x10^{-12}$ (C/N) and 0.5 respectively (Niezrecki et al., 2001), compared to the PSI-5H4E,'s $320x10^{-12}$ (C/N) and 0.44 respectively (http://piezo.com/prodsheet2sq5H.html) and the PSI-5A4E's $190x10^{-12}$ (C/N) and 0.35 respectively (http://piezo.com/prodsheet1sq5A.html); the PSI-5H4E was chosen for its relative high d_{31} value, high breakdown strength, readily available and especially for its affordable cost.

Generally, bimorph and unimoprh cantilever actuators are flexural bending actuators, which could produce large deflection with a lightweight and compact size. Other types of piezoelectric actuators, such as the multilayers stack and piezoelectric motors, can usually produce large force but very small displacement. For these reasons bimorph and unimorph cantilever actuators are considered to have more merits for the flapping wing micro aerial vehicle application.

The bimorph (serial connection type) cantilever has a better performance under the same applied electrical field (Sitti et al., 2001) than unimorph actuators, however, during half of a cycle the electric field is anti-parallel to its polarisation, and therefore it is subject to depolarization. Another issue is its relative poor mechanical strength because of its full ceramic structure if without any elastic layer. Usually an elastic layer, for example a metal layer is sandwiched between the two piezoelectric layers to improve its mechanical strength. Also bimorph actuators are more difficult to make. For these reasons, the unimorph type actuator is chosen in this study.

3.2. Analytic study and FEA modelling of unimorph cantilever actuators

Analytical treatment of the unimorph cantilever actuator was carried out by using the constitutive equations for piezoelectric materials, based on Smits's and Wang's works. Smits's method is more fundamental and helps in understanding the physics of the problem concerned. Wang's work is of more practical use. The analytical equations at quasi-static operation for unimorph cantilever actuator in this study are mainly based on Wang's work (Wang et al., 1999).

In this study, Finite element analysis (FEA) is also adopted to investigate the performance of the actuator. FEA is a numerical procedure for analysing engineering problems, which are too complicated to be solved by classical analytical methods (Krishnamoorthy, 1995). The finite element models based on Hamilton's principle for piezoelectric beam and plate structures has been reported (Saravanos, 1997; Yao and Uchino, 2001; Burman et al., 2002). A more detailed review of using the finite element method in the analysis and simulation of smart piezoelectric materials and structures

can be found in literature (Mackerle, 2003).

ANSYS software is a commercial FEA modelling solution package, which is good at dealing with different mechanical problems, including the static, dynamic structural analysis, both would be linear and nonlinear approach, heat transform, fluid, acoustic, electro-magnetic and electro-mechanical problems etc. FEA modelling of the unimorph cantilever type actuators by ANSYS 8.1 software has been developed in this study. When developing the FEA modelling, the bonding between the piezoelectric material and the metal shim is assumed to be perfect, and the thickness of the bonding layer is negligible. The piezoelectric properties of the poled PZT-5H including Young's Modulus and piezoelectric coefficients are anisotropic. However, for simplifying the complexity and comparing with Wang's work (Wang et al., 1999) in which the quasi-static displacement, blocking force and resonant frequencies of the unimorph actuators are discussed in the assumption of an isotropic Young's Modulus of PZT-5H ceramic, the Young's Modulus of PZT-5H ceramic is assumed isotropic here, but the compliances c_{11}, c_{12}, c_{13}, c_{33}, c_{44}, and coefficients ε_{11}, ε_{22}, ε_{33}, e_{31}, e_{33}, e_{15} are considered anisotropic in the FEA modelling of the unimorph actuator adopted in this research. Three-dimensional SOLID5 element is used in all of these modelling because it has large deflection and stress when used in the structural and piezoelectric analyses. Usually the meshing is made by dividing the length and width in a fixed 1mm distance, and keep the thickness of the two material layers in one section respectively to make all the elements in a uniform Tetragonal shape. Therefore, the total elements of this modelling are 800 and the total nodes are 1353. Table III.1 summarises the materials parameters used in the FEA modelling and analytic calculation.

Table III.1 Material properties for analytic and FEA calculations (http://piezo.com)

Material	**PZT-5H**	**Titanium Alloy I (Ti/94.5/Al 3/V 2.5)**	**Titanium Alloy II (Ti/90/Al 6/V 4)**	**Stainless Steel (Fe/Cr18/Ni 9/Ti)**	**Mo**	**Usage**
Young's Modulus (GPa)	62	103.5	110	200	324.8	FEA Analytic
Density (Kg/ m^3)	7800	4450	4420	7900	10220	FEA Analytic
Young's Modulus ratio A ($E_{elastic}/E_{Piezo}$)	—	1.67	1.77	3.23	5.24	Analytic
Density ratio C ($\beta_{elastic}/\beta_{Piezo}$)	—	5.71E-01	5.67E-01	1.01E+00	1.31E +00	Analytic
Poisson's ratio	—	0.27	0.27	0.28	0.293	FEA
d31(m/V)	320×10^{-12}	—	—	—	—	Analytic
ε11	3130	—	—	—	—	FEA
ε22	3130	—	—	—	—	FEA
ε33	3400	—	—	—	—	FEA
e31	-12	—	—	—	—	FEA
e33	22.22	—	—	—	—	FEA
e15	19.39	—	—	—	—	FEA
c11(N/m^2)	126e+9	129.33e+9	137.45e+9	255.68e+9	428.9 8e+9	FEA
c12(N/m^2)	79.5e+9	47.83+9	50.83e+9	99.43e +9	177.7 8e+9	FEA
c13(N/m^2)	84.1e+9	—	—	—	—	FEA
c33(N/m^2)	117e+9	—	—	—	—	FEA
c44(N/m^2)	23.0e+9	40.75e+9	43.3 e +9	78.13e+9	125.6e +9	FEA

3.3. Analytical and FEA modelling of piezoelectric fans

Once the FEA modelling of the unimorph cantilever actuators has been developed, the FEA modelling for piezoelectric fans was developed by changing the length of the PZT-5H piezoceramic, whilst keeping the elastic layer (substrate) at a constant length. The relationships between the PZT patch locations, patch to elastic layer length ratio, patch to beam thickness ratio and the maximum tip deflection in a piezoelectric fan have been investigated.

The dynamic response of a piezoelectric fan configuration where the substrate layer has different length with the piezoelectric material layer was derived, after obtaining the solution for the dynamic response of a piezoelectric unimorph cantilever actuator at first. Finally, a configuration resembles the actual structure which includes three different sections: a section for clamping, a piezoelectric active section and a passive blade

section used in the experiments were discussed. More details are presented in chapter 4.

3.4. Fabrication of the piezoelectric fan

The ways to bond the metal and the piezoelectric material affects the performance of the actuators prominently, so the investigating on the optimized bonding conditions is necessary before the fabrication of the fans. From the understanding of bonding mechanisms, experiments for obtaining optimized bonding condition were designed and executed.

Piezoelectric fans made by bonding a PZT-5H ceramics with a Molybdenum or stainless steel elastic layer at different thicknesses were then fabricated by applying these optimized bonding conditions.

3.4.1. Adhesive Selection

Most adhesives in use are a combination of components each designed for different functions in the bonded joint. An adhesive can contain any number of the following components: (1) the adhesive base or binder; (2) a hardener (for thermosetting types); (3) accelerators, inhibitors, or retardants; (4) diluents; (5) solvents; (6) fillers; and (7) carriers or reinforcements.

The adhesive base is generally the primary component of any adhesive and is the constituent from which the name of the adhesive is derived. A hardener is a substance added to the adhesive that causes a chemical reaction, which cures the adhesive. Accelerators, inhibitors, and retardants control the adhesive's rate of curing. Diluents are liquid components that are added to the adhesive to reduce the concentration of the adhesive base. They usually reduce the viscosity of the adhesive. Solvents are closely related in that they thin the adhesive to make it more spreadable. The difference is that solvents disperse the adhesive base. Fillers are included in the adhesive if the adhesive properties are insufficient alone. Often, fillers are used for reducing cost, improving structural strength, encouraging conductivity, and other similar applications. Carriers or

reinforcements are used to support the adhesive during application or storage.

Adhesives can be classified into a number of different categories, but the most convenient system is categorization by chemical composition. Table III.2 shows a summary of major structural adhesives categorized. Table III.3 tabulates the appropriate adhesives to use for particular adherends.

Table III.2 Categorization of Structural Adhesives (Messler, 1993)

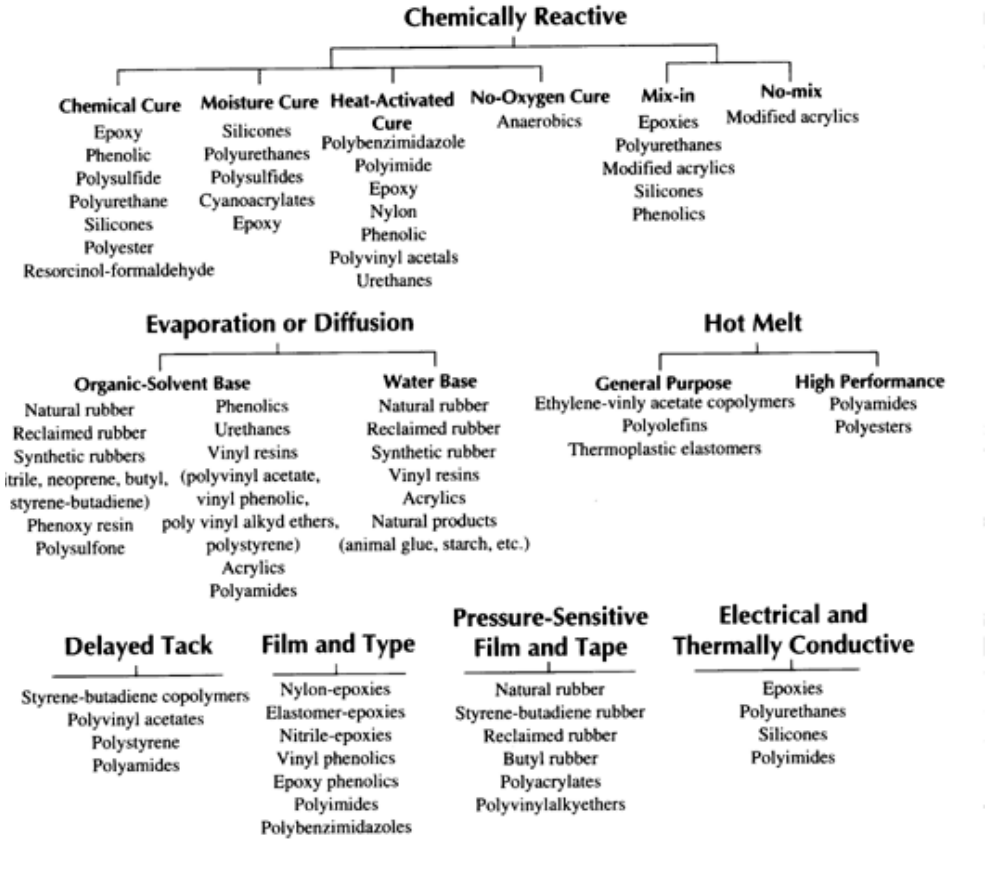

Table III.3 Metal-adhesive compatibility chart (Messler, 1993)

Adhesive	Metal																
	Al	Ag	Au	Be	Brass\ Bronze	Cd	Cu	Mg	Ni	Pb	Sn	Steel	Stainless Steel	Ti	U	W	Zn
Acrylics					•		•					•	•				
2nd generation acrylics	•																
Anaerobics			•		•	•	•										
Cyanoacrylates	•						•	•		•							•
Epoxies		•	•	•	•		•	•	•	•	•	•	•	•	•	•	•
Epoxy-phenolics	•		•	•				•		•		•	•	•			
Modified epoxies	•																
Modified phenolics	•																
Neoprene-phenolics	•				•		•	•									
Nitrile-epoxies	•			•										•			•
Nitrile-phenolics				•		•	•	•	•			•	•	•			
Nitrile-rubbers																•	
Nylon-epoxy				•	•		•	•	•								
Polyacrylates										•	•						
Polyamides									•								
Polybenzimidazoles				•					•			•	•				
Polymides				•					•			•	•	•			
Polyurethanes				•	•		•	•		•							
Polyvinyl acetates								•									
Polyvinyl alkyl ether		•	•							•	•						•
Silicones	•				•		•	•		•							
Styrene-butadiene											•						
Vinyl-plasticols	•																
Vinyl-phenolics								•	•								

When fabricating the piezofans, the main task is to bond the PZT ceramics with different metal shims (stainless steel, Molybdenum etc). The piezo material is a commercial PZT ceramic PZT-5H with Nickel electrodes on both sides, therefore the bonding of PZT with elastic layers becomes effectively the bonding between Nickel and the elastic layers.

According to the above metal-adhesive compatibility chart, epoxy is suitable for the bonding between Nickel and Titanium, Nickel and Stainless steel, but it is not clear whether it is suitable for Molybdenum. The EPO-TEK 301-2 epoxy made by Epoxy Technology is chosen as the epoxy because of its popularity. The main property parameters for the EPO-TEK 301-2, obtained from the manufacturer's web (http: //www.Epotek.com), is shown in Table III.4. The Molybdenum is chosen as the elastic layer for the bonding strength test, because according to the analytic calculation, the combination of PZT-5H and Molybdenum can achieve the highest quasi-static displacement; the procedures for bonding the Molybdenum and Nickel shims are shown in Figure 3.2.

Table III.4 The main property parameters for the EPO-TEK 30 1(http://www.epotek.com)

Physical Properties:	
*Color: Part A: Clear/Colorless Part B: Clear/Colorless	Weight Loss:
*Consistency: Pourable Liquid	@ 200°C: 0.01%
*Viscosity (@ 100 RPM/23°C): 225 – 425 cPs	@ 250°C: 0.46%
Thixotropic Index: N/A	@ 300°C: 2.19%
*Glass Transition Temp.(Tg): ≥80°C (Dynamic Cure 20—200°C /ISO 25 Min; Ramp -10—200°C @ 20°C/Min)	Operating Temp:
	Continuous: - 55°C to 200°C
Coefficient of Thermal Expansion (CTE):	Intermittent: - 55°C to 300°C
Below Tg: 37 x 10^{-6} in/in/°C	Storage Modulus: 298,719 psi
Above Tg: 118 x 10^{-6} in/in/°C	Ions: Cl^- 61 ppm
Shore D Hardness: 80	Na^+ 104 ppm
Lap Shear Strength @ 23°C: > 2,000 psi	NH_4^+ Not detectable
Die Shear Strength @ 23°C: ≥ 15 Kg / 5,100 psi	K^+ Not detectable
Degradation Temp. (TGA): 360°C	*Particle Size: N/A
Optical Properties @ 23°C:	
Index of Refraction: 1.5318 @ 589 nm	Spectral Transmission: > 94% @ 320 nm > 99% @ 400-1200 nm > 98% @ 1200-1600 nm
Electrical & Thermal Properties:	
Thermal Conductivity: N/A	Volume Resistivity: ≥ 2 x 10^{12} Ohm-cm
Dielectric Constant (1 KHz): 3.80	Dissipation Factor (1 KHz): 0.012

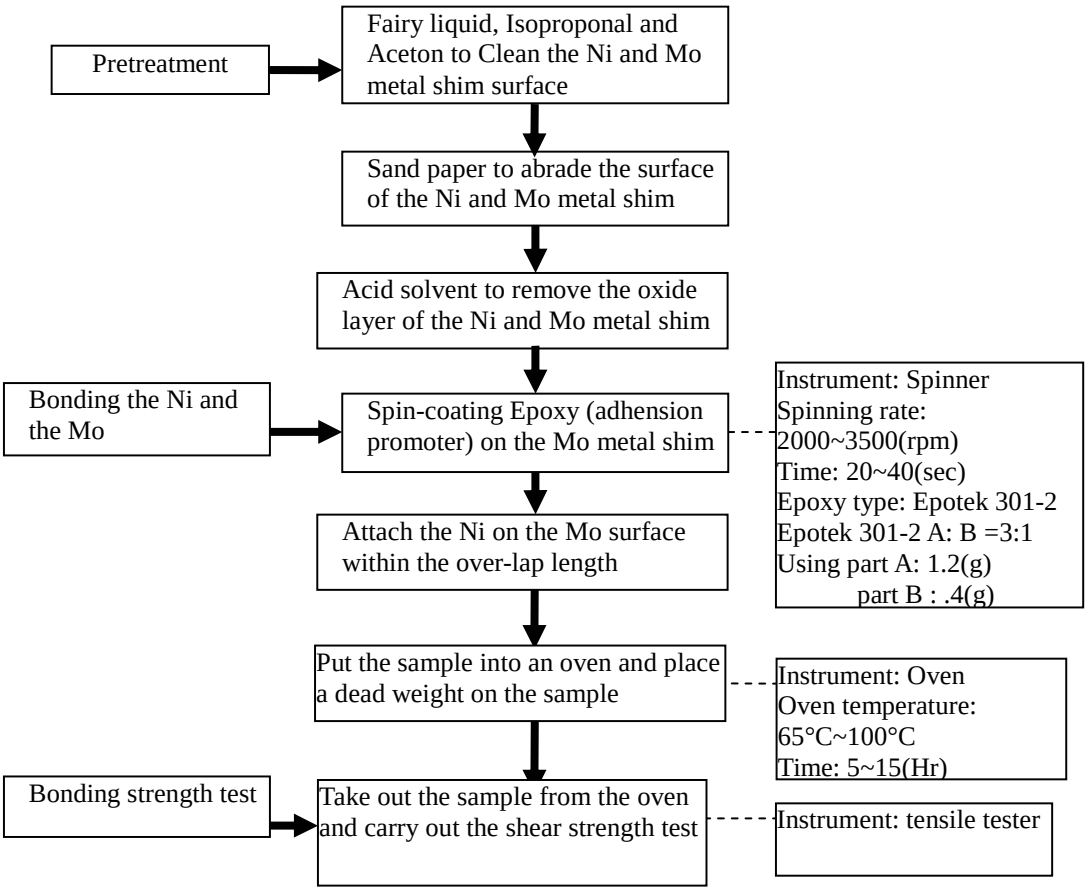

Figure 3.2 The bonding procedures of Ni to Mo

It was found that the oxide layer on the surface of the Nickel shim could be removed after etching in the nitrate acid for one minute. However, for Molybdenum shim, it takes about 10 minute to achieve the same. A wetting test, which is to spread some water onto the surface of the etched surface to see if the water can covered all of the surface, is used to verify whether the oxide layer is removed or not. The wetting test time interval is one minute. The spin coater was used to spread epoxy onto the surface of the Molybdenum metal shims, and then the Nickel and Molybdenum metal shims are bonded together, put the sample into an oven at a pre-determined temperature, and apply a dead weight onto the sample during the curing.

Although the above procedures were designed for the bonding with Molybdenum metal shims and the piezoelectric ceramics with Nickel electrode, the optimized bonding conditions are believed to be applicable for different metal shims such as the stainless steel and Titanium. According to the above compatibility chart, the epoxy are suitable for all these different metals, so no further bonding experiments for these metals were carried out.

3.4.2. The strength of the Bond

The strength of a bond is expressed by the failure load per unit area of the joint. For the simple lap joint as shown in Figure 3.3 which is used in this bonding study, the most widely adopted methods to characterize the strength of the joint is by tensile shear strength tests.

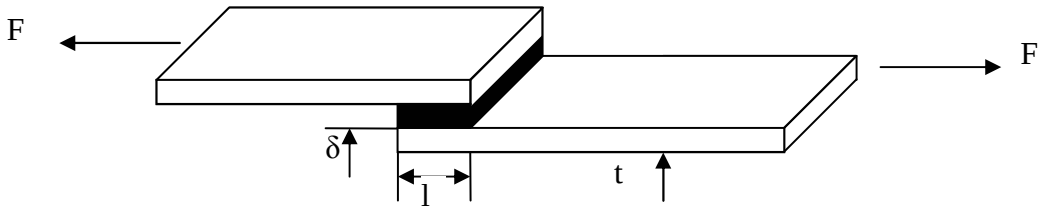

Figure 3.3 Simple lap joint and tensile shear strength test: b-adherend breadth; t-adherend thickness; l-lap length; δ-bond line thickness

In this type of loading the forces act in the plane of the adhesive layer. Shear strength is expressed by the ratio of failure load to bond area:

$$\tau_u = F / A \quad (\mathrm{N/m^2}) = F / lb \ (\mathrm{N/m^2}) \tag{3-1}$$

The Zwick/Z010 tensile tester manufactured by Zwick Inc. (Figure 3.4 (a) and Figure 3.4 (b)) was used to carry out the bonding shear strength test. The Zwick/ Z010 is a table top type tensile tester controlled by a PC. There were two jigs with this machine, the lower one was fixed on the main frame and the upper one can move upward or downward with various crosshead speed, we can use the jigs to clamp the samples and adjust appropriate crosshead speed by computer to proceed the test, the crosshead speed we used in the test was 0.5 mm/min.

The maximum load is 10 kN, and the maximum working height is 1,041 mm, maximum working width is 42 mm, and with no limitation in depth. The maximum crosshead speed is 1,000 mm/min; all the specifications of the Zwick/Z010 are listed on the Table III.5.

Figure 3.4 (a) Zwick/Z010 tensile tester

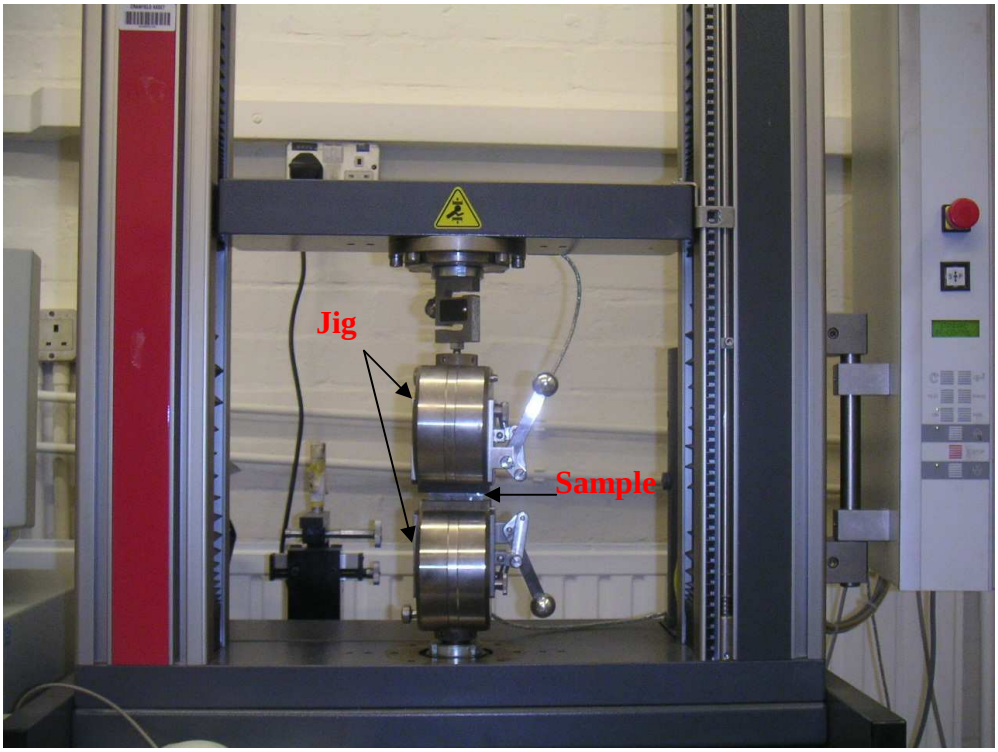

Figure 3.4 (b) Zwick/Z010 tensile tester

Table III.5 The specification of Zwick/Z010 tensile tester

Series	Z0.5	Z005	Z010	Z020
• Type	table top	table top	table top	table top
• Max. load, kN	0.5	5	10	20
• Working area, max.				
* Height, mm	596	561/1,061	1,041	1,041
* Width, mm	no limit	420	420	420
* Depth, mm	99.5	no limit	no limit	no limit
• Max. crosshead speed, mm/min	1,500	500	1,000	500
• Crosshead travel resolution, µm	0.226	0.05	0.09	0.045
• Max. power consumption, kVA	0.4	0.6	0.6	0.6

It is well known that the mechanical properties of bonded joints are the highest at loads in tension or compression. It has been established that the stresses induced by internal forces are not uniformly distributed within the area of bonding. Usually, the strength of adhesive is considerably lower than that of the material (metals in this case) to be bonded; as a result, there is a concentration of stresses at the end of the joint as shown in Figure 3.5.

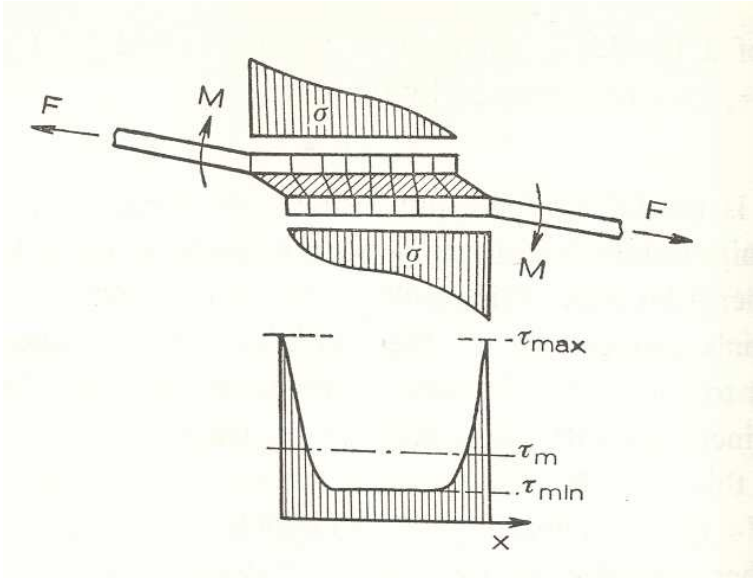

Figure 3.5 Non-uniform stress distribution along the bond area of a simple lap joint under load (exaggerated): σ-tensile stress distribution in the adherends; τ- shear stress distribution in the adhesive layer; M-bending moment due to the eccentricity of the force F.

Volkersen (Messler, 1993) proposed a theory with certain assumptions, such as identical adherends with equal thickness *t*, equal modulus of elasticity *E* and the validity of Hooke's law; it is possible to determine the relationship between adhesive layer displacement and adherend elongation. Proceeding from a second order linear differential equation he obtained the equation:

$$\tau(x) = \tau_m \frac{\sqrt{\frac{1}{2}\Delta}}{\sinh\sqrt{2\Delta}} \left\{ \cosh\left(\frac{x}{l}\sqrt{2\Delta} \right) + \cosh\sqrt{2\Delta}\left(1 - \frac{x}{l} \right) \right\} \tag{3-2}$$

It is seen that the non-uniform stress distribution can be expressed by the dimensionless factor Δ:

$$\Delta = \frac{Gl^2}{Et\delta} \tag{3-3}$$

Where *G* is the shear modules of the adhesive, *l* is the lap length, δ is the bond line thickness, and *t* is the adherend thickness, which can refer to figure 3.3. The stress concentration factor can be written as follows:

$$n = \frac{\tau_{\max}}{\tau_m} = f(\Delta) = \frac{1}{k}\coth\frac{1}{k} \tag{3-4}$$

where $\frac{1}{k} = \sqrt{\frac{1}{2}\Delta} = l\sqrt{\frac{G}{Et\delta}}$

The strength of the joint may be calculated from:

$$F = \tau_m A = \frac{\tau_{\max}}{n} lb \tag{3-5}$$

where *b* is the adherend breadth.

The factor Δ is, in principle, valid for all materials, since it contains the most important constants characterizing them. If given materials are to be bonded with a given adhesive, the G/E ratio is a fixed one. Since it is known that the bond line thickness should be the smallest possible, δ may be assumed a constant and what is left over is only the l^2/t ratio, and a so-called "joint factor" *f*, is defined:

$$f = \sqrt{t}/l \tag{3-6}$$

Hence, under comparable conditions and for a given adhesive, simple lap joint strengths are constants at constant values of *f*, and it has been found that, for a given adhesive-adherend combination, bond failure stresses are generally proportional to the square root of *f*:

$$\tau_m = \alpha\sqrt{f} = \alpha t^{\frac{1}{4}} \cdot l^{-\frac{1}{2}} \tag{3-7}$$

where α is a constant.

These considerations were used to determine the most appropriate overlap length l after the initial tests. If *l* is too long, the materials (Ni or Mo) may fail before the bond failure. If *l* is too small, the non-uniform stress distribution as shown in Figure 3.5 may be too big and the force at failure was too small, both lead to large measurement error. The best overlap length was found to be 6 mm.

3.5. The set up for the characterisation of the piezofan

Once the piezoelectric fans have been fabricated according to these optimized bonding conditions, the characterization of the piezoelectric fans was carried out. These include the setting up for measuring the tip displacement and the blocking force at the quasi-static conditions; and a high speed camera system for dynamic characterisation. The experiment results were then compared with the FEA modelling ones.

3.5.1. The set up for the quasi-static characterization

The scheme of the set up for characterizing the quasi-static displacement and blocking force of the piezoelectric fans is shown in Figure 3.6. It consists of a driving system which includes a signal generator, a high voltage amplifier, and an oscilloscope; a quasi-static displacement measuring part including an optical fibre sensor and its power supply unit; a blocking force measuring part including a load cell strain gauge and a strain gauge amplifier. The tip displacement and the blocking force were measured at the quasi-static state, because the optical fibre sensor and the load cell strain gauges are suitable for the application in low frequency only. Operating frequency less than 1Hz is recommended.

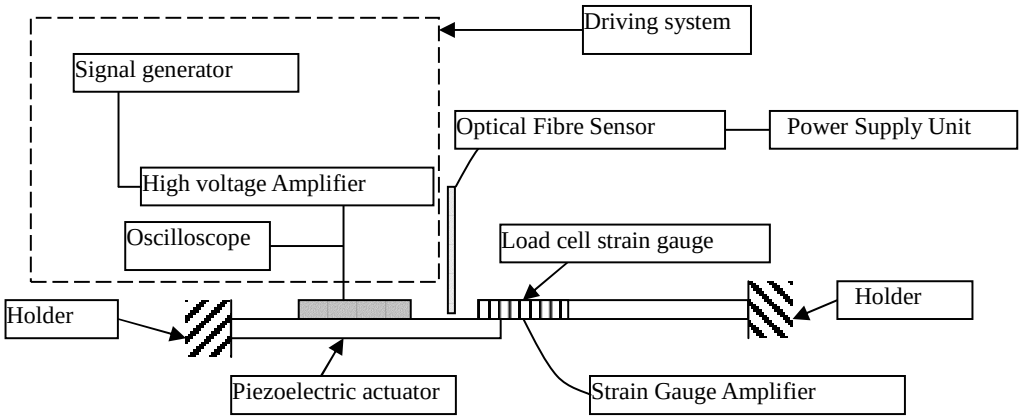

Figure 3.6 The scheme of set up for the displacement and blocking force characterization at quasi-static conditions

3.5.1.1. The Quasi-static displacement and blocking force measurement

An Optical sensor (PHILTEC Ltd, model D20, Figure 3.7) with a measuring range up to 1.27 mm has been adopted to measure the quasi-static displacement of piezoelectric fans. It is used when a target having a vibratory motion parallel to the axis of the sensor. A calibration is needed before the actual measurement; the calibration data is shown in Figure 3.8.

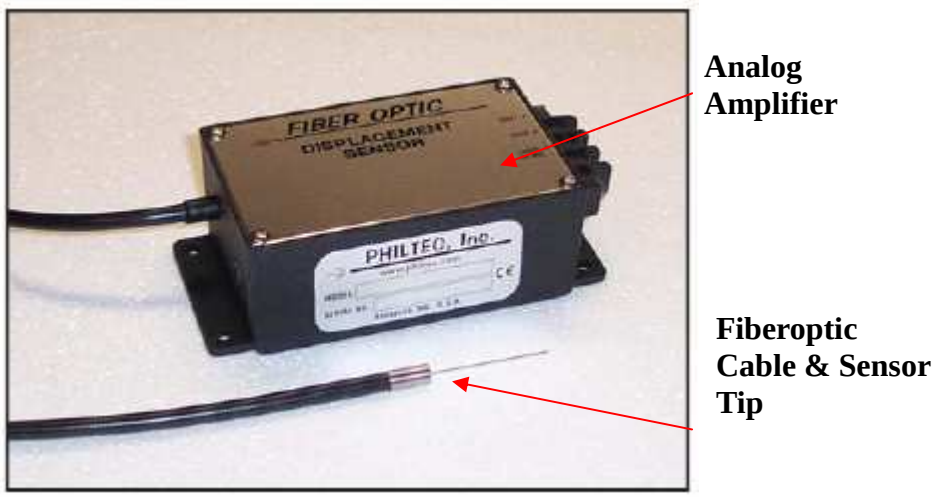

Figure 3.7 The Optical sensor (PHILTEC Ltd, model D20)

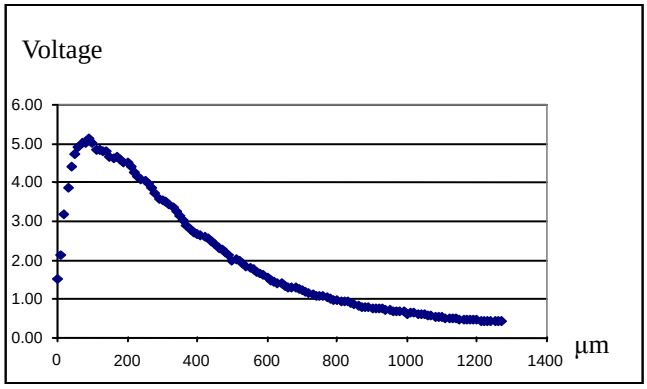

Figure 3.8 The calibration of the optical sensor (PHILTEC Ltd, model D20)

A load cell gauge sensor (Omega, model LCL-113G, Figure 3.9) with the measuring capacity up to 113 gram (about 1N) is adopted for measuring the blocking force of piezoelectric fans. A calibration is also needed before the measuring: The calibration data is shown in Figure 3.10.

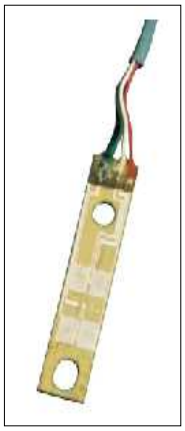

Figure 3.9 Load cell gauge sensor Omega, model LCL-113G

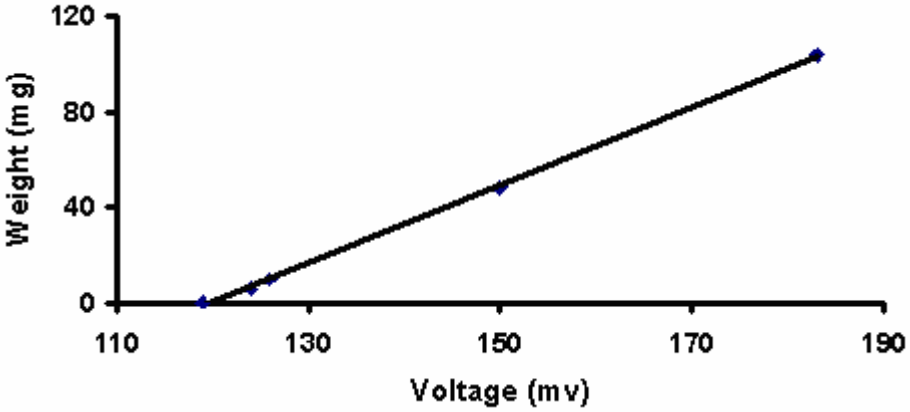

Figure 3.10 The calibration of the load cell gauge sensor

3.5.1.2. The Driving system

A piezoelectric fan needs an external voltage to drive it. The function generator (INSTEK 8216A, 0.3Hz~3MHz) can provide a voltage at a particular frequency and waveform (e.g. sine, square, triangle etc); this will be amplified by a high voltage amplifier to produce an output which can drive a piezoelectric fan to the required amplitude. An oscilloscope (HP, 54603B, 60MHz) is used to check the real voltage, operating frequency and the waveforms. An in-house high voltage amplifier was used in this study.

The circuit diagram of the high voltage amplifier is shown in Figure 3.11. This system with a single high voltage (HV) operational amplifier (op amp) can provide the output voltage from -180V to +180V. The HV op amp was obtained from the supplier Apex Microtechnology, model PA90, along with an evaluation kit, EK11, which included the necessary PCB and components. The data sheets for the PA90 and EK11 is available from the Apex Microtechnology (http://eportal.apexmicrotech.com/mainsite/index.asp). This is an inverting op amp design. Basic electronics state that for an inverting op amp, the gain is given by –Rf/Ra, where Rf is the feedback resistor and Ra is the resistor on the invert input of the op-amp. The gain for the circuit diagram in the figure is -33. This allows a -5Vdc signal to be amplified to +165V. However, to avoid the depolarization in the piezoelectric material, only positive output voltage from this high voltage amplifier was considered.

The output voltage from the PA90 HV op amps depends on the maximum voltage the dc power supply units (PSU) can offer (for an PA90 HV, the maximum voltage from power supply is ±200V which is obtained from the data sheet in Apex Microtechnology website). To drive the PA90 circuit as shown in Figure 3.11, a supply voltage of -180Vdc and +180Vdc was required, this was provided by four PSU connected in series, as shown in Figure 3.12.

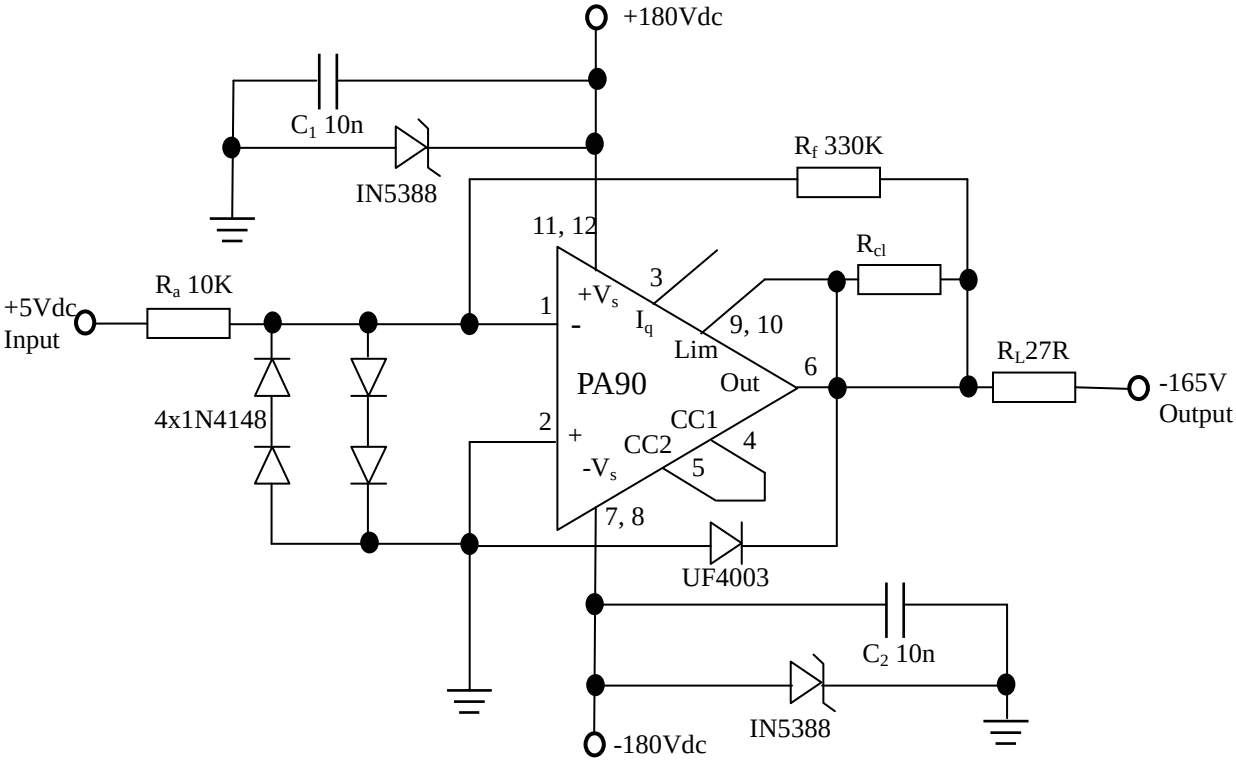

Figure 3.11 Circuit diagram for the PA90 Apex Microtechnology high voltage operational amplifier. Output range is -180V to +180V

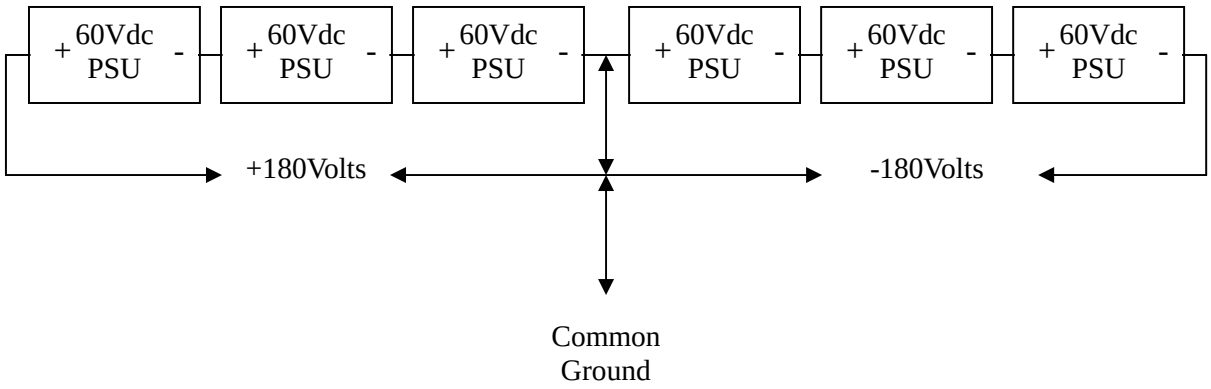

Figure 3.12 Power Supply Unit series arrangement

The current applying to the piezoelectric fans is a basic design requirement of the high voltage amplifier in order to provide enough current on the device.

Current calculation can be obtained from:

$$I = \frac{dq}{dt} = \frac{d(CV)}{dt} = C\frac{dV}{dt} \tag{3-8}$$

Where I is the current, C is the capacitance and V is the voltage.

Assume $V = V_0 \sin \omega t$ (3-9)

So $\frac{dV}{dt} = \omega V_0 \cos \omega t$ (3-10)

Therefore the maximum current is

$$I = 2\pi f V_0 C \tag{3-11}$$

The capacitance can be obtained from the equation (3-12),

$$C = \varepsilon_r \varepsilon_0 \frac{A}{d} \tag{3-12}$$

where ε_0 is the dielectric constant of vacuum which is $8.854 \times 10^{-12} Fm^{-1}$, ε_r is the relative dielectric constant of the dielectric material, A is the area and d is the thickness.

If the working frequency for a piezoelectric fan which consists of one layer of PZT-5H with a thickness of 127 μm, and of the dimensions 40mm x 10mm is below 100 Hz, the

amplitude of the working voltage is 180V, the ε_r is 3800 for the PZT-5H, then the capacitance is 79.5nF, and the maximum current would be 8.9 mA. This is far less than 167 mA-the upper limit of the PA 90. A photograph of the high voltage amplifier is shown in Figure 3.13.

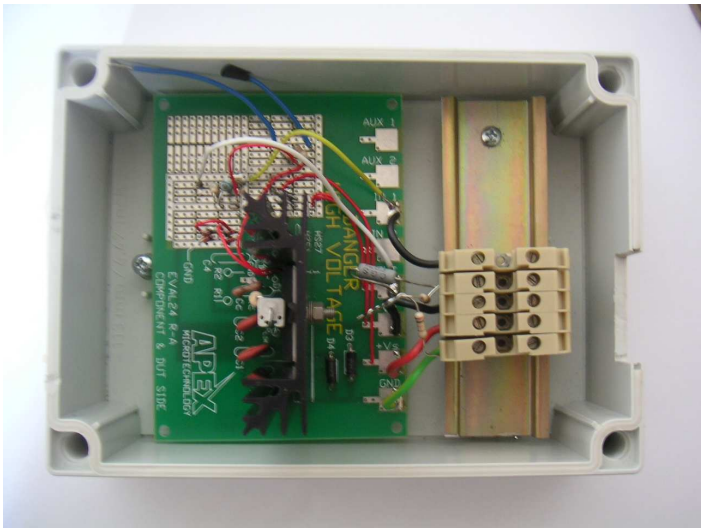

Figure 3.13 The high voltage amplifier

3.6. The coupled piezofans and dynamic motion characterisation

To mimic the three DOF's (Degree of Freedom) complex motion pattern of an insect flapping, multi-piezoelectric actuators are required. For example, two unimorph piezoelectric fans in parallel connected to a wingspan should be able to provide two DOF motions including flapping and twist motion by controlling their phase difference.

The schematic set up for the two DOF motion characterizations of a coupled piezoelectric fan is shown in Figure 3.14. The same wave (usually sinusoidal) signal from a function generator was supplied to two high voltage amplifiers. One is applied to an amplifier and then one piezoelectric fan directly; another one is connected to an in-house made phase delay circuit (which can achieve 0 to 180 degree phase delay) at first, before being connected to the other amplifier and then the other piezoelectric fan. A wing consisted of a pair of wing spars and a wing skin was attached to the two piezoelectric fans to make them coupled. The wing spar was made of carbon fibre

reinforced plastic (CFRP) and the wing skin was made of a flexible polymer material. The piezofans were clamped perpendicularly in parallel and both the flapping and twisting motions of the coupled piezofans were in the horizontal direction. A single 2MP Photron APX high-speed camera fitted with a 60mm (f2.8) Nikon lens fixed perpendicular to the plane of the coupled piezoelectric fans was used to record both the flapping and twisting motions of the wing at different operating frequencies when the coupled piezoelectric fans are under the same applied voltage $170V_{pp}$.

A frame rate of 2000 frames/s was used for an area of interest of 61.25mm x 61.25mm, that corresponded to a mean resolution of 67 µm per pixel. The camera was controlled by a PC system. For the motion characterization, the camera was used at first to take photographs of a ruler for calibration, which is located in the same plane with the edge of wing and perpendicular to the camera. Then the photographs of the vibrating wing were taken continuously for about one second to collect just over 2000 photographs, which covered a few full cycles of the vibration (the vibration frequency was usually between 10 to 100 Hz). The dynamic displacement data were obtained by comparing photographs over a full cycle and directly measuring the photographs showing the largest displacement. The real set up is shown in Figure 3.15.

Analysis of the data was completed manually using commercially available photograph software (for example, Photoshop®). Firstly, the photograph of the ruler for the calibration was analysed; a specific length equals certain pixels, then the resolution of each pixel was obtained (67 µm/per pixel); Then, all images in a full cycle were assessed to find two photographs, which show the extreme oscillation positions of the edge of the wing in a full cycle. Then the coordinates of the point 1 and point 2 in these two photographs were obtained. Therefore, the difference of the coordinates of the pixels at point 1 and point 2 can be obtained. At last, the displacement of point 1 and point 2 could be obtained by multiplying these differences of the coordinates of the pixels and the length of each pixel. The mean value of the dynamic displacement at point 1 and point 2, which equals to the displacement at the mid point between point 1 and point 2, was treated as the flapping displacement of the wing.

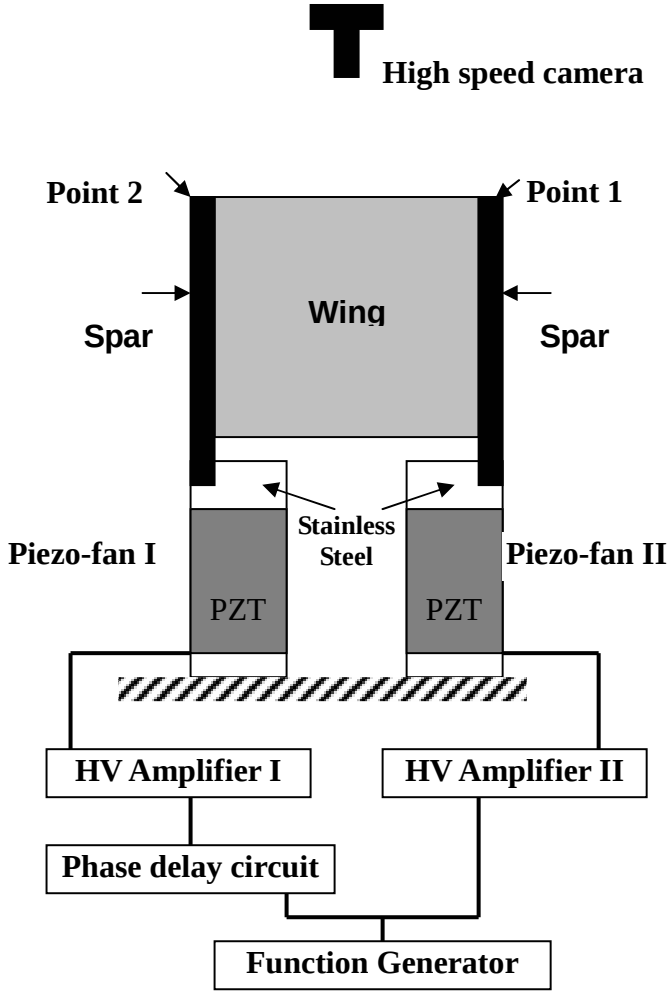

Figure 3.14 The scheme of phase control for the coupled piezoelectric fans

For measuring the twisting motion of the wing, all images in a full cycle were assessed to find two photographs, which show the two extreme twisting positions of the edge of the wing in a full cycle. Then do a superposition of these two photographs to get a new photograph. Therefore, there are two point 1s (one is marked as point 1, another marked as point 1') and point 2s (one is called point 2, another called point 2') in this new picture. If point 1 and 1', point 2 and 2' are noted respectively, then connecting the point 1 to point 2, and point 1' to point 2' would form two lines, the degree of the twisting magnitude of the wing is defined as the angle between these

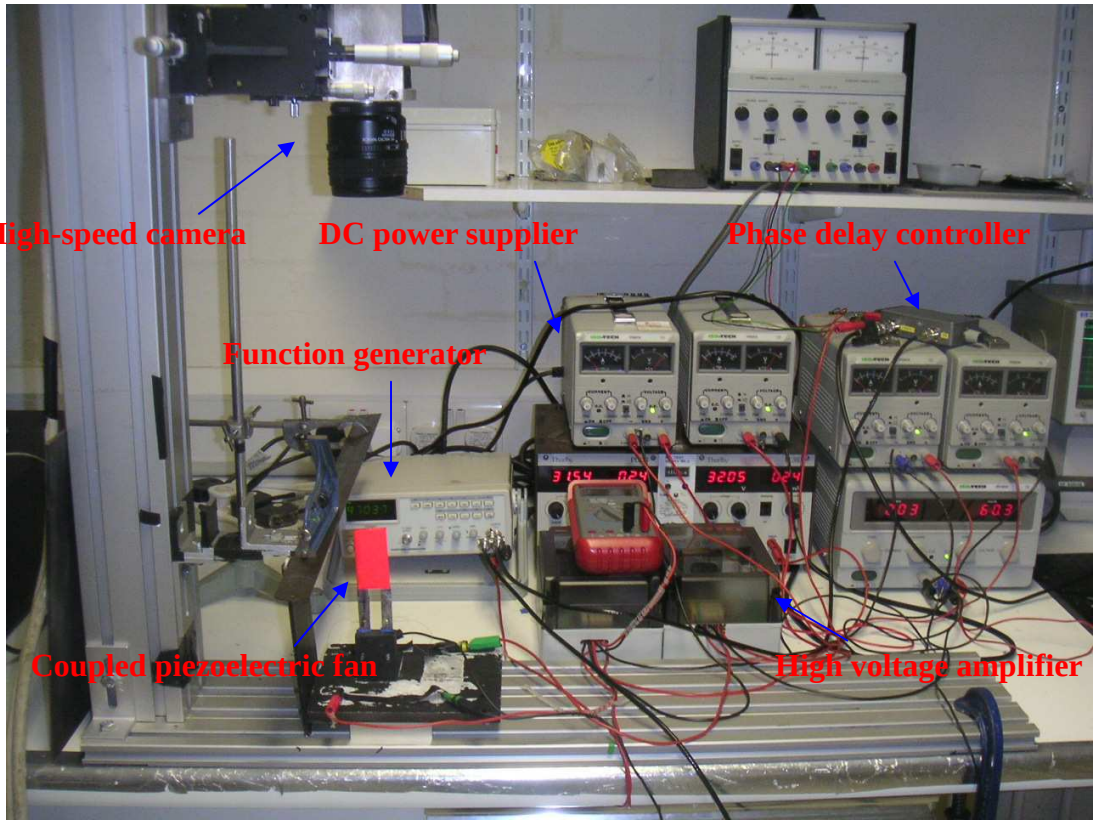

Figure 3.15 Picture of the set up for measuring the dynamic performance of the coupled piezofans.

two lines. And the distance between the two mid points of the two lines is taken as the flapping displacement magnitude of the wing vibration. Figure 3.16 shows schematically how the flapping and twisting magnitude were obtained for cases (a) mainly flapping and (b) mainly twisting motions.

Let **P1**, **P2** represent the coordinates of the point 1 and point 2, and **P1'**, **P2'** represent the coordinates of the point 1' and point 2', respectively, then from simple geometry consideration we can have:

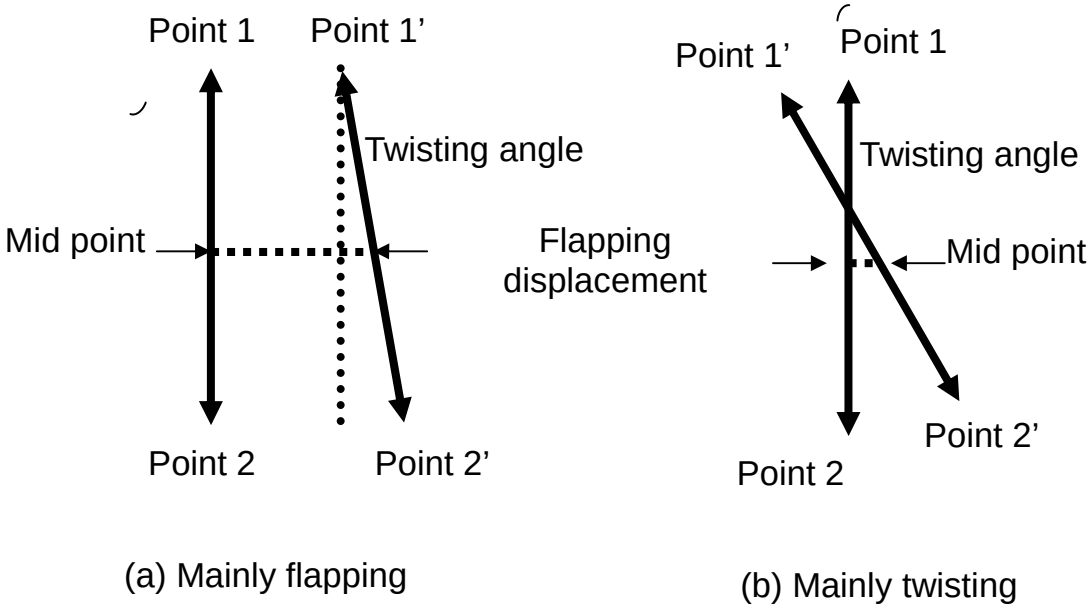

Figure 3.16 Schematic drawing on how the flapping and twisting magnitudes were obtained from two superpositioned high speed camera pictures. The line connecting points 1 (1') and 2 (2') represents the top edge of the wing

Flapping = ½[| (**P2'-P2)**+(**P1'-P1**) |] (3-13)

Twisting = 2 ASIN{0.5[| (**P2'-P2)**-(**P1'-P1**) |]/ | (**P2-P1**) | } (3-14)

Where | (**P2-P1**) | is the length of the top edge of the wing. The twisting angle can also be obtained directly from the directions of the two lines **P1P2** and **P1'P2'**, as shown in Figure 3.16.

The dynamic displacement of the piezoelectric fans themselves was obtained similarly. The top edge of the piezofan replaces the top edge of the wing.

If there is no phase difference between the two voltage inputs to the piezofan I and piezofan II, i.e. the phase delay is 0 degree, and then the two piezofans will vibrate in parallel, which enables the wingspan and the wing to flap only. However, when there is a phase delay of 180 degrees, the two piezofans are out of phase, which will produce a twisting motion in the wingspan. Adjusting and controlling the phases between 0 to 180 degrees between the two piezofans could provide the flapping and twisting for the wingspan which is a key for flapping flight control.

A phase delay circuit based on an all pass filter electrical circuit was designed to provide the phase delay between 0 to 180 degrees (Figure 3.17).

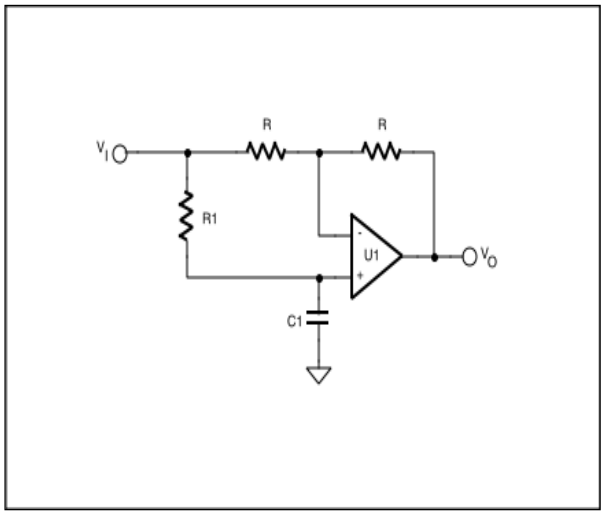

Figure 3.17 The phase delay circuit

The phase delay can be described by equation (3-15), where ω is the frequencies in rad/s, or2*pi*f, when f is in Hertz; the equation is a function of the signal frequency, resistor R_1, and Capacitor C_1.

$$phase(rad) = \tan^{-1}\left[\frac{\frac{2\omega}{R_1C_1}}{\omega^2 - \left[\frac{1}{R_1C_1}\right]^2}\right] \qquad (3\text{-}15)$$

A potentiometer (variable resistor) which can be varied from 0 to 1MΩ for the R_1 value, the C_1 value equals 0.1 µF and the resistor R being 100Ω were adopted. These can vary R_1C_1 values from 0 to 0.1, which can achieve the phase delay from 0 to 180 degrees at frequencies less than 100 Hz. A photograph of the phase delay controller is shown in Figure 3.18.

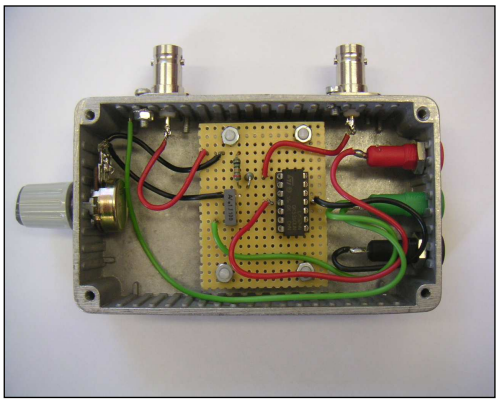

Figure 3.18 The phase delay circuit (Where R=100Ω, R1=0-1M Ω, C1=0.1μF)

Assuming the frequency of the signal is less than 100 Hz, varying the R_1C_1 value from 0 to 0.14, the theoretical phase delays at different frequencies from 0 to 100 Hz are shown in Figure 3.19. The actual phase delay of the two input voltages can be read directly from the wave forms on the oscilloscope, as shown in Figure 3.20.

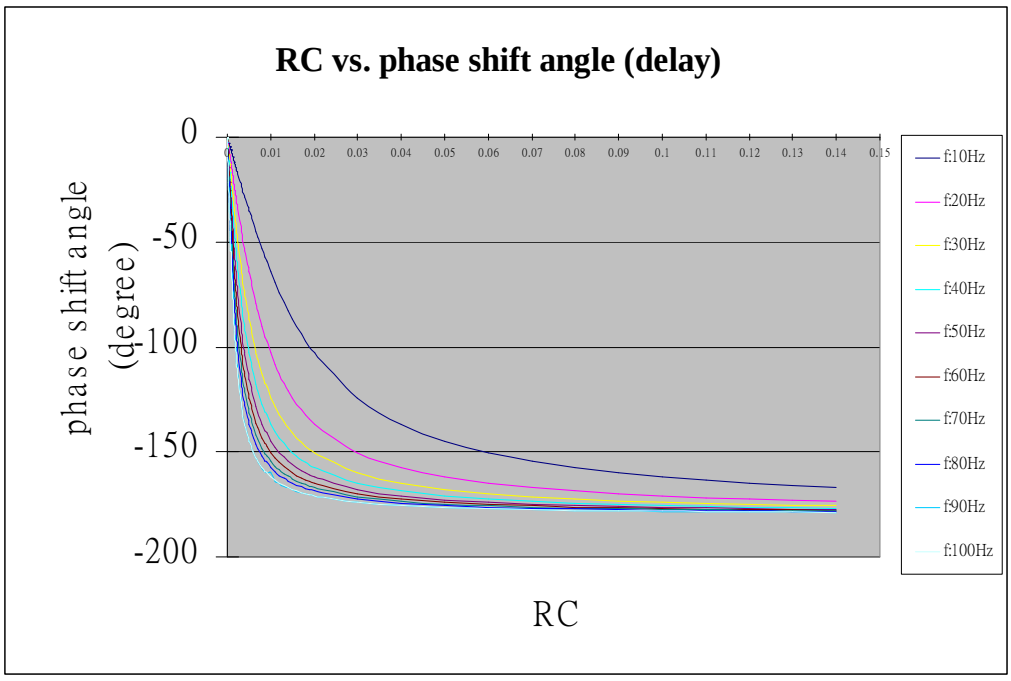

Figure 3.19 The phase delay degrees at different RC values

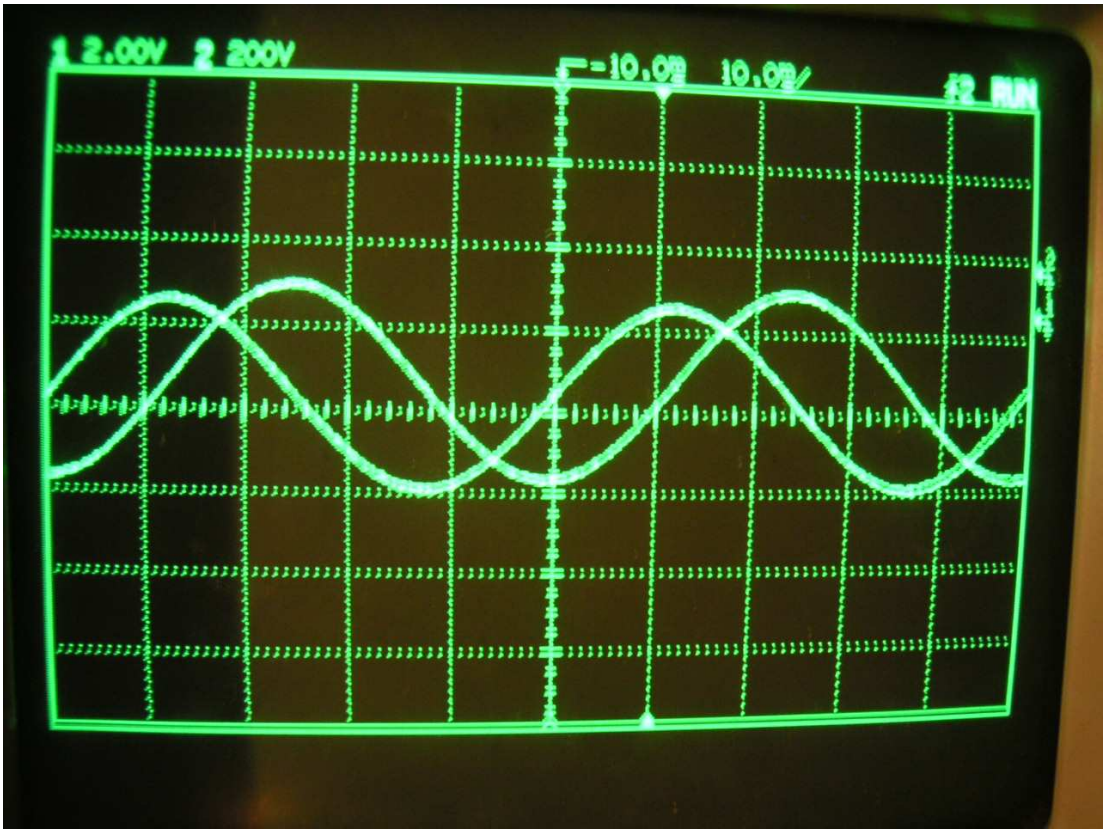

Figure 3.20 Phase-delay of the two signals can be read directly from the two wave forms on the oscilloscope**.**

CHAPTER 4

THEORETICAL ANALYSIS

This chapter gives a theoretical analysis of the piezofan structures. Starting from the basic state equations for piezoelectric materials, the detailed derivation of equations relating the properties of piezoelectric actuators, such as their bending amplitude and resonant frequency with their materials and geometrical parameters are presented in this chapter. Firstly we deal with the quasi-static operation, then move to the more complex dynamic operation. For dynamic operation we start from simple structure, namely unimorph cantilever, then to more complex piezofan structures which have non-uniform cross section along its length. Forced vibration and the free vibration are discussed. It should be noted the all the main equations can be found in literature. Mathematical derivations are presented in details here to aid the understanding of the mechanisms involved, and also to serve as a reference on the systematic treatment of the related problems.

4.1 Analysis for unimorph actuators at quasi-static operation

The governing equations for unimorph devices have been investigated by many researchers; the following derivation resembles Smits's work (Smits et al., 1991).

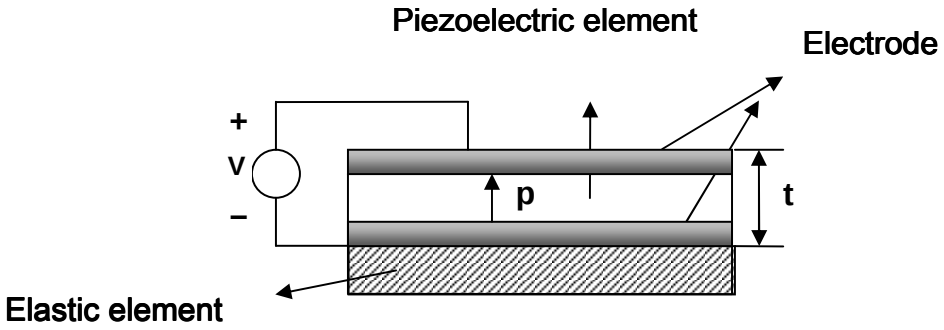

Figure 4.1 Schematic configuration of a piezoelectric unimorph

A unimorph configuration is shown in Figure 4.1. It consists of a piezoelectric element between electrodes joined over its entire length to an elastic element; this is often a metal or a dielectric such as glass or Si wafer.

The state equations for piezoelectric material are: (ANSI/IEEE [1987]):

$$S_{ij} = s^{E}_{ijkl} T_{kl} + d_{ijm} E_m \tag{4-1}$$

$$D_n = d_{nkl} T_{kl} + \varepsilon^{T}_{nm} E_m \tag{4-2}$$

Where the strain tensor is denoted by S_{ij}, stress tensor is denoted by T_{kl}, the electric field by E_m, the dielectric displacement by D_n, the permittivity at constant stress by ε^{T}_{nm} , the piezoelectric coefficient tensor by d_{nkl} and the compliance tensor at constant electric field by s^{E}_{ijkl}.

It is customary to reduce the number of subscripts by using the symmetry of S and T. Subscripts are replaced according to the following scheme: 11→1, 22→2, 33→3, 23→4, 13→5, 12→6.

Hence, the basic equations for piezo materials are

$$S^{p}_{1} = s^{p}_{11} T^{p}_{1} + d_{31} E_3 \tag{4-3}$$

$$D^{p}_{3} = d_{31} T^{p}_{1} + \varepsilon_{33} E_3 \tag{4-4}$$

Where *p* denotes piezo material, then the internal energy is

$$U^{p} = 1/2 S^{p}_{1} T^{p}_{1} + 1/2 D^{p}_{3} E_3 \tag{4-5}$$

Where $1/2 S^{p}_{1} T^{p}_{1}$ is the elastic energy and the $1/2 D^{p}_{3} E_3$ is the electric energy.

If there is only the piezo material as shown in Figure 4.2, when an electric field parallel to the polarization was applied, then the piezo material expands along the thickness direction and contracts in the length direction.

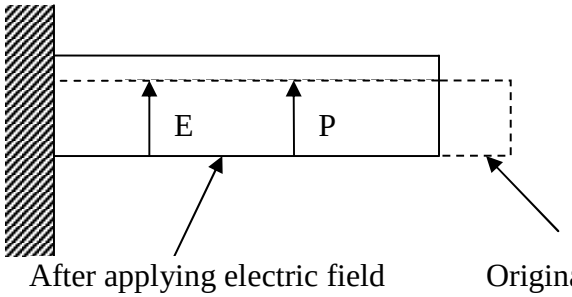

Figure 4.2 Schematic of piezo material before and after the applying of electric field parallel to the polarization (not to the scale)

but if there is another elastic layer (generally is metal shim, or Si) bonded to the piezo material, the piezo material tends to become shorter after applying an electric field , while the elastic layer resists the contraction caused by the piezo material, therefore, the force acting upon the piezo is tensile directed outward, and the force acting on the elastic layer is compressional directed inward, so the whole cantilever beam bends upwardly, at equilibrium there are bending moments M^{p} and M^{el}, as Figure 4.3 shows,

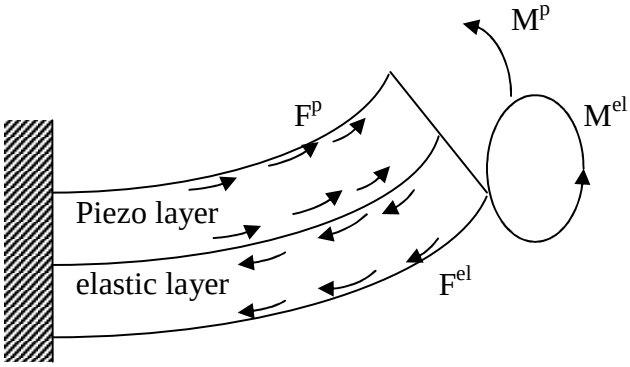

Figure 4.3 Schematic of the force and moment diagram in an unimorph after applying an electric field

The strain due to the tensional force F^{p} in piezo layer is S_p^F

$$S_p^F = \frac{F^p}{wh_p} \cdot s_{11}^p \tag{4-6}$$

Where w is the width of the cross section of the piezo layer, h_p is the height of the piezo material and s_{11}^p is the compliance of the piezo layer.

The strain due to the force F^{el} in the elastic layer is S_{el}^F

$$S_{el}^F = \frac{F^{el}}{wh_{el}} \cdot s_{11}^{el} \tag{4-7}$$

Where w is the width of the of elastic layer, and h_{el} is the height of the elastic layer and s_{11}^{el} is the compliance of the elastic layer.

The strain at the low surface of the piezo layer due to the bending moment is S_p^M

$$S_p^M = \frac{h_p}{2} \cdot \frac{M^p}{EI} \tag{4-8}$$

E and I are the Young's module and inertial moment of the piezo layer, respectively.

The strain at the upper surface of the elastic layer due to the bending moment is S_{el}^M

$$S_{el}^M = \frac{h_{el}}{2} \cdot \frac{M^{el}}{E^{el} I^{el}} \tag{4-9}$$

E_{el} and I_{el} are the Young's module and inertial moment of the elastic layer, respectively.

The strain due to the electric field in the piezo layer is S^E

$$S^E = d_{31} \cdot E_3 \tag{4-10}$$

where d_{31} is the transverse piezoelectric coefficient and E_3 is the electric field in the z-axis.

For the piezo material, the total strain is S^p,

$$S^p = S_p^F + S_p^M + S^E \tag{4-11}$$

For the elastic layer, the total strain is S^{el},

$$S^{el} = S_{el}^F + S_{el}^M \tag{4-12}$$

Because the total strain at the lowest surface of the piezo layer S^p equals to the total strain at the uppermost surface of the elastic layer S^{el}, so

$$\frac{F^p}{wh_p} \cdot s_{11}^p + \frac{h_p}{2} \cdot \frac{M^p}{E^p I^p} + d_{31} \cdot E_3 = -\frac{F^{el}}{wh_{el}} \cdot s_{11}^{el} - \frac{h_{el}}{2} \cdot \frac{M^{el}}{E^{el} I^{el}} \tag{4-13}$$

and the piezo and elastic layer have the same curvature R after the bending, so

$$R = \frac{M^{el}}{E^{el} I^{el}} = \frac{M^p}{E^p I^P} \tag{4-14}$$

And

$$\frac{E^p}{E^{el}} = \frac{S_{11}^{el}}{S_{11}^p} \quad ,$$

So,

$$M^{el} = M^P \left(\frac{h_{el}}{h_p}\right)^3 \left(\frac{S_{11}^p}{S_{11}^{el}}\right) \tag{4-15}$$

At the equilibrium, the total force should be zero, so

$$F^p = F^{el} = F \tag{4-16}$$

and total momentums should be zero as well, so

$$M^P + M^{el} - F\left(\frac{h_p}{2} + \frac{h_{el}}{2}\right) = 0 \tag{4-17}$$

From (15) and (17), we obtain,

$$M^P = \frac{F(h_p + h_{el})}{2\left[1 + \left(\frac{h_{el}}{h_p}\right)^3 \cdot \left(\frac{s_{11}^p}{s_{11}^{el}}\right)\right]} \tag{4-18}$$

From (13) and (18), we obtain,

$$F = -\frac{d_{31} E_3 w h_p h_{el} \left[s_{11}^{el} (h_p)^3 + s_{11}^p (h_{el})^3\right]}{K} \tag{4-19}$$

Where $K = 4s_{11}^p s_{11}^{el} h_{el} (h_p)^3 + 4s_{11}^p s_{11}^{el} (h_{el})^3 h_p + (s_{11}^p)^2 (h_{el})^4 + (s_{11}^{el})^2 (h_p)^4 + 6s_{11}^p s_{11}^{el} (h_{el})^2 (h_p)^2$

(4-20)

From this the deflection at the tip, the curvature and the internal energy of the beam can be calculated. Similarly, the response of unimorph under different loading conditions can be obtained.

In summary, the response of an unimorph under different loading conditions can be

expressed by a 4 x 4 matrix equation, as follows:

$$\begin{pmatrix}\alpha\\ \delta\\ \nu\\ Q\end{pmatrix} = A\begin{bmatrix} \frac{12L}{Kw} & \frac{6L^2}{Kw} & \frac{2L^3}{K} & \frac{-6d_{31}BL}{K} \\ \frac{6L^2}{Kw} & \frac{4L^3}{Kw} & \frac{3L^4}{2K} & \frac{-3d_{31}BL}{K} \\ \frac{2L^3}{K} & \frac{3L^4}{2K} & \frac{3L^5 w}{5K} & \frac{-d_{31}BL^3 w}{K} \\ \frac{-6d_{31}BL}{K} & \frac{-3d_{31}BL}{K} & \frac{-d_{31}BL^3 w}{K} & \frac{Lw}{Ah_p}\left(\varepsilon_{33}^T - \frac{d_{31}^2 h_{el}\left(s_{11}^{el}h_p^3 + s_{11}^P h_{el}^3\right)}{K}\right) \end{bmatrix}\begin{pmatrix}M\\ F\\ P\\ V\end{pmatrix} \tag{4-21}$$

V= applied electric voltage L= actuator length

M= moment w= actuator width

F = force h_{el}= the thickness of metal layer

P= uniform load h_p= the thickness of piezo layer

α= bending angle ε_{33}^T = the permittivity at constant stress

δ = tip deflection s_{11}^{el} = Elastic Compliance of metal layer

ν = volume displacement s_{11}^{p} = Elastic Compliance of piezo material

Q = electrical charge d_{31}= Piezoelectric coefficient

$$A = s_{11}^{el}s_{11}^{P}\left(s_{11}^{p}h_{el} + s_{11}^{el}h_p\right) \qquad B = \frac{h_{el}\left(h_{el} + h_p\right)}{\left(s_{11}^{p}h_{el} + s_{11}^{el}h_p\right)}$$

Wang et al. (1998) also derived analytical expressions relating the bending resonant frequency, tip deflection, blocking force, equivalent moment with the geometrical dimensions, Young's modulus, densities and piezoelectric coefficients of the cantilever unimorph actuators. The formula is summarized as following:

For the 1st bending resonance of a unimorph cantilever has the formula as shown in equation (4-22),

$$f_r = \frac{3.52t}{4\pi L^2}\sqrt{\frac{E_p}{3\rho_p}}\left[\frac{A^2B^4 + 2A(2B + 3B^2 + 2B^3) + 1}{(1+BC)(AB+1)(1+B)^2}\right]^{1/2} \tag{4-22}$$

Where $A = E_m / E_p$, $B = t_m / t_p$, $C = \rho_m / \rho_p$, $t_m + t_p = t$

f_r : Fundamental bending resonance

E_m : Young's modulus of passive elastic layer (metal)

E_p : Young's modulus of piezoelectric layer

t_m : Thickness of passive elastic layer (metal)

t_p : Thickness of piezoelectric layer

t : Total thickness of the unimorph cantilever

ρ_m : Density of passive elastic layer (metal)

ρ_p : Density of piezoelectric layer

L: Length of the unimorph actuator

A: Young's modulus ratio of metal layer and piezoelectric layer

B: Thickness ratio of metal layer and piezoelectric layer

C: Density ratio of metal layer and piezoelectric layer

For an unimorph cantilever, the tip deflection is expressed as equation (23),

$$\delta = \frac{3L^2}{2t} \cdot \frac{2AB(1+B)^2}{A^2B^4 + 2A(2B + 3B^2 + 2B^3) + 1} \cdot d_{31}E_3 \tag{4-23}$$

It can be proved that this gives the same value as Smit's matrix (Smit et al., 1991).

Equation (4-23) is under the condition of a fixed actuator thickness t (the piezoelectric layer thickness plus the elastic layer thickness). Sometimes, for obtaining the displacement for the fixed piezoelectric layer thickness with various elastic layer thicknesses, then transforming $t_p = t/(1+B)$, so equation (4-23) becomes equation (4-24)

$$\delta = \frac{3L^2}{2t_p} \cdot \frac{2AB(1+B)}{A^2B^4 + 2A(2B + 3B^2 + 2B^3) + 1} \cdot d_{31}E_3 \tag{4-24}$$

For blocking force, the unimorph cantilever has the formula as equation (4-25)

$$F_{bl} = \frac{3wt^2 E_p}{8L} \cdot \frac{2AB}{(AB+1)(B+1)} \cdot d_{31} E_3 \tag{4-25}$$

Where w is the width of the cantilever, and E_p is the Young's modulus for piezoelectric layer, E_3 is the electric field in Z-axis.

In this project, equations (4-22)-(4-25) were used mainly to calculate the quasi-static properties of piezoelectric unimorph cantilevers for their simplicity.

4.2 Analysis for piezoelectric fan at dynamic operation

The dynamic response of a piezoelectric unimorph cantilever will be derived first, then for the piezofan configuration where the passive layer has different length with the active layer. Finally a configuration resembles the actual structure used in the experiments will be discussed. In this final configuration, there are three different sections: a section for clamping, a piezoelectric active section and a passive blade section.

4.2.1 Unimorph cantilever beam

4.2.1.1 Dynamic treatment of a cantilever bar

A cantilever beam is a beam that is completely fixed at one end and completely free at the other end, which is shown in Figure 4.4.

Figure 4.4 Schematic of a cantilever bar

From a textbook on mechanics (Thomson, 1993), the equation of the transversal displacement for a uniform cantilever beam is

$$EI\frac{\partial^4 Z(x,t)}{\partial x^4}+m\frac{\partial^2 Z(x,t)}{\partial t^2}+b\frac{\partial Z(x,t)}{\partial t}=f(x,t) \tag{4-26}$$

First, consider no damping, so *b*=0, and no external force, so *f(x,t)*=0, and the equation becomes

$$EIZ''''+\rho A\ddot{Z}=0 \tag{4-27}$$

Here ‘ represents ∂/∂x, and a dot on top represents time derivation ∂/∂t. ρ is the mass density and A the cross section area of the beam.

Let $Z(x,t)=\phi(x)T(t)$, then the equation becomes

$$EI\phi''''(x)T(t)+\rho A\phi(x)\ddot{T}(t)=0 \tag{4-28}$$

Assuming $T(t)=T(t)e^{i\omega t}$, then the equation (4-28) becomes equation (4-29), and finally can be simplified to the equation (4-32).

$$EI\phi''''(x)T(t)-\rho A\omega^2\phi(x)T(t)=0 \tag{4-29}$$

This leads to

$$EI\phi''''(x)-\rho A\omega^2\phi(x)=0 \tag{4-30}$$

$$\phi''''(x)-\frac{\rho A\omega^2}{EI}\phi(x)=0 \tag{4-31}$$

$$\phi''''(x)-\beta^4\phi(x)=0 \tag{4-32}$$

The general solution to the above equation is

$$\phi=C_1\cos\beta x+C_2\sin\beta x+C_3\cosh\beta x+C_4\sinh\beta x \tag{4-33}$$

Considering the boundary conditions, which are

$\phi(0) = 0$, displacement at root=0 (4-34)

$\phi'(0) = 0$, slope at root=0 (4-35)

$\phi''(L) = 0$, bending moment at the free end=0 (4-36)

$\phi'''(L) = 0$, shear force at free end=0 (4-37)

From (4-34) and (4-35) we obtain

$$\begin{cases} C_1 + C_3 = 0 \\ C_2\beta + C_4\beta = 0 \end{cases} \Rightarrow \begin{cases} C_3 = -C_1 \\ C_4 = -C_2 \end{cases} \quad \beta \neq 0 \tag{4-38}$$

So $\phi = C_1(\cos\beta x - \cosh\beta x) + C_2(\sin\beta x - \sinh\beta x)$

$\phi'(x) = C_1(-\sin\beta x - \sinh\beta x)\beta + C_2(\cos\beta x - \cosh\beta x)\beta$

From (4-36) and (4-37) we obtain

$$C_1(-\cos\beta L - \cosh\beta L)\beta^2 + C_2(-\sin\beta L - \sinh\beta L)\beta^2 = 0 \tag{4-39}$$

$$C_1(\sin\beta L - \sinh\beta L)\beta^3 + C_2(-\cos\beta L - \cosh\beta L)\beta^3 = 0 \tag{4-40}$$

To have non-trivial solutions, the determinant must be zero

$$\begin{vmatrix} +\cos\beta L + \cosh\beta L & +\sin\beta L + \sinh\beta L \\ -\sin\beta L + \sinh\beta L & \cos\beta L + \cosh\beta L \end{vmatrix} = 0 \tag{4-41}$$

$$(\cos\beta L + \cosh\beta L)^2 - (\sin\beta L + \sinh\beta L)(\sinh\beta L - \sin\beta L) = 0$$

$$\cos^2\beta L + \cosh^2\beta L + 2\cos\beta L\cosh\beta L - \sin^2\beta L + \sin^2\beta L = 0$$

$$2 + 2\cos\beta L + \cosh\beta L = 0$$

$$1 + \cos\beta L\cosh\beta L = 0$$

(4-42)

The first three roots are

$$\beta_1 = \frac{1.88}{L}, \beta_2 = \frac{4.69}{L}, \beta_3 = \frac{7.85}{L} \tag{4-43}$$

Therefore the corresponding natural frequencies are

$$\frac{\rho A}{EI}\omega_i^2 = \beta_i^4, \quad \omega_i = \sqrt{\frac{EI}{\rho A}} \cdot \beta_i^2 \Rightarrow \omega \propto \frac{1}{L^2}\sqrt{\frac{EI}{\rho A}} \tag{4-44}$$

And $\frac{C_2}{C_1} = -\frac{\cos\beta_i L + \cosh\beta_i L}{\sin\beta_i L + \sinh\beta_i L}$

Therefore, the solution is

$$\phi_i = C_1\left[(\cos\beta_i x - \cosh\beta_i x) - \frac{\cos\beta_i L + \cosh\beta_i L}{\sin\beta_i L + \sinh\beta_i L}(\sin\beta_i x - \sinh\beta_i x)\right] \qquad (4\text{-}45)$$

C_1 is an arbitrary constant and the first three mode shapes are shown in Figure 4.5

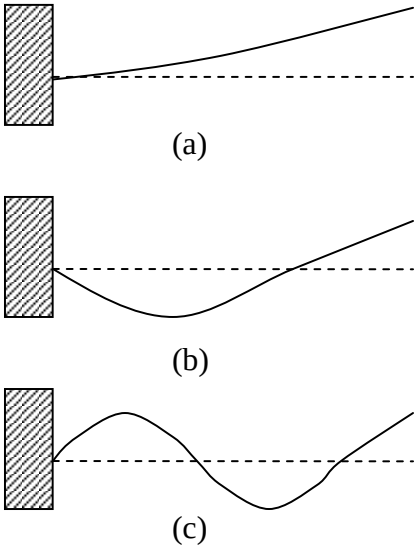

Figure 4.5 The mode shapes of a cantilever beam
(a) first mode (b) second mode (3) third mode

Put the $Z = \sum \phi_i T_i$ into the original equation

$$EI\sum_i \phi_i'''' T_i + m\sum_i \phi_i \ddot{T}_i + b\sum_i \phi_i \dot{T}_i = f(x,t)$$

$$EI\sum_i \beta^4 \phi_i T_i + m\sum_i \phi_i \ddot{T}_i + b\sum_i \phi_i \dot{T}_i = f(x,t)$$

$$\sum_i \phi_i (m\omega_i^2 T_i + m\ddot{T}_i + b\dot{T}_i) = f(x,t)$$

$$\sum_i \phi_i (\ddot{T}_i + b/m\dot{T} + \omega_i^2 T_i) = \frac{1}{m} f(x,t) \tag{4-46}$$

Consider a damping that is proportional to the velocity or frequency, then

$$\frac{b}{m} = 2\omega_i \gamma$$

Then $$\sum_i \phi_i (\ddot{T}_i + 2\omega_i \gamma \dot{T} + \omega_i^2 T_i) = \frac{1}{m} f(x,t) \tag{4-47}$$

For simplicity, considering $\frac{1}{m} f(x,t) = 0$ at first,

Therefore,

$$\ddot{T}_i + 2\omega_i \gamma \dot{T}_i + \omega_i^2 T_i = 0$$

Let $T_i = d_i \cdot e^{\xi_i t}$

$$\dot{T}_i = d_i \xi_i \cdot e^{\xi_i t}$$

$$\ddot{T}_i = \xi_i^2 \cdot d_i e^{\xi_i t}$$

$$(\xi^2 + 2\omega_i \gamma \xi + \omega_i^2)\, T_i = 0$$

$$(\xi_i^2 + 2\omega_i \gamma \xi_i + \omega_i^2) = 0$$

$$\xi_i = \frac{-2\omega_i \gamma \pm \sqrt{4\omega_i^2 \gamma^2 - 4\omega_i^2}}{2}$$

$$= \frac{-2\omega_i \gamma \pm 2\omega_i \sqrt{\gamma^2 - 1}}{2}$$

$$= -\omega_i \gamma \pm \omega_i \sqrt{\gamma^2 - 1}$$

$$= -\omega_i \gamma \pm \omega_i j \sqrt{\frac{1}{\gamma^2} - 1}$$

$$= \omega_i (\pm \gamma j \sqrt{\frac{1}{\gamma^2} - 1} - \gamma) \qquad j^2 = -1$$

Assume, $\gamma \langle\langle 1$ so

$$\xi_i = \omega_i (\pm \gamma j \sqrt{\frac{1}{\gamma^2} - 1} - \gamma)$$

$$\sim \omega_i (\pm j - \gamma) = j\omega_i (\pm 1 + j\gamma)$$

So, $T_i = e^{j\omega_i t(1 + j\gamma)} = e^{j\omega_i t} \cdot e^{-\omega_i \gamma t}$

The constant d_i is omitted.

Therefore the complete solution for T_i is

$$T_i = e^{j\omega_i t(1+j\gamma)} = e^{-\omega_i \gamma t} \cdot (A_i \cos \omega_i t + B_i \sin \omega_i t) \tag{4-48}$$

Assume the initial conditions are $T_i(0) = A_{i0}$

$\dot{T}_i(0) = B_{i0}$ So $A_i = A_{i0}$

$\omega_i B_i = B_{i0}$, $B_i = \dfrac{B_{i0}}{\omega_i}$

$$T_i = e^{-\omega_i \gamma t} \cdot (A_{i0} \cos \omega_i t + \frac{B_{i0}}{\omega_i} \sin \omega_i t)$$

If $\begin{cases} C_{i0} \cos \delta_{i0} = A_{i0} \\ C_{i0} \sin \delta_{i0} = \dfrac{B_{i0}}{\omega_i} \end{cases} \Rightarrow \tan \delta_{i0} = \dfrac{B_{i0}}{A_{i0}\omega_i}$

$$T_i = e^{-\omega_i \gamma t} \cdot C_{i0} \cos(\omega_i t + \delta_{i0})$$

omitting the constant, $T_i = e^{-\omega_i \gamma t} \cdot \cos(\omega_i t + \delta_{i0})$

Therefore, the complete solution is

$$Z(x,t) = \sum \phi_i T_i = \sum_i \phi_i(x) T_i(t)$$

$$= C \sum_i e^{-\omega_i \gamma t} \cos(\omega_i t + \delta_{i0}) \cdot \left[\cos \beta_i x - \cosh \beta_i x - \frac{\cos \beta_i L + \cosh \beta_i L}{\sin \beta_i L + \sinh \beta_i L} \cdot (\sin \beta_i x - \sinh \beta_i x) \right] \tag{4-49}$$

4.2.1.2 The forced vibration of a cantilever beam

From equation (4-47)

$$\sum_i \phi_i(\ddot{T}_i + 2\omega_i\gamma\dot{T}_i + \omega_i^2 T_i) = \frac{1}{m} f(x,t)$$

For a force vibration, assume $\frac{1}{m} f(x,t) = f_0 \cos(\omega t)$

$$\sum_i \phi_i(\ddot{T}_i + 2\omega_i\gamma\dot{T}_i + \omega_i^2 T_i) = f_0 \cos(\omega t)$$

Since ϕ_i is an eigenvector of the equation, due to the orthogonality, there is

$$\int_0^L \sum_{i\neq j} \phi_i\phi_j dx = 0$$

So, $\ddot{T}_i + 2\omega_i\gamma\dot{T}_i + \omega_i^2 T_i = \int \phi_i f_0 \cos(\omega t)dx / (\int \phi_i^2 dx) = F_{Di}\cos(\omega t)$ (4-50)

Let $T_i = A_i \cos(\omega t) + B_i \sin(\omega t) = D_i \cos(\omega t + \delta_i)$

$$\dot{T}_i = -D_i\omega\sin(\omega t + \delta_i)$$

$$\ddot{T}_i = -D_i\omega^2 \cos(\omega t + \delta_i)$$

$$-D_i\omega^2\cos(\omega t+\delta_i) - D_i\omega\sin(\omega t+\delta_i)\cdot 2\omega_i\gamma + \omega_i^2 D_i\cos(\omega t+\delta_i) = F_{Di}\cos(\omega t)$$

$$D_i(\omega_i^2-\omega^2)(\cos\omega t\cdot\cos\delta_i - \sin\omega t\cdot\sin\delta_i) - D_i\omega(\sin\omega t\cos\delta_i + \cos\omega t\sin\delta_i)2\omega_i\gamma = F_{Di}\cos(\omega t)$$

$$[D_i(\omega_i^2-\omega^2)\cos\delta_i - D_i\omega\sin\delta_i\times 2\omega_i\gamma - F_{Di}]\cos(\omega t) - [D_i(\omega_i^2-\omega^2)\sin\delta_i - D_i\omega\cos\delta_i\times 2\omega_i\gamma]\sin\omega t = 0$$

So, $D_i(\omega_i^2-\omega^2)\cos\delta_i - D_i\omega\sin\delta_i\times 2\omega_i\gamma - F_{Di} = 0$

$$D_i(\omega_i^2-\omega^2)\sin\delta_i - D_i\omega\cos\delta_i\times 2\omega_i\gamma = 0$$

$$D_i(\omega_i^2-\omega^2)\sin\delta_i = 2\omega\omega_i D_i\gamma\cos\delta_i$$

$$t_g\delta_i = \frac{2\omega\omega_i\gamma}{\omega_i^2-\omega^2}$$

$$(\omega_i^2-\omega^2)\cos\delta_i - 2\omega_i\omega\gamma\cdot\sin\delta_i = F_{Di}/D_i$$

$$(\omega_i^2-\omega^2)\sin\delta_i - 2\omega_i\omega\ \gamma\cdot\cos\delta_i = 0$$

So $(\omega_i^2 - \omega^2)^2 + (2\omega_i\omega\gamma)^2 = (F_{Di}/D_i)^2$

$$D_i = \frac{F_{Di}}{\sqrt{(\omega_i^2 - \omega^2)^2 + (2\omega_i\omega\gamma)^2}}$$

Therefore, the steady state solution of the forced vibration is

$$T_i = \frac{F_{Di}}{\sqrt{(\omega_i^2 - \omega^2)^2 + (2\omega_i\omega\gamma)^2}}\cos(\omega t + \delta_i) \tag{4-51}$$

$$\delta_i = arctg\frac{2\omega_i\omega\gamma}{(\omega_i^2 - \omega^2)} = tg^{-1}\frac{2\omega_i\omega\gamma}{(\omega_i^2 - \omega^2)} \tag{4-52}$$

Finally, the complete solution for a forced vibration for a cantilever bar is

$$Z(x,t) = \sum_i \phi_i T_i$$

$$= C_0 \sum e^{-\omega r_i \gamma t}\cos(\omega_i t + \Delta_{i0}) \cdot \left[\cos\beta_i x - \cosh\beta_i x - \frac{\cos\beta_i L + \cosh\beta_i L}{\sin\beta_i L + \sinh\beta_i L}\cdot(\sin\beta_i x - \sinh\beta_i x)\right] \cdot$$

$$\frac{F_{Di}}{\sqrt{(\omega_i^2 - \omega^2)^2 + (2\omega_i\omega\gamma)^2}}\cos(\omega t + \delta_i) \tag{4-53}$$

$\Delta_0 = t_g^{-1}\frac{B_0}{A_0\omega_i}$, $C_0 = \sqrt{A_o^2 + B_0^2/\omega_i^2}$ are determined by the initial conditions. (4-54)

$$\delta_i = t_g^{-1}\frac{2\omega\omega_i\gamma}{(\omega_i^2 - \omega^2)} \tag{4-55}$$

At resonant frequency

$\omega = \omega_i$

The steady vibration part reaches the maximum and the amplitude is

$$\frac{F_{Di}}{\sqrt{4\omega_i^2\gamma^2}} = \frac{F_{Di}}{2\omega_i\gamma} \tag{4-56}$$

Which is inversely proportional to the damping factor $\omega_i\gamma$.

4.2.1.3 Bending neutral axis of a unimorph cantilever beam

A piezoelectric unimorph cantilever beam is shown in Figure 4.6.

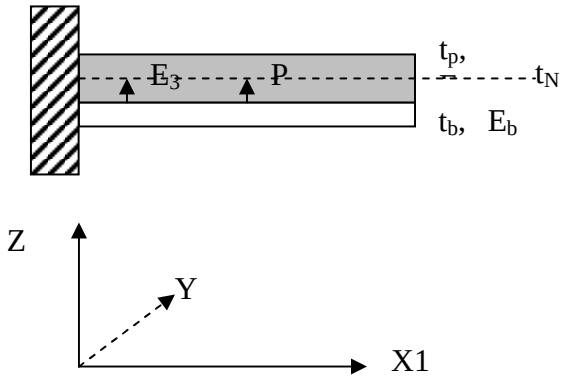

Figure 4.6 The scheme of a piezoelectric unimorph cantilever beam

$t_{N,}$ is the position of the neutral axis for bending.

Let u being the transverse displacement, then the longitudinal displacement =-zu' (x,t), z is the distance from the neutral axis, and the longitudinal strain= -zu'' (x,t),

The variables are S and E, the constitutive equations are

$$T_{ij} = C_{ijkl}^{E} S_{kl} - e_{kij} E_k \tag{4-57}$$

$$D_j = e_{jkl} S_{kl} + \varepsilon_{jk}^{s} E_k \tag{4-58}$$

or

$$T_1 = C_{11} \cdot S_1 - e_{31} E_3 \tag{4-59}$$

$$D_3 = e_{31} S_1 + \varepsilon_{33}^{s} E_3 \tag{4-60}$$

Notice $\varepsilon_{33}^{s} = \varepsilon_{33}^{T}(1 - k_{31}^2)$ (4-61)

$$e_{31} = d_{31} \cdot C_{11} = d_{31} \cdot E_p \tag{4-62}$$

$$S_1 = -zu''(x,t) \tag{4-63}$$

$$T_1 = C_{11} S_1 - e_{31} E_3 = -C_{11} zu''(x,t) - e_{31} E_3 \tag{4-64}$$

$$D_3 = -e_{31} z u^{"}(x,t) + \varepsilon_{33}^{s} E_3 \tag{4-65}$$

Total force=0

$$\int_{-t_N}^{t_- - t_n} \sigma_p dz + \int_{-t_b - t_N}^{-t_n} \sigma_b dz = 0 \tag{4-66}$$

$$\sigma_p = -E_p z u^{"}, \quad \sigma_b = -E_b z u^{"} \tag{4-67}$$

$$-E_p u^{"} . \frac{1}{2}\left[\left(t_p - t_N\right)^2 - {t_N}^2\right] - E_b \cdot u^{"} \cdot \frac{1}{2}\left[{t_N}^2 - (t_N + t_b)^2\right] = 0$$

$$E_p\left({t_p}^2 - 2t_p t_N\right) + E_b\left(-t_b^2 - 2t_p t_N\right) = 0$$

$$E_p {t_p}^2 - E_b {t_b}^2 = t_N (2E_b t_b + 2t_p E_p)$$

$$t_N = \frac{1}{2} \cdot \frac{E_p {t_p}^2 - E_b {t_b}^2}{E_b t_b + t_p E_p} \tag{4-68}$$

If t_N is assumed within the substrate layer, then

$$t_N = \frac{1}{2} \cdot \frac{E_b {t_b}^2 - E_p {t_p}^2}{E_b t_b + t_p E_p} \tag{4-69}$$

4.2.1.4 Enthalpy of a piezoelectric cantilever beam

So far, we have

$$S_1 = -zu''(x,t)$$
$$T_1 = -E_p z u'' - e_{31} E_3$$
$$D_3 = -e_{31} z u'' + \varepsilon_{33}^s E_3$$

If there is a voltage $\Delta\Phi$ between the top and bottom of the PZT electrode, the electric field E_3 within the PZT cannot be regarded as a constant, it depends on the position Z inside the piezo material,

$\nabla \cdot D = 0$, hence, $\frac{\partial D_3}{\partial z} = 0$

$$-e_{31} u'' + \varepsilon_{33} \frac{\partial E_3}{\partial z} = 0 \qquad (4\text{-}70)$$

Electrical potential is Φ, $-\nabla\Phi = E_3$

$$-\frac{\partial \Phi}{\partial z} = E_3 \quad \Rightarrow \quad -e_{31} u'' - \varepsilon_{33} \frac{\partial^2 \Phi}{\partial z^2} = 0$$

Assume $\Phi = \Phi_1 Z + \Phi_2 Z^2 + \Phi_0$

So $\Phi_2 = \frac{1}{2} \cdot \frac{\partial^2 \Phi}{\partial Z^2} = -\frac{1}{2} \cdot \frac{e_{31}}{\varepsilon_{33}} u''$

$$\Phi(t_p - t_N) = -\frac{1}{2} \cdot \frac{e_{31}}{\varepsilon_{33}} u''(t_p - t_N)^2 + \Phi_1(t_p - t_N) + \Phi_0$$
$$\Phi(-t_N) = -\frac{1}{2} \cdot \frac{e_{31}}{\varepsilon_{33}} u''(t_N)^2 + \Phi_1(-t_N) + \Phi_0$$
$$\Phi(t_p - t_N) - \Phi(-t_N) = \Delta\Phi$$
$$\Delta\Phi = \Phi_1 t_p - \frac{1}{2} \cdot \frac{e_{31}}{\varepsilon_{33}} u''\left[(t_p - t_N)^2 - t_N^2\right]$$
$$\Phi_1 = \frac{\Delta\Phi}{t_p} + \frac{1}{2} \cdot \frac{e_{31}}{\varepsilon_{33}} u''\left[t_p - 2t_N\right]$$

only relative potential is meaningful $\Rightarrow \Phi_0 = 0$

So $\Phi = -\frac{1}{2}\cdot\frac{e_{31}}{\varepsilon_{33}}u^{"}z^2 + \left[\frac{1}{2}\cdot\frac{e_{31}}{\varepsilon_{33}}u^{"}(t_p - 2t_N) + \frac{\Delta\Phi}{t_p}\right].z$ (4-71)

$$E_3 = -\frac{\partial\Phi}{\partial z} = -\frac{\Delta\Phi}{t_p} - \frac{1}{2}\cdot\frac{e_{31}}{\varepsilon_{33}}u^{"}\left(t_p - 2t_N\right) + \frac{e_{31}}{\varepsilon_{33}}u^{"}.z = -\frac{\Delta\Phi}{t_p} - \frac{1}{2}\cdot\frac{e_{31}}{\varepsilon_{33}}u^{"}\left(t_p - 2t_N - 2z\right)$$ (4-72)

Internal energy $U_p = \frac{1}{2}\cdot S_1\cdot T_1 + \frac{1}{2}\cdot E_3\cdot D_3$ (4-73)

Enthalpy $H = u - \vec{D}\cdot\vec{E} = \frac{1}{2}\cdot S_1\cdot T_1 - \frac{1}{2}\cdot E_3\cdot D_3$ (4-74)

So, $H = \frac{1}{2}\times\left(-zu^{"}\right)*\left(-E_p zu^{"} - e_{31}E_3\right) - \frac{1}{2}E_3\left(-e_{31}\cdot zu^{"} + \varepsilon_{33}^s E_3\right)$

$$= \frac{1}{2}E_p u^{"2}z^2 + \frac{1}{2}e_{31}E_3 zu^{"} + \frac{1}{2}e_{31}zu^{"}E_3 - \frac{1}{2}\varepsilon_{33}^s E_3^2$$

$$= \frac{1}{2}E_p u^{"2}z^2 + e_{31}E_3 u^{"}z - \frac{1}{2}\varepsilon_{33}^s E_3^2$$

$$= \frac{1}{2}E_p u^{"2}z^2 + e_{31}u^{"}z\left(-\frac{\Delta\Phi}{t_p} - \frac{e_{31}}{2\varepsilon_{33}}u^{"}\left(t_p - 2t_N - 2z\right)\right)$$

$$-\frac{1}{2}\varepsilon_{33}^s\left[\left(-\frac{\Delta\Phi}{t_p} - \frac{e_{31}}{2\varepsilon_{33}}u^{"}\left(t_p - 2t_N - 2z\right)\right)\right]^2$$

$$= \frac{1}{2}E_p u^{"2}z^2 - \frac{e_{31}\cdot z\cdot\Delta\Phi}{t_p}u^{"}\cdot z$$

$$-\frac{e_{31}^{\ 2}}{2\varepsilon_{33}}u^{"2}\cdot\left(t_p - 2t_N - 2z\right)z - \frac{1}{2}\varepsilon_{33}\left[\frac{\Delta\Phi^2}{t_p^{\ 2}} + \frac{2\Delta\Phi}{t_p}\cdot\frac{e_{31}}{2\varepsilon_{33}}u^{"}\left(t_p - 2t_N - 2z\right)\right]$$

$$-\frac{1}{2}\varepsilon_{33}\cdot\left(\frac{e_{31}}{2\varepsilon_{33}}\right)^2\cdot u^{"2}\cdot\left(t_p - 2t_N - 2z\right)^2$$

$$= \left[\frac{1}{2}E_p\cdot z^2 - \frac{e_{31}^{\ 2}}{2\varepsilon_{33}}\cdot\left(t_p - 2t_N - 2z\right)\cdot z - \frac{1}{2}\varepsilon_{33}\cdot\left(\frac{e_{31}}{2\varepsilon_{33}}\right)^2\cdot\left(t_p - 2t_N - 2z\right)^2\right]u^{"2}$$

$$\left[\frac{1}{2}E_p\cdot z^2-\frac{e_{31}{}^2}{2\varepsilon_{33}}\cdot\left(t_p-2t_N-2z\right)\cdot z-\frac{1}{2}\varepsilon_{33}\cdot\left(\frac{e_{31}}{2\varepsilon_{33}}\right)^2\cdot\left(t_p-2t_N-2z\right)^2\right]u^{"2}$$

$$\left[-\frac{e_{31}\cdot z\Delta\Phi}{t_p}z-\frac{1}{2}\frac{\Delta\Phi}{t_p}e_{31}\left(t_p-2t_N-2z\right)\right]u^{"}-\frac{1}{2}\varepsilon_{33}\left(\frac{\Delta\Phi}{t_p}\right)^2$$

$$=\left[\frac{1}{2}\left(E_p+\frac{e_{31}{}^2}{\varepsilon_{33}}\right)z^2-\frac{e_{31}{}^2}{8\varepsilon_{33}}\left(t_p-2t_N\right)^2\right]u^{"2}+\left(-\frac{1}{2}\frac{\Delta\Phi}{t_p}e_{31}\left(t_p-2t_N\right)\right)u^{"}-\frac{1}{2}\varepsilon_{33}\left(\frac{\Delta\Phi}{t_p}\right)^2$$

$$=\left(a_2z^2+a_3\right)u^{"2}+a_4u^{"}+a_5 \tag{4-75}$$

$$a_2=\frac{1}{2}\left(E_p+\frac{e_{31}{}^2}{\varepsilon_{33}^s}\right)\qquad\qquad\varepsilon_{33}^s=\varepsilon_{33}^T\left(1-k_{31}^2\right) \tag{4-76}$$

$$a_3=-\frac{e_{31}{}^2}{8\varepsilon_{33}^s}\left(t_p-2t_N\right)^2 \tag{4-77}$$

$$a_4=-\frac{\Delta\Phi}{2t_p}\cdot e_{31}\left(t_p-2t_N\right) \tag{4-78}$$

$$a_5=-\frac{1}{2}\varepsilon_{33}\left(\frac{\Delta\Phi}{t_p}\right)^2 \tag{4-79}$$

4.2.1.5 Equation of motion for a piezoelectric cantilever beam

The kinetic energy of the substrate is:

$$T_b = \frac{1}{2}\rho_b t_b \dot{y}^2 = \frac{1}{2}\rho_b A_b \dot{y}^2 \int_0^L dx \quad \text{(Basak et al., 2005)} \tag{4-80}$$

The kinetic energy of the piezo layer is:

$$T_p = \frac{1}{2}\rho_p t_p \dot{y}^2 = \frac{1}{2}\rho_p A_p \dot{y}^2 \int_0^L dx \quad \text{(Basak et al., 2005)} \tag{4-81}$$

and the potential for the substrate layer is

$$U_b = \int \frac{1}{2} T \cdot S dV = \frac{1}{2} E_b \int S^2 dV$$

$$= \frac{1}{2} E_b \int_{-t_b - t_N}^{-t_N} \left(Zy''\right)^2 dz \int_0^L dx \int dy$$

$$= \frac{1}{2} E_b y''^2 \int_{-t_b - t_N}^{-t_N} z^2 dz \int_0^L dx \int dy$$

$$= \frac{1}{2} E_b y''^2 I_{bN} \int_0^L dx \int dy \tag{4-82}$$

$$I_{bN} = \int dy \int_{-t_b - t_N}^{-t_N} z^2 dz \tag{4-83}$$

is the moment of inertia relative to the neutral axis for the substrate layer

Enthalpy of the piezoelectric layer $H_p = \int H dV$

$$\int H dV = \int \left[\left(a_2 z^2 + a_3\right)u''^2 + a_4 u'' + a_5\right] dV$$

$$= \int_0^L dx \int_{-t_N}^{t_p - t_N} \left[\left(a_2 z^2 + a_3\right)u''^2 + a_4 u'' + a_5\right] dz \cdot \int_0^{width} dy$$

$$= \int_0^L dx \int dy \left[a_2 \int_{-t_N}^{t_p - t_N} z^2 dz u''^2 + a_3 t_p u''^2 + \left(a_4 u'' + a_5\right) t_p \right]$$

$$= \int_0^L dx \left[\left(a_2 \int_{-t_N}^{t_p - t_N} z^2 dz + a_3 A_p \right) u''^2 + \left(a_4 u'' + a_5\right) A_p \right] \tag{4-84}$$

$$I_{pN} = \int dy \int_{-t_N}^{t_p - t_N} z^2 dz \tag{4-85}$$

is the moment of inertia of the piezo layer relative to the neutral axis.

Lagrangian $L = T_b + T_p - u_b - H_p$ (4-86)

And the equation of motion is obtained by $\delta \int_{t_1}^{t_2} L dt = 0$ where δ represents a variation operation.

i.e. $\delta \int_{t_1}^{t_2} dt \int_0^L dx [\frac{1}{2}\rho_b A_b \dot{y}^2 + \frac{1}{2}\rho_p A_p \dot{y}^2 - \frac{1}{2} E_b I_{bN} y''^2$

$- (a_2 I_{PN} + a_3 A_P) y''^2 - (a_4 y'' + a_5) A_p] = 0$ (4-87)

Next is to calculate the variation δ .

Noting that $\delta(\dot{y}) = \frac{\partial(\delta y)}{\partial t}$ (4-88)

and $\delta(y') = \frac{\partial(\delta y)}{\partial x}$ (4-89)

$$\delta \int_{t_1}^{t_2} dt \int_0^L dx \, \frac{1}{2} \rho_b A_b \dot{y}^2 = \int_0^L dx \int_{t_1}^{t_2} dt \, \rho_b A_b \dot{y} \, \delta(\dot{y}) = \int_0^L dx \int_{t_1}^{t_2} dt \, \rho_b A_b \dot{y} \frac{d}{dt}(\delta y)$$

$$= \int_0^L dx \cdot [\rho_b A_b \dot{y} \delta y \Big|_{t_1}^{t_2} - \int_{t_1}^{t_2} dt \, \rho_b A_b \ddot{y} \delta y]$$

$$= -\int_0^L dx \cdot \int_{t_1}^{t_2} dt \cdot \rho_b A_b \ddot{y} \delta y \,, \tag{4-90}$$

used $\delta y(x_1,t_1) = \delta y(x_1,t_2) = 0$ as required by the variation method.

$$\delta \int \frac{1}{2} E_b I_{bN} y''^2 \int dt dx = \delta \int_{t_1}^{t_2} dt \int_0^L dx \cdot \frac{1}{2} E_b I_{bN} y''^2 = \int_{t_1}^{t_2} dt \int_0^L dx \cdot E_b I_{bN} y'' \frac{d^2 \delta y}{d^2 x}$$

$$= \int dt \int dx \cdot E_b I_{bN} y'' \frac{\partial}{\partial x} \delta \left(\frac{\partial y}{\partial x} \right) = \int_{t_1}^{t_2} dt \cdot E_b I_{bN} y'' \delta y' \Big|_0^L - E_b I_{bN} \int dt \int dx \cdot y''' \delta y'$$

$$= \int_{t_1}^{t_2} dt \cdot E_b I_{bN} y^{''} \delta y' \Big|_0^L - E_b I_{bN} \int_{t_1}^{t_2} dt \left(y''' \delta y \Big|_0^L - \int y'''' \delta y dx \right)$$

$$= \int_{t_1}^{t_2} dt \cdot E_b I_{bN} y^{''} \delta y' \Big|_0^L - \int_{t_1}^{t_2} dt \cdot E_b I_{bN} y''' \delta y \Big|_0^L + E_b I_{bN} \int_0^L y'''' dx \int_{t_1}^{t_2} dt \delta y$$

$$= E_b I_{bN} \int_{t_1}^{t_2} dt \cdot \int_0^L dx \cdot y'''' \delta y \tag{4-91}$$

Here we have used

$$y^{''} \delta y' \Big|_0^L = 0 \text{ , and} \tag{4-92}$$

$$y''' \delta y \Big|_0^L = 0 \tag{4-93}$$

Which lead to boundary condition requirements (either free end or clamped end conditions).

The variation for the remaining terms can be performed in the same way.

Finally, the variation is

$$\int_0^L dx \int_{t_1}^{t_2} dt \left[-\left(\rho_b A_b + \rho_p A_p\right) \ddot{y} + E_b I_{bN} y'''' + \left(2a_2 I_{pN} + 2a_3 A_P\right) y'''' \right] \delta y = 0 \tag{4-94}$$

Since δy is arbitrary, this requires

$$\left(E_b I_{bN} + 2a_2 I_{pN} + 2a_3 A_P\right) y'''' - \left(\rho_b A_b + \rho_p A_p\right) \ddot{y} = 0 \tag{4-95}$$

This is the equation of motion for the piezoelectric cantilever beam.

The equation is of the similar form for the uniform cantilever bar (equation (4-27)), so

$$\omega_i = \sqrt{\frac{\left(E_b I_{bN} + 2a_2 I_{PN} + 2a_3 A_p\right)}{\rho_b A_b + \rho_p A_p}} \cdot \beta_i^2 \tag{4-96}$$

$$= \frac{n_i^{\,2}}{L^2} \sqrt{\frac{\left(E_b I_{bN} + 2a_2 I_{PN} + 2a_3 A_p\right)}{\rho_b A_b + \rho_p A_p}}$$

$$\beta_i = \frac{n_i}{L}, \quad n_1 = 1.88, n_2 = 4.69, n_3 = 7.85 \tag{4-97}$$

$$Y = \sum_i \phi_i T_i$$

$$\phi_i = C_1 \left[\cos \beta_i x - \cosh \beta_i x - \frac{\cos \beta_i L + \cosh \beta_i L}{\sin \beta_i L + \sinh \beta_i L} \cdot (\sin \beta_i x - \sinh \beta_i x) \right] \tag{4-98}$$

$$T_i = ...$$

Everything else is the same as for the uniform cantilever bar.

To summarise, the equation of motion:

$$\left(E_b I_{bN} + 2a_2 I_{pN} + 2a_3 A_P\right) y'''' - \left(\rho_b A_b + \rho_p A_p\right) \ddot{y} = 0$$

$$a_2 = \frac{1}{2}\left(E_p + \frac{e_{31}^{\ 2}}{\varepsilon_{33}^s}\right) = \frac{1}{2} E_p \left(1 + \frac{E_p d_{31}^{\ 2}}{\varepsilon_{33}^s}\right) = \frac{1}{2} E_p \left(1 + \frac{E_p d_{31}^{\ 2}}{\varepsilon_{33}^T \left(1 - k_{31}^2\right)}\right)$$

$$a_3 = -\frac{e_{31}^{\ 2}}{8\varepsilon_{33}^s}\left(t_p - 2t_N\right)^2 = -\frac{E_p^2 d_{31}^2}{8\varepsilon_{33}^T \left(1 - k_{31}^2\right)}\left(t_p - 2t_N\right)^2$$

$$a_4 = -\frac{\Delta\Phi}{2t_p} e_{31}\left(t_p - 2t_N\right) = -\frac{\Delta\Phi}{2t_p} \cdot E_p \cdot d_{31} \cdot \left(t_P - 2t_N\right)$$

$$a_5 = -\frac{1}{2}\varepsilon_{33}^s \left(\frac{\Delta\Phi}{t_p}\right)^2 = -\frac{1}{2}\varepsilon_{33}^T \left(1 - k_{31}^2\right) \cdot \left(\frac{\Delta\Phi}{t_P}\right)^2$$

4.2.1.6 Dynamic analysis of a piezoelectric fan without a substrate space at the fixed end

A piezoelectric fan without a substrate space at the fixed end is shown in Figure 4.7. The piezoelectric fan is divided into two sections, if the fixed (clamping) point is deemed as the origin in the coordinate, then section one is from the origin to length L_1, in this section the piezoelectric layer and the substrate have the same length; section two is from the length L_1 to L_2, and without a piezoelectric layer.

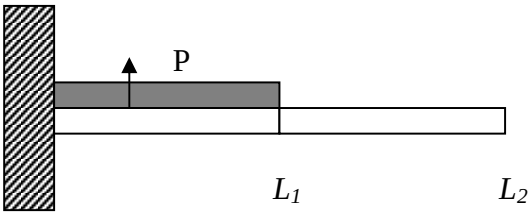

Figure 4.7 The scheme of a piezoelectric fan without substrate space at the fixed end

The section one can be treated as a cantilever unimorph piezoelectric beam and the section two can be treated as a pure cantilever beam.

So, in section one,

$$\left(E_b I_{bN} + 2a_2 I_{pN} + 2a_3 A_p\right) y'''' - \left(\rho_b A_b + \rho_p A_p\right) \ddot{y} = 0 \qquad 0 \le x \le L_1 \tag{4-99}$$

$$E_c I_c y'''' - \rho_c A_c \ddot{y} = 0 \qquad L_1 \le x \le L_2 \tag{4-100}$$

The boundary conditions are

$$y(0) = 0\ , \tag{4-101}$$

$$y'(0) = 0\ , \tag{4-102}$$

$$y''(L_2) = 0\ , \tag{4-103}$$

$$y'''(L_2) = 0 \tag{4-104}$$

And natural conditions at L_1

$$u_1(L_1) = u_2(L_1), \tag{4-105}$$

$$u_1'(L_1) = u_2'(L_1), \tag{4-106}$$

$$\left(E_b I_{bN} + 2a_2 I_{pN} + 2a_3 A_P\right) u_1''(L_1) = E_c I_c u_2''(L_1), \tag{4-107}$$

$$\left(E_b I_{bN} + 2a_2 I_{pN} + 2a_3 A_P\right) u_1'''(L_1) = E_c I_c u_2'''(L_1) \tag{4-108}$$

From the equations, assuming the solutions for the two regions

$$y_1 = u_1 T_1(t) \qquad 0 \le x \le L_1 \tag{4-109}$$

$$y_1 = u_2 T_1(t) \qquad L_1 \le x \le L_2 \tag{4-110}$$

$$u_1 = c_1 \cos\beta x + c_2 \sin\beta x + c_3 \cosh\beta x + c_4 \sinh\beta x, \quad 0 \le x \le L_1 \tag{4-111}$$

$$u_2 = c_5 \cos\alpha x + c_6 \sin\alpha x + c_7 \cosh\alpha x + c_8 \sinh\alpha x), \quad L_1 \le x \le L_2 \tag{4-112}$$

$$u_1(0) = 0 \quad \Rightarrow \quad c_1 + c_3 = 0 \quad \Rightarrow c_3 = -c_1 \tag{4-113}$$

$$u_1'(0) = 0 \quad \Rightarrow \quad c_2\beta + c_4\beta = 0 \quad \Rightarrow c_4 = -c_2 \tag{4-114}$$

Therefore,

$$u_2' = -c_5\alpha \sin\alpha x + c_6\alpha \cos\alpha x + c_7\alpha \sinh\alpha x + c_8\alpha \cosh\alpha x)$$

$$u_2'' = -c_5\alpha^2 \cos\alpha x - c_6\alpha^2 \sin\alpha x + c_7\alpha^2 \cosh\alpha x + c_8\alpha^2 \sinh\alpha x)$$

$$u_2''' = c_5\alpha^3 \sin\alpha x - c_6\alpha^3 \cos\alpha x + c_7\alpha^3 \sinh\alpha x + c_8\alpha^3 \cosh\alpha x)$$

$$u_2''(L_2) = 0 \quad \Rightarrow \quad -c_5 \cos\alpha L_2 - c_6 \sin\alpha L_2 + c_7 \cosh\alpha L_2 + c_8 \sinh\alpha L_2 = 0 \qquad (4\text{-}115)$$

$$u_2'''(L_2) = 0 \quad \Rightarrow \quad c_5 \sin\alpha L_2 - c_6 \cos\alpha L_2 + c_7 \sinh\alpha L_2 + c_8 \cosh\alpha L_2 = 0 \qquad (4\text{-}116)$$

The four natural bounding conditions at L_1 above will produce four more equations. Therefore, there are eight unknowns, which are C_1 to C_8, and eight equations.

The determinant must be zero to produce a 8x8 matrix equation $f(\alpha, \beta, L) = 0$

And also,

$$\beta = \left[\frac{(\rho_b A_b + \rho_p A_p)\omega^2}{2a_2 I_{PN} + 2a_3 A_p + E_b I_{bN}} \right]^{1/4} \qquad (4\text{-}117)$$

$$\alpha = \left(\frac{\rho_c A_c \omega^2}{E_c I_c} \right)^{1/4} \qquad (4\text{-}118)$$

Therefore, the above equation becomes $f(\omega, L) = 0$, which can be used to obtain the natural frequencies ω_i and the mode shape.

The matrix calculation can be done by computer programs for example Matlab software.

4.2.1.7 Dynamic analysis of a piezoelectric fan with a substrate space at the fixed end

A piezoelectric fan with a substrate space at the fixed end is shown in Figure 4.8. This piezoelectric fan can be divided into three sections, if the fixed (clamping) point is deemed as the origin, section one is from the origin to length L_1; section two is from the length L_1 to L_2, and section three is from the length L_2 to L_3. The PZT layer has the same length with the substrate in the section two; however, there is no piezoelectric layer in

section I and III.

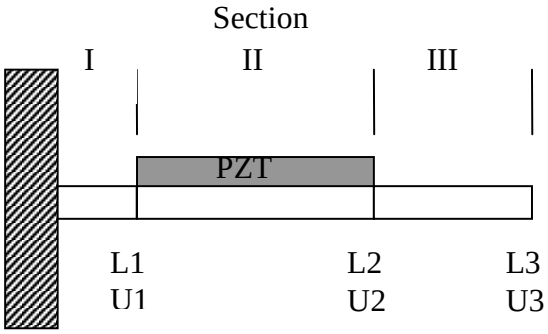

Figure 4.8 The scheme of a piezoelectric fan with a substrate space at the fixed end

Following the similar procedures as in 4.2.1.6.

In section I, there are four constants to be determined, C_1, C_2, C_3, and $C4$, and the boundary conditions are $u_1(0)=0 \quad u_1^{'}(0)=0$, which lead to

$$C_3=-C_1, \tag{4-119}$$

$$C_4=-C_2, \tag{4-120}$$

In section II, there are four, constants to be determined, C_5, C_6, C_7, and C_8, and the boundary conditions are natural boundary conditions at L_1.

$$u_1(L_1)=u_2(L_1), \tag{4-121}$$

$$u_1^{'}(L_1)=u_2^{'}(L_1), \tag{4-122}$$

$$\left(E_bI_{bN}+2a_2I_{pN}+2a_3A_P\right)u_2^{''}(L_1)=E_cI_cu_1^{''}(L_1), \tag{4-123}$$

$$\left(E_bI_{bN}+2a_2I_{pN}+2a_3A_P\right)u_2^{'''}(L_1)=E_cI_cu_1^{'''}(L_1), \tag{4-124}$$

In section III, there are four constants to be determined, C_9, C_{10}, C_{11}, and C_{12}, and the boundary conditions

$$u_3^{''}(L_3)=0, \tag{4-125}$$

$$u_3'''(L_3)=0, \tag{4-126}$$

And the natural boundary conditions at L_2;

$$u_3(L_2)=u_2(L_2), \tag{4-127}$$

$$u_3'(L_2)=u_2'(L_2), \tag{4-128}$$

$$\left(E_bI_{bN}+2a_2I_{pN}+2a_3A_P\right)u_2''(L_2)=E_cI_cu_3''(L_2), \tag{4-129}$$

$$\left(E_bI_{bN}+2a_2I_{pN}+2a_3A_P\right)u_2'''(L_2)=E_cI_cu_3'''(L_2), \tag{4-130}$$

Therefore, from the boundary conditions and natural boundary conditions at L_1 and L_2 can produce 12 equations and there are 12 constants to be determined. This will produce a 12x12 matrix problem, and this problem could be solved by computer programme such as Matlab software.

CHAPTER 5

RESULTS AND DISCUSSION

5.1 Bonding conditions optimization

14 samples have been bonded under different conditions, with variable parameters such as the spinning rate and time when spreading the epoxy onto the surface of the Mo sheet; the oven temperature and curing time when curing the epoxy in a oven; whether or not to apply sandpaper abrasion on the surface of the samples, and whether or not to apply a adhesion promoter before spreading the epoxy. The detailed parameters used in the 14 samples and their respective lap shear strengths are summarized in Table V.1.

The shear strength was obtained by dividing the shear force just before a breakdown by the overlap area, hence larger shear force at breakdown would lead to larger shear strength because the overlap area is the same 6mm x 50mm for all the samples. Figure 5.1 shows the measured relationships between the shear force and the displacement for samples no 11, 12, 13 and 14. The Nr. 1, 2, 3, 4 refer the sample no 11, 12, 13, 14 in the Table V.1. It can be seen that the shear force increases with the strain (displacement) monotonically, until a suddenly drop - which indicates a breakdown had happened.

From Table V.1, the sample no 12 achieved highest shear strength 2.95 MPa, so the optimized adhesive bonding conditions when using Epo-TEK 301-2 epoxy for the fabrication of piezoelectric fans could be summarized as the following:

- Spreading method: spinner
- Spin rate: 3,500 rpm
- Spin time: 20s,
- Curing temperature: 100 °C
- Curing time: 5 hours
- Sandpaper abrasion: not applied

- Adhesive promoter: not applied
- Dead weight: 2kg

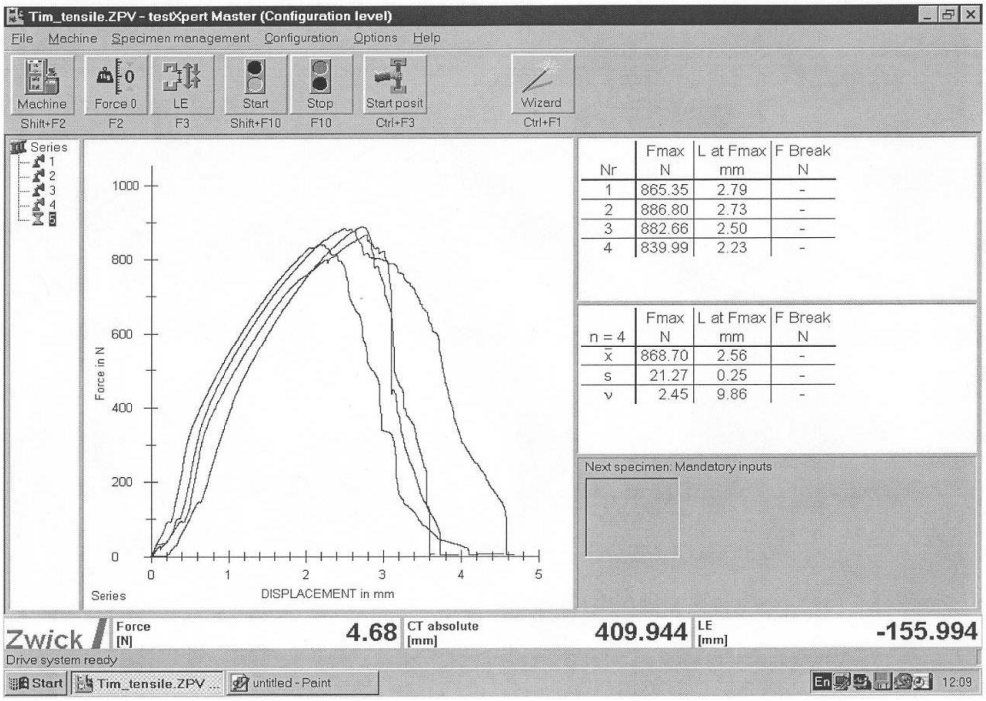

Figure 5.1 The measured relationships between the shear force and the displacement for samples 11, 12 13 and 14

Table V.1 Summary of the experimental parameters for the bonding optimization

sample	1	2	3	4	5	6	7
	Ni/Mo	Ni/Mo	Ni/Mo	Ni/Mo	Ni/Mo	Ni/Mo	Ni/Mo
Adhesion Promoter (g)	—	—	—	0.8 on Mo	—	—	—
Sand paper (grit)	4000	4000	4000	4000	4000	4000	4000
Spin rate (rpm)	2500	2000	3000	2500	razor	razor	3500
Spin time(s)	20	20	20	20	—	—	20
Epoxy amount (g)	1.6 on Mo	1.6 on Mo	1.6 on Mo	1.6 on Mo	1.6 on Mo	1.6 on Mo	1.6 on Mo
Oven temperature (℃)	100	100	65	65	65	25	100
Oven time (hr)	15	15	15	15	15	5 days	15
Dead weight (kg)	2	2	2	2	2	2	2
Over-lap length (mm)	6	6	6	6	6	6	6
Shear force (N)	681.79	577.83	549.42	111.29	427.87	228.14	872.85
Shear strength (MPa)	2.27	1.93	1.83	0.37	1.426	0.76	2.91
Ave. thickness of epoxy (μm)	9.3	12.9	4.9	3.7	2.8	10.5	10.8
sample	8	9	10	11	**12**	13	14
	Ni/Mo	Ni/Mo	Ni/Mo	Ni/Mo	**Ni/Mo**	Ni/Mo	Ni/Mo
Adhesion Promoter (g)	—	0.8 on Mo	—	—	—	—	—
Sand paper (grit)	4000	4000	—	—	—	—	—
Spin rate (rpm)	3000	2500	2500	3500	**3500**	3500	3500
Spin time(s)	20	20	20	20	**20**	40	20
Epoxy amount (g)	1.6 on Mo	1.6 on Mo	1.6 on Mo	1.6 on Mo	**1.6 on Mo**	1.6 on Mo	1.6 on Mo
Oven temperature (℃)	100	100	100	100	**100**	100	100
Oven time (hr)	15	15	15	15	**5**	15	15
Dead weight (kg)	2	2	2	2	**2**	2	4
Over-lap length (mm)	6	6	6	6	**6**	6	6
Shear force (N)	757.20	557.51	760.63	865.35	**885.80**	882.68	839.99
Shear strength (MPa)	2.52	1.86	2.53	2.88	**2.95**	2.94	2.80
Ave. thickness of epoxy (μm)	7.7	15.3	6.6	10.7	**6.0**	11.1	6.7

The respective experiments are discussed in the following sections from 5.1.1 to 5.1.7 for more detailed understanding.

5.1.1 The effect of the spin rate

The lap shear strength for samples prepared with different spin rates for epoxy spreading, while all other conditions were kept the same have been measured and the results are shown in Table V.2. It can be observed that higher spin rate lead to higher shear strength. This is understandable since higher spin rate enables a thin epoxy layer-

which leads to higher shear strength.

Table V.2 Lap shear strength vs. different spin rate

Samples no.	2	1	8	7
Spin rate (rpm)	2000	2500	3000	3500
Shear force (N)	577.83	681.79	757.20	872.85
Shear strength (MPa)	1.93	2.27	2.52	2.91

5.1.2 The effect of the spin time

The lap shear strength for samples prepared with different spin time for epoxy spreading, while all other conditions were kept the same have been measured and the results are shown in Table V.3. It can be seen that there is no significant difference in shear strength when the spinning time is changed from 20 s to 40 s. This suggests that after a short time of spin (20 s for example), the thickness of the epoxy reaches a plateau, so no further experiments were carried out for this parameter.

Table V.3 Lap shear strength vs. different spin time

Samples no.	11	13
Spin time (s)	20	40
Shear force (N)	865.35	882.68
Shear strength (MPa)	2.88	2.94

5.1.3 The effect of the curing temperature

The lap shear strength for samples prepared with different oven temperatures for epoxy curing, while all other conditions were kept the same have been measured and the results are shown in Table V.4. It can be seen that higher curing temperature produced higher lap shear strength. This is in agreeing with the data sheet of EPO-TEK 301-2 from the supplier. The suggested oven temperature is at least 80ºC, but not exceeding 150 ºC. Therefore 100 º C was chosen as the curing temperature, to prevent the thermal

stress from getting too high.

Table V.4 Lap shear strength vs. different oven temperature

Samples no.	6	3	8
Oven temperature (℃)	25	65	100
Shear force (N)	228.14	549.42	760.6
Shear strength (MPa)	0.76	1.83	2.52

5.1.4 The effect of the curing time

The lap shear strength for samples prepared with different curing time in the oven, while all other conditions were kept the same have been measured and the results are shown in Table V.5. From these results it can be seen that there is little difference in terms of shear strength for the samples cured between 5 and 15 hours, so no more experiments were carried out for this parameter.

Table V.5 Lap shear strength vs. different curing time

Samples no.	11	12
Curing time (hr)	15	5
Shear force (N)	865.35	886.80
Shear strength (MPa)	2.88	2.95

5.1.5 The effect of the sandpaper abrasion

The lap shear strength for samples prepared with applying sandpaper abrasion or not onto the surface of the Mo sheet has been measured and the results are shown in Table V.6. The samples no.1 and 10 were prepared under the same conditions except that sandpaper abrasion was used for the sample No.1 but not for the No.10. It can be observed that the sample with no sandpaper abrasion had higher lap shear strength. As a result, no sandpaper abrasion was used for all the following samples.

Table V.6 Shear strength vs. applying sandpaper abrasion

Samples no.	1	10
Sandpaper abrasion using	yes	no
Shear force (N)	681.79	760.63
Shear strength (MPa)	2.27	2.53

5.1.6 The effect of the adhesion promoter

The lap shear strength for samples prepared with applying an adhesion promoter or not has been measured and the results are shown in Table V.7. The samples no.1 and 9 were prepared under the same conditions except that an adhesion promoter (Volan, Aldrich) was used for the sample No.9 but not for the No.1. It can be observed that the sample without using adhesion promoter had higher shear strength. As a result, no adhesion promoter was used for all the following samples.

Table V.7 Shear strength vs. applying adhesion promoter

Samples no.	1	9
adhesion promoter using	no	yes
Shear force (N)	681.79	557.51
Shear strength (MPa)	2.27	1.86

5.1.7 The effect of the dead weight

The lap shear strength for samples prepared with different dead weight applied onto the sample surface during curing has been measured and the results are shown in Table V.8. The sample no.11 and 14 were prepared under the same parameters, but with dead weights of 2 and 4kg respectively applied on top of the samples during the curing in the oven. The shear strength was 2.88 MPa for the sample no.11. During the lap shear strength test experiments for the sample No.14, the Ni shim was broken at 840N, before any bonding failure. So larger deadweight may still be good for bonding, but it may cause the PZT to crack. Considering the fact that the dead weight of 2 kg achieved the

lap shear strength of 2.88MPa already, which is near the break point for the Ni shim, therefore 2 kg as the dead weight is considered enough.

Table V.8 Shear strength vs. dead weight

Samples no.	11	14
Dead weight (kg)	2	4
Shear force (N)	865.35	>839.99
Shear strength (MPa)	2.88	>2.80

In summary, the optimised conditions for bonding the Molybdenum and Nicole metal shims are: for the over-lap length 6mm, the spin rate is 3,500 rpm with spin time 40s, curing temperature 100º C and curing time 5 hours, applied dead weight 2kg and without using sandpaper abrasion and adhesion promoter. The obtained maximum shear strength is 2.95Mpa.

According to the Metal-adhesive compatibility chart, Table III.3 in chapter 3, the epoxy is suitable for bonding between two metals. Assuming there is no significant difference in terms of optimization for bonding conditions between two different metals, for example, between Ni and Ti, or between Ni and Stainless steel, the above optimised bonding conditions were considered applicable for all the sample bonding preparations.

5.2 Unimorph cantilever actuators

5.2.1 Quasi-static displacement calculation and modelling

5.2.1.1 Analytic and FEA calculations

Formulae (4-22) to (4-25) in chapter 4 were used to obtain analytical solutions for unimorph piezoelectric cantilever actuators, which consisted of a piezoelectric PZT patch (PSI-5H4E, Piezo Systems, Inc) with a 127 µm thickness and Titanium alloy I (Ti/94.5/Al 3/V 2.5), Titanium alloy II (Ti/94.5/Al 3/V 2.5), Stainless steel (Fe/Cr18/Ni

9/Ti) and Molybdenum (all from Goodfellow Ltd, UK) as the elastic layers with different thickness.

Considering the unimorph cantilever actuators with 40 mm in length and 10 mm in width, Figure 5.2 shows the calculated tip displacement as functions of the thickness ratio ($t_{elastic}/t_{piezo}$) for cantilevers with the same dimensions but with different elastic materials, under the same applied voltage of 127 V. It can be seen from this figure, the tip displacement increases initially with the increasing thickness ratio, and reach a maximum at the ratio range from 0.235 for Mo to 0.29 for Stainless steel, depending on the exact elastic layer. After the peak, the tip displacement decrease with the increasing thickness ratio. All four cantilevers followed the similar profile. Table V.9 summarises the results of analytical calculation for the maximum tip displacement, the blocking force, and the 1st and 2nd resonant frequencies for the aforementioned cantilevers.

Comparing the four cantilevers with different elastic layers, around the peaks, under the same applied voltage of 127 volts, the PZT/Mo cantilever gives the largest tip displacement 2.27 mm, followed by stainless steel's 2.16 mm. The two PZT/Ti cantilevers had the smallest tip displacements 1.96-1.98 mm. Considering the fact that stainless steel is the cheapest among the four alloys, and can achieve a decent maximum tip displacement and also higher tip displacement than the PZT/Mo cantilever when the thickness ration is larger than 0.5, stainless steel was chosen as the elastic materials for most of the future cantilever actuators.

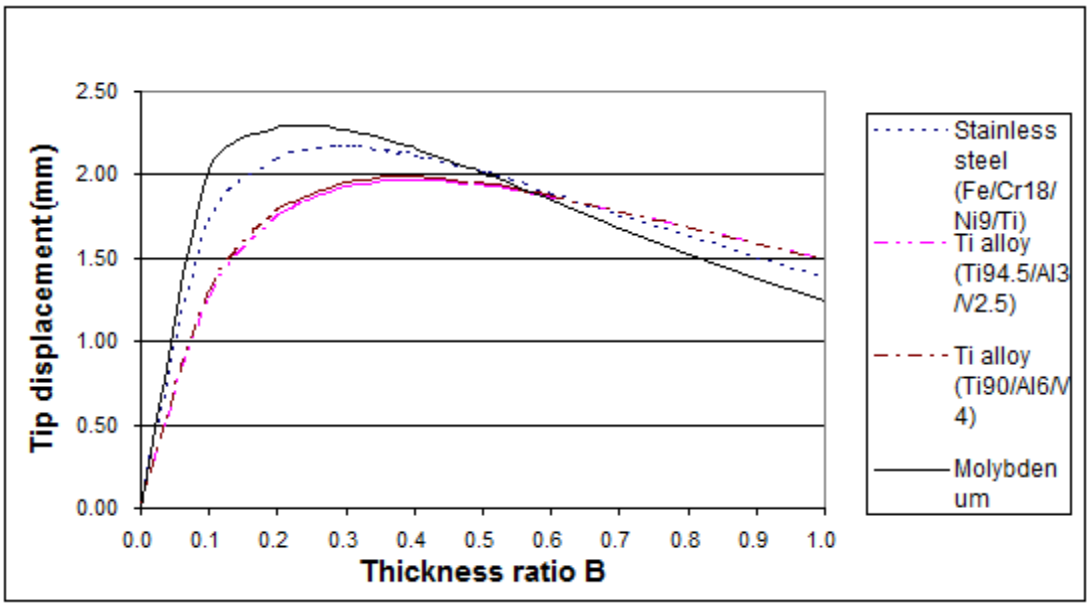

Figure 5.2 Tip deflections as functions of substrate/piezoceramic thickness ratio for unimorph actuator (L=40mm, w=10mm, thickness of piezoceramic is 127 μm)

The analytic calculation results for these cantilevers are summarised in Table V.9. For the blocking force, a maximum value 40,887 μN for the PZT/Mo cantilever actuator was obtained. For the resonant frequency, the first resonant frequency 59.4 Hz and second resonant frequency 372.2 Hz for the same actuator were obtained.

FEA programming has been developed to model the properties of these unimorph cantilevers, and the modelled results are summarised in Table V.10. Figure 5.3 shows the modelling results for the 1st and 2nd resonance modes.

Table V. 9 Summary of analytic results (L=40mm, w=10mm, thickness of the PZT patch was 127 μm)

material	Titanium alloy I (Ti/94.5/Al 3/V 2.5)	Titanium alloy II (Ti/90/Al 6/V 4)	Stainless Steel (Fe/Cr18/Ni 9/Ti)	Mo
B factor ($t_{elastic}/t_{Piezo}$)	0.40	0.39	0.29	0.235
Thickness of metal shim (μm)	51	50	37	30
Total thickness(μm)	178	177	164	157
Max tip deflection (mm)	1.96	1.98	2.16	2.27
Blocking force (μN)	33,632	34,107	37,410	40,887
1st resonant frequency (HZ)	60.7	61.0	59.4	59.9
2nd resonance mode(HZ)	380.3	382.2	372.2	375.5

Table V.10 Analytic and FEA Calculation of an unimorph cantilever beam, in the case of L=40mm, w=10mm, thickness of PZT is 127 μm

substrate	Item	Analytic calculation	FEA calculation	Error (%)
Titanium alloy I (Ti/94.5/Al 3/V 2.5) thickness=51μm	Max tip deflection (mm)	1.96	**1.88**	**4**
	Blocking force(μN)	33,632	**33,022**	**1.8**
	1st resonance mode(HZ)	60.7	**63.27**	**4**
	2nd resonance mode(HZ)	380.3	**395.98**	**3.9**
Titanium alloy II (Ti/90/Al 6/V 4) thickness=50μm	Max tip deflection (mm)	1.98	**1.89**	**4.5**
	Blocking force(μN)	34,107	**33,531**	**1.7**
	1st resonance mode(HZ)	61.0	**63.72**	**4.2**
	2nd resonance mode(HZ)	382.2	**396.78**	**3.6**
Stainless Steel (Fe/Cr18/Ni 9/Ti) thickness=37μm	Max tip deflection (mm)	2.16	**2.06**	**4.6**
	Blocking force(μN)	37,410	**36,491**	**2.4**
	1st resonance mode(HZ)	59.4	**61.9**	**4**
	2nd resonance mode(HZ)	372.2	**387.3**	**3.9**
Mo thickness=30μm	Max tip deflection (mm)	2.29	**2.21**	**3.6**
	Blocking force(μN)	40,887.5	**39,816**	**2.6**
	1st resonance mode(HZ)	59.9	**62.38**	**1.6**
	2nd resonance mode(HZ)	375.5	**390.34**	**3.8**

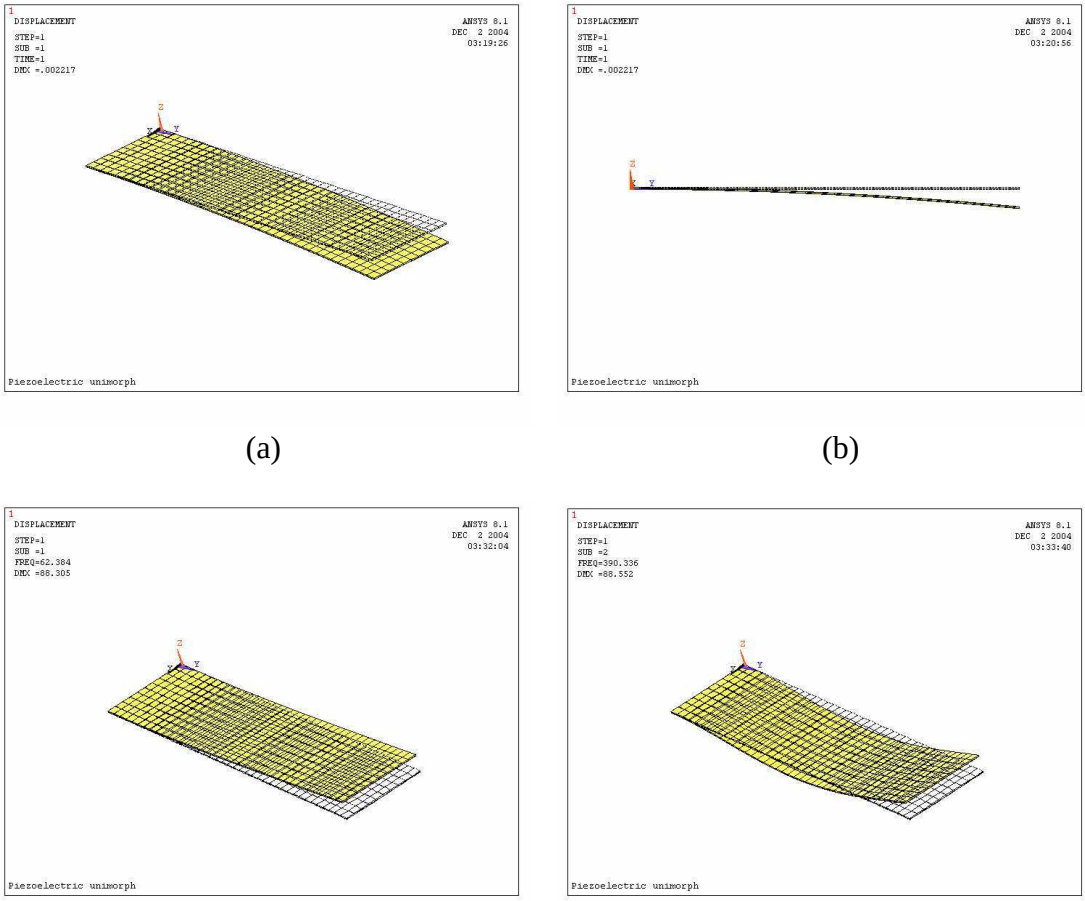

Figure 5.3 FEA calculation of an unimorph cantilever beam, in the case of L=40mm, w=10mm, thickness of piezoceramic is 127 μm and thickness of Mo metal shim is 30 μm. (a) The max tip deflection (2.21 mm); (b) The max tip deflection (front view); (c) The 1st resonance mode (62.38 Hz); (d) The 2nd resonance mode (390.34 Hz)

These FEA results were compared with the values obtained from the analytical calculations. The good agreement between the FEA modelling and the analytical results served as a validation of the FEA programming. Comparing the analytic and FEA results, it can be seen that the difference for the maximum tip deflection between the two methods is less than 4.6%, and less than 2.6% for the blocking force, less than 4.2% for the 1st resonance frequency and less than 3.9% for the 2nd resonance frequency. Based on these, further FEA modellings were developed for other structures which may not have simple analytical solutions, such as the fan configuration with which the PZT and the elastic layer have different lengths.

5.2.1.2 Maximum power output

The aim of this research is to develop a piezoelectric fan system for the application of flapping wing micro aerial vehicles, so it is not good enough to achieve a maximized tip displacement. More consideration on the blocking force and operating frequency, and the power output for the actuators have to be taken into account. For this purpose, the relationships between the displacement, blocking force and the resonant frequency of a linear piezoelectric actuator will be considered.

According to the definitions, the blocking force has the same value as the maximum actuating force produced by an actuator under a constant applied voltage, but at the opposite direction. If there is no force applied at the tip of the actuator, then the actuator can achieve the maximum displacement. As the force applied at the tip of the actuator is increased, the quasi-static displacement will decrease. Finally, finally, when there is no tip displacement, the applied force is the blocking force. The half value of the blocking force times the quasi-static displacement is the maximum work a piezoelectric actuator can perform under a certain applied voltage (Niezrecki et al., 2001), so to achieve the maximum work for a piezoelectric unimorph cantilever actuator requires the optimization of the thickness for the PZT and the substrates.

Consider unimorph cantilevers of the dimensions 40 mm x 10 mm, but with different PZT thicknesses, such as 127µm, 191µm mm and 267µm. These are all the ceramic PZT thicknesses available from the Piezo Systems, Inc. Assuming the elastic layer of the unimorph is stainless steel and the applied voltage is 170 V. Figure 5.4 shows the calculated quasi-static tip displacements of the cantilevers as functions of the thickness of the stainless steel for the three PZT thicknesses. It can be seen that the cantilever with the thinnest PZT patch produced the largest quasi-static tip displacement 2.90 mm when the thickness of the stainless steel is 40 µm. If a 50µm thick stainless steel shim was used instead the quasi-static tip displacement would be 2.83 mm, there is only a 3 % difference between the two.

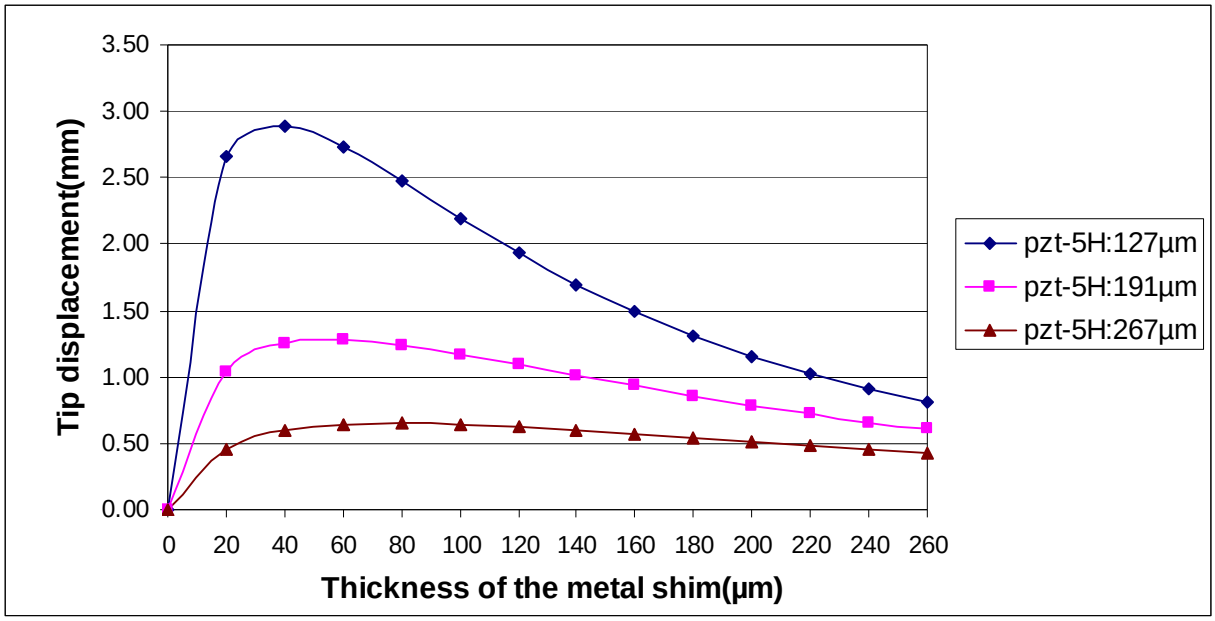

Figure 5.4 Cantilever tip displacements as functions of the thickness of the stainless steel shims for the three different PZT thicknesses under the applied voltage 170 V.

Figure 5.5 shows the profiles of blocking forces as functions of the thickness of the stainless steel for the three different PZT thicknesses for the same cantilevers concerned under a voltage of 170 V. It can be observed that a thicker PZT leads to a higher blocking force. For a constant thickness of the PZT patch, a thicker substrate will lead to a thicker total actuator thickness, which is proportional to the blocking force under a constant applied electric field, so the thicker substrate will lead a higher blocking force.

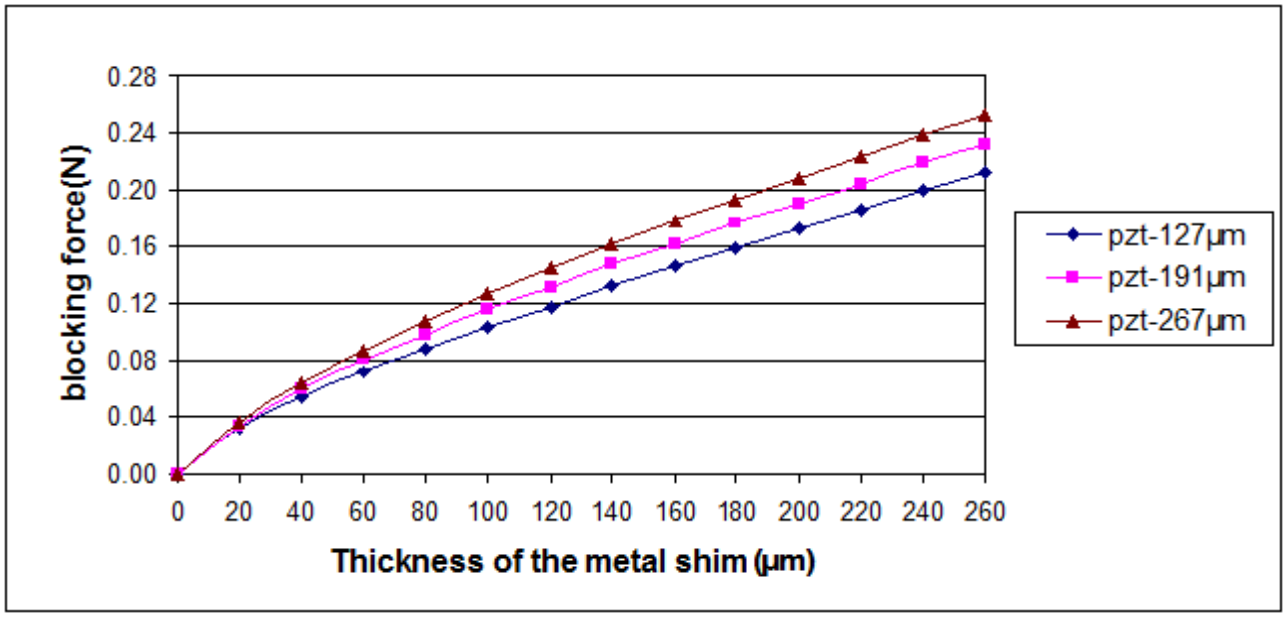

Figure 5.5 Blocking force for various PZT piezoelectric patch thickness under 170 V applied voltage

Figure 5.6 shows that for a fixed thickness of the PZT patch, a thicker substrate would lead to a thicker total thickness of the actuator, which in turn would lead to a higher 1st resonant frequency. Similarly, for a fixed thickness of the stainless steel substrate, a thicker PZT patch would lead to a thicker total thickness of the actuator, which in turn would lead to a higher 1st resonant frequency (Figure 5.6).

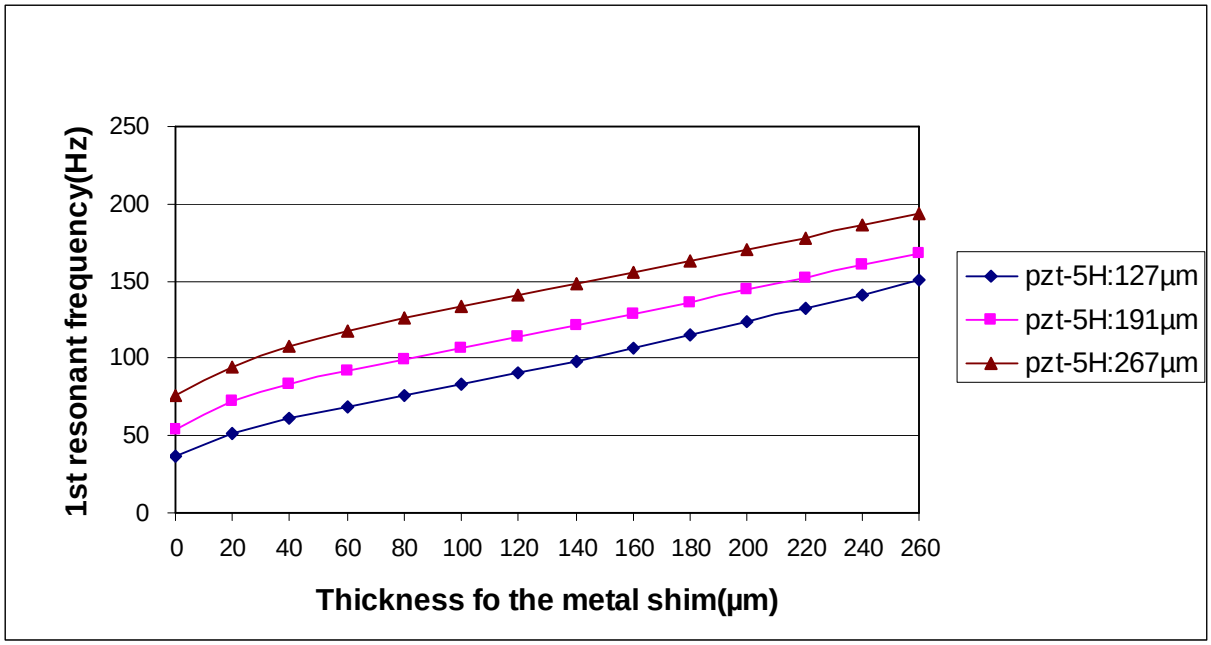

Figure 5.6 1st resonant frequencies for various PZT piezoelectric patch thickness

Figure 5.7 shows the calculated work outputs as functions of the stainless steel thickness of the unimorph piezoelectric cantilever actuators with 40 mm length and 10 mm width. It shows that the thinnest 127µm thickness for PZT could achieve the highest work output 0.114 Joule when the thickness of the stainless steel shim is 125 µm.

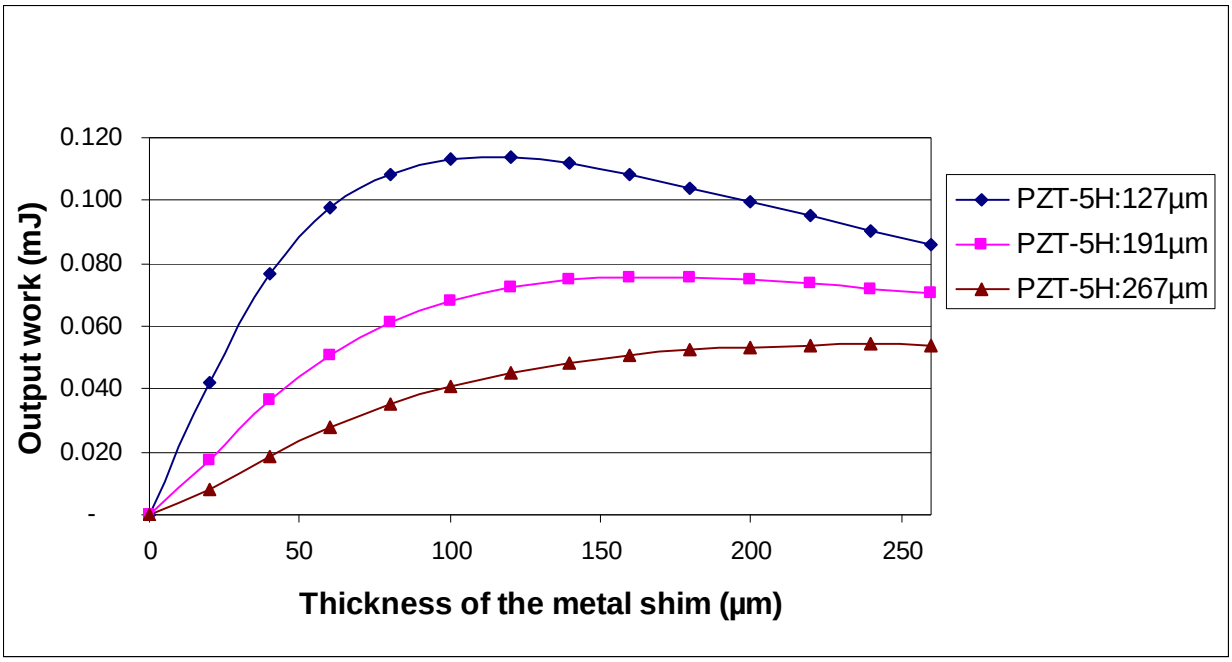

Figure 5.7 Work output for various PZT piezoelectric patch thickness under 170 V applied voltage

The power output could be calculated by multiplying work output and the operating frequency, so if the actuator operates in the resonant frequency (f_r), the maximum power output could be obtained by multiplying the work output and the resonant frequency. Figure 5.8 shows the power output as functions of the thickness of the stainless steel shim (the length of the actuator is 40mm). Although the combination of the 127µm PZT-5H with the 125µm stainless steel, could produce the maximum work output (Figure 5.7), but, as is shown in Figure 5.8, thicker stainless steel metal shim will lead to larger power output. This is due to the higher resonant frequencies for the thicker stainless steel shim. Also, some constrains should be taken into consideration. Generally speaking, for most of the flying creatures, their wing beating frequency is less than 100 Hz (Dickinson et al., 1999) for aerodynamic reason, so our actuators should be operated below 100 Hz. From Figure 5.6, if the 1st resonance is limited to less than 100 Hz, the limiting thickness for the stainless steel for three different PZT (127µm, 191µm and 267µm) should be 150µm, 80µm and 30µm respectively.From Figure 5.8, their power outputs are 11.3 mW, 6 mW, and 2 mW respectively. Therefore, at operating frequency below 100 Hz, the best configuration is a 127µm PZT-5H with a 150µm stainless steel,

which could generate 11.3 mW power.

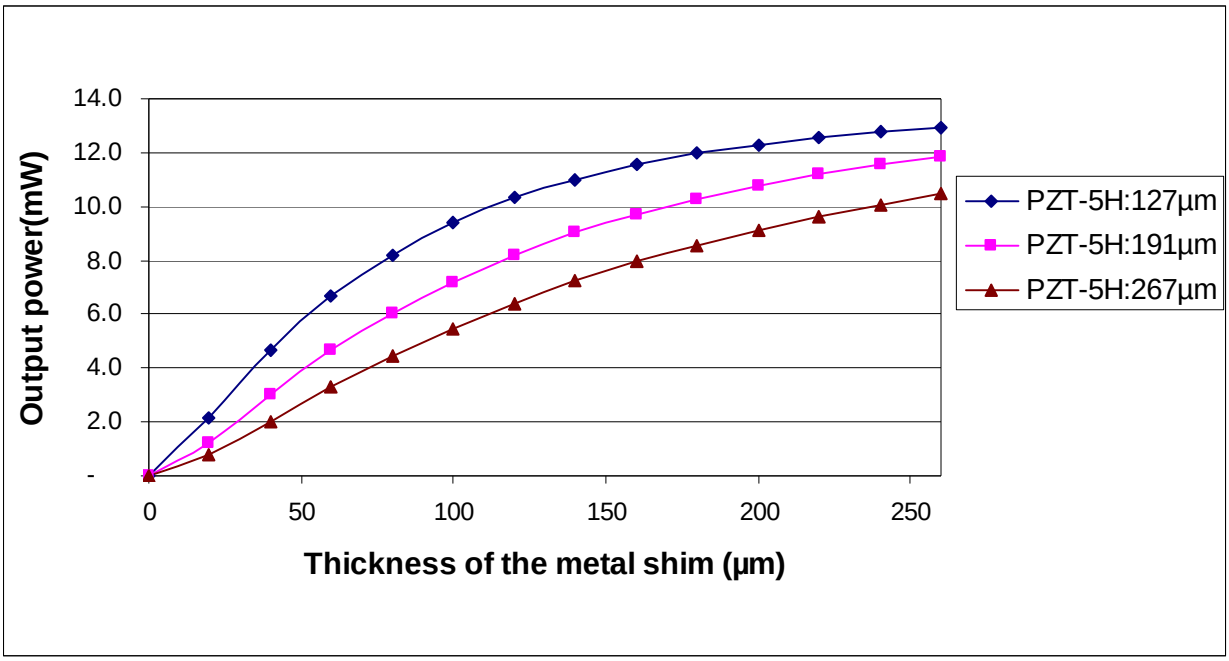

Figure 5.8 Power output in various PZT piezoelectric patch thickness (L=40mm)

However, for practical reasons, there is a limited selection of thickness for the stainless steel shim. From the supplier Goodfellow UK, the relevant thicknesses are 50µm, 125µm, and 250µm. Table V.11 summarises the calculated maximum quasi-static displacement, blocking force and work output for nine different actuators consisting of three different thickness of PZT patches including 127µm, 191µmm and 267µm, and three different thickness of stainless steel shims including 50 µm, 125µm, and 250µm, with the length equalling 40 mm, 30 mm respectively and the width equalling 10 mm, under a 170 V applied voltage. Although the actuator with the combination of a 50µm thick stainless steel and a 127µm thick PZT patch can produce the largest quasi-static displacement, however the work output in a cycle and the power output for this combination are not the largest. The optimized design to achieve the maximum work output is the combination of a 127 µm thick PZT patch and a 125 µm thick stainless steel, which can achieve a work output 0.113 mJ, and a power output of 10.5 mW. Therefore the best design, which can produce the highest power output, is the actuator with a 127 µm thick PZT patch and a 125µm thick stainless steel.

Table V.11 Calculated properties of different unimorph piezoelectric cantilever actuators

L (mm)	W (mm)	T_m (μm)	T_p (μm)	Displacement (δ) (mm)	Blocking force (F_b) (N)	work (0.5 δ* F_b) (mJ)	1st resonant frequency (fr) (Hz)	Power (0.5 δ* F_b* fr) (m-Watt)
40	10	50	127	2.83	0.063	0.089	64.6	5.7
40	10	50	191	1.27	0.070	0.044	87.2	3.9
40	10	50	267	0.63	0.075	0.024	112.8	2.7
40	10	125	127	1.87	0.121	0.113	92.6	10.5
40	10	125	191	1.07	0.136	0.073	115.5	8.4
40	10	125	267	0.62	0.149	0.046	143.3	6.6
40	10	250	127	0.86	0.206	0.088	145.7	12.9
40	10	250	191	0.63	0.225	0.071	164.3	11.7
40	10	250	267	0.44	0.246	0.054	189.7	10.3
30	10	50	127	1.59	0.083	0.067	114.9	7.6
30	10	50	191	0.72	0.093	0.033	155.0	5.2
30	10	50	267	0.35	0.101	0.018	200.5	3.6
30	10	125	127	1.05	0.162	0.085	164.6	14.0
30	10	125	191	0.60	0.181	0.055	205.3	11.2
30	10	125	267	0.35	0.199	0.035	254.7	8.8
30	10	250	127	0.48	0.275	0.066	259.1	17.1
30	10	250	191	0.36	0.301	0.053	292.1	15.6

5.3 Piezoelectric fans

5.3.1 Piezoelectric fan optimization at quasi-static operation

5.3.1.1 FEA modelling

In the last section, piezoelectric unimorph cantilever actuators were investigated. As having been discussed before, this type of piezoelectric actuator can produce a relatively small displacement only. Next, another configuration will be investigated, namely the fan configuration where the passive elastic layer is longer than the active PZT layer. These piezoelectric fan actuators have been proved capable of producing much larger displacement. Unlike the unimorph cantilever structure, for the piezofan structure there is no simple analytical equation to calculate its performance parameters such as the tip displacement, the blocking force, etc. As having been discussed before, computer matrix calculations are usually required for the calculation of the resonant frequencies for these structures. In this section, we will mainly apply the FEA technique to investigate the performance of the piezofan actuators.

The relationships between the tip displacement and the length and the thickness ratios of the PZT patch to the elastic layer, PZT patch location in a piezofan under a constant voltage were first modelled in order to achieve the maximum tip displacement. The optimisation of the thickness ratio of the PZT to the stainless steel elastic layer was carried out in the last section. Two more variations were considered: one was to change the length of the PZT patch whilst keeping the length of the stainless steel shim a constant (Figure 5.9a). The PZT patch length was varied from 0 to 40 mm (the width 10 mm and the thickness 191 μm were kept constant), the stainless steel shim dimensions (40 mm x 10mm x 50 μm) were kept constants; The other was to keep PZT patch and stainless steel shim lengths the same but varying the location of the PZT patch. The PZT patch was 30 mm in length and the stainless steel shim was 40 mm long. The material parameters used in the FEA are listed in Table III.1.

It can be seen from Figure 5.9b that the longer the PZT patch the larger the static tip displacement. Hence, if the largest tip displacement is to be achieved, the PZT patch should cover the whole length of the metal shim. Figure 5.9c shows the modelled relationship between the PZT patch length and the 1st resonant frequency of the fan. It can be observed that the longer the PZT patch the higher the first resonant frequency of the piezoelectric fan. This is apparent since a longer PZT patch increases the stiffness of the whole piezoelectric fan, so the first resonant frequency is increased.

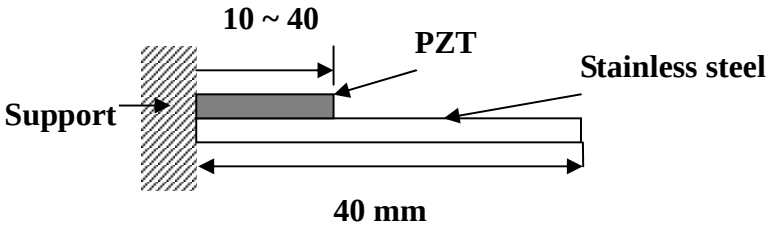

(a)

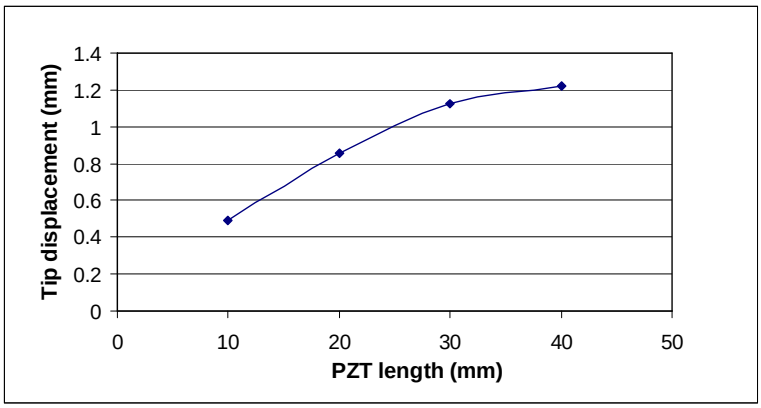

(b)

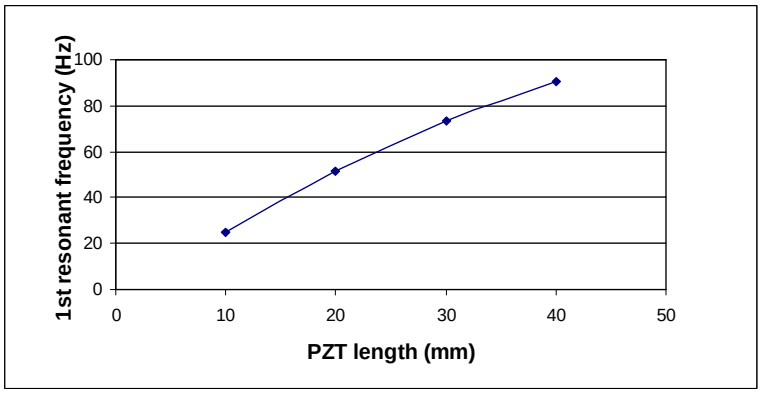

(c)

Figure 5.9 FEA results of the effect of the PZT patch length: (a) Schematic; (b) on the static tip displacement and (c) on the 1st resonant frequency

Figure 5.10 shows (a) the schematic of the piezoelectric fan; (b) the relationships between the tip displacement and (c) the 1st resonant frequency with the PZT patch location. It can be seen that for the location of the PZT patch (as represented by the left of the PZT patch), further away from the clamping position leads to a smaller maximum tip displacement under a certain driving voltage (Figure 5.10b). So, if a larger tip displacement is required, the PZT patch should be placed as close to the clamping position as possible. The 1st resonant frequency of the fan also decreases with the PZT patch moving away from the clamping location (Fig. 5.10c).

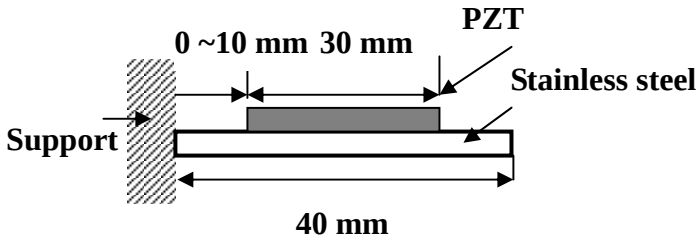

(a)

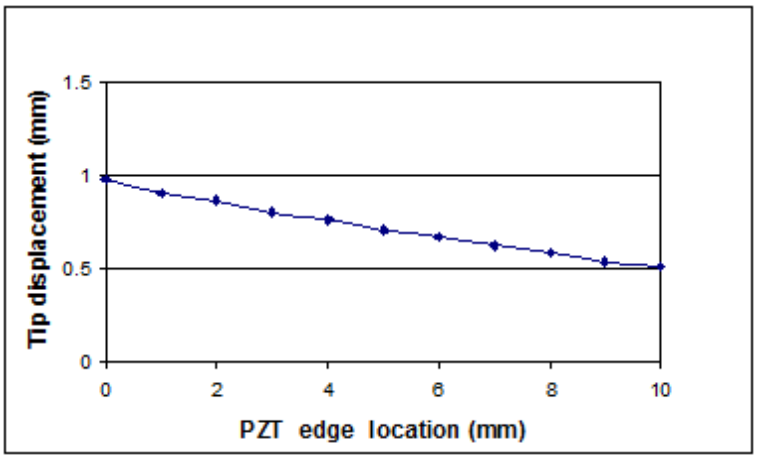

(b)

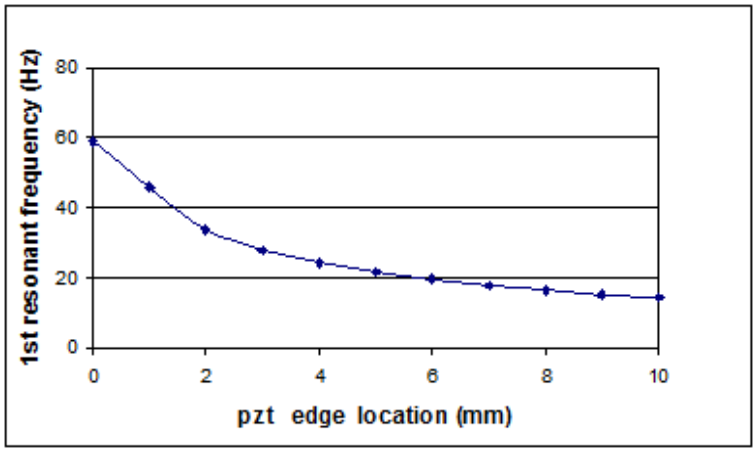

(c)

Figure 5.10 FEA results of the effect of the PZT patch location: (a) Schematic; (b) on the static tip displacement and (c) on the 1st resonant frequency

5.3.1.2 Piezoelectric fan with discrete PZT patches

Another variation of the fan configuration investigated is that the active part is consisted of two or more discrete PZT patches. Two situations were investigated. Case 1 is a piezoelectric fan consisted of two discrete PZT patches with a total length 30 mm, so each one is 15 mm long and 10 mm wide. The PZT thickness is 191 µm and the stainless steel is 43 mm in length, 10 mm in width and 125 µm in thickness. As for Figure 5.10 there is a 3 mm gap between the clamping and the edge of the first PZT patch. The gap between the two PZT patches varied from zero to 9 mm (Fig. 5.11 (a)). Case 2 is a structure consisted of three same PZT patches, each are 10 mm x10 mm x 191µm in dimensions. The stainless steel has the same dimensions as for the Case 1. Again, there is a 3 mm space for clamping at the edge of the first PZT patch. The gaps between two PZT patches are kept same and varied from zero to 4 mm (Figure 12 (a)). The material properties used in FEA are summarised in Table III.1.

Figure 5.11 shows (a) the schematic of the piezofan with two discrete PZT patches; (b) the relationships between the tip displacement and (c) the 1st resonant frequency with the gap between the two PZT patches. It can be seen from Figure 5.11 (b) that the bigger

gap between two PZT patch is, the smaller is the tip displacement at quasi-static condition. Hence, if a larger quasi-static tip displacement is required, the PZT patches should be bonded as close as possible. It can also be observed from Figure 5.11 (c) that the bigger gap between two PZT patch is, the lower first resonant frequency of the piezofan is. Figure 5.12 shows (a) the schematic of the piezo fan with three discrete PZT patches; (b) the relationships between the tip displacement and (c) the 1st resonant frequency with the gap distance between any two PZT patches. From Figure 5.12 (b) it can be seen that bigger gap leads to a smaller quasi-static tip displacement under a certain voltage. It can also be observed from Figure 5.12 (c) that a bigger gap between PZT patches leads to a lower first resonant frequency of the piezoelectric fan. These results suggest that to have discrete PZT patches does not improve the quasi-static performance of the piezofan actuator in terms of larger tip displacement and higher resonant frequency.

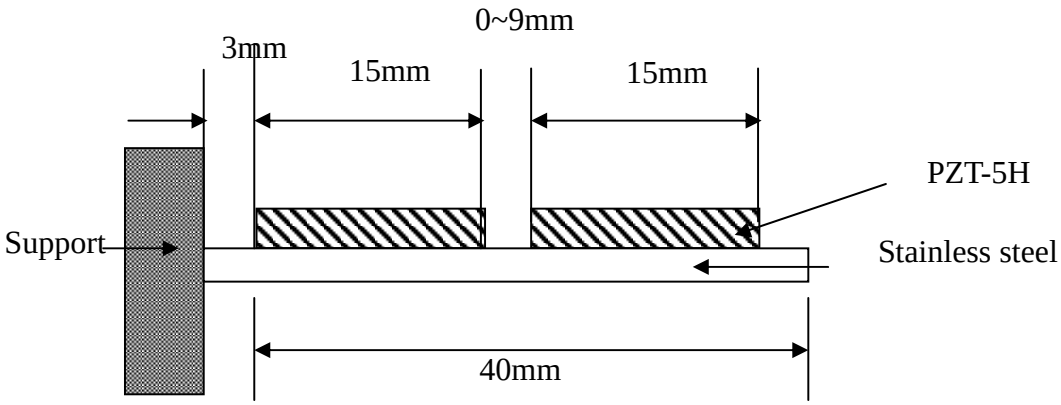

(a)

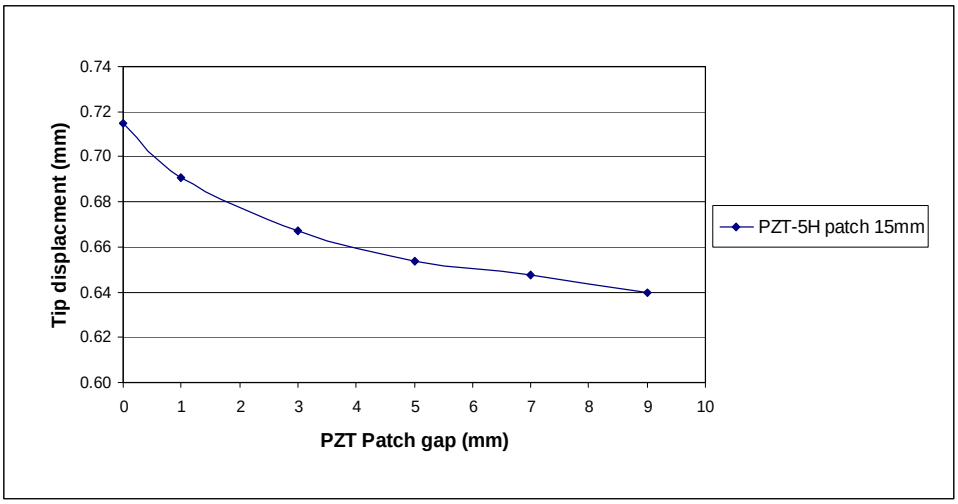

(b)

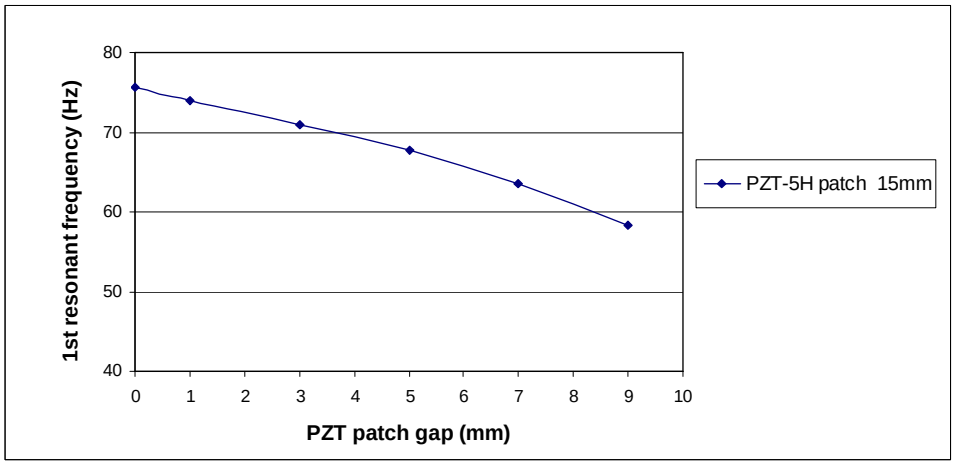

(c)

Figure 5.11 FEA results on the effect of the discrete PZT patch (two patches): (a) Scheme; (b) on the static tip displacement and (c) on the 1st resonant frequency.

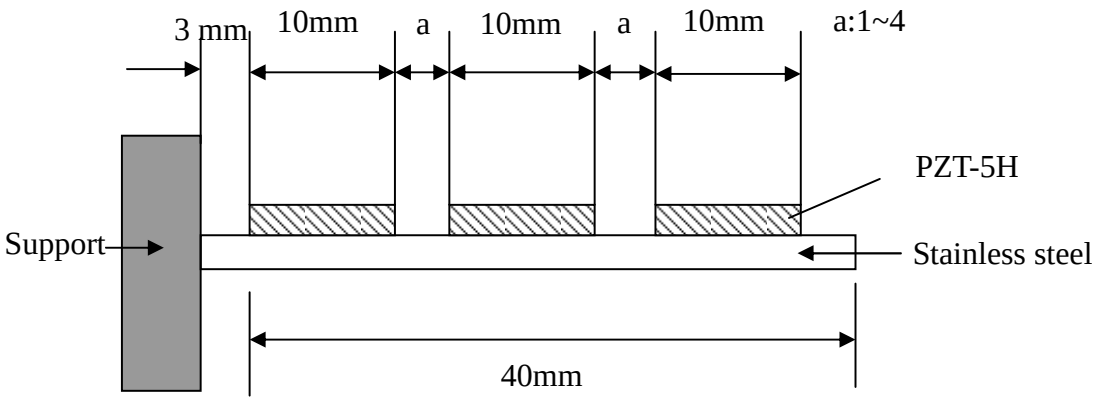

(a)

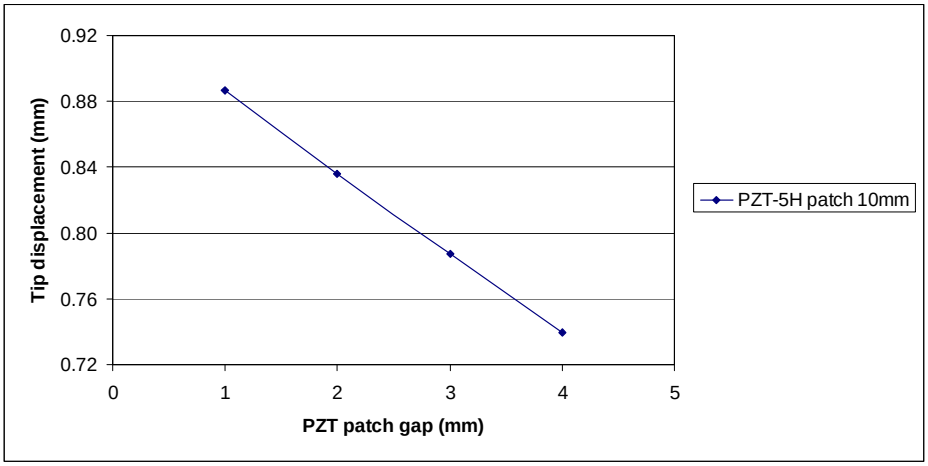

(b)

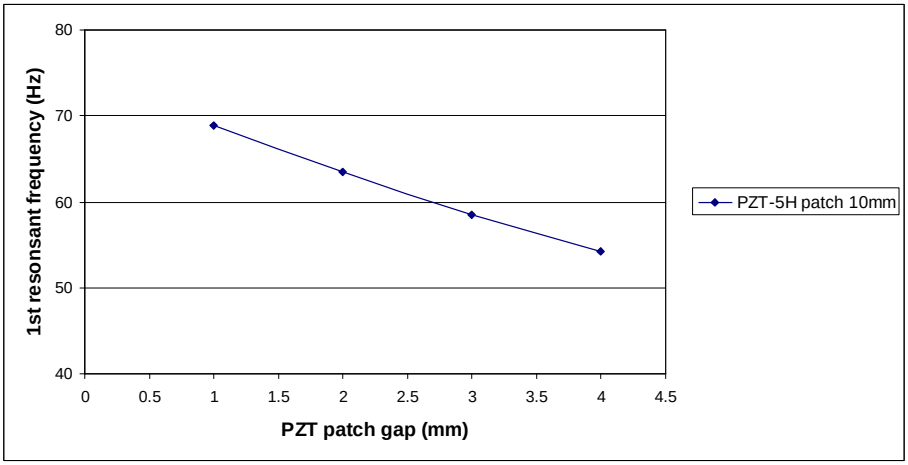

(c)

Figure 5.12 FEA results on the effect of the discrete PZT patch (three patches): (a) Scheme; (b) on the static tip displacement and (c) on the 1st resonant frequency

5.3.1.3 Measurement results

A piezofan with the PZT patch 30 mm and the metal shim 40 mm in lengths (and both were 10 mm in width) was prepared (Figure 5.13a) and its quasi-static tip displacements at voltages from 0~70V were measured by the optical fibre sensor as described in chapter 3. Figure 5.13b shows its static tip displacement as a function of the driving voltage between 0 and 70 V. The static tip displacement was 401 μm under 70 V, and it was nearly a linear relationship between the tip displacement and the driving voltage. Also observed was the good agreement between the measured results and the FEA values (Figure 5.13b). The blocking force at the tip of the fan was measured to be 12.8 mN at 70 V, which was also in good agreement with the FEA modelling. The tip displacements for driving voltages above 70V were outside the measurement range of the optical fibre sensor used, so a linear extrapolation against voltage was used to estimate the static tip displacements of the piezoelectric fan at voltages above 70 V.

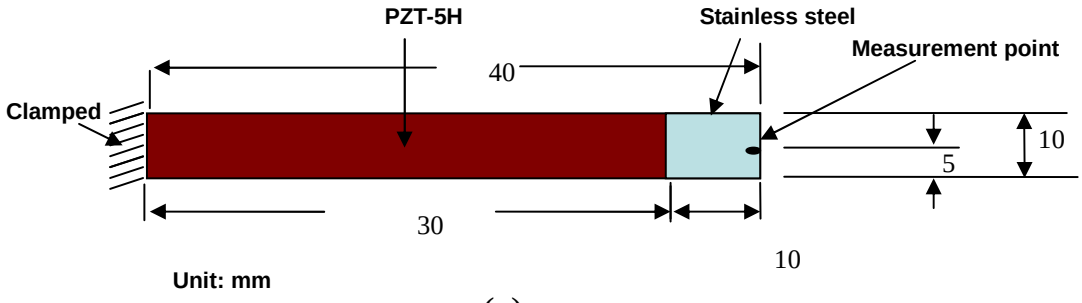

(a)

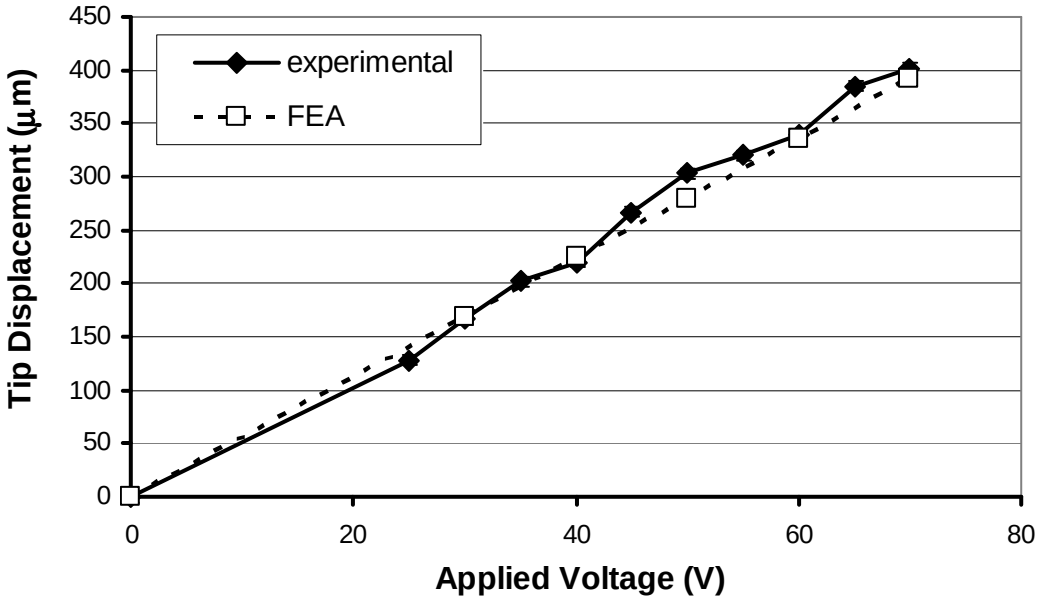

(b)

Figure 5.13 The piezofan and its tip displacement under an applied voltage from 0 to 70 V. (a) Schematic; (b) FEA and measurement results at quasi-static frequency.

5.3.2 Piezoelectric fan at resonance operation

5.3.2.1 Analytical and FEA calculations

For the piezofan as shown schematically in Figure 4.7, we work out the equation to calculate the resonant frequencies below.

The section one can be treated as a cantilever unimorph piezoelectric beam and the section two can be treated as a pure cantilever beam. From chapter 4, assuming the solutions for the two regions for the free vibration,

$$y_1 = u_1 T_1(t) \qquad 0 \le x \le L_1$$

$$y_1 = u_2 T_1(t) \qquad L_1 \le x \le L_2$$

$$u_1 = c_1 \cos\beta x + c_2 \sin\beta x + c_3 \cosh\beta x + c_4 \sinh\beta x, \quad 0 \le x \le L_1$$

$$u_2 = c_5 \cos\alpha x + c_6 \sin\alpha x + c_7 \cosh\alpha x + c_8 \sinh\alpha x), \quad L_1 \le x \le L_2$$

where

$$\beta = \left[\frac{\left(\rho_b A_b + \rho_p A_p\right)\omega^2}{2a_2 I_{PN} + 2a_3 A_p + E_b I_{bN}} \right]^{1/4}$$

$$\alpha = \left(\frac{\rho_c A_c \omega^2}{E_c I_c} \right)^{1/4}$$

From the boundary conditions, equations (4-113) to (4-116), we have

$C_1 + C_3 = 0$

$C_2 + C_4 = 0$

$$-c_5 \cos\alpha L_2 - c_6 \sin\alpha L_2 + c_7 \cosh\alpha L_2 + c_8 \sinh\alpha L_2 = 0$$

$$c_5 \sin\alpha L_2 - c_6 \cos\alpha L_2 + c_7 \sinh\alpha L_2 + c_8 \cosh\alpha L_2 = 0$$

From the natural boundary conditions at L_1, equations (4-105) to (4-108), we have

$$c_1 \cos\beta L_1 + c_2 \sin\beta L_1 + c_3 \cosh\beta L_1 + c_4 \sinh\beta L_1 - c_5 \cos\alpha L_1 - c_6 \sin\alpha L_1 - c_7 \cosh\alpha L_1 - c_8 \sinh\alpha L_1 = 0 \quad (5\text{-}1)$$

$$-c_1\beta \sin\beta L_1 + c_2\beta \cos\beta L_1 + c_3\beta \sinh\beta L_1 + c_4\beta \cosh\beta L_1 + c_5\alpha \sin\alpha L_1 - c_6\alpha \cos\alpha L_1 - c_7\alpha \sinh\alpha L_1 - c_8\alpha \cosh\alpha L_1 = 0 \quad (5\text{-}2)$$

$$-c_1\beta^2 Y_1 \cos\beta L_1 - c_2\beta^2 Y_1 \sin\beta L_1 + c_3\beta^2 Y_1 \cosh\beta L_1 + c_4\beta^2 Y_1 \sinh\beta L_1 + c_5\alpha^2 Y_2 \cos\alpha L_1 + c_6\alpha^2 Y_2 \sin\alpha L_1 - c_7\alpha^2 Y_2 \cosh\alpha L_1 - c_8\alpha^2 Y_2 \sinh\alpha L_1 = 0 \quad (5\text{-}3)$$

$$c_1\beta^3 Y_1 \sin\beta L_1 - c_2\beta^3 Y_1 \cos\beta L_1 + c_3\beta^3 Y_1 \sinh\beta L_1 + c_4\beta^3 Y_1 \cosh\beta L_1 - c_5\alpha^3 Y_2 \sin\alpha L_1 + c_6\alpha^3 Y_2 \cos\alpha L_1 - c_7\alpha^3 Y_2 \sinh\alpha L_1 - c_8\alpha^3 Y_2 \cosh\alpha L_1 = 0 \quad (5\text{-}4)$$

Here $Y_1 = \left(E_b I_{bN} + 2a_2 I_{pN} + 2a_3 A_P\right)$ (5-5)

$Y_2 = E_c I_c$ (5-6)

The above 8 equations can be written as a matrix form:

$$\begin{pmatrix} & & \\ & 8\times 8 & \\ & & \\ & & \\ & & \\ & & \\ & & \\ & & \\ & & \end{pmatrix}\begin{pmatrix} c_1 \\ c_2 \\ c_3 \\ c_4 \\ c_5 \\ c_6 \\ c_7 \\ c_8 \end{pmatrix} = \begin{pmatrix} 0 \\ 0 \\ 0 \\ 0 \\ 0 \\ 0 \\ 0 \\ 0 \end{pmatrix} \tag{5-7}$$

To have meaningful $c_1 \ldots c_8$, the determinant of the 8x8 matrix must be 0. Matlab software was used to carry out the calculation. Figure 5.14 shows a typical plot of the determinant as a function of angular frequency. The resonant frequency (73.4 Hz) was obtained by dividing 2π the angular frequency (461.2) at which the determinant equals zero ($73.4 = 461.2/2\pi$).

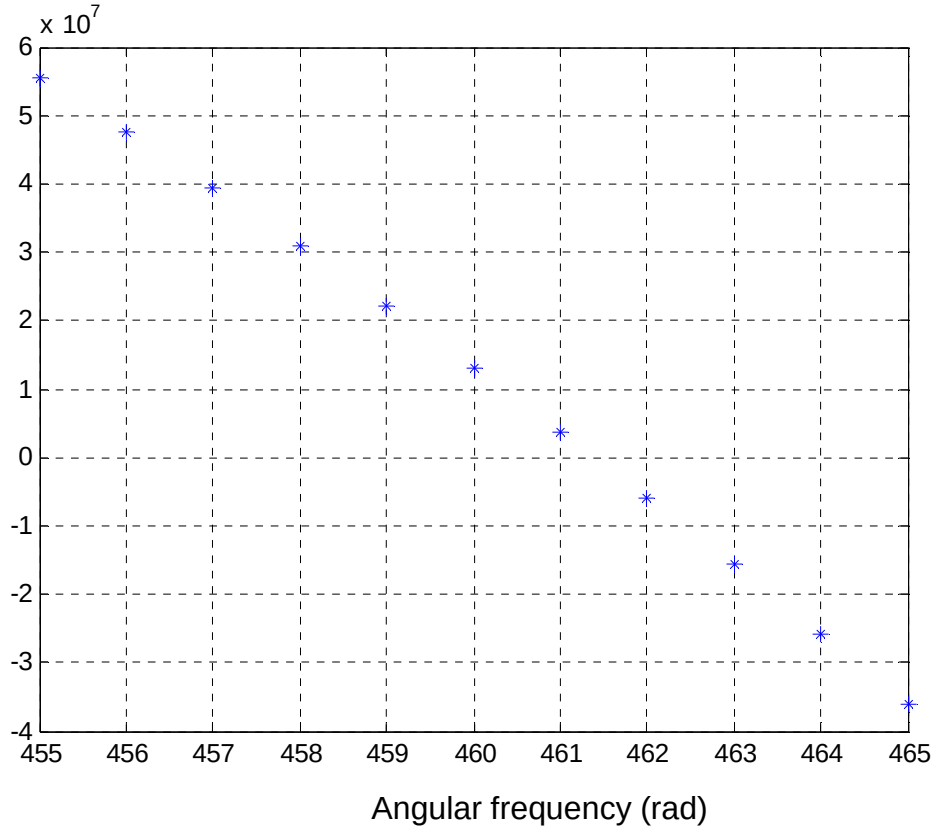

Figure 5.14 A typical Matlab plot of the determinant of the matrix as a function of the angular frequency

For a piezofan of dimensions as shown in Figure 5.1a, namely, the PZT patch 30 mm, the metal shim 40 mm in lengths, and both were 10 mm in width, the parameters used in the Matlab calculation are summarised in Table V.12.

Table V.12 Summary of parameters used for the analytical calculation

Symbol	Meaning	Value	Unit
ρ_b	density of the stainless steel	7900	kg/m^3
ρ_p	density of the piezo layer	7800	kg/m^3
A_b	cross section area of the substarte layer	1.25E-06	m^2
A_p	cross section area of the piezo layer	1.27E-06	m^2
E_b	Young's modulus for the substrate layer	2.00E+11	pa(N/m^2)
E_p	Young's modulus for the piezo layer	6.20E+10	pa(N/m^2)
I_{pn}	moment of inertia relative to the neutral axis for the piezo layer	1.3E-14	m^4
I_{bn}	moment of inertia relative to the neutral axis for the sub layer	2.8E-15	m^4
w	width	1.0E-02	m
$\rho_c=\rho b$	density of the third section layer	7900	kg/m^3
$A_c=A_b$	area of the third section	1.25E-06	m^2
$E_c=E_b$		2.00E+11	pa(N/m^2)
$I_c=I_b$	moment of inertia for the sub layer	1.6E-15	m^4
I_p	moment of inertia for the piezo layer	1.7E-15	m^4
t_b	thickness of the sub layer	1.25E-04	m
t_p	thickness of the piezo layer	1.27E-04	m
t_N (assume within the piezo layer)	neutral axis position	-3.23E-05	m
d1	the distance of central line of A_p to the t_N	9.58E-05	m
d2	the distance of central line of A_b to the t_N	3.02E-05	m

d_{31}	transverse piezo coefficient	-3.20E-10	m/voltage
${}^{T}\varepsilon_{33}/\varepsilon_0$		3400	
${}^{s}\varepsilon_{33}/\varepsilon_0$		2741.76	
ε_0		8.85E-12	Fm-1
${}^{T}\varepsilon_{33}$		3.01E-08	Fm-1
${}^{s}\varepsilon_{33}$		2.43E-08	Fm-1
k_{31}	transverse coupling factor	0.44	
a_2	Equation (4-76)	39107452001	
a_3	Equation (4-77)	-7.44E+01	
V_0	Voltage	170	Volt
a_4	Equation (4-78)	2544.75	
a_4A_p	Equation	3.23E-03	
$Y_1(2a_2*I_{pn}+2a_3*A_p+E_b*I_{bn})$	Equation (4-95)	1.4E-03	
$Y_2(E_bI_b)$	Equation (4-95)	3.26E-04	
L_1	Metal shim length	3.0E-02	m
L_2	Piezo layer length	4.0E-02	m

The calculated first resonant frequency is 74.2 Hz; this compares to the FEA results 73.8 Hz (from Figure 5.9). It can be seen that the agreement between the analytical calculation and FEA modelling was within 0.6% with each other. More comparison will be presented latter.

For the configuration as shown in Figure 4.8, reproduced below, which is a better representative of the real piezofan, there are three sections. Section one is from the origin to length L_1; section two is from the length L_1 to L_2, and section three is from the length L_2 to L_3. The PZT layer has the same length with the substrate in the section two; however, there is no piezoelectric layer in section I and III.

Assume the solutions are:

$$u_1 = c_1\cos\alpha x + c_2\sin\alpha x + c_3\cosh\alpha x + c_4\sinh\alpha x, \quad 0 \le x \le L_1 \tag{5-8}$$

$$u_2 = c_5\cos\beta x + c_6\sin\beta x + c_7\cosh\beta x + c_8\sinh\beta x, \quad L_1 \le x \le L_2 \tag{5-9}$$

$$u_3 = c_9 \cos\alpha x + c_{10} \sin\alpha x + c_{11} \cosh\alpha x + c_{12} \sinh\alpha x, \quad L_2 \le x \le L_3 \tag{5-10}$$

In section I, there are four constants to be determined, C_1, C_2, C_3, and $C4$, and the boundary conditions are $u_1(0) = 0$ $u_1'(0) = 0$, which lead to

Section

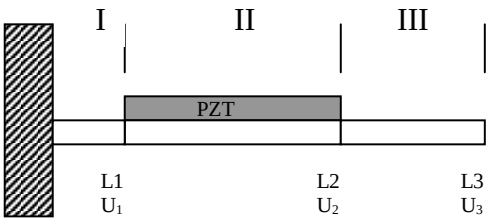

Reproduced Figure 4.8 The scheme of a piezofan in practice

$$C_1 + C_3 = 0, \tag{5-11}$$

$$C_2 + C_4 = 0. \tag{5-12}$$

In section III, there are four constants to be determined, C_9, C_{10}, C_{11}, and C_{12}, and the boundary conditions $u_3''(L_3) = 0, u_3'''(L_3) = 0$ which leads to

$$-c_9 \cos\alpha L_3 - c_{10} \sin\alpha L_3 + c_{11} \cosh\alpha L_3 + c_{12} \sinh\alpha L_3 = 0 \tag{5-13}$$

$$c_9 \sin\alpha L_3 - c_{10} \cos\alpha L_3 + c_{11} \sinh\alpha L_3 + c_{12} \cosh\alpha L_3 = 0 \tag{5-14}$$

In section II, there are four constants to be determined, C_5, C_6, C_7, and C_8, and the boundary conditions are natural boundary conditions at L_1.

$$c_1 \cos\alpha L_1 + c_2 \sin\alpha L_1 + c_3 \cosh\alpha L_1 + c_4 \sinh\alpha L_1 - c_5 \cos\beta L_1 - c_6 \sin\beta L_1 - c_7 \cosh\beta L_1 - c_8 \sinh\beta L_1 = 0 \tag{5-15}$$

$$-c_1\alpha\sin\alpha L_1 + c_2\alpha\cos\alpha L_1 + c_3\alpha\sinh\alpha L_1 + c_4\alpha\cosh\alpha L_1 + c_5\beta\sin\beta L_1 - c_6\beta\cos\beta L_1 - c_7\beta\sinh\beta L_1 - c_8\beta\cosh\beta L_1 = 0 \tag{5-16}$$

$$-c_1\alpha Y_2\cos\alpha L_1 - c_2\alpha^2 Y_2\sin\alpha L_1 + c_3\alpha^2 Y_2\cosh\alpha L_1 + c_4\alpha^2 Y_2\sinh\alpha L_1 + c_5\beta^2 Y_1\cos\beta L_1 + c_6\beta^2 Y_1\sin\beta L_1 - c_7\beta^2 Y_1\cosh\beta L_1 - c_8\beta^2 Y_1\sinh\beta L_1 = 0 \tag{5-17}$$

$$c_1\alpha^3 Y_2\sin\alpha L_1 - c_2\alpha^3 Y_2\cos\alpha L_1 + c_3\alpha^3 Y_2\sinh\alpha L_1 + c_4\alpha^3 Y_2\cosh\alpha L_1 - c_5\beta^3 Y_1\sin\beta L_1 + c_6\beta^3 Y_1\cos\beta L_1 - c_7\beta^3 Y_1\sinh\beta L_1 - c_8\beta^3 Y_1\cosh\beta L_1 = 0$$

(5-18)

And the natural boundary conditions at L_2;

$$c_5\cos\beta L_1 + c_6\sin\beta L_1 + c_7\cosh\beta L_1 + c_8\sinh\beta L_1 - c_9\cos\alpha L_1 - c_{10}\sin\alpha L_1 - c_{11}\cosh\alpha L_1 - c_{12}\sinh\alpha L_1 = 0 \quad (5\text{-}19)$$

$$-c_5\beta\sin\beta L_1 + c_6\beta\cos\beta L_1 + c_7\beta\sinh\beta L_1 + c_8\beta\cosh\beta L_1 + c_9\alpha\sin\alpha L_1 - c_{10}\alpha\cos\alpha L_1 - c_{11}\alpha\sinh\alpha L_1 - c_{12}\alpha\cosh\alpha L_1 = 0 \quad (5\text{-}20)$$

$$-c_5\beta^2 Y_1\cos\beta L_1 - c_6\beta^2 Y_1\sin\beta L_1 + c_7\beta^2 Y_1\cosh\beta L_1 + c_8\beta^2 Y_1\sinh\beta L_1 + c_9\alpha^2 Y_2\cos\alpha L_1 + c_{10}\alpha^2 Y_2\sin\alpha L_1 - c_{11}\alpha^2 Y_2\cosh\alpha L_1 - c_{12}\alpha^2 Y_2\sinh\alpha L_1 = 0 \quad (5\text{-}21)$$

$$c_5\beta^3 Y_1\sin\beta L_1 - c_6\beta^3 Y_1\cos\beta L_1 + c_7\beta^3 Y_1\sinh\beta L_1 + c_8\beta^3 Y_1\cosh\beta L_1 - c_9\alpha^3 Y_2\sin\alpha L_1 + c_{10}\alpha^3 Y_2\cos\alpha L_1 - c_{11}\alpha^3 Y_2\sinh\alpha L_1 - c_{128}\alpha^3 Y_2\cosh\alpha L_1 = 0 \quad (5\text{-}22)$$

In matrix form, these equations can be written as

$$\begin{pmatrix} & & \\ & 12\times 12 & \\ & & \end{pmatrix}\begin{pmatrix} c_1 \\ c_2 \\ c_3 \\ c_4 \\ c_5 \\ c_6 \\ c_7 \\ c_8 \\ c_9 \\ c_{10} \\ c_{11} \\ c_{12} \end{pmatrix} = \begin{pmatrix} 0 \\ 0 \\ 0 \\ 0 \\ 0 \\ 0 \\ 0 \\ 0 \\ 0 \\ 0 \\ 0 \\ 0 \end{pmatrix} \quad (5\text{-}23)$$

To have meaningful $c_1 \ldots c_{12}$, the determinant of the 12x12 matrix must be 0. Matlab software was used to carry out the calculation.

These calculations were carried out for a few piezofan configurations, Table V.13 summaries the calculated first resonant frequencies. It also summarises the 1st mode frequencies as obtained from FEM and the experimental measured 1st resonant frequencies. From this table V.13, it is clear that for thick metal shims, the FEA and the

analytical results agrees with each other very well. However, for the thinnest metal shim (50 μm), discrepancy exists between the FEM and the analytical values. This was probably due to several factors including the low mesh density for the thin layers, the assumption of an isotropic Young's Modulus of the PZT-5H ceramic and neglecting the bonding layer between PZT ceramic and the metal shim. From the table we can also see that the measured resonant frequencies (with the nominal gap distance being 3 mm) matched those theoretical ones (FEM or analytical) with the gap distances range from 3 to 7 mm, depending on the individual piezofan. This is understandable considering the variable conditions of the clamping therefore the deviation of the actual clamping length from its nominal value. The nominal clamping length for all the measured samples was 7 mm and there was a nominal 3 mm distance from the clamping edge to the start of the piezoelectric ceramics. If the clamping was perfect, the whole length of the clamping (7 mm) was clamped firmly, then the actual distance from the clamping edge to the start of the ceramics equals to its nominal value (3 mm). However, if the clamping was not perfect, part of the clamping length was still movable when the fan vibrates, then the effective distance from the clamping to the start of the ceramics will be larger than its nominal value 3 mm.

Table V.13 Summary of the analytical, FEA and experimental measured 1st resonant frequency for a few piezofan configurations

Distance from Clamping L_1 (m)	PZT Length L_2-L_1 (m)	Metal Length L_3-L_1 (m)	PZT Thickness t_p (m)	Metal Thickness t_b (m)	FEA 1st Mode (Hz)	Analytical 1st Mode (Hz)	Experimental 1st Mode (Hz)	Sample
0.003	0.03	0.04	0.000127	0.000125	67.1	70.9	**50.8**	Ba2
0.005	0.03	0.04	0.000127	0.000125	56.3	57.8		Ba2
0.007	**0.03**	**0.04**	**0.000127**	**0.000125**	**48.6**	**49**		Ba2
0.003	0.03	0.04	0.000191	0.00005	26.7	32	**28.2**	Ab1
0.004	**0.03**	**0.04**	**0.000191**	**0.00005**		**27.3**		Ab1
0.005	0.03	0.04	0.000191	0.00005	16.4	24		Ab1
0.003	**0.04**	**0.04**	**0.000191**	**0.00005**	**20**	**23.7**	**23.8**	Bb1
0.005	0.04	0.04	0.000191	0.00005	15.2	18		Bb1
0.003	0.03	0.04	0.000191	0.000125	71.6	73.5	**48.1**	Ab2
0.005	0.03	0.04	0.000191	0.000125	57.5	57.6		Ab2
0.007	**0.03**	**0.04**	**0.000191**	**0.000125**	**48.4**	**47.9**		Ab2

5.3.2.2 Measurement results

A few unimorph piezofans were prepared and their dynamic performances were investigated. Two different types of the piezoelectric fans, named type A, and type B, as shown in Figure 5.15 (a), were investigated. Both of them have 3 mm space from the clamping edge to the edge of the PZT patch. This is necessary to prevent the PZT being broken by the mounting base during the vibration. The only difference between them is the PZT patch of the type A which has 10 mm space from the top edge of the actuator, while there is no such space in Type B. So, the lengths of the PZT patchs are 30 mm in type A, and 40 mm in type B.

Notes were given to distinguish these actuators. The lengths of the PZT-5H patch in 30 mm and 40 mm were noted by capitals A and B respectively, as described above. The thickness of PZT-5H, either 127μm or 191μm, was noted by lower case letters a and b; the thickness of stainless steel, 50μm or 125μm, was noted by number 1 and 2; Therefore, if a piezofan was noted Aa1, that means that piezofan had 30 mm length of PZT-5H patch, the thickness of PZT patch is 127μm and the stainless steel is 50 μm thick.

Four actuators Ab1, Ab2, Ba2, and Bb1 were prepared for investigating the dynamic performances by the high-speed camera system. Figure 5.15 (b) shows the measured vibration magnitudes at the tip of piezofans as functions of frequency for the bending mode under a sinusoidal voltage of 170 V_{pp}. These show that the vibration amplitudes of these piezofans increased with the increasing frequency at first and peaked at their respective first resonant frequency, after that it decreased with the increasing frequency. Take an example of Ba2. This piezoelectric fan has the PZT patch of the dimensions 40mm x 10mm x 127μm, and the stainless steel of the dimensions 43mm x 10mm x 125μm. For frequencies below 46Hz, the bending displacement magnitude was very small, close to 3 mm. The displacement increased with the increasing frequency and peaked at 13.2 mm at the frequency 50.8.Hz, after that it decreased with the increasing frequency and was close to 3 mm again for frequencies higher than 57 Hz. The mechanical quality factor of the system, as defined by $f/\Delta f$, where Δf is the frequency difference between the two half maximum points, can be obtained from this profile and found to be equal to 10.4. Table V.14 summaries the properties of these piezofans. From this table, it can be seen that longer PZT length (comparing Bb1 with Ab1), thicker PZT thickness (comparing Ba2 with Ab2), and thicker metal shim (comparing Ab1 with Ab2) leads to higher quality factor.

Normally, the piezofan operating at its first resonant frequency has the largest dynamic displacement than at any other resonant frequencies, therefore, the value ($f_r*\delta$), namely the first resonant frequency (f_r) times the vibration amplitude (δ) can be regarded as a criteria to judge the performances of these piezoelectric fans (Taylor et al., 2003). The first resonant frequency of these piezoelectric fans are 28.2Hz, 48.1Hz, 50.8Hz, and 23.8Hz for Ab1, Ab2, Ba2, and Bb1, respectively; the corresponding vibration amplitudes at the first resonant frequencies are 7.2mm, 8.3mm, 13.2mm and 22.1mm, respectively. The ($f_r*\delta$) values of these piezofans Ab1, Ab2, Ba2, Bb1 are 203.1, 399, 670.6, 526 respectively. According to this criterion, the Ba2 had the best performance among these four piezofans (Table V.14). This agrees with the conclusion obtained at the quasi-static operation, as discussed in the last section 5.2.1.

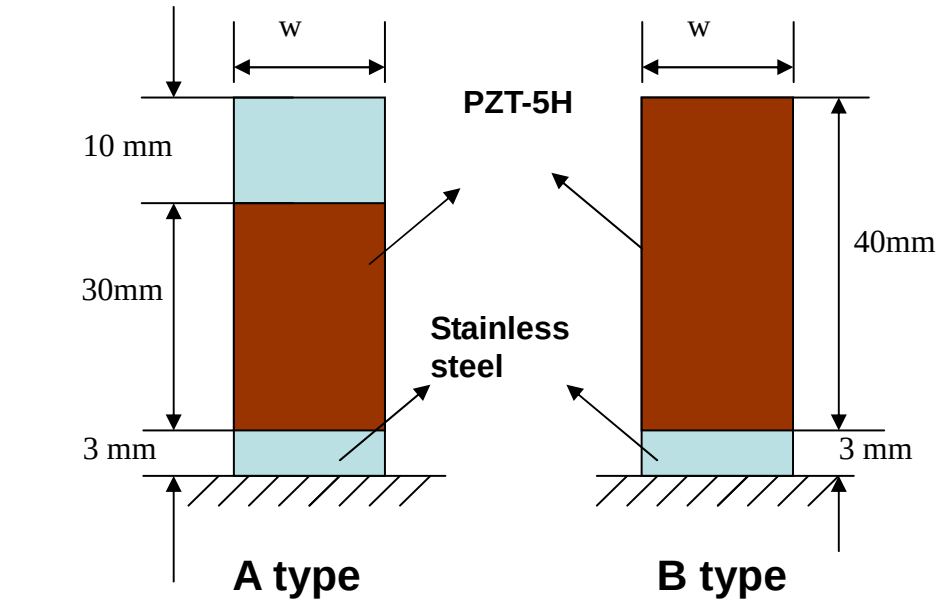

(a)

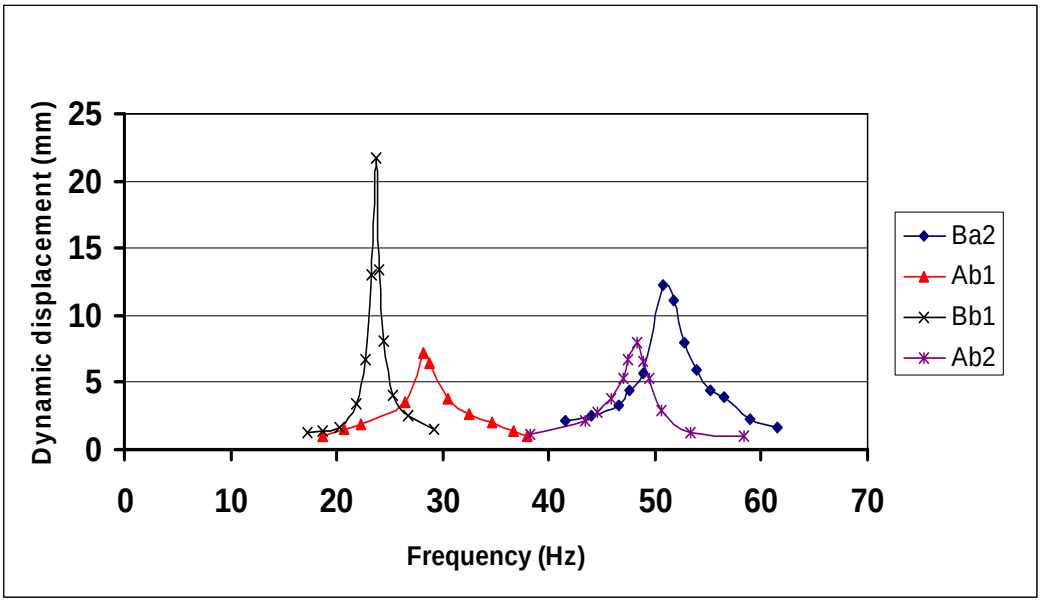

(b)

Figure 5.15 The measured bending displacement amplitude of different piezoelectric fans as functions of the operating frequency under 170 Vpp. (a) scheme (b) measurement results.

Table V.14 Summary of the piezofan performance for a few configurations

Sample	PZT Length	Metal Length	PZT Thickness	Metal Thickness	Experimental (f_r)	Δf at 3db	Quality Factor	Vibration Magnitude	$f_r\delta$
	L_2-L_1 (mm)	L_3-L_1 (mm)	t_p (mm)	t_b (mm)	1st Mode (Hz)	(Hz)	$f_r/\Delta f$	δ(mm)	
Ba2	30	40	0.127	0.125	50.8	4.9	10.4	13.2	670.6
Ab1	30	40	0.191	0.05	28.2	4	7	7.2	203.1
Bb1	40	40	0.191	0.05	23.8	1.2	19.8	22.1	526
Ab2	30	40	0.191	0.125	48.1	4	12	8.3	399

5.3.3 Two DOF motion of the coupled piezofans

5.3.3.1 FEA modelling of the coupled piezofans

FEA modelling and high speed camera photography were used to characterise the dynamic behaviours of the coupled piezofans as shown schematically in Figure 5.16. The two piezoefans were the Ba2 type, with the PZT patch of the dimensions 40mm x 10mm x 127μm, and the elastic stainless steel layer of the dimensions 43mm x 10mm x 125 μm, so the total length of the piezoefan was 43 mm, with the PZT bonded 10mm from one end of the stainless steel. There were a 3 mm distance between the clamping and the edge of the PZT patch and 7 mm of stainless steel for clamping. A pair of spars made of carbon fibre reinforced plastic (CFRP) connected with a flexible polymer skin formed a wing and the wing was attached to the two piezofans clamped in parallel to form the coupled piezofans. The gap between the two fans, therefore also the gap between the two spars, was varied from 10 mm to 2 mm.

Figure 5.17 shows the results of the FEA modal analysis. The first mode was pure bending (a), at 23.7 Hz. The second mode was pure twisting (b), at 58.0 Hz and the third mode was a mixture of bending and twisting (c) at 62.9 Hz. The material parameters used for the polymer and the CFRB in the FEA are listed in Table V.15.

Table V.15 Summary of the wing material parameters used in the FEA.

Material	polymer	CFRB
Thickness (μm)	50	100
Width (mm)	30	2
Young's Modulus (GPa)	8	200
Density (Kg/ m^3)	1534	1750
Poisson's ratio	0.27	0.27

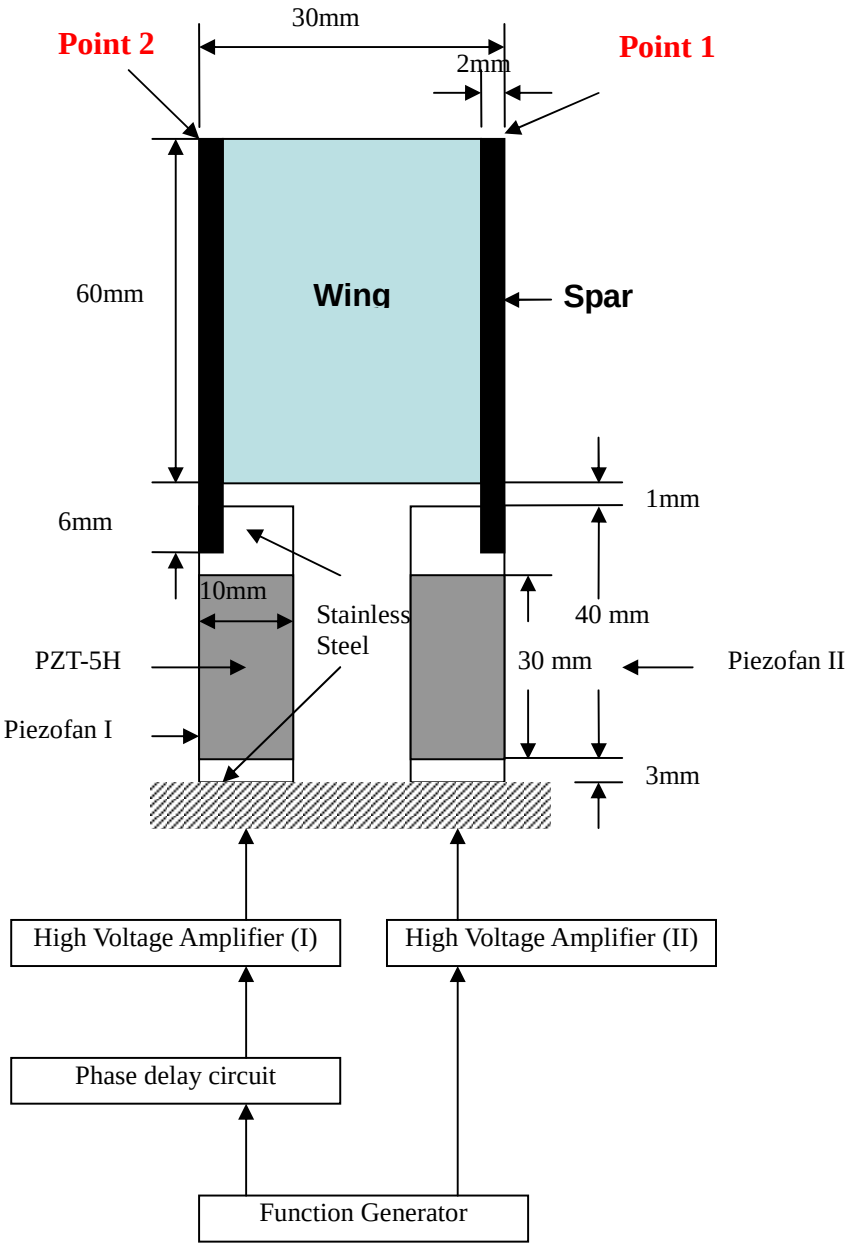

Figure 5.16 Schematic of the coupled piezofans system

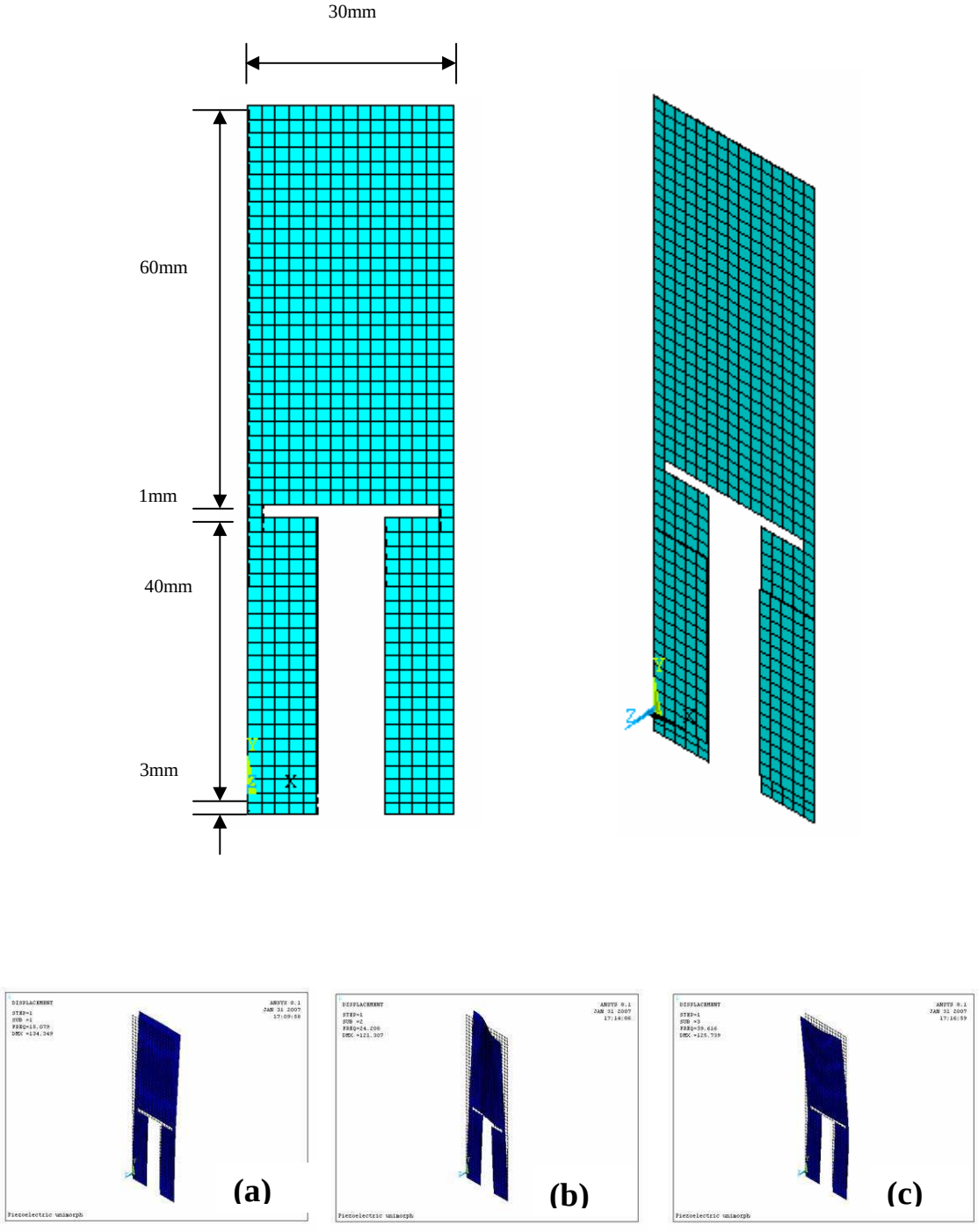

Figure 5.17 FEA modal analyses of the coupled piezofans: (a) 1st bending mode-23.7Hz; (b) 2nd twisting mode-58.0Hz; (c) 3rd mixed bending and twisting mode-62.9Hz

5.3.3.2 Measurement of the 2DOF motion of the coupled piezofans

Figure 5.18 shows typical pictures produced by superimposing two high speed camera images of the two extreme positions of the wing within a vibration cycle, for the set-up as shown in Figure 5.16, without any phase delay between the two input voltages 170 V_{pp} at frequencies (a) 13.8; (b)16.7; (c)18.2; (d)19.8; (e)21.4; (f)22.3; (g)24.9; (h)26.4; (i)27.7; (j)29.6; (k)32.2; (l)43.2; (m)44.4; (n)46.1; (p)47.4; (q)48.3; (r)49.7; (s)50.7; (t)51.8; (u)52.8; (v)54.5; (w)56.7 Hz. The PZT patch in both the actuators was of the dimensions 40mm x 10mm x 127μm, and the stainless steel was of the dimensions 43mm x 10mm x 125 μm. Both the flapping and twisting motion of the wing were obtained as described in Chapter 3. It was found that the flapping displacement was peaked at 20 mm at the frequency 22.3.Hz. The twisting motion peaked at 16º at the frequency 47.4Hz. Figure 5.19 shows the flapping and twisting amplitudes as functions of frequency for this pair of actuators. The quantitative discrepancy on the mode frequencies between the FEA modelled and actually measured values could be contributed by a few factors, such as the uncertainty of the Young's modulus for the CFRP spars and the polymer skin used in the FEA modelling, the non-perfect clamping at the foot of the piezofans, and also the difficulty to have two identical piezofans to drive the wing.

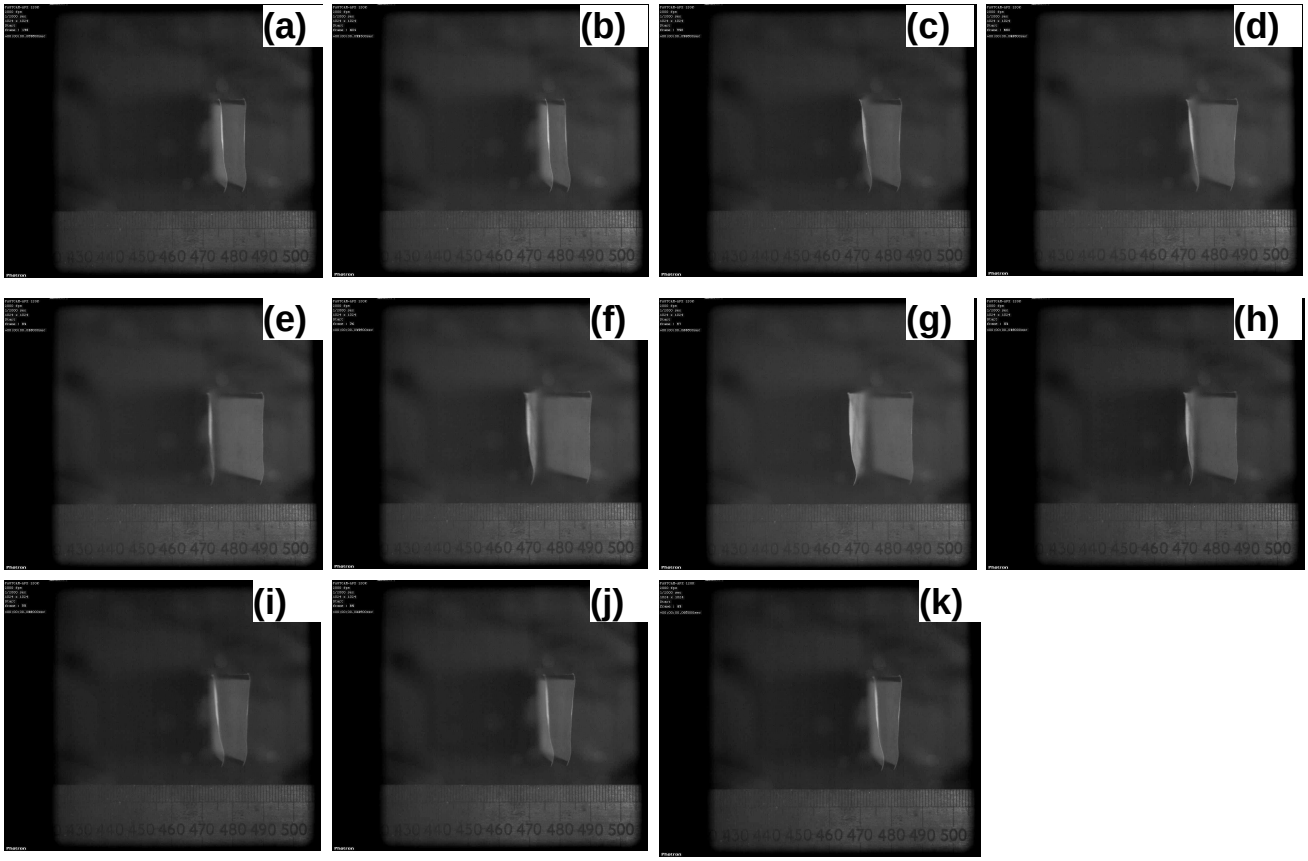

Figure 5.18.1 Typical pictures produced by superimposing two high speed camera images of the two extreme positions of the wing within a vibration cycle without any phase delay between the two input voltages 170 V_{pp} at frequencies (a) 13.8; (b)16.7; (c)18.2; (d)19.8; (e)21.4; (f)22.3; (g)24.9; (h)26.4; (i)27.7; (j)29.6; (k)32.2.

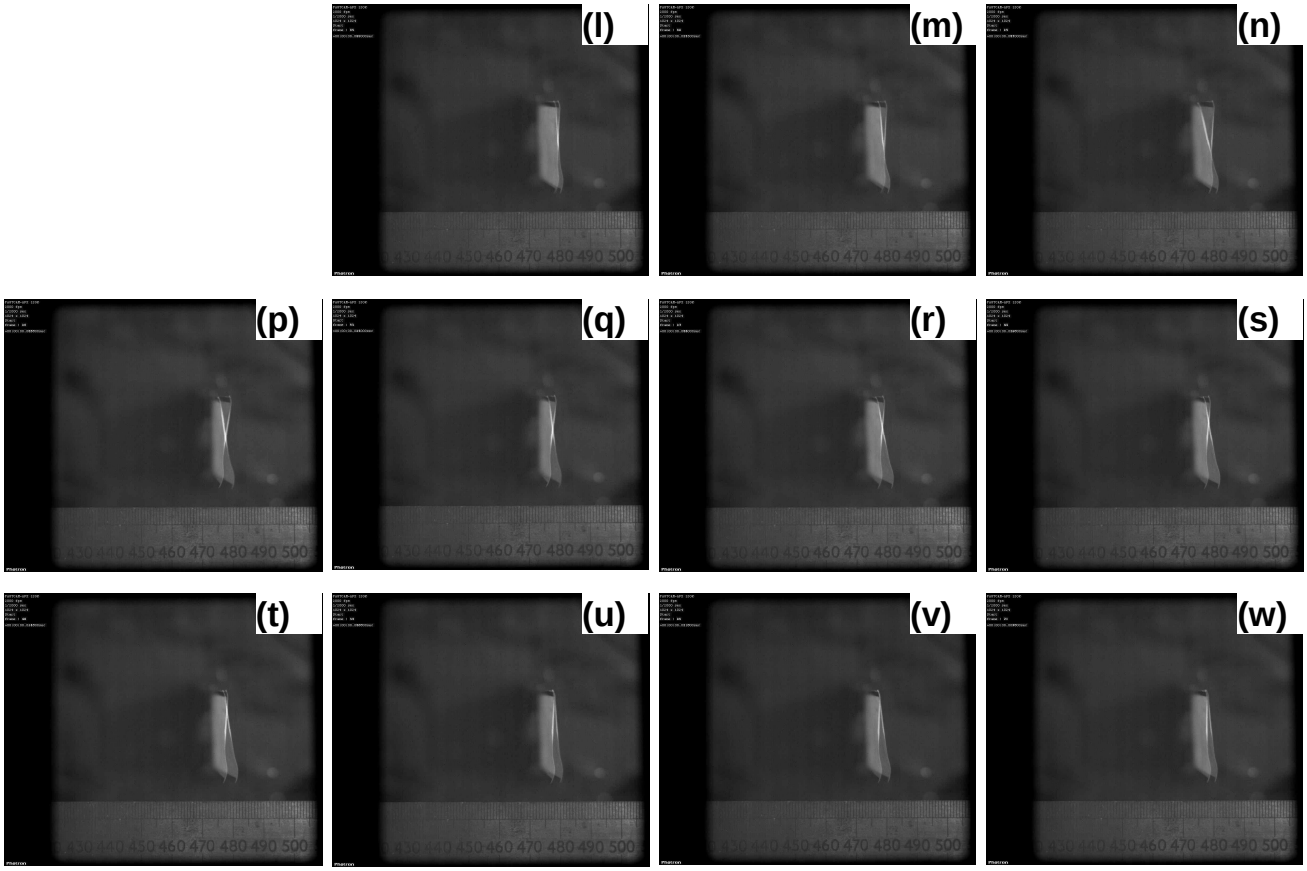

Figure 5.18.2 Typical pictures produced by superimposing two high speed camera images of the two extreme positions of the wing within a vibration cycle without any phase delay between the two input voltages 170 V_{pp} at frequencies (l)43.2; (m)44.4; (n)46.1; (p)47.4; (q)48.3; (r)49.7; (s)50.7; (t)51.8; (u)52.8; (v)54.5; (w)56.7 Hz

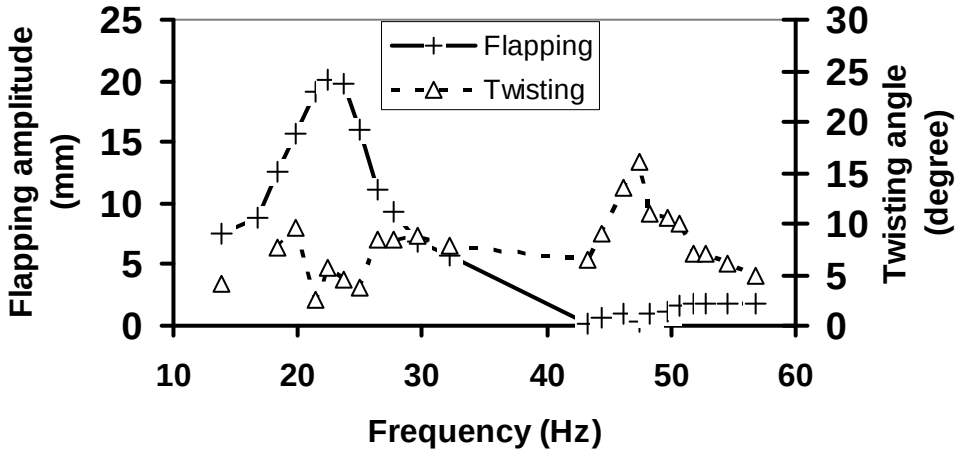

Figure 5.19 The measured flapping and twisting motion amplitude of the wing as functions of the operating frequency driving by the two coupled piezofans under 170 V_{pp}.

Before going further to quantitative analysis, we need to discuss the errors associated with these measurements.

(1) The uncertainty in the selection of images. The images as shown in Figure 5.18 were obtained by superimposing two images selected from hundreds of high speed camera pictures which represented the two opposite extreme positions in one cycle of the vibration. There are some uncertainties, about two frames, in the selection of these two images. The two images were selected usually from those at the vibration extreme positions and those showing little movements between the two adjacent images. For all the measurements, the camera speed was 2000 fps (frame per second). If the frequency of the vibration is f, then 2000/f images will be recorded in a cycle, and ideally the two images should be apart by 1000/f frames. Assuming the vibration is $V\sin(2\pi ft)$ where V is the vibration amplitude, then the two images selected should be close to $V\sin(\pi/2)$ and $-V\sin(\pi/2)$. The time difference between the two adjacent images were 1/2000 and the displacement error from two frames around $V\sin(\pi/2)$ is $V\sin(\pi/2)-V\sin(\pi/2\pm f/1000) \approx Vf^2/2000000$. This equals to 0.125V% when f=50Hz, i.e., 0.025 mm if V=25 mm and 0.025º if V=25 º. These are small.

(2) The uncertainty in determining the coordinates and line directions. Figure 5.20 shows a typical superimposed image from which the flapping and twisting motions were obtained. Due to the limited contrast, especially the non-straight-line of the top of the wing, it is not very clear where exactly are the corners (point 1 and 2 in Figure 3.16) of the wing, which leads to the uncertainty for the determination of the coordinates of the two corners (**P1**, **P2**, **P1'**, and **P2'**) and the line directions. From the experience, the error bar for the coordinates is about ±5 pixels, i.e. 50/115=0.43 mm. The error bar for the line direction is about ±1.5^{o} reflecting the curved wing edge as shown in Figure 5.20.

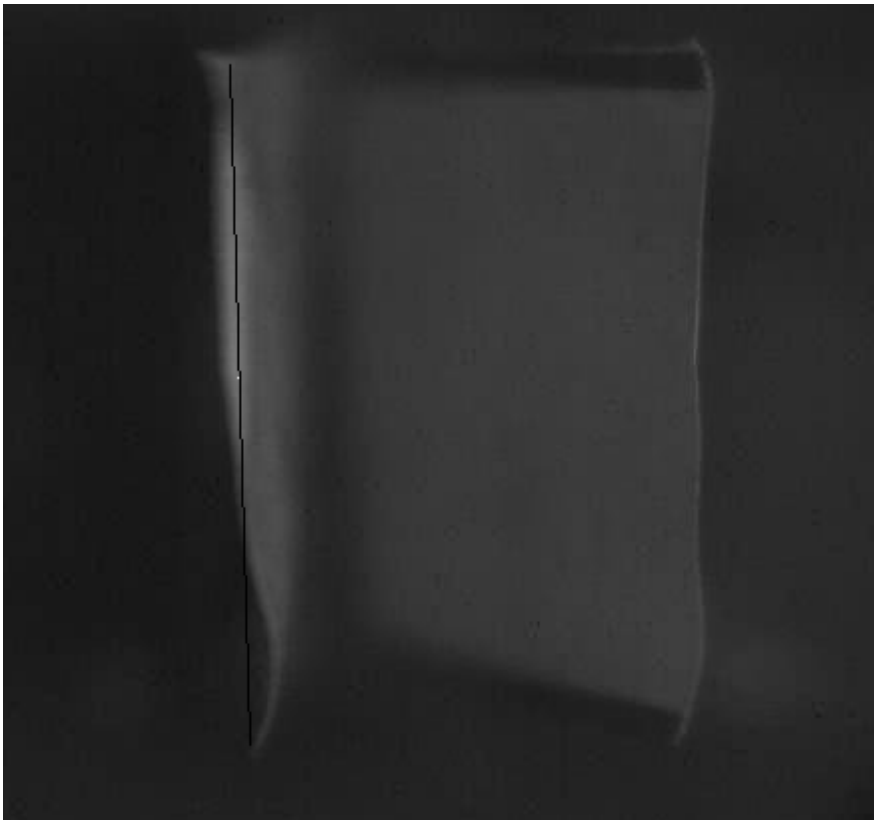

Figure 5.20 Typical superimposed images for the analysis of the flapping and twisting motions of the wing at phase delay=0.

(3) The difficulty to have two identical piezofans as the actuators. For the system shown as in Figure 5.16, if the piezofan I and II are identical and there is no

phase difference between the two input signals (i.e. phase delay = 0), the two piezofans should vibrate in parallel at around the first resonant frequency. However, it is very difficult if not impossible to have two identical pizofans in terms of their resonant frequencies and vibration amplitude. As every piezofan is produced individually, any difference in the width and lengths of the PZT patch and the stainless steel shim, the relative position of the PZT patch on the metal shim, and the exact clamping conditions etc, all can lead to the variation of the resonant frequency and amplitude. Further more, the vibration amplitude also depends on the exact piezoelectric coefficient of the PZT patch and the condition of the bonding layer, as well as the geometrical factors. As discussed before, differences in resonant frequency and the vibration amplitude at resonance will lead to different vibration amplitudes at any frequencies for the two piezofans. This means that, at any frequency, even at phase delay=0, the two piezofans may not vibrate in parallel, one will vibrate with a larger amplitude than the other. This will show an apparent twisting motion for the wing. Figure 5.21 shows an example of superimposed images of the wing driven by two piezofans with slightly different resonant frequencies at a frequency close to their first resonant frequencies at the phase delay = 0. At this frequency (close to their respective first resonances) ideally there should be no twisting motion at all. Instead, an apparent twisting of 9.6^{o} was observed. This is about the same as the twisting at the second resonance mode (twisting mode) of the system. We believe this is the main reason why the apparent twisting motion (Figure 5.19) around the first resonant frequency between 19.8 and 32.2 Hz was so high. Since the flapping displacement is very big around the first resonant frequency, this effect is most apparent around the first resonant frequency. For these reasons, the error bar for the twisting values around the first resonant frequencies are expected to be very big, probably at the same level as the observed twisting angles. It is therefore very difficult to do any quantitative analysis. The effect of different resonant frequency on the flapping motion of the wing was found to be much smaller, as shown in Figure 5.19, the flapping displacements around the second resonance between 43.2 and 56.7 Hz were small relative to the flapping motion at the first resonant frequencies.

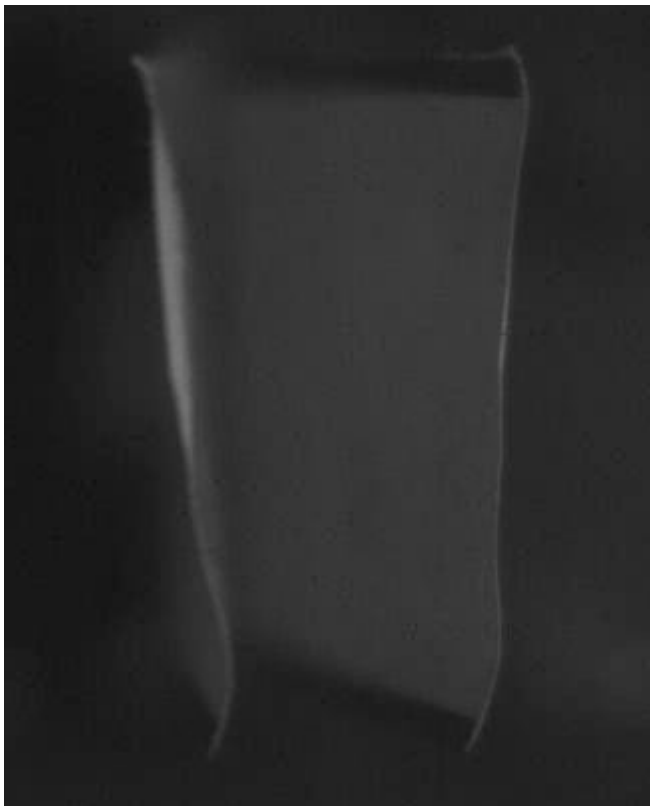

Figure 5.21 The superimposed images of the wing at 19.8Hz at phase delay=0. An apparent twisting movement was observed at around the first resonant frequency due to the different vibration amplitude of the two piezofan actuators.

(4) From the above discussion, it is apparent the flapping and the twisting motions of the wing also depend very much on the stiffness of the wing skin materials, as well as the piezofan actuators. We consider two extreme cases here: (i) If the skin materials is infinitely soft (the stiffness coefficient c_{ij}=0), the whole system as shown in Figure 5.16 will act like two independent piezofans. At any frequency, the two piezofans will vibrate in parallel when the phase-delay = 0 and in anti-phase when the phase-delay = 180 º. The flapping amplitude will be at its maximum when the phase-delay = 0 and reduce to zero when the phase-delay = 180 º, and the twisting motion will be at its maximum when the phase-

delay =180 º and reduce to zero when the phase-delay =0. Changing the phase-delay will change the flapping and twisting amplitudes of the wing. However, if there is a difference of the 1st resonant frequencies f_1 and f_2 of the two piezofans, the flapping and apparent twisting will depends on the operating frequency f and the value of f_2- f_1. (ii) If the skin material is infinitely stiff (the compliance coefficients s_{ij}=0), then the whole system must be treated as a single body and it has its unique resonant frequencies, the first mode being bending and the second mode being twisting. In this case, the resonant frequency of the individual actuator piezofan I and II or the difference between the two has little to do with the performance of the wing. Apparently the actual wing is between the above two extremes, with a finite stiffness coefficients c_{ij}>0. The system has its unique bending and twisting mode resonance frequencies but the performance could be affected by the difference in resonant frequencies of the individual piezofan actuators. Every effort was made to fabricate the piezofans as identical as possible.

(5) From the discussion in (4), ideally there should be a systematic study on the effect of different skin materials. The skin material used in this study, a very thin polymer, was suggested by our collaborative researchers in the aerodynamics department. A more in-depth study on the effect of different skin materials was not possible due to the time limit of this PhD project.

5.3.3.3. 2DOF motion control by phase differentiated drive

The control of a coupled piezoelectric fans system by a phase differentiated drive for the flapping wing MAV applications is the aim of this research. The bending and twisting motions of the wing at and away from their respective resonant frequencies as functions of the phase difference (phase delay) between the applied voltages to the two piezofans were then characterized. Table V.16 and V.17 summarises the bending and twisting amplitudes of the wing as functions of operating frequency for the set-up as shown in Figure 5.16 under two input voltages 170 V_{pp} at different phase delays between the two respectively. The gap between the two piezofans was 10 cm. Figure 5.22 and 5.23 depict the flapping and twisting amplitudes of the wing as functions of operating frequency under two input voltages 170 V_{pp} at different phase delays between the two, respectively. From these two figures, it can be observed that the flapping motion had a resonance at around 22Hz, and the vibration amplitude was the largest at phase-delay = 0 and reduced with the increasing phase-delay. The amplitude reached minimum when the phase-delay = 180º, about a quarter of the value when the phase-delay = 0. The twisting motion was peak around 49 Hz, and, contrary to the flapping, its amplitude increased with the increasing phase-delay. The twisting amplitude for the phase-delay = 0 was only about half of the value for the phase-delay = 180º. However, as discussed in the last section, the error bar for the twisting movement was very large, especially for the frequencies near the bending mode resonance, when there was inevitably a difference of the resonant frequency between the two piezofans. For this reason we will not try to draw any conclusions from the quantitative analysis of the twisting data around the flapping mode resonant frequency. The slight increase of the flapping motion around the frequency 50Hz might also due to the increase of the error around the twisting resonance there.

Figures 5.22 and 5.23 show that it is possible to change both the flapping and twisting motions of the flapping wing simply by varying the phase-delays between the two input signals. At frequencies around the 1st resonance, i.e. the flapping mode resonance, increasing the phase-delay from 0 to 180º lead to the reduced flapping motion. At frequencies around the 2nd resonance, i.e. the twisting mode resonance, increasing the

phase-delay from 0 to 180º lead to the increased twisting motion. However, due to the difficulty in obtaining precisely the same piezofan actuators, it is not clear from this study what are the effects of changing phase-delay on the twisting motion around the flapping resonate frequency, and the effects on the flapping motion around the twisting resonate frequency. Nevertheless, the flapping at frequencies far away from the flapping resonance were found to be very small, then figures 5.22 could be well-represented by Figures 5.24, which shows only the flapping motion around the flapping resonate frequencies at different phase-delays. Similarly, Figure 5.25 shows the twisting motion around the twisting resonate frequencies only at different phase-delays. As shown by these two figures, the flapping and twisting motions can all be adjusted simply by changing the phase-delays between the two input signals.

Table V.16: The flapping amplitude as a function of operating frequency at different phase-delays. Unit: mm.

	13.8 Hz	16.7 Hz	18.3 Hz	19.8 Hz	21.4 Hz	22.3 Hz	23.6 Hz	24.9 Hz	26.4 Hz	27.7 Hz	29.6 Hz	32.2 Hz	43.3 Hz	44.4 Hz	46.1 Hz	47.4 Hz	48.3 Hz	49.7 Hz	50.7 Hz	51.8 Hz	52.8 Hz	54.5 Hz	56.8 Hz
0º	7.51	8.83	12.61	15.64	19.09	20.09	19.70	16.00	11.13	9.39	6.88	5.74	0.1	0.6	0.9	0.3	0.9	1.1	1.6	1.8	1.8	1.8	1.8
30º	6.87	7.57	11.22	13.74	19.04	19.87	19.57	15.74	10.61	8.43	6.17	4.96	1	1.7	1.1	2	1.4	2	1.7	2	2.2	2.3	2.5
60º	5.96	6.7	9.52	12.74	17.96	19.52	18.87	14.61	9.83	7.65	5.83	4.65	2	1.1	0.9	3	1.4	1.4	0.1	1.3	0.2	0.5	0
90º	4.96	5.74	8.78	11.48	16.52	18.66	17.13	12.52	8.85	7.02	5.17	4.14	2.5	1.5	1.9	1.7	1.4	1	0.9	0.7	0.5	1.2	1.5
120º	3.70	4.26	6.26	8.00	11.39	11.91	11.43	9.57	7.15	5.61	4.65	3.3	1.9	1.8	1.1	1.3	1.2	0.6	0.1	0.7	0.1	1.3	1.4
150º	2.52	2.78	2.96	5.22	7.83	8.46	8.09	6.35	4.30	3.48	2.83	2.61	1.2	1.4	2.7	0.5	1	0.1	0.5	0.7	1.1	1.6	2.2
180º	1.62	1.73	1.83	2.61	4.74	4.91	4.83	3.91	2.91	1.91	1.85	1.74	0.6	0.1	0.8	0.1	0.5	1	1	1	1.3	2	2

Table V.17: The twisting amplitude as a function of operating frequency at different phase-delays. Unit: degree.

	13.8 Hz	16.7 Hz	18.3 Hz	19.8 Hz	21.4 Hz	22.3 Hz	23.6 Hz	24.9 Hz	26.4 Hz	27.7 Hz	29.6 Hz	32.2 Hz	43.3 Hz	44.4 Hz	46.1 Hz	47.4 Hz	48.3 Hz	49.7 Hz	50.7 Hz	51.8 Hz	52.8 Hz	54.5 Hz	56.8 Hz
0º	4.12		7.58	9.56	2.63	5.76	4.45	3.79	8.4	8.4	8.73	7.91	6.5	9	13.5	16	11	10.5	10	7	7	6	5
30º	4.28	3.29	7.58	8.9	5.11	3.13	2.63	1.98	5.44	7.25	5.76	4.45	13	10.5	15.5	16	13	12	11	9.5	7.5	6.5	6
60º	3.29	4.28	6.92	9.23	10.22	7.58	1.65	2.63	15.19	12.54	10.22	12	15	17	16.5	21	18.5	16.5	11.5	13	9	8.5	7
90º	4.28	6.59	6.92	10.55	12.54	12.87	7.58	9.56	14.2	13.53	13.2	9	16	17.5	23	27	27	21	19	15.5	13	10.5	9
120º	4.61	5.6	11.21	5.6	11.54	12.7	13.53	12.7	14.36	4.45			19	20	24	29	30	26	21	16	13	11	10
150º	9.56	10.55	11.21	13.53	11.54	8.73	5.13	3.95					20.5	20	26	31	30.5	28	21	20	17	16	13
180º	8.57	3.95	5.6		13.03	11.05	4.28	8.9	5.11	3.29	0.33	1.98		22	24	26	30.5	32	30	26	23	22	21

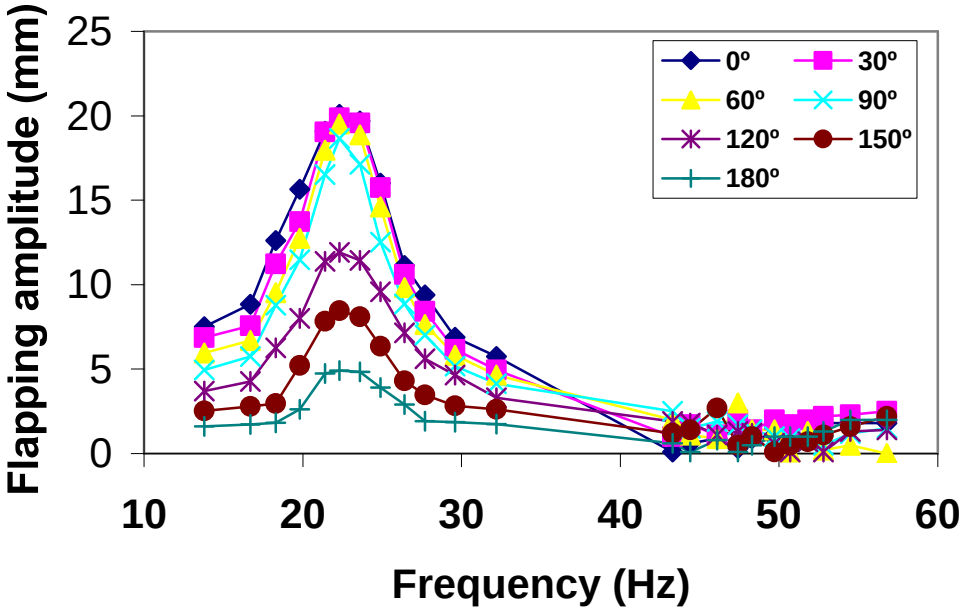

Figure 5.22 The flapping amplitude as a function of operating frequency at different phase-delays

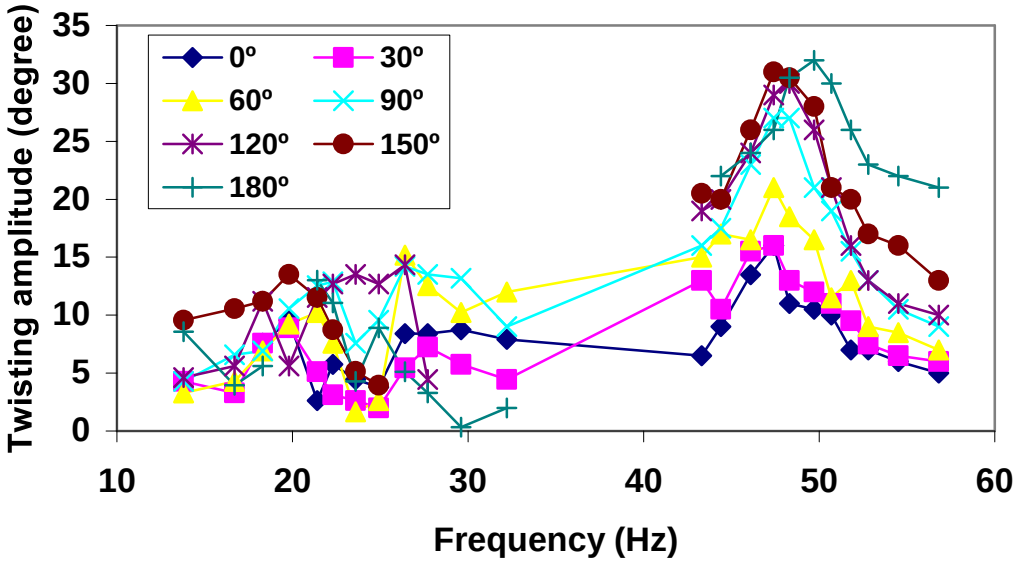

Figure 5.23 The twisting amplitude as a function of operating frequency at different phase-delays

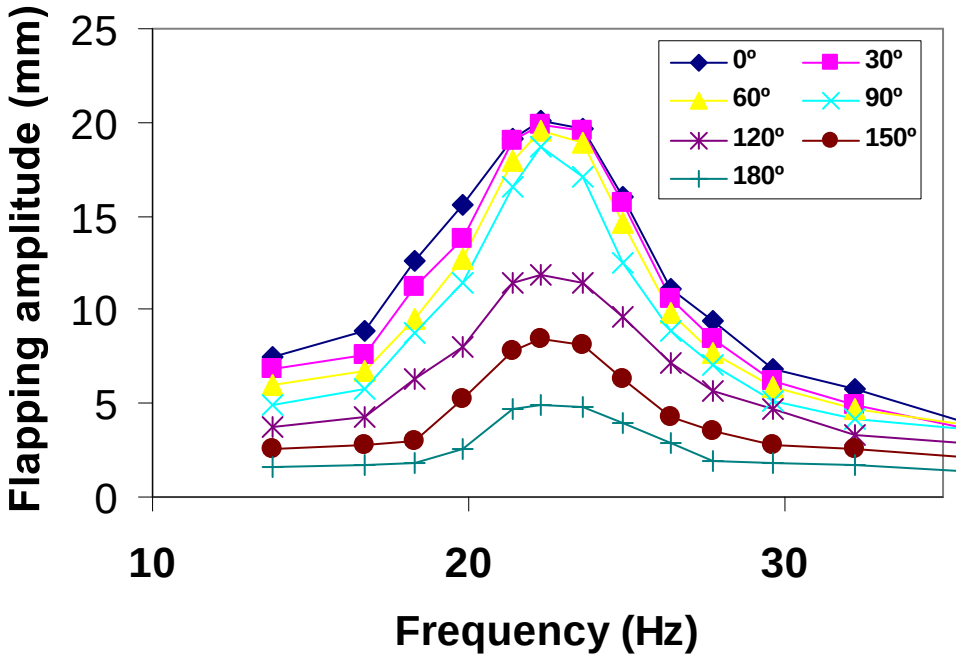

Figure 5.24 The flapping amplitude as a function of operating frequency at different phase-delays at around the flapping resonant frequency.

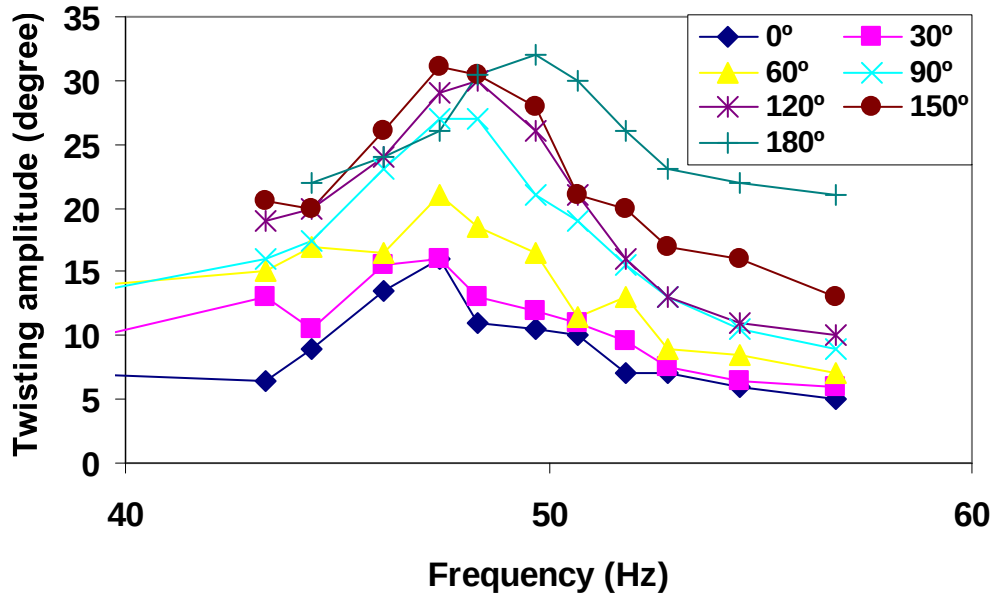

Figure 5.25 The twisting amplitude as a function of operating frequency at different phase-delays at around the twisting resonate frequency.

5.3.3.4. The effect of the distance betweenthe two piezofans

The effect of the distance between the two piezofan actuators on the flapping and twisting motions of the wing was also investigated. Table V.18 summarises the flapping and twisting amplitudes of the wing driven by two piezoefans at different phase-delays with a gap distance =10 mm, and the superimposed high speed camera images from which the data were obtained. Similar data for the gap distances 8, 5 and 2 mm are summarised in Table V.19, V.20 and V.21, respectively. Both the flapping and twisting were recorded at their respective resonate frequencies. Namely, the flapping were measured at 26.2, 26.3, 26.0 and 26.2 Hz for gap distance 10, 8, 5 and 2 mm, respectively; and the twisting were measured at 53.6, 49.1, 51.4 and 47.4 Hz for gap distance 10, 8, 5 and 2 mm, respectively. Changing the gap distance involves de-clamping at least one of the piezofan, varying the distance between the two piezofans, and then re-clamping the piezofans. These results show that the flapping resonate frequency of the system changed little (from 26.0 to 26.3 Hz) after these manoeuvres, but noticeable difference in twisting resonate frequencies (from 47.4 to 53.6 Hz) was resulted. However, these changes were not monotonic as the change of the gap distance, therefore were most likely due to the change of the effective clamping distances in the re-clamping, as discussed before.

Figure 5.26 shows the phase delay dependence of the bending displacement and the twisting angle (Figure 5.27) for the system. The measured values were represented by symbols ♦, □, ▲, and x and their corresponding polynomial fittings by solid, dashed, dotted, dash and dotted curves for the gap equals to 10, 8, 5 and 2 mm respectively. The effect of the gap distance between the two fans was also investigated and results were shown in Figure 5.26 as well. When the gap distance was 10 mm and the voltages V_{pp}=170 V applied to the two piezoelectric fans were in phase (phase delay = 0º), the amplitude of the bending movement of the wing reached 23.4 mm and resonated at 26.2 Hz. When the phase delay of the two driving voltages was increased and all the other conditions remained the same, the mode of the wing movement remained the pure bending and also resonated at the same frequency, but with a reduced amplitude. When the two driving voltages were anti-parallel (phase delay = 180º), the amplitude of the

resonant bending displacement was reduced to minimum 1.8 mm. When the gap between the two wing spars was reduced from 10 mm to 8 mm (and further to 5 and 2 mm) and all the other conditions were kept the same, the bending displacement increased but the dependence on the phase delay was similar (Figure 5.26).

Table V.18 Flapping and twisting motion of the wing driven by two piezoefan with a gap distance =10 mm at different phase-delays.

Flapping amplitude (Resonant frequency: 26.2Hz)

Phase delay (degree)	**0**	**30**	**60**	**90**
Flapping amplitude				
(mm)	**(23.43)**	**(22.83)**	**(21.60)**	**(19.03)**
Phase delay (degree)	**120**	**150**	**180**	
Flapping amplitude		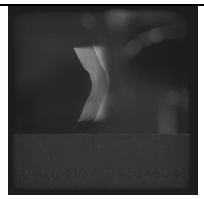	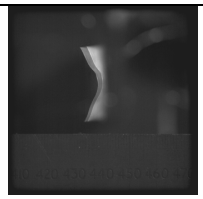	
(mm)	**(14.83)**	**(6.43)**	**(1.80)**	

Twisting amplitude (Resonant frequency: 53.6Hz)

Phase delay (degree)	0	30	60	90
Twisting amplitude	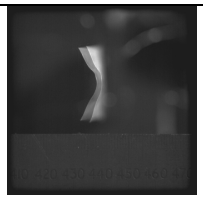	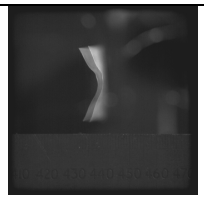		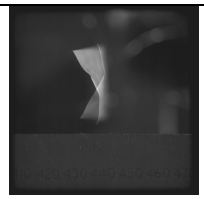
(degree)	0	0	13	32
Phase delay (degree)	120	150	180	
Twisting amplitude	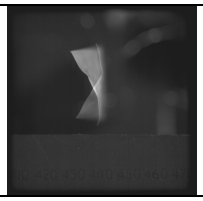	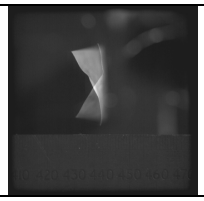	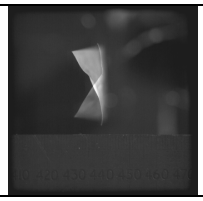	
(degree)	36	39	41	

Table V.19 Flapping and twisting motion of the wing driven by two piezoefan with a gap distance =8 mm at different phase-delays.

Flapping amplitude (Resonant frequency: 26.3Hz)

Phase delay (degree)	0	30	60	90
Flapping amplitude	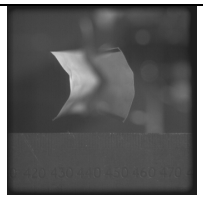	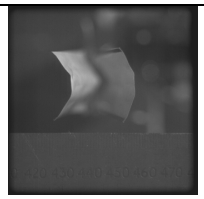	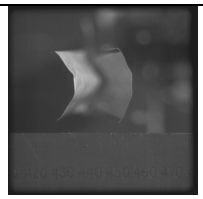	
(mm)	(25.51)	(24.93)	(22.87)	(19.73)
Phase delay (degree)	120	150	180	
Flapping amplitude		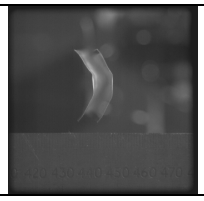	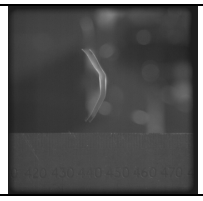	
(mm)	(15.47)	(7.77)	(2.16)	

Twisting amplitude (Resonant frequency: 49.1Hz)

Phase delay (degree)	0	30	60	90
Twisting amplitude			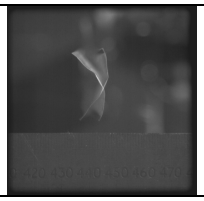	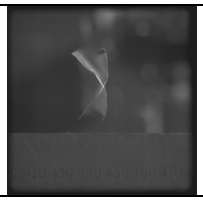
(degree)	0	0	22	45
Phase delay (degree)	120	150	180	
Twisting amplitude		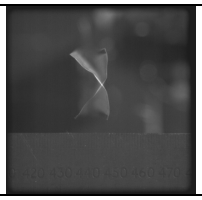	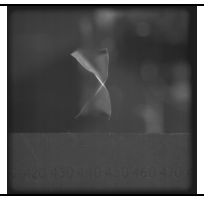	
(degree)	47	48	49	

Table V.20 Flapping and twisting motion of the wing driven by two piezoefan with a gap distance =5 mm at different phase-delays.

Flapping amplitude (Resonant frequency: 26.0Hz)

Phase delay (degree)	0	30	60	90
Flapping amplitude	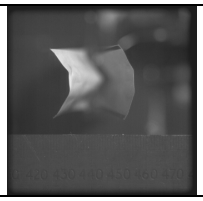	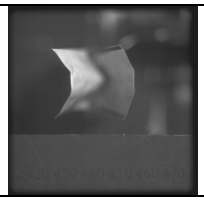	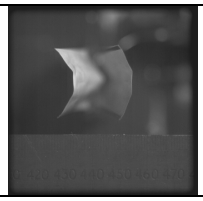	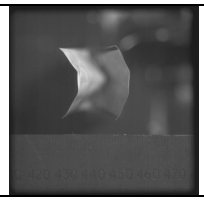
(mm)	27.07	25.14	23.33	20.24
Phase delay (degree)	120	150	180	
Flapping amplitude	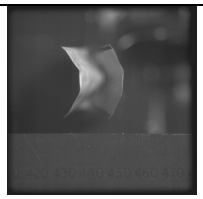	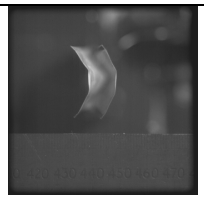	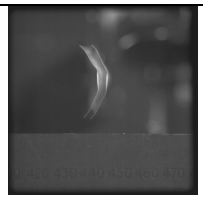	
(mm)	17.01	10.48	3.61	

Twisting amplitude (Resonant frequency: 51.4Hz)

Phase delay (degree)	0	30	60	90
Twisting amplitude	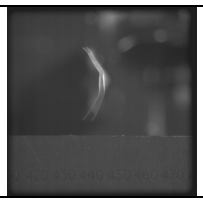	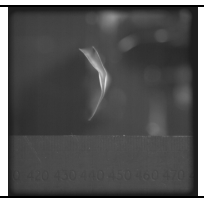	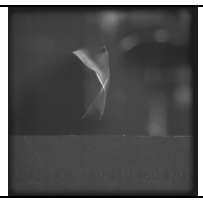	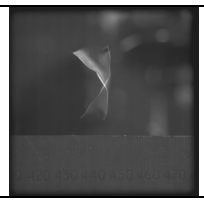
(degree)	0	2	40	45
Phase delay (degree)	120	150	180	
Twisting amplitude	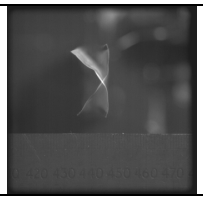	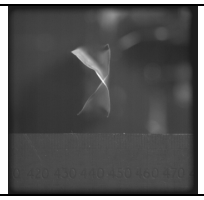	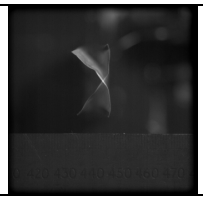	
(degree)	50	55	54	

Table V.21 Flapping and twisting motion of the wing driven by two piezoefan with a gap distance =2 mm at different phase-delays

Flapping amplitude (Resonant frequency: 26.2Hz)

Phase delay (degree)	0	30	60	90
Flapping amplitude	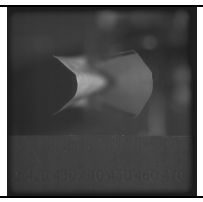	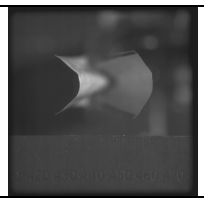	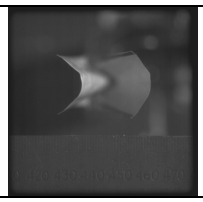	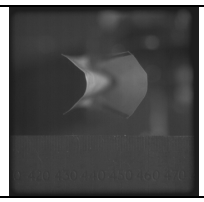
(mm)	29.39	28.58	27.06	23.85
Phase delay (degree)	120	150	180	
Flapping amplitude	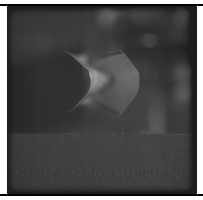	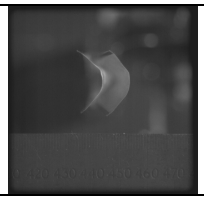	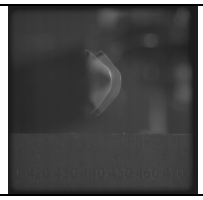	
(mm)	19.22	10.98	3.99	

Twisting amplitude (Resonant frequency: 47.4Hz)

Phase delay (degree)	0	30	60	90
Twisting amplitude	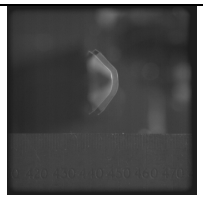	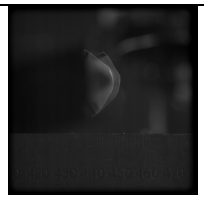	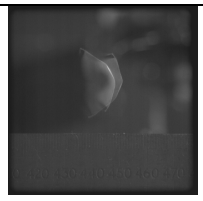	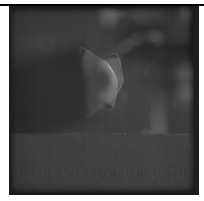
(degree)	0	16	42	50
Phase delay (degree)	120	150	180	
Twisting amplitude	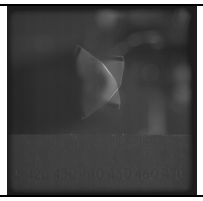	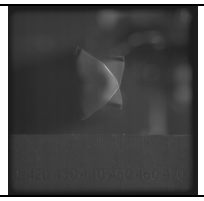	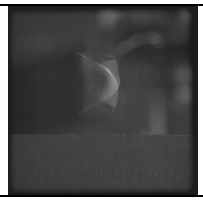	
(degree)	66	67	65	

If the frequency of the two driving voltages was increased from 26.2 Hz to 53.6 Hz, the same as its second mode frequency, the wing motion became a pure twisting. The two wing spars as represented by point 1 and point 2 in Figure 5.16 were always moving in the opposite directions and the middle line did not move in the ideal case. When the gap distance was 10 mm and the voltages V_{pp}=170 V applied to the two piezofans were in phase (phase delay = 0º), the twisting angle of the wing was minute, close to 0 degree at 53.6 Hz. When the phase delay of the two driving voltage was increased and all the other conditions remained the same, the wing movement was found remain at the pure twisting mode and also resonate at the same frequency, but with an increased twisting amplitude. When the two driving voltages were close to anti-parallel (phase delay = 180º), the resonate twisting angle reached 41º (Figure 5.27). When the gap between the two wing spars was reduced from 10 mm to 8 mm (and further to 5 and 2 mm) and all the other conditions were kept the same, the wing twisting increased but its dependence on the phase delay was similar (Figure 5.27).

The motional amplitude dependence on the gap distance between the two spars could be interpreted by the air damping consideration. The air damping to the wing movement increases with its cross section, and the effective cross section of the wing is proportional to the gap distance. So the reduced gap distance lead to a reduced air damping, therefore to increased vibration amplitude. In fact, linear relationships (with negative slump rates) were found existed between both the bending and twisting amplitudes and the gap distance (Figure 5.28), suggesting the air damping was linearly proportional to the cross section area of the wing.

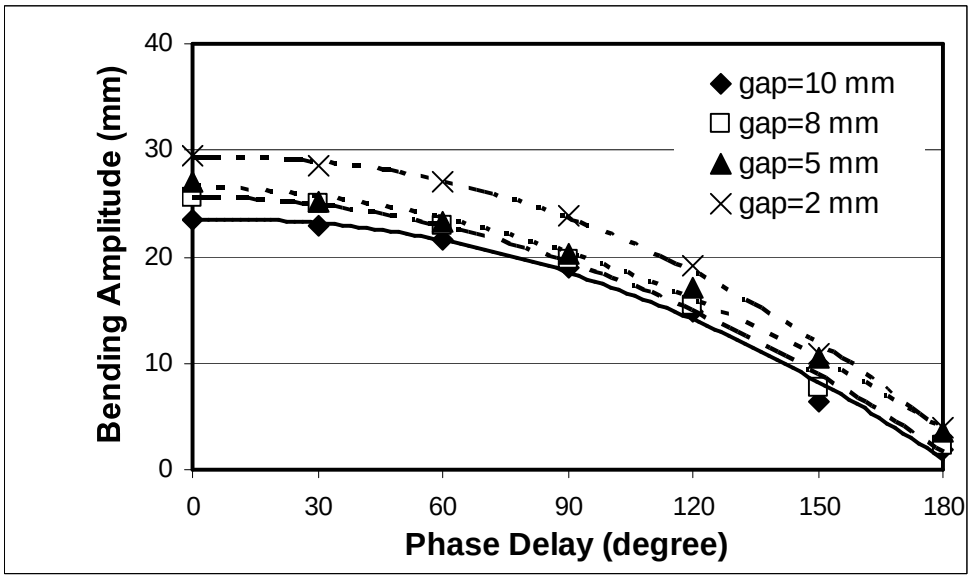

Figure 5.26 The phase delay dependence of the motion amplitude of the bending modes of the wing driving by the coupled piezoelectric fans under 170 V_{pp} at different gap distances between the two spars

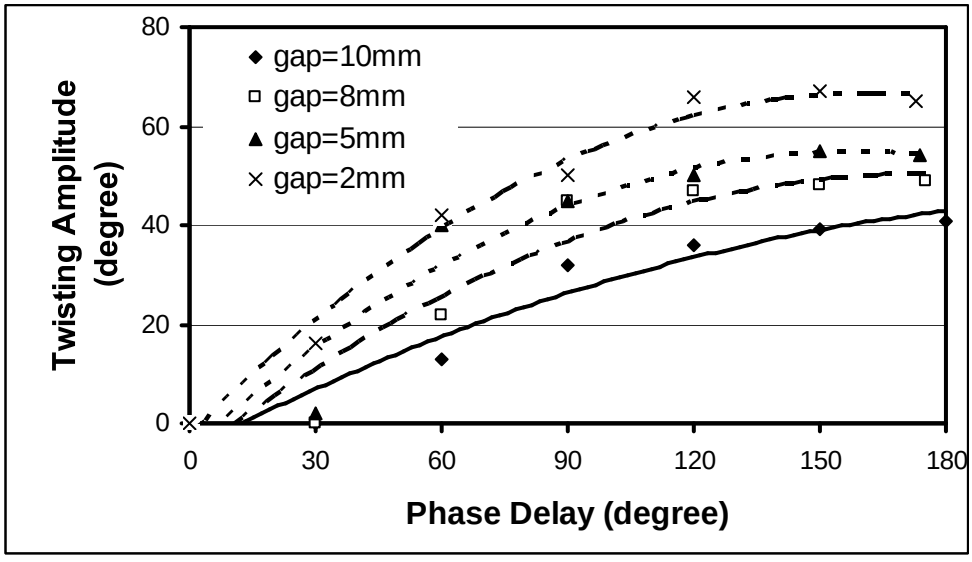

Figure 5.27 The phase delay dependence of the motion amplitude of twisting modes of the wing driving by the coupled piezoelectric fans under 170 Vpp at different gap distances between the two spars

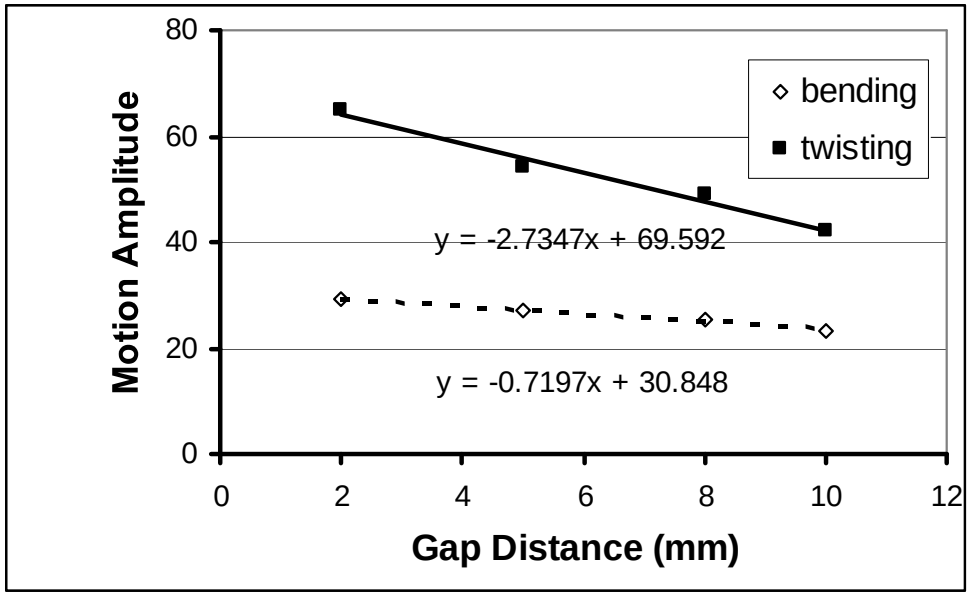

Figure 5.28 The dependence on the gap distance of the motio amplitude for the bending and twisting modes of of the wing driving by the coupled piezoelectric fans under 170 Vpp.

CHAPTER 6

CONCLUSIONS

With an aim of developing an easy method for the actuation and control of two DOF motions, namely the flapping and twisting motions for a wing of MAV, investigations were carried out for a piezoelectric actuated system in this project. This involved the analysis, modelling, optimization, fabrication and characterisation of a piezoelectric cantilever at first, then for the piezofan, and finally for coupled piezofans structures. Specifically:

1. The optimised conditions for bonding a piezoelectric PZT patch with metal shims such as Nickel, Molybdenum and stainless steel elastic layers have been investigated. The optimised parameters are: the spin rate for spreading the epoxy is 3,500 rpm, with a spin time 20s; the curing temperature is 100℃ and the curing time is 5 hours, applied dead weight is 2 kg and no need to use the sandpaper abrasion or adhesion promoter. The obtained maximum shear strength is 2.95 MPa.

2. For a piezoelectric fan made from a stainless steel layer with a fixed length and a PZT patch layer which may be shorter than the stainless steel, a longer PZT patch lead to larger quasi-static tip displacement and higher resonant frequencies for the piezoelectric fan.

3. For a piezoelectric fan made from a stainless steel layer and a PZT patch with a fixed length shorter than the stainless steel, when the location of the PZT patch is further away from the clamping position, a smaller quasi-static tip displacement and lower resonant frequencies resulted. Therefore, if a larger quasi-static tip displacement is required, the PZT patch should be placed as close to the clamping position as possible.

4. The tip displacement of a piezofan at its bending resonant frequency was

boosted by nearly 10 times compared to the displacement at quasi-static frequency.

5. Analytical and finite element modelling were used to study the performance of the piezoelectric unimorph cantilever and piezofan structures. Good agreements were obtained between the analytical, FEM and experimental results. It was found for the application of flapping wing actuation application, the best thicknesses of the materials available were the 127 μm thick PZT-5H and the 125 μm thick stainless steel. This thickness combination can produce the largest f*δ value with f< 100 Hz for both the flapping and twisting resonant frequencies.

6. The phase delay between the driving voltages supplied to the two coupled piezofans was found capable to change the flapping and twisting motions of the wing attached to the two piezofans. The flapping motion of the wing and the coupled piezofans around the flapping resonance reduces with the increasing phase delay. The twisting motion around the twisting resonance increases with the increasing phase delay.

7. The phase delay between the driving voltages supplied to the two coupled piezofans can also change the flapping and twisting motions at frequencies far away from their respective resonant frequencies. The exact format of the effect depends on the stiffness of the wing itself.

8. The gap between the two piezofans (also the gap between the wing spars) can also affect the flapping and twisting motions of the wing. Linear relationships (with negative slump rates) were found to exist between both the bending and twisting amplitudes and the gap distance, and this can be interpreted as due to air damping which was linearly proportional to the cross-sectional area of the wing.

CHAPTER 7

FUTURE WORK

Some possible future works are recommended:

1. Material selection for higher transverse piezoelectric coefficient d_{31}, and the electromechanical coupling factor k_{31}.

   In this study, only one type of PZT ceramic PSI-5H4E was used to produce piezoelectric fans, for its relatively high d_{31} and k_{31} values, high Curie temperature and affordable cost. However, single crystals like PMN-PT and PZN-PT have much higher $d_{31,}$ and k_{31} values, but they are not ordinary piezoelectric materials, they are relaxor, and their Curie temperatures are lower. To increase the tip displacement, blocking force, and the electrical mechanical energy transformation of the piezoelectric fans, it is worthwhile to use these single crystals to investigate their relationships between their $d_{31,}$ k_{31} values and their dynamic behaviours.

2. Single piezoelectric fan with a wing

   Different piezoelectric fans with the same length and width, but different in thickness were used to form coupled piezoelectric fans and been evaluated in this project. Future work is recommended to investigate the dynamic performance of a single piezoelectric fan attached with a wing, to understand the behaviours of a piezoelectric fan under different loading (wing can be regarded as a loading to the piezoelectric fan) conditions.

3. Wing design

   Only one type of materials was used in this study to form the wing, which is the polymer film for the skin, and the carbon fibre reinforced plastic for the spars. Future work is suggested to investigate the effect of wings produced by different materials to the dynamic response of a coupled piezoelectric fan system.

4. Piezofan manufacture

   The quantitative analysis of the effect of the phase-delay on the flapping and twisting motions, especially at frequencies away from their respective resonant frequencies, were hampered greatly by the difficulty in obtaining identical piezofans with the identical first resonant frequency and vibration amplitude. This situation can be improved, at least partially, by manufacturing the piezofans on industrial scale, or more likely, by purchasing piezofans from an industrial supplier. For the same purpose, a sample holder (clamping base) made from very hard and very smooth surface materials, such as stainless steel, should be able to reduce the effect of non-perfect clamping of the piezofan.

5. Wind tunnel test for the aerodynamic of the coupled piezoelectric fan systems

   Aerodynamic force produced by the coupled piezoelectric fan systems has not be been measured in this study, due to the unavailability of the measuring equipment during the time of my project. A setting up of the wind tunnel test for the EPSRC project (EP/C511190/1: Development and Aeroelastic Optimisation of a Piezoelectric Powered Flapping Wing Micro Air Vehicle), which supported this study as well, by the aeronautic department in Cranfield, is in progress. It is suggested to obtain the aerodynamic force of the coupled piezoelectric fan, in collaboration with the aeronautic department in the future, to investigate the relationships between the aerodynamic force produced and the whole coupled piezoelectric fan systems in this study, to realize the benefits to the application of a piezoelectric powered flapping wing micro aero vehicle.

CHAPTER 8

REFERENCES

Acikalin, T., Raman, A. and Garimella, S. V. (2003). Two-dimensional streaming flows induced by resonating thin beams. *Journal of the Acoustical Society of America*, 114, p. 1785–1795.

Acikalin, T., Wait, S.M., Garimella, S.V. and Raman, A. (2004). Experimental investigation of the thermal performance of piezoelectric fans. *Heat Transfer Engineering*, 25, p. 4–14.

Acikalin, T., Garimella, S. V., Raman, A. and Petroski, J. (2007). Characterization and optimization of the thermal performance of miniature piezoelectric fans. *International Journal of Heat and Fluid Flow*, 28(4), p. 806-820.

August, J. A. and Joshi, S. P. (1996). Preliminary Design of Smart Structure Fins for High Speed Missiles. *SPIE Smart Structures and Materials: Industrial and Commercial Applications of Smart Structures Technologies*, 2721, p. 58-65.

Austin, F. and Van Nostrand, W. C. (1995). Shape Control of an Adaptive Wing for Transonic Drag Reduction. *Smart Structures and Materials 1995: Industrial and Commercial Applications of Smart Structures Technologies*, 2447, p. 45-55.

Bailo, K. C., Brei, D. and Grosh, K. (1998a). Investigation of the Effect of the Angle of Incidence on Polymeric Piezoelectric Acoustic Transducer. *Performance 1998 ASME IMECE: Vibration and Noise Control*, 97, p. 85-92.

Bailo, K. C., Brei, D. and Grosh, K. (1998b). Polymeric Piezoelectric Acoustic Semi-Circular Transducers. *SPIE Smart Structures and Materials: Smart Structures and Integrated Systems*, 3320, p. 150-160.

Barron, B., Li, W. G. and Haertling, G. H. (1996). Temperature Dependent Characteristics of Cerambow Actuators. *IEEE International Symposium on Applications of Ferroelectrics*, 96, p. 305-308.

Basak, S., Raman, A. and Garimella, S. V. (2005). Dynamic response optimization of piezoelectrically excited thin resonant beams. *Trans. Of ASME*, 127, p. 18-26.

Brennan, M. J., Elliott, S.J. and Pinnington, R. J. (1997). The dynamic coupling between piezoceramic actuators and a beam. *Journal of the Acoustical Society of America.*, 102, p. 1931-1942.

Bruneau, H., Le Letty, R., Claeyssen, F., Barillot, F., Lhermet, N. and Bouchilloux, P. (1999). Semi-Passive and Semi-Active Vibration Control Using New Amplified

Piezoelectric Actuators. *Proceedings of the SPIE—The International Society for Optical Engineering*, 3668, p. 814-822.

Burman, P., Raman, A. and Garimella, S. V. (2002). Dynamics and topology optimization of piezoelectric fans. *IEEE Trans. Components and Packaging Technology*, 25, p. 113–121.

Capozzoli, M., Gopalakrishnan, J., Hogan, K., Massad, J., Tokarchik, T., Wilmarth, S., Banks, H. T., Mossi, K. M., and Smith, R. C. (1999). Modeling Aspects Concerning THUNDER Actuators. *Proceedings of the SPIE—The International Society of Optical Engineering*, 3667, p. 719-727.

Chandra, R. and Chopra, I. (1999). Actuation of Trailing Edge Flap in a Wing Model Using a Piezostack Device. *Journal of Intelligent Material Systems and Structures*, 9, p. 847-853.

Chandran, S., Kugel, V. D. and Cross, L. E. (1996). Characterization of the Linear and Non-Linear Dynamic Performance of Rainbow Actuator. *Proceedings of the Tenth IEEE International Symposium on Applications of Ferroelectrics*, 2, p. 743-756.

Chandran, S., Kugel, V. D. and Cross, L. E. (1997). Crescent: A Novel Piezoelectric Bending Actuator. *Proceedings of the SPIE—the International Society for Optical Engineering*, 3041, p. 461-469.

Chonan, S., Jiang, Z. W. and Koseki, M. (1996). Soft-Handling Gripper Driven by Piezoceramic Bimorph Strips. *Smart Materials and Structures*, 5, p. 407-414.

Christopher, N., Diann, B., Sivakumar. B., and Andrew, M. (2001). Piezoelectric Actuation: State of the Art. *The Shock and vibration digest*, 33, p. 269-280.

Clement, J. W., Brei, D. and Moskalik, A. J. (1998). Bench-Top Characterization of an Active Rotor Blade Flap System Incorporating C-Block Actuators. *Proceedings of the AIAA/ASME/ASCE/AHS/ASC 39th Structures, Structural Dynamics and Materials Conference*, 4, p. 2857-2869.

Cox, A., Monopoli, D., Cveticanin, D., Goldfarb, M. and Garcia, E. (2002). The development of elastodynamic components for piezoelectrically actuated flapping micro air vehicles. *Journal of Intelligent Material Systems and Structures*, 13, p. 611-615.

Crawley, E. F. and de Luis, J. (1987). Use of piezoelectric actuators as elements of intelligent structures. *AIAA Journal*, 25, p. 1373-1385.

Dickinson, M. H., Lehmann, F. and Sane, S. (1999). Wing rotation and the aerodynamic basis of insect flight. *Science*, 284, p. 1954-1960.

Devoe, D. L. and Pisano, A. P. (1997). Modeling and optimal design of piezoelectric cantilever microactuators. *Journal of Microelectromechanical system*, 6, p. 266–270.

Dogan, A., Fernandez, J. F., Uchino, K. and Newnham, R. E. (1996). The Cymbal Electromechanical Actuator. *IEEE International Symposium on Applications of Ferroelectrics*, 1, p. 213-216.

Dogan, A., Uchino, K. and Newnham, R. E. (1997). Composite Piezoelectric Transducer with Truncated Conical Endcaps 'Cymbal'. *IEEE Transactions on Ultrasonics, Ferroelectrics, and Frequency Control*, 44, p. 597-605.

Elissalde, C. and Cross, L. E. (1995). Dynamic Characteristics of Rainbow Ceramics. *Journal of the American Ceramic Society*, 78, p. 2233-2236.

Ellington, C.P. (1999). The novel aerodynamics of insect flight: applications to micro-air vehicles. *Journal of Experimental Biology*, 202, p. 3439-3448.

Wakeling, J.M. and Ellington, C.P. (1996). Dragonfly Flight. *The journal of Experimental Biology*, 200, p. 557-582.

Ellington, C.P., van den Berg, C., Willmott, A.P. and Thomas, A. (1996). Leading-edge vortices in insect flight, *Nature*, 384, p. 626-630.

Ervin, J. and Brei, D. (1998). Recurve Piezoelectric-Strain-Amplifying Actuator Architecture. *IEEE/ASME Transactions on Mechatronics*, 3, p. 293-301.

Ervin, J. (1999). Design, Characterization, and Assessment of the Recurve Actuation Architecture. *Ph.D. dissertation, University of Michigan*.

Fearing, R.S., Chiang, K.H., Dickinson, M.H., Pick, D.L., Sitti, M. and Yan, J. (2000). Wing transmission for a micromechanical flying insect, *in: Proc. IEEE Int. Conf. Robotics and Automation, San Francisco, CA, USA, 2000*, p. 1509-1516.

Fukami, A., Yano, M., Tokuda, H., Ohki, M. and Kizu, R. (1994). Development of Piezo-Electric Actuators and Sensors for Electronically Controlled Suspension. *International Journal of Vehicle Design*, 15, p. 348-357.

Fuller, C. R. and Gibbs, G. P. (1994). Active Control of Interior Noise in a Business Jet Using Piezoceramic Actuators. *Noise conference*, Ft. Lauderdale, Florida, May 1-4 1994, p. 389-394.

Fuller, C. R., Guigou, C. and Gentry, C. A. (1996). Foam-PVdF Smart Skin for Active Control of Sound. *Proceedings of the SPIE—The International Society for Optical Engineering*, 2721, p. 26-37.

Fulton, M. and Ormiston, R. A. (1998). Use of Piezoelectric Actuators as Elements of Intelligent Structures. Proceedings of the 54th American Helicopter Society Forum, Washington, D.C.

Gibbs, G. and Fuller, C. (1992). Excitation of thin beams using asymmetric piezoelectric actuators. *Journal of Acoustical Society of America*, 92, p. 3221-3227.

Giurgiutiu V. Active-materials induced-strain actuation for aeroelastic vibration control. *The Shock and Vibration Digest*, 2000, 32(5), p.55-368.

Gogola, M. and Goldfarb, M. (1999). Design of a PZT-Actuated Proportional Drum Brake. *IEEE/ASME Transactions on Mechatronics*, 4, p. 409-416.

Grasmeyer, J. M. and Keennon, M.T. (2001). Development of Black Widow Micro Air Vehicle. *American Institute of Aeronautics and Astronautics*, No. 2001-0127.

Haertling, G. H. (1994a). Chemically Reduced PLZT Ceramics for Ultra High Displacement Actuators, *Ferroelectrics*, 154, p. 101-106.

Haertling, G. H. (1994b). Rainbow Ceramics—A New Type of Ultra High Displacement Actuator. *American Ceramic Society Bulletin*, 73(1), p. 93-96.

Herakovic, N. (1996). Die Untersuchung der Nutzung des Piezoeffektor zur Ansteurung fluide Ventille. *Ph.D. dissertation, University of Aachen, Germany*.

Honda, Seiichi. (1952). On the Characteristics of Miscellaneous Piezoelectric Vibrators in Stiffness Control, *Sci. Rept. RZTU*., B-3(2), p. 95 - 114.

Hooker, M. W. (1997). Properties and Performance of Rainbow Piezoelectric Actuator Stacks. *Proceedings of the SPIE—the International Society for Optical Engineering*, 3044, p. 413-420.

Hopkins, M., Henderson, D., Moses, R., Ryall, T., Zimcik, D., and Spangler, R. (1998). Active Vibration Suppression Systems Applied to Twin Tail Buffeting. *Proceedings of the SPIE—the International Society for Optical Engineering*, 3326, p. 27-33.

Houde-Walter, W. R. (1985). Single-Mode Fibre Manipulation with Inchworm Piezoelectric Translators. In: *Proceedings of the First International Conference on Integrated Optical Circuit Engineering*, 517, D. B. Ostrowski and S. Sriram, eds., SPIE, Bellingham, Washington, p. 147-149.

Ifju, P. G. Jenkins, D. A., Ettinger, S., Lian, Y. and Shyy, W. (2002). Flexible-Wing-Based Micro Air Vehicles, *American Institute of Aeronautics and Astronautics*, No. 2002-0705.

Ihara, A. and Watanabe, H. (1994). On the flow around flexible plates, oscillating with large amplitude, *Journal of Fluid Structure*, 8, p. 601–619.

Ikeda, T. (1990). Fundamentals of Piezoelectricity. *Oxford University Press*, p.16

Jacot, A. D. and Calkins, F. T. (2000). Boeing Active Flow Control System (BAFCS). *Proceedings of the SPIE 7th International Symposium on Smart Structures and Materials*, Newport Beach, California, March 5-9.

Kaneko, T., Ohmi, T., Ohya, N. and Kawahara, N. (1998). A Compact and Quick-Response Dynamic Focusing Lens. *Sensors and Actuators*, A70, p. 92-97.

Koratkar, N. A. and Chopra, I. (1999). Design, Fabrication and Testing of a Mach Scaled Rotor Model with Trailing-Edge Flaps. *Annual Forum Proceedings—American Helicopter Society*, 1, p. 558-578.

Krishnamoorthy, C. S. (1995). Finite Element Analysis: Theory and Programming. *Tata McGraw-Hill*, ISBN 0074622102, 9780074622100.

Kugel, V. D., Chandran, S. and Cross, L. E. (1997). A Comparative Analysis of Piezoelectric Bending-Mode Actuators. *Proceedings of the SPIE—the International Society of Optical Engineering*, 3040, p. 70-80.

Lee, T., and Chopra, I. (1999). Development and Validation of a Refined Piezostack-Actuated Trailing Edge Flap Actuator for a Helicopter Rotor. *Proceedings of the SPIE—the International Society for Optical Engineering*, 3668, p. 22-36.

Le Letty, R., Claeyssen, F., Lhermet, N. and Bouchilloux, P. (1997). A New Amplified Piezoelectric Actuator for Precise Positioning and Active Damping. *Proceedings of the SPIE—The International Society for Optical Engineering*, 3041, p. 496-504.

Li, X., Shih, W. Y., Aksay, I. A. and Shih, W. H. (1999). Electromechanical Behaviour of PZT-Brass Unimorphs. *Journal of the American Ceramic Society*, 82(7), p. 1733–40.

Loh, B.G., Hyun, S., Ro, P.I. and Kleinstreuer, C. (2002). Acoustic streaming induced by ultrasonic flexural vibrations and associated enhancement of convective heat transfer. *Journal of the Acoustical Society of America*, 111, p. 875–883

Mauck, L. D. and Lynch, C. S. (1999). Piezoelectric Hydraulic Pump. *SPIE Smart Structures and Materials 1999: Smart Structures and Integrated Systems*, 3668, p. 844-852.

Martinez, D. R., Hinnerichs, T. D. and Redmond, J. R. (1996). Vibration Control for Precision Manufacturing Using Piezoelectric Actuators. *Journal of Intelligent Material Systems and Structures*, 7, p. 182-191.

McGowan, A. R., Wilkie, W. K., Moses, R. W., Lake, R. C., Florance, J. P., Wieseman, C. D., Reaves, M. C., Taleghani, B. K., Mirick, P. H. and Wilbur, M. L. (1998). Aeroservoelastic and Structural Dynamics Research on Smart Structures Conducted at NASA Langley Research Centre. *Proceedings of the SPIE—the International Society for Optical Engineering*, 3326, p. 188-201.

Mackerle, J. (2003). Smart materials and structures—a finite element approach—an addendum: a bibliography (1997–2002). *Journal of Modelling and Simulation In Materials Science and Engineering.* 11, p. 707-744.

Madangopal, R., Khan, Z. A. and Agrawal, S. K. (2004). Energetics-Based Design of

Small Flapping Wing Air Vehicles. *International Conference for Robotics and Automation*, 11, No. 4, P. 2367 – 2372.

Madangopal, R., Khan, Z. A. and Agrawal, S. K. (2005). Biologically Inspired Design of Small Flapping Wing Air Vehicles Using Four Bar Mechanisms and Quasi-Steady Aerodynamics. *Journal of Mechanical Design*, 127, (2005) p. 809-816.

McMichael, J. M., and Francis, M. S. (1997). Micro Air Vehicles - Towards a New Dimension in Flight. US DARPA/TTO Report, 1997.

Messler, R. W. (1993). Joining of Advanced Materials. *Butterworth-Heinemann, Stoneham, Massachusetts*. ISBN 0750690089, 9780750690089.

Michelson, R.C. and Naqvi, M. A. (2003). Beyond Biologically-Inspired Insect Flight. *Low RE Aerodynamics on Aircraft Including Applications in Emerging UAV Technology, RTO-AVT von Karman Institute for Fluid Dynamics Lecture series.*

Mohri, N., Furutani, K., Shirai, K., and Enami, T. (1997). Forced Discharge Dispersion by Dot-Matrix Method. *CIRP Annals—Manufacturing Technology*, 46, p. 139-142.

Moskalik, A. J. and Brei, D. (1999). Force-Deflection Behavior of Piezoelectric C-Block Actuator Arrays. *Smart Materials and Structures*, 8, p. 531-543.

Nasser, K., Leo, D. J. and Cudney, H. (2000). Compact Piezohydraulic Actuation System. *Proceedings of the SPIE 7th International Symposium on Smart Structures and Materials*, 3991, p.312-322, Newport Beach, California, March 5-9.

Niezrecki, C., Brei, D., Balakrishnan, S. and Moskalik, A. (2001). Piezoelectric actuation: state of the art. *The shock and vibration digest*, 33, p. 269-280**.**

Oh, P. Y. (2004). Flying Insect Inspired Vision for Micro-Air-Vehicle Navigation. *Autonomous Unmanned Vehicles Systems International Symposium (AUVSI)*, Anaheim, CA, August 2004.

Park, H. C., Kim, K. J., Lee, S., Lee, S. Y., Cha, Y. J., Yoon, K. J. and Goo, N. S. (2004). Biomimetic Flapping Devices Powered by Artificial Muscle Actuators. *Proceedings of 2004 US-Korea Conference on Science, Technology and Entrepreneurship*, Durham, NC, USA, August 12-14, 2004.

Park, J. K. and Moon, W. K. (2004). Constitutive relations for piezoelectric benders under various boundary conditions. *Sensors and Actuators A: Physical*, 117(1), p.159-167.

Pokines, B. J. and Garcia, E. (1998). A Smart Material Microamplification Mechanism Fabricated Using LIGA. *Smart Materials and Structures*, 7, p. 105-112.

Pornsin-Sirirak, T. N., Lee, T., Nassef, S.W., Tai, H., Ho, Y.CC.M and Keennon, M, MEMS Wing Technology for a Battery-powered Ornithopter, *The 13th IEEE Annual International Conference on MEMS*, Miyazaki, Japan, January 23-27, 2000, p. 709-804.

Prechtl, E. F. and Hall, S. R. (1997). Design of a High Efficiency Discrete Servo Flap Actuator for Helicopter Rotor Control. *Proceedings of the SPIE—the International Society for Optical Engineering*, 3041, p. 158-182.

Raney, D. L. and Slominski, E. C. (2003). Mechanization and control concepts for biologically inspired micro aerial vehicles. *AIAA 2003-5354, AIAA Guidance, Navigation and Control Conference*, Austin, Texas, August 11-14.

Redmond, J. and Barney, P. (1997). Vibration Control of Stiff Beams and Plates Using Structurally Integrated PZT Stack Actuators. *Journal of Intelligent Material Systems and Structures*, 8, p. 525-535.

Richard A. Bizzigotti, Electromechanical translation apparatus, US Patent number: 3902085 (1975).

Rosen, C. Z., Hiremath, B. V., Newnham, R. E. (1992). Piezoelectricity. *Springer,* p. 13

Royster, L. H. (1970). The Flextensional Concept: A New Approach to the Design of Underwater Acoustic Transducers. *Applied Acoustics*, 3, p. 117-126.

Samak, D. K. and Chopra, I. (1996). Design of High Force High Displacement Actuators for Helicopter Rotors. *Smart Materials and Structures*, 5, p. 58-67.

Saravanos, D. A. (1997). Mixed Laminate Theory and Finite Element for Smart Piezoelectric Composite Shell Structures. *Journal of American Institute of Aeronautics and Astronautics,* 35, No. 8, p. 1327-1333.

Sawyer, C. B. (1931). The Use of Rochelle Salt Crystals for Electrical Reproducers and Microphones. *Proceedings of the Institute of Radio Engineers*, 19, p. 2020-2029.

Schmidt, R. R. (1994). Local and average transfer coefficients on a vertical surface due to convection from a piezoelectric fan. *Procs. ITHERM* , p. 41–49.

Shakeri, C., Bordonaro, C. M., Noori, M. N. and Champagne, R. (1999). Experimental Study of THUNDER: A New Generation of Piezoelectric Actuators. *Proceedings of the SPIE—the International Society for Optical Engineering*, 3675, p. 63-71.

Shyy, W., Berg, M. and Ljungqvist, D. (1999). Flapping and flexible wings for biological and micro air vehicles. *Prog. in Aerospace Sci*, 35, p. 455-505.

Sitti, M. (2001). PZT actuated four bar mechanism with two flexible links for micromechanical flying insect thorax, *IEEE Int. Conf. Robotics and Automation*, Seoul, South Korea, p.3893-3900.

Sitti, M., Campolo, D., Yan, J., Fearing, R. S., Su, T., Taylor, D. and Sands, T. D. (2001). Development of PZT and PZN-PT based unimorph actuators for micromechanical flapping mechanisms. *IEEE lnt. Conf. Robotics and Automation*, Seoul, South Korea, p.3839-3846.

Smith, D. R., Kibens, V., Pitt, D. M. and Hopkins, M. A. (1999). Effect of Synthetic Jet Arrays on Boundary Layer Control. SPIE *Smart Structures and Materials 1999: Industrial and Commercial Applications of Smart Structures Technologies,* 3674, p. 401-409.

Smits, J. G., Dalke, S. I. and Cooney, T. K. (1991). The constituent equations of piezoelectric bimorphs. *Sensors and Actuators A: Physical*, 28, p. 41-61.

Smits, J.G., Choi, W. and Ballato, A. (1997). Resonance and anti-resonance of symmetric and asymmetric cantilevered piezoelectric flexors. *IEEE Trans. Ultrason. Ferroelectr. Freq. Control*, 44, p. 250-258.

Smits, J. G. and Cooney, T. K. (1991). The effectiveness of a piezoelectric bimorph actuator to perform mechanical work under various constant loading conditions, *Ferroelectrics*, 119, p. 89-105.

Singh, B., Ramasamy, M., Chopra, I., and Leishman, J. G. (2005). Experimental Studies on Insect Based Biomimetic Flapping Wings for Micro Hovering Air Vehicles. *46th Annual Structural Dynamics and Materials Conference*, Austin, TX. April 18-20.

Steel, M. R., Harrison, F. and Harper, P. G. (1978). The Piezoelectric Bimorph:An Experimental and Theoretical Study of Its Quasistatic Response. *Journal of Physics D: Applied Physics*, Vol. 11, p. 979-989.

Straub, F. K., Ngo, H. T., Anand, V. and Domzalski, D. B. (1999). Developmentof a Piezoelectric Actuator for Trailing Edge Flap Control of Rotor Blades. SPIE *Symposium on Smart Structures and Materials*, 3688, Newport Beach, California, March 1-4, p. 2-13.

Sugawara, Y., Onitsuka, K., Yoshikawa, S., Xu, Q. C., Newnham, R. E. and Uchino, K. (1992). Metal-Ceramic Composite Actuators. *Journal of the American Ceramic Society*, 75, p. 996-998.

Taylor, G., Nudds, R., and Thomas, A. (2003). Flying and swimming animals cruise at a Strouhal number tuned for higher power efficiency, *Nature*, 425, p. 707-711.

Thomson, W. T. (1993). Theory of Vibration With Applications (4th Edition). *Prentice Hall*, p. 146-185.

Toda, M. (1981). Voltage-induced large amplitude bending device-PVF2 bimorph - its properties and applications. *Ferroelectrics*, 32, p. 127-133.

Toda, M. (1979). Theory of air flow generation by a resonant type PVF2 bimorph

cantilever vibrator. *Ferroelectrics*, 22, p. 911–918.

Toda, M. and Osaka, S. (1977). Type of Electro-Motional Devices-PVF2 Piezoelectric Materials. *Abstracts of Japanese FMA*, p. 171.

Tzou, H. S. (1989). Development of a Light-Weight Robot End-Effector Using Polymeric Piezoelectric Bimorph. *in Proceedings of the 1989 International Conference on Robotics and Automation*, 3, p. 1704-1709.

Wait, S. M., Acikalin, T., Garimella, S. V., Raman, A. (2004). Piezoelectric fans for the thermal management of electronics. In: *Procs. Sixth ISHMT/ASME Heat and Mass Transfer Conference, Kalpakkam, India, January 5–7*. Paper No. HMT-2004-C76, p. 447–452

Wang, Q. and Cross, L. E. (1998). Performance analysis of piezoelectric cantilever bending actuators. *Ferroelectrics*, 215, p. 187-213.

Wang, Q. Zhang, Q. Xu, B., Liu, R. and Cross, L. E. (1999) Nonlinear piezoelectric behaviour of ceramic bending mode actuators under strong electric fields, *Journal Of Applied Physics*, 86(6), p. 3352-3360.

Wang, Q. and Cross, L. E. (1999). Constitutive equations of symmetrical triple-layer piezoelectric benders. *IEEE Trans. Ultrason. Ferroelec. Freq. Contr*. 46, p. 1343–1351.

Wu, T., Ro, P., Kingon, A. and Mulling, J. (2003). Piezoelectric resonating structures for microelectronic cooling. *Smart Materials and Structures*, 12, p. 181-187.

Xu, B., Zhang, Q. M., Kugel, V. D., Wang, Q. and Cross, L. E. (1996). Optimization of Bimorph Based Double Amplifier Actuator under Quasistatic Situation. *Proceedings of the Tenth IEEE International Symposium on Applications of Ferroelectrics*, Vol. 1, East Brunswick, New Jersey, August 18-21, p. 217-220.

Yan, J., Wood, R. J., Avadhanula, S., Sitti, M. and Fearing, R.S. (2001). Towards flapping wing control for a micromechanical flying insect, in: *IEEE Int. Conf. Robotics and Automation.* Seoul, South Korea, May 21-26, p. 3901-3908.

Yan, J., and Fearing, R. S. (2003). Wing Force Map Characterization and Simulation for the Micromechanical Flying Insect. *Proceedings of the 2003 IEEE/RSJ Int. Conf. Intelligent Robots and Systems.* Las Vegas. Nevada, October, p. 1343-1349.

Yang, R., Jouaneh, M. and Schweizer, R. (1996). Design and Characterization of a Low-Profile Micropositioning Stage. *Precision Engineering*, 18, p. 20-29.

Yao, K. and Uchino, K. (2001). Analysis on a composite cantilever beam coupling a piezoelectric bimorph to an elastic blade, *Sensors and Actuators A: Physical*, 89, p. 215-221.

Yoo, J., Hong, J. and Cao, W. (2000). Piezoelectric ceramic bimorph coupled to thin

metal plate as cooling fan for electronic devices. *Sensors and Actuators A: Physical*, 79, p. 8-12.

Websites:

http://eportal.apexmicrotech.com/mainsite/index.asp
http://piezo.com/prodsheet1sq5A.html
http://piezo.com/prodsheet2sq5H.html
http://www.edoceramic.com
http: //www.Epotek.com
http://www.physikinstrumente.com

Chapter 9

Appendices

A: FEA Coupled Piezofan programme

```
/COM,ANSYS RELEASE 10.0    UP20050718       10:29:29    11/17/2006
/input,menust,tmp,'',,,,,,,,,,,,,,,1
/GRA,POWER
/GST,ON
/PLO,INFO,3
/GRO,CURL,ON
/CPLANE,1
/REPLOT,RESIZE
WPSTYLE,,,,,,,,0
RESUME,'piezofanmelingcfrp60+6mm steel','db','C:\JAMES\',0,0
/COM,ANSYS RELEASE 10.0    UP20050718       10:31:06    11/17/2006
/PREP7
!*
MPTEMP,,,,,,,,
MPTEMP,1,0
MPDE,DENS,4
MPDATA,DENS,4,,1570
/DIST,1,0.924021086472,1
/REP,FAST
/DIST,1,0.924021086472,1
/REP,FAST
/DIST,1,1.08222638492,1
/REP,FAST
/DIST,1,0.924021086472,1
/REP,FAST
/DIST,1,1.08222638492,1
/REP,FAST
/DIST,1,0.924021086472,1
/REP,FAST
/DIST,1,1.08222638492,1
/REP,FAST
/DIST,1,0.924021086472,1
/REP,FAST
/DIST,1,1.08222638492,1
/REP,FAST
/DIST,1,0.924021086472,1
/REP,FAST
/DIST,1,0.924021086472,1
/REP,FAST
/DIST,1,1.08222638492,1
/REP,FAST
/DIST,1,0.924021086472,1
/REP,FAST
/DIST,1,1.08222638492,1
/REP,FAST
/DIST,1,1.08222638492,1
/REP,FAST
/DIST,1,1.08222638492,1
/REP,FAST
/DIST,1,0.924021086472,1
/REP,FAST
/DIST,1,0.924021086472,1
/REP,FAST
/DIST,1,1.08222638492,1
/REP,FAST
/DIST,1,0.924021086472,1
/REP,FAST
/DIST,1,1.08222638492,1
/REP,FAST
/DIST,1,0.924021086472,1
/REP,FAST
/DIST,1,0.924021086472,1
/REP,FAST
/DIST,1,1.08222638492,1
```

```
/REP,FAST
/DIST,1,0.924021086472,1
/REP,FAST
/DIST,1,1.08222638492,1
/REP,FAST
/DIST,1,0.924021086472,1
/REP,FAST
/DIST,1,0.924021086472,1
/REP,FAST
/DIST,1,1.08222638492,1
/REP,FAST
/DIST,1,1.08222638492,1
/REP,FAST
/DIST,1,0.924021086472,1
/REP,FAST
!*
FLST,2,9,6,ORDE,5
FITEM,2,7
FITEM,2,-8
FITEM,2,10
FITEM,2,12
FITEM,2,-17
VCLEAR,P51X
EPLOT
VPLOT
!*
!*
MPTEMP,,,,,,,,
MPTEMP,1,0
MPDE,DENS,4
MPDATA,DENS,4,,2000
MPTEMP,,,,,,,,
MPTEMP,1,0
MPDE,DENS,4
MPDATA,DENS,4,,2000
!*
MPTEMP,,,,,,,,
MPTEMP,1,0
MPDE,DENS,4
MPDATA,DENS,4,,2000
FLST,2,9,6,ORDE,5
FITEM,2,7
FITEM,2,-8
FITEM,2,10
FITEM,2,12
FITEM,2,-17
VGLUE,P51X
FLST,5,2,6,ORDE,2
FITEM,5,15
FITEM,5,-16
CM,_Y,VOLU
VSEL, , , ,P51X
CM,_Y1,VOLU
CMSEL,S,_Y
!*
CMSEL,S,_Y1
VATT,       4, ,   2,       0
CMSEL,S,_Y
CMDELE,_Y
CMDELE,_Y1
!*
/ZOOM,1,SCRN,0.343349,-0.153499,0.386580,-0.180096
FLST,5,5,6,ORDE,5
FITEM,5,7
FITEM,5,10
FITEM,5,12
FITEM,5,14
FITEM,5,17
CM,_Y,VOLU
VSEL, , , ,P51X
CM,_Y1,VOLU
CMSEL,S,_Y
!*
CMSEL,S,_Y1
```

```
VATT,       2, ,   2,       0
CMSEL,S,_Y
CMDELE,_Y
CMDELE,_Y1
!*
/UI,MESH,OFF
/AUTO,1
/REP,FAST
/ZOOM,1,SCRN,0.336698,-0.273184,0.476366,-0.569072
CM,_Y,VOLU
VSEL, , , ,      13
CM,_Y1,VOLU
CMSEL,S,_Y
!*
CMSEL,S,_Y1
VATT,       1, ,   1,       0
CMSEL,S,_Y
CMDELE,_Y
CMDELE,_Y1
!*
/ZOOM,1,SCRN,0.506295,-0.356299,0.556176,-0.522528
CM,_Y,VOLU
VSEL, , , ,       8
CM,_Y1,VOLU
CMSEL,S,_Y
!*
CMSEL,S,_Y1
VATT,       2, ,   2,       0
CMSEL,S,_Y
CMDELE,_Y
CMDELE,_Y1
!*
FLST,5,9,6,ORDE,5
FITEM,5,7
FITEM,5,-8
FITEM,5,10
FITEM,5,12
FITEM,5,-17
CM,_Y,VOLU
VSEL, , , ,P51X
CM,_Y1,VOLU
CHKMSH,'VOLU'
CMSEL,S,_Y
!*
VSWEEP,_Y1
!*
CMDELE,_Y
CMDELE,_Y1
CMDELE,_Y2
!*
/AUTO,1
/REP,FAST
NSEL,S,LOC,Y,-3e-3, -3e-3
NPLOT
FINISH
/SOL
!*
ANTYPE,2
!*
MSAVE,0
!*
MODOPT,LANB,10
EQSLV,SPAR
MXPAND,0, , ,0
LUMPM,0
PSTRES,0
!*
MODOPT,LANB,10,0,10000, ,OFF
FLST,2,12,1,ORDE,4
FITEM,2,101
FITEM,2,-106
FITEM,2,376
FITEM,2,-381
!*
```

```
/GO
D,P51X, ,0, , , ,ALL, , , , ,
/STATUS,SOLU
SOLVE
FINISH
/POST1
SET,LIST
```

B: MatLab programme for two sections piezofan

```
% Program to find natural frequencies: determinant is expressed as function
% of omega
L1=0.03;  % Figures in metres
L2=0.04;
% Following Values need to be adjusted as appropriate
rho_c=7900;
A_c=0.00000125;
E_c=200000000000;
I_c=0.0000000000000016;
rho_b=7900;
A_b=0.00000125;
rho_p=7800;
A_p=0.00000127;
a_2=39107452001;
I_pn=0.000000000000013;
a_3=-74.4;
A_p=0.00000127;
E_b=200000000000;
I_bn=0.0000000000000028;
% Beginning of Loop
for omega=460:1:480;
    x=(rho_c*A_c*omega^2/(E_c*I_c))^0.25;
    y=((rho_b*A_b+rho_p*A_p)*omega^2/(2*a_2*I_pn+2*a_3*A_p+E_b*I_bn))^0.25;
    y1=2*a_2*I_pn+2*a_3*A_p+E_b*I_bn;
    y2=E_c*I_c;
    A=[1              0              1              0              0
0              0              0;
      0              1              0              1              0
0              0              0;
      0              0              0              0              -
cos(L2*x)       -sin(x*L2)      cosh(x*L2)          sinh(x*L2);
      0              0              0              0
sin(x*L2)        -cos(x*L2)      sinh(x*L2)          cosh(x*L2);
      cos(y*L1)       sin(y*L1)       cosh(y*L1)       sinh(y*L1)       -
cos(x*L1)       -sin(x*L1)      -cosh(x*L1)         -sinh(x*L1);
      -y*sin(y*L1)    y*cos(y*L1)     y*sinh(y*L1)     y*cosh(y*L1)
x*sin(x*L1)      -x*cos(x*L1)    -x*sinh(x*L1)       -x*cosh(x*L1);
      -y^2*y1*cos(y*L1)  -y^2*y1*sin(y*L1)  y^2*y1*cosh(y*L1)
y^2*y1*sinh(y*L1)   x^2*y2*cos(x*L1)    x^2*y2*sin(x*L1)   -x^2*y2*cosh(x*L1)
-x^2*y2*sinh(x*L1);
      y^3*y2*sin(y*L1)   -y^3*y2*cos(y*L1)  y^3*y2*sinh(y*L1)
y^3*y2*cosh(y*L1)   -x^3*y2*sin(x*L1)  x^3*y2*cos(x*L1)   -x^3*y2*sinh(x*L1)
-x^3*y2*cosh(x*L1)];
    f=det(A);
    plot(omega,f,'*');
    hold on;
end;
grid on;
```

C: MatLab programme for three sections piezofan

```
% Program to find natural frequencies: determinant is expressed as function
% of omega
L1=0.003;  % Figures in metres
L2=0.033;
L3=0.043;
% Following Values need to be adjusted as appropriate
rho_c=7900;
A_c=0.00000125;
E_c=200000000000;
I_c=0.0000000000000016;
rho_b=7900;
A_b=0.00000125;
rho_p=7800;
A_p=0.00000191;
a_2=39107452001;
I_pn=0.000000000000028;
a_3=-93.2;
```

```
A_p=0.00000191;
E_b=200000000000;
I_bn=0.0000000000000049;
% Beginning of Loop
for omega=455:1:465;
    x=(rho_c*A_c*omega^2/(E_c*I_c))^0.25;
    y=((rho_b*A_b+rho_p*A_p)*omega^2/(2*a_2*I_pn+2*a_3*A_p+E_b*I_bn))^0.25;
    y1=2*a_2*I_pn+2*a_3*A_p+E_b*I_bn;
    y2=E_c*I_c;
    A=[1                0                1                0                0
0                0                0                0                0
0                0;
      0                1                0                1                0
0                0                0                0                0
0                0;
      0                0                0                0                0
0                0                0               -cos(x*L3)       -
sin(x*L3)      cosh(x*L3)          sinh(x*L3);
      0                0                0                0                0
0                0                0                sin(x*L3)       -
cos(x*L3)      sinh(x*L3)          cosh(x*L3);
      cos(x*L1)        sin(x*L1)        cosh(x*L1)       sinh(x*L1)       -
cos(y*L1)       -sin(y*L1)      -cosh(y*L1)         -sinh(y*L1)          0
0                0                0;
      -x*sin(x*L1)    x*cos(x*L1)     x*sinh(x*L1)     x*cosh(x*L1)
y*sin(y*L1)      -y*cos(y*L1)    -y*sinh(y*L1)       -y*cosh(y*L1)         0
0                0                0;
      -y2*x^2*cos(x*L1)  -y2*x^2*sin(x*L1)  y2*x^2*cosh(x*L1)
y2*x^2*sinh(x*L1)   y1*y^2*cos(y*L1)    y1*y^2*sin(y*L1)   -y1*y^2*cosh(y*L1)
-y1*y^2*sinh(y*L1)        0                0                0                0;
     y2*x^3*sin(x*L1)   -y2*x^3*cos(x*L1)  y2*x^3*sinh(x*L1)   y2*x^3*cosh(x*L1)
-y1*y^3*sin(y*L1)    y1*y^3*cos(y*L1)   -y1*y^3*sinh(y*L1)     -y1*y^3*cosh(y*L1)
0                0                0                0;
      0                0                0                0
cos(y*L2)       sin(y*L2)       cosh(y*L2)       sinh(y*L2)       -cos(x*L2)
-sin(x*L2)      -cosh(x*L2)         -sinh(x*L2);
      0                0                0                0                -
y*sin(y*L2)    y*cos(y*L2)     y*sinh(y*L2)      y*cosh(y*L2)     x*sin(x*L2)
-x*cos(x*L2)    -x*sinh(x*L2)       -x*cosh(x*L2);
      0                0                0                0                -
y1*y^2*cos(y*L2)  -y1*y^2*sin(y*L2)  y1*y^2*cosh(y*L2)    y1*y^2*sinh(y*L2)
y2*x^2*cos(x*L2)    y2*x^2*sin(x*L2)   -y2*x^2*cosh(x*L2)     -y2*x^2*sinh(x*L2);
      0                0                0                0
y1*y^3*sin(y*L2)  -y1*y^3*cos(y*L2)  y1*y^3*sinh(y*L2)   y1*y^3*cosh(y*L2)   -
y2*x^3*sin(x*L2) y2* x^3*cos(x*L2)   -y2*x^3*sinh(x*L2)     -y2*x^3*cosh(x*L2)];
    f=det(A);
    plot(omega,f,'*');
    hold on;
end;
grid on;
```

D: publications for Hsien-Chun Chung

1. Hsien-Chun Chung, R. W. Whatmore and Zhaorong Huang, (2006). *Coupled piezoelectric fans with 2DOF motion for the application of Micro Air Vehicle,* Ferroelectrics UK 2006 conference, p.67.

2. Simon J.Croucher, Nicholas J.Lawson, Kranti K. Lal Kummari, Hsien-Chun Chung, Zhaorong Huang and Roger Whatmore, (2006). *Stereoscopic PIV Analysis of an Oscillating Piezoelectric Unimorph, ,* 13th Int Symp on Applications of Laser techniques to Fluid Mechanics Lisbon, Portugal, 2006.

3. Z. Huang, G. Leighton, R. Wright, F. Duval, H.C. Chung, P. Kirby and R.W. Whatmore, (2007). *Determination of the piezoelectric coefficients and elastic constant of thin films by laser scanning vibrometry techniques,* Sensors and Actuators A135, p.660-665.

4. K.K.Lal Kummari, S. J.Croucher, N. J.Lawson, E. E. Liani, G. Allegri, S. Guo, Hsien-Chun Chung, and Z. Huang, *The application of piezoelectric actuator and compliant structures to achieve flapping wing motion for a MAV*, Journal of Materials Science & Engineering, **26**, 642 (2008).

5. Hsien-Chun Chung, K. Lal Kummari, S. J.Croucher, N. J.Lawson, S. Guo, R.W. Whatmore, Z. Huang, (2008). *Coupled Piezoelectric Fans with Two Degree of Freedom Motion for the Application of Flapping Wing Micro Aerial Vehicles*, Sensors and Actuators A: Physical. **147**, 607-612 (2008).

6. Hsien-Chun Chung, K. Lal Kummari, S. J.Croucher, N. J.Lawson, S. Guo, Z. Huang, (2008). *Development of Piezoelectric Fans for Flapping Wing Applications*, Sensors and Actuators A: Physical, in press.

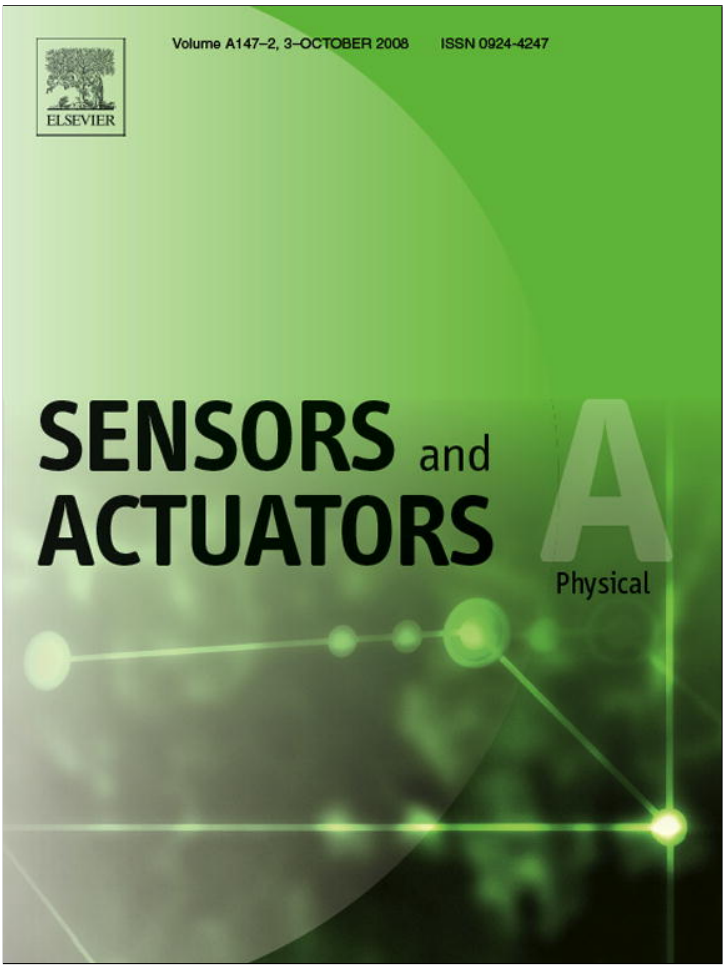

Sensors and Actuators A 147 (2008) 607–612

Contents lists available at ScienceDirect

Sensors and Actuators A: Physical

journal homepage: www.elsevier.com/locate/sna

Coupled piezoelectric fans with two degree of freedom motion for the application of flapping wing micro aerial vehicles

Hsien-Chun Chung[a], K. Lal Kummari[a], S.J. Croucher[b], N.J. Lawson[b], S. Guo[b], Z. Huang[a,*]

[a] Department of Materials, School of Applied Sciences, Cranfield University, Bedford MK43 0AL, UK
[b] Department of Aerospace Engineering, School of Engineering, Cranfield University, Bedford MK43 0AL, UK

ARTICLE INFO

Article history:
Received 17 April 2008
Received in revised form 3 June 2008
Accepted 17 June 2008
Available online 26 June 2008

Keywords:
Piezoelectric fan
Flapping
Twisting
Resonance
FEM
MAV

ABSTRACT

Piezoelectric fans consisting of a piezoelectric layer and an elastic metal layer were prepared by epoxy bonding and a coupled flexible wing was formed by a pair of carbon fibre reinforced plastic wing spars and polymer skin attached to two piezoelectric fans. Two sinusoidal voltages with phase differences were then used to drive the coupled piezoelectric fans. High speed digital cameras were used to characterize the two degree of freedom (DOF) motion of the wing and these results were compared to finite element model of the wing and the coupled piezoelectric fans. It has been observed that the phase delay between the driving voltages applied to the coupled piezoelectric fans plays an important role in the control of the flapping and twisting motions of the wing and this set-up has the potential for application to the control of flapping wings for micro aerial vehicles.

1. Introduction

The interest in flapping wing micro aerial vehicles (MAV) has resulted in substantial work in recent years [1–3]. A MAV is defined as a semiautonomous airborne vehicle, measuring less than 15 cm in any dimension, weighing not more than 140 g, which can fly up to 2 h for a range of 10 km [1]. As demonstrated by flying birds and insects, flapping flight is advantageous for its superior manoeuvrability and lifting capability at low flight speeds [3,4]. Flapping wing systems as inspired by insect flight generally involve the wing completing pitching, yawing and sweeping components of motion over a flapping cycle [5]. Different mechanisms such as pneumatic and motor-driven actuators have been applied to mimic this complex flapping motion, but these mechanisms often suffer from heavy weight and mechanical system complexity [5].

Piezoelectric materials especially lead zircornate titanate (PZT) are widely used in smart structures as sensors and actuators due to their high bandwidth, high output force, compact size, and high power density [6]. However, the piezoelectric effect is intrinsically very small and only a small deflection can be expected directly from the bending piezoelectric unimorph/bimorph. Therefore some kind of motion amplification mechanisms are required to achieve large deflection. Fearing et al. [7–9] developed piezoelectrically actuated four-bar mechanisms for micromechanical flying insect thorax. Cox et al. [10] reported three piezoelectrically activated four-bar and five-bar linkage systems for the electromechanical emulation of mesoscale flapping flight. Park et al. [11] developed a four-bar linkage system driven by lightweight piezo-composite actuator to mimicking the flapping wing system of insects.

A simpler motion amplification mechanism is a piezoelectric fan (piezofan) which couples a piezoelectric unimorph to an attached flexible blade and is capable of producing large deflections especially at resonance. Piezofans were first investigated in the late seventies [12]. In the last few years the demand for portable electronic devices has brought interest in the use of piezofans as a compact, low power, noiseless air cooling technology for applications such as laptop computers and DVD players [13,14]. We have investigated the optimization and characterization of individual piezofan structure at quasi-static and dynamic operations in a separate report [15]. In this paper we report the investigation on using two coupled piezofans in parallel driven by sinusoidal voltages with different phase delays between them to realise the flapping and twisting movements of the wing structure. The main purpose of using piezofan as actuators is to facilitate this simple actuation mechanism to obtain two degree of freedom motion (2DOF), namely the flapping and twisting, of the wing and to develop meth-

* Corresponding author at: Department of Materials, School of Applied Sciences, Cranfield University, Building 70, Bedford MK43 0AL, UK. Tel.: +44 1234 750111; fax: +44 1234 751346.
E-mail address: Z.Huang@Cranfield.ac.uk (Z. Huang).

0924-4247/$ – see front matter © 2008 Elsevier B.V. All rights reserved.
doi:10.1016/j.sna.2008.06.017

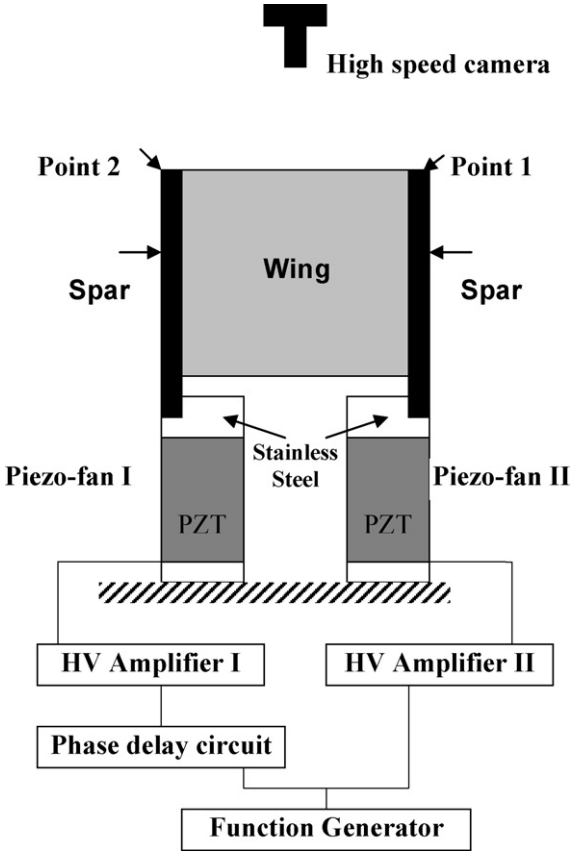

Fig. 1. The schematic set-up for the coupled piezoelectric fans with the attached wing and their vibration measurement by high speed camera photography.

ods for the control of its 2DOF motion. The experimental and finite element analysis and the effect of phase delay to the flapping and twisting of the wings attached to the coupled piezofans will be presented.

2. Experimental

Piezofans were prepared by bonding together a stainless steel metal shim with a piezoelectric PZT patch using epoxy glue EPOTEK 301-2 (Epoxy Technology, USA). The PZT wafers (PSI-5H4E) and stainless steel foils (Fe/Cr15/Ni7/Mo2.25) were purchased from commercial sources [15]. The schematic set-up for the 2DOF motion is shown in Fig. 1. The two piezoelectric fans were of the unimorph type, with the PZT patch of the dimensions 30 mm × 10 mm × 127 μm, and the elastic stainless steel layer of the dimensions 43 mm × 10 mm × 125 μm, so the total length of the piezoelectric fan was 43 mm. A 3 mm gap existed between the clamping and the start of the PZT patch in order to prevent the ceramic layer from broken during vibration. A pair of spars made of carbon fibre reinforced plastic (CFRP) connected with a flexible polymer skin formed the wing and the wing was attached to the two piezoelectric fans clamped in parallel to form the coupled fans. The gap between the two fans, therefore also the gap between the two spars, was varied from 10 mm to 2 mm.

The same wave (usually sinusoidal) signal from a function generator was split and supplied to two high voltage amplifiers. One of the split signals was then amplified and applied to one piezofan directly whilst the second signal was connected to an in-house made phase delay circuit (which can achieve 0° to 180° phase delay) before being connected to the other amplifier and then the other piezofan. The piezofans were clamped perpendicularly in parallel and both the flapping and twisting motions are in the horizontal direction. This enabled a high speed camera (Photron APX) fixed above the piezofans to record both the flapping and the twisting motions of the wing. A frame rate of 2000 frames/s was used with an area of interest of 61.25 mm × 61.25 mm, which corresponded to a mean resolution of 67 μm per pixel. The camera was controlled by a computer system to record 1 s of data corresponding to 2000 images. The 2000 images covered several full cycles of the vibration (the frequency was usually between 10 to 100 Hz). The displacement data was then obtained by comparing images over a full cycle and directly analysing the image showing the largest displacement. ANSYS finite element modelling (FEM) was used to model the behaviours of the coupled piezofans and the wing attached to it.

3. Results and discussion

3.1. Characterization of the dynamic motions for the coupled piezofans

Fig. 2 shows the results of the FEM modal analysis. The first mode was pure bending or flapping, at 23.7 Hz (a). The second mode was pure twisting (b), at 58 Hz and the third mode contained both bending and twisting at 62.9 Hz. The material parameters used in the FEM are listed in Table 1.

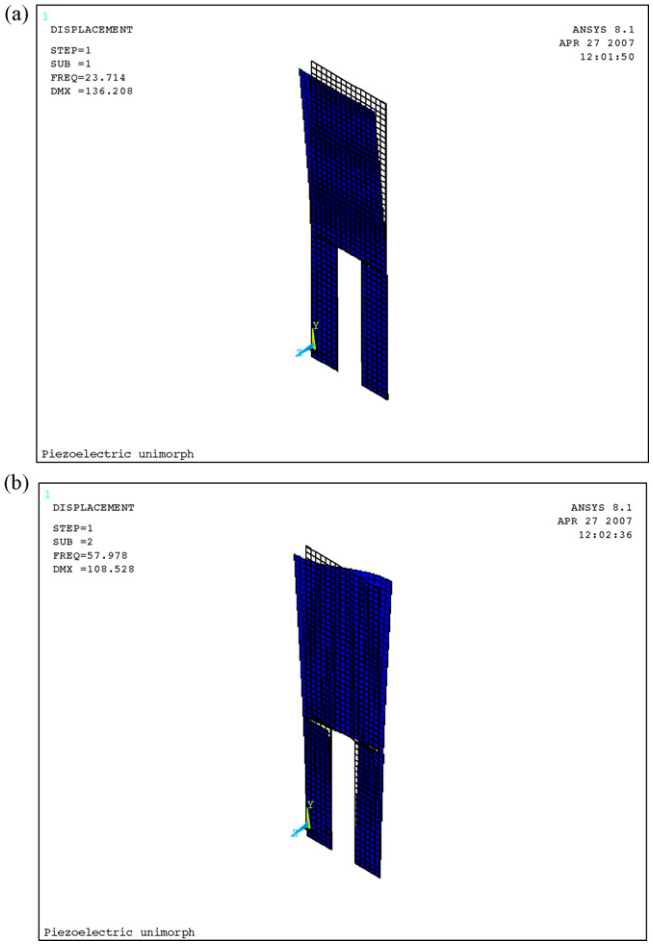

Fig. 2. The finite element modelling modal analysis for the coupled piezoelectric fans systems as shown in Fig. 1: (a) first mode bending, 23.7 Hz; (b) second mode twisting, 58 Hz.

Table 1
Material property parameters used for the finite element modelling

Material	PZT 5H	Stainless steel	Polymer	CFRB
Thickness (μm)	127	125	50	100
Width (mm)	10	10	–	2
Young's modulus (GPa)	62	200	8	200
Density (kg/m^3)	7800	7900	1534	1750
Poisson's ratio	–	0.28	0.27	0.27
d_{31} (10^{-12} m/V)	−320	–	–	–
ε_{11}	3130	–	–	–
ε_{22}	3130	–	–	–
ε_{33}	3400	–	–	–
e_{31}	−12	–	–	–
e_{33}	22.22	–	–	–
e_{15}	19.39	–	–	–
c_{11} (10^9 N/m^2)	126	255.68	–	–
c_{12} (10^9 N/m^2)	79.5	99.43	–	–
c_{13} (10^9 N/m^2)	84.1	–	–	–
c_{33} (10^9 N/m^2)	117	–	–	–
c_{44} (10^9 N/m^2)	23.0	78.13	–	–

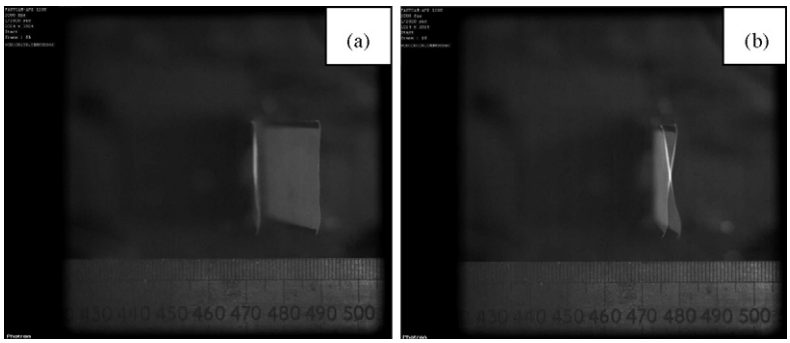

Fig. 3. Typical images produced by superimposing two high speed camera images of the two extreme positions of the wing within a vibration cycle at frequencies (a) 22.3 Hz and (b) 47.4 Hz. The driving voltage was 170V_{pp}.

Fig. 3 shows typical pictures produced by superimposing two high speed camera images of the two extreme positions of the wing within a vibration cycle, without any phase delay between the two input voltages 170V_{pp} at frequencies (a) 22.3 and (b) 47.4 Hz. Both the flapping and twisting motion of the wing were obtained. It was found that the flapping displacement was peaked at 20 mm at the frequency 22.3 Hz. The twisting motion was found peaked at 16° at the frequency 47.4 Hz. Fig. 4 shows the flapping and twisting amplitudes as functions of frequency for the wing. The quantitative discrepancy on the mode frequencies between the FEM modelled and actually measured values could be contributed to a number of factors. These include the uncertainty of the Young's modulus for the CFRB spars and the polymer skin used in the FEM modelling, the non-perfect clamping at the foot of the piezofans, and probably most importantly the unmatched piezofans to drive the wing. A number of these factors will now be discussed in more detail.

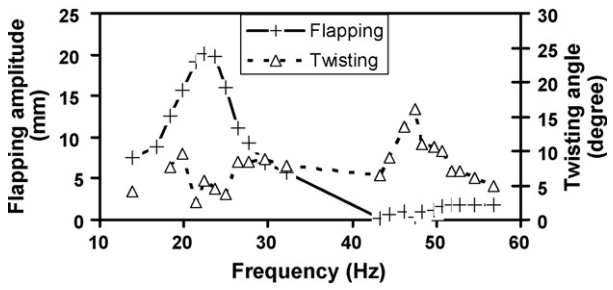

Fig. 4. The measured flapping and twisting motion amplitudes of the wing as functions of the operating frequency driving by the two coupled piezofans under 170V_{pp}.

Unmatched piezofans. For the system shown in Fig. 1, if piezofans I and II were identical, with no phase difference between the two input signals (i.e. phase delay = 0), the two piezofans would be expected to vibrate in parallel at around the first resonant frequency. However, for many reasons it is not possible to have two identical piezofans in terms of their resonant frequencies and vibration amplitudes. As every piezofan is produced individually, any difference in the width and length of the PZT patch and the stainless steel shim, the relative position of the PZT patch on the metal shim, and the exact clamping conditions, etc., all can lead to the variation of the resonant frequency and amplitude. Furthermore, the vibration amplitude also depends on the exact piezoelectric coefficient of the PZT patch and the condition of the bonding layer, as well as the geometrical factors. This means that, at any frequency, even at phase delay = 0, the two piezofans may not vibrate in parallel, or one may vibrate with a larger amplitude than the other. This will show an apparent twisting motion for the wing. Since, around the first resonant frequency, the flapping displacement is at a maximum this mismatch in piezofan displacement appears to be at its greatest. For this reason, the spread of the measurement data of the twisting motion around the first resonant frequencies is expected to be the largest, as confirmed by measurements (Fig. 4). The effect of different resonant frequencies on the flapping motion of the wing was found to be much smaller, as shown in Fig. 4, where the flapping motion around the second resonance was smaller relative to the flapping motion at the first resonant frequency.

Stiffness of the wing skin materials. The flapping and the twisting motions of the wing also depend very much on the stiffness of the wing skin material, as well as the piezofan actuators. We con-

sider two extreme cases here: (i) If the skin material is infinitely soft (the stiffness coefficient $c_{ij} = 0$), the whole system as shown in Fig. 1 will act like two independent piezofans. At any frequency, the two piezofans will vibrate in parallel when the phase delay = 0° and in anti-phase when the phase delay = 180°. The flapping amplitude will be at its maximum when the phase delay = 0 and reduce to zero when the phase delay = 180°, and the twisting motion will be at its maximum when the phase delay = 180° and reduce to zero when the phase delay = 0. Changing the phase delay will change the flapping and twisting amplitudes of the wing. However, if there is a difference of the first resonant frequencies f_1 and f_2 of the two piezofans, the flapping and apparent twisting will depend on the operating frequency f and the value of $f_2 - f_1$. (ii) If the skin material is infinitely stiff (the compliance coefficients $s_{ij} = 0$), then the whole system must be treated as a single body and it has its unique resonant frequencies, the first mode being bending and the second mode being twisting. In this case, the resonant frequency of the individual actuator piezofans I and II or the difference between the two will have a limited effect on the performance of the wing. In fact, the actual wing will be between the above two extremes, with a finite stiffness coefficients $c_{ij} > 0$. The system has its unique bending and twisting mode resonance frequencies but the performance could be affected by the difference in resonant frequencies of the individual piezofan actuators. Every effort was made to fabricate the piezofans as identical as possible. The effect of different skin materials is a subject for further study. It is expected that a thin and light but stiff material—like an insect wing, is the best.

3.2. Two DOF motion control by phase differentiated drive

Fig. 5 illustrates measurement results of (a) the flapping and (b) twisting vibration amplitudes of the wing as functions of operating frequency under two input voltages $170V_{pp}$ with different phase delays between them. The gap between the two piezofans was 10 cm. It can be observed that the flapping motion had a resonance at around 22 Hz, and the vibration amplitude was the largest at phase delay = 0 and reduced with the increasing phase delay. The amplitude reached a minimum when the phase delay equalled 180°, about a quarter of the value at the phase delay = 0. The twisting motion peaked around 49 Hz, and, contrary to the flapping, its amplitude increased with the increasing phase delay. The twisting amplitude for the phase delay = 0 was about half of the value for the phase delay = 180°. However, as discussed in the last section, the amplitude mismatch generated twisting movement was significant for the frequencies near the flapping resonance, when there was inevitably a difference of the resonant frequency between the two piezofans. The slight increase of the flapping motion around the frequency 50 Hz may also due to the increase of the amplitude mismatch around the twisting resonance there (Fig. 4).

Fig. 5 shows that it is possible to change both the flapping and twisting motions of the flapping wing simply by varying the phase delay between the two input signals. At frequencies around the first resonance, i.e. the flapping mode resonance, increasing the phase delay from 0° to 180° lead to the reduced flapping motion. At frequencies around the second resonance, i.e. the twisting mode resonance, increasing the phase delay from 0° to 180° lead to increased twisting motion. However, due to the difficulty in obtaining matched piezofan actuators, it is not clear from this study what are the effects of changing phase delay on the twisting motion around the flapping resonant frequency, and the effects on the flapping motion around the twisting resonant frequency. Nevertheless, the flapping at frequencies far away from the flapping resonance was found to be insignificant.

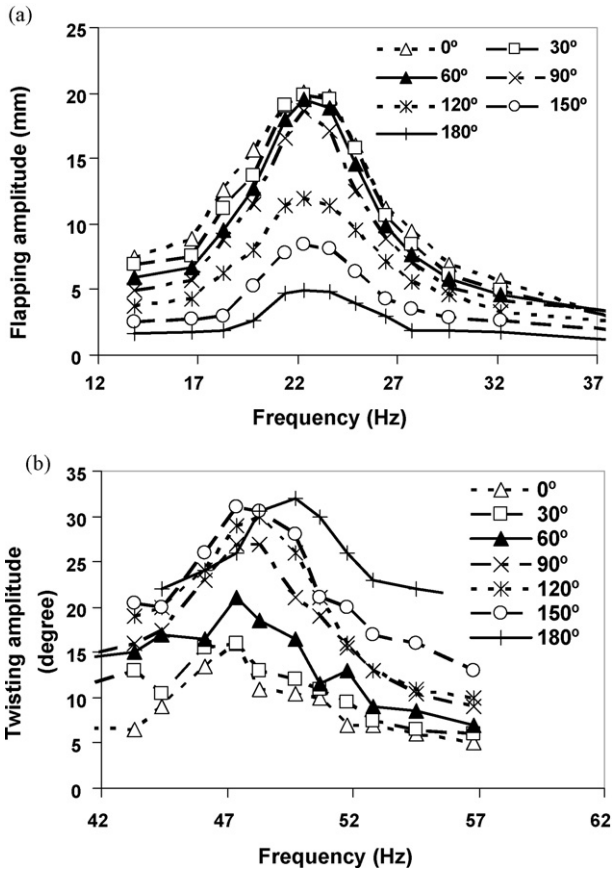

Fig. 5. The measured vibration amplitudes as functions of frequency at different phase delays at around (a) the flapping and (b) the twisting resonances.

3.3. The effect of the gap distance between the two piezofans

The effect of the distance between the two piezofan actuators on the flapping and twisting motions of the wing was also investigated. Both the flapping and twisting were recorded at their respective resonant frequencies. For example, the flapping were measured at 26.2, 26.3, 26.0 and 26.2 Hz for gap distances 10, 8, 5 and 2 mm, respectively; and the twist angles were measured at 53.6, 49.1, 51.4 and 47.4 Hz for gap distances 10, 8, 5 and 2 mm, respectively. Changing the gap distance involves de-clamping at least one of the piezofan, varying the distance between the two piezofans, and then re-clamping the piezofans. These results show that the flapping resonant frequency of the system changed a small amount (e.g. from 26.0 to 26.3 Hz) after these manoeuvres, but noticeable difference in twisting resonant frequencies (from 47.4 to 53.6 Hz) resulted. However, these changes were not monotonic with the change of the gap distance and were therefore most likely to be due to the change of the effective clamping distances in the re-clamping, which leads to the change of the resonant frequency of the piezofan, as discussed before.

Fig. 6 shows the measured phase delay dependence of (a) the bending displacement and (b) the twisting angle for the same system. The measured values were represented by symbols ♦, □, ▲, and × and their corresponding polynomial fittings by solid, dashed, dotted, and dash and dotted curves for the gap equals to 10, 8, 5 and 2 mm, respectively. The effect of the gap distance between the two fans was also shown in the figure. When the gap distance was 10 mm and the voltages $V_{pp} = 170$ V applied to the two piezoelectric fans were in phase (phase delay = 0°), the amplitude of the bending movement of the wing reached 23.4 mm and resonated at

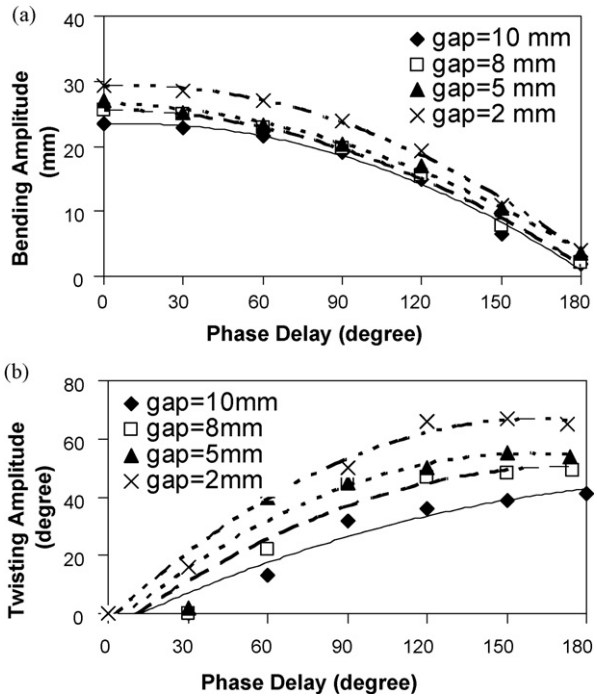

Fig. 6. The phase delay dependence of the vibration amplitude of the bending and twisting modes of the wing driving by the coupled piezoelectric fans under 170V_{pp} at different gap distances between the two spars: (a) bending mode; and (b) twisting mode.

26.2 Hz. If the phase delay of the two driving voltages was increased and all the other conditions remained the same, the mode of the wing movement remained the pure bending and also resonated at the same frequency, but with a reduced amplitude. In addition, if the two driving voltages were anti-parallel (phase delay = 180°), the amplitude of the resonant bending displacement was reduced to minimum of 1.8 mm. When the gap between the two wing spars was reduced from 10 to 8 mm (and further to 5 and 2 mm) and all the other conditions were kept the same, the bending displacement increased but the dependence on the phase delay was similar (Fig. 6a).

If the frequency of the two driving voltages was increased from 26.2 to 53.6 Hz, the same as its second mode frequency, the wing motion became a pure twisting. In this case, the two wing spars as represented by point 1 and point 2 in Fig. 1 were always moving in the opposite directions with the middle line not moving. When the gap distance was 10 mm and the voltages V_{pp} = 170 V applied to the two piezofans were in phase (phase delay = 0°), the twisting angle of the wing was minute, close to 0° at 53.6 Hz. If the phase delay of the two driving voltage was increased and all the other conditions remained the same, the wing movement was found to remain at the pure twisting mode and also resonate at the same frequency, but with an increased twisting amplitude. For the case with the two driving voltages set to anti-parallel (phase delay = 180°), the resonant twisting angle reached 41° (Fig. 6b). It was also found, if the gap between the two wing spars was reduced from 10 to 8 mm (and further to 5 and 2 mm) and all the other conditions were kept the same, the wing twisting increased but its dependence on the phase delay was similar (Fig. 6b).

The motional amplitude dependence on the gap distance between the two spars could be interpreted by consideration of the air damping effect. In this case, the damping of the wing movement would increase in proportion to its cross-sectional area where the effective cross-section of the wing is proportional to the gap

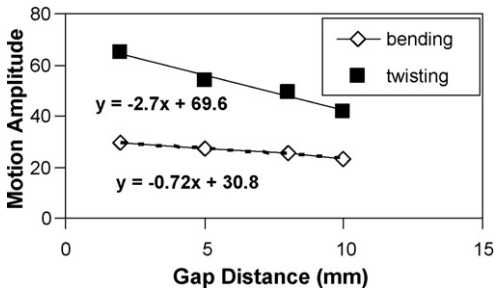

Fig. 7. The vibration amplitudes of the bending and twisting motions of the wing as functions of the gap distance between the two spars. The nearly linear relationship suggests that the air damping effect was responsible for the decreasing vibration amplitude with the increasing gap distance.

distance [16]. So the reduced gap distance would lead to a reduced aerodynamic damping and hence an increased vibration amplitude. To this end, a nearly linear relationship (with negative slump rates) was found to exist between both the bending and twisting amplitudes and the gap distance (Fig. 7), further reinforcing this proposed damping dependency.

4. Conclusions

Coupled piezoelectric fans were formed by clamping two fans in parallel and attaching a flexible wing made of two stiff carbon fibre reinforced plastic wing spars and a soft polymer skin. The dynamic behaviours of the wing were modelled by FEM modal analysis and investigated by using high speed digital cameras. It was found both the mode and the amplitude of the wing motion depend strongly on frequency. The degrees of motion of the wing increased by nearly 10 times at resonant frequencies as compared to the motion at frequencies far away from the resonance. It was found that the phase delay between the driving voltages supplied to the two coupled piezoelectric fans play a critical role in the control of the flapping and twisting motions of the wing. The bending amplitude of the wing reduced with the increasing phase delay and the twisting movement increased with an increasing phase delay.

Acknowledgements

This work was financially supported by the UK EPSRC Grant Flapping Wing MAV EP/C511190/1 and Platform Grant EP/D506638/1. We thank Prof. R.W. Whatmore of Tyndall National Institute, Ireland for invaluable discussions.

References

[1] W. Shyy, M. Berg, D. Ljungqvist, Flapping and flexible wings for biological and micro air vehicles, Progress in Aerospace Science 35 (1999) 455–505.
[2] D.L. Raney, E.C. Slominski, Mechanization and control concepts for biologically inspired micro aerial vehicles, in: AIAA 2003-5354, AIAA Guidance, Navigation and Control Conference, Austin, TX, August 2003.
[3] C.P. Ellington, The novel aerodynamics of insect flight: applications to micro-air vehicles, Journal of Experimental Biology 202 (1999) 3439–3448.
[4] C.P. Ellington, C. Van den Berg, A.P. Willmott, A. Thomas, Leading-edge vortices in insect flight, Nature 384 (1996) 626–630.
[5] M.H. Dickinson, F. Lehmann, S. Sane, Wing rotation and the aerodynamic basis of insect flight, Science 284 (1999) 1954–1960.
[6] C. Niezrecki, D. Brei, S. Balakrishnan, A. Moskalik, Piezoelectric actuation: state of the art, The Shock and Vibration Digest 33 (2001) 269–280.
[7] R.S. Fearing, K.H. Chiang, M.H. Dickinson, D.L. Pick, M. Sitti, J. Yan, Wing transmission for a micromechanical flying insect, in: Proceedings of the IEEE International Conference on Robotics and Automation, San Francisco, CA, USA, 2000, pp. 1509–1516.
[8] M. Sitti, PZT actuated four bar mechanism with two flexible links for micromechanical flying insect thorax, in: Proceedings of the IEEE International Conference on Robotics and Automation, South Korea, 2001, pp. 3893–3900.

[9] J. Yan, R.J. Wood, S. Avadhanula, M. Sitti, R.S. Fearing, Towards flapping wing control for a micromechanical flying insect, in: Proceedings of the IEEE International Conference on Robotics and Automation, South Korea, 2001, pp. 3901–3908.
[10] A. Cox, D. Monopoli, D. Cveticanin, M. Goldfarb, E. Garcia, The development of elastodynamic components for piezoelectrically actuated flapping micro air vehicles, Journal of Intelligent Material Systems and Structures 13 (2002) 611–615.
[11] H.C. Park, K.J. Kim, S. Lee, S.Y. Lee, Y.J. Cha, K.J. Yoon, N.S. Goo, Biomimetic flapping devices powered by artificial muscle actuators, in: UKC2004 US–Korea Conference on Science, Technology and Entrepreneurship, August 2004.
[12] M. Toda, Voltage-induced large amplitude bending device – PVF2 bimorph – its properties and applications, Ferroelectrics 32 (1981) 911.
[13] J. Yoo, J. Hong, W. Cao, Piezoelectric ceramic bimorph coupled to thin metal plate as cooling fan for electronic devices, Sensors & Actuators A 79 (2000) 8–12.
[14] T. Wu, P. Ro, A. Kingon, J. Mulling, Piezoelectric resonating structures for microelectronic cooling, Smart Materials & Structures 12 (2003) 181–187.
[15] H.-C. Chung, K.L. Kummari, S.J. Croucher, N.J. Lawson, E. Liani, S. Guo, R.W. Whatmore, Z. Huang, Development of piezoelectric fans for loaded applications, Sensors and Actuators A, submitted for publication.
[16] J. Katz, A. Plotkin, Low-Speed Aerodynamics, 2nd ed., Cambridge University Press, 2005.

Biographies

Hsien-Chun Chung received his MSc degree in system engineering in 1999 from Chung Cheng Institute of Technology, Taiwan. Now, he is a PhD student in the Nanotechnology Centre, Department of Materials in Cranfield University working on piezoelectric actuators, especially for the application as a power plant system for flapping wing micro-air-vehicles.

Kranti Kiran Lal Kummari is a PhD student in the School of Applied Science at Cranfield University working on piezoelectrically actuated flapping wing micro-air-vehicle project funded by EPSRC. He received his Masters degree in aerospace engineering from Salford University, Manchester, UK. His undergraduate degree was in mechanical engineering from Sree Nidhi Institute of Science and Technology, Hyderabad, India.

Simon Croucher obtained his MSc in aerospace dynamics in Cranfield University, 2002 and BE in aeronautical engineering, City University, London, 2000. Currently he is working at RWDI-Anemos, Consulting Wind Engineers, Dunstable, UK. His current fields of interest are flapping wing aerodynamics.

Nicholas J. Lawson received his PhD in mechanical engineering in 1995 from Loughborough University. After completing a post-doctoral position at the University of Melbourne, he joined the Department of Aerospace, Power and Sensors at Cranfield University in 1999 as a lecturer before moving to the Department of Aerospace Sciences as a senior lecturer in 2003. He has recently been appointed as a reader in aerodynamics and his research interests are the application and development of particle image velocimetry (PIV) and laser Doppler anemometry (LDA) techniques. He is also qualified as a commercial pilot flying for the National Flying Laboratory Centre at Cranfield University.

Shijun Guo received his PhD in aerospace engineering at University of Hertfordshire in 1993. He joined Cranfield University in 2003 as a senior lecturer in aircraft composite structures and aeroelasticity. Prior to the current position he was a senior lecturer at two other UK universities for 8 years, a research fellow at the Oxford University and the City University, London, over 3 years. Prior to these academic positions he had 10 years of work experience in aerospace industry. His current research is focused on multidisciplinary optimization and aeroelastic tailoring of composite wing and fin structures, piezoelectric powered MAV flapping-wings, smart multi-functional structures and composite structural health monitoring.

Zhaorong Huang obtained his PhD in condensed matter physics in 1989 in the Institute of Physics Chinese Academy of Sciences, Beijing, China. After that he worked on a variety of subjects related to the microstructural and electrical property characterization of functional materials. He joined Nanotechnology group of Cranfield University in 1996 and is now a Senior Research Fellow. His current research interests include the development of characterization methods for mechanical and electromechanical properties of piezoelectric thin films using interferometry and vibrometry techniques, microstructural characterization of materials by scanning electron microscopy/transmission electron microscopy/focused ion beam, piezoelectric actuators, and multifunctional multiferroic materials and devices.

Development of Piezoelectric Fans for Flapping Wing Application

Hsien-Chun Chung[1], K. Lal Kummari[1], S. J.Croucher[2], N. J.Lawson[2], S. Guo[2], R. W. Whatmore[3], and Z. Huang[1*]

[1]Department of Materials, School of Applied Sciences, Cranfield University, Beds, MK43 0AL, UK

[2]Department of Aerospace Engineering, School of Engineering, Cranfield University, Beds, MK43 0AL, UK

[3]Tyndall National Institute, Lee Maltings, Prospect Row, Cork, Ireland

[*]Corresponding author e-mail: Z.Huang@Cranfield.ac.uk

Abstract

A piezoelectric fan (piezofan) which couples a piezoelectric unimorph to an attached flexible blade is able to produce a large deflection especially at resonance. The fundamental resonant frequencies (f_r) of the piezofan structures have been calculated by an analytical method and finite element modelling, and these were compared with experimental measurements. Good agreements have been obtained between them. The free tip deflection at quasi-static operation or/and the vibration amplitude at dynamic operation (A) of the piezofans have been experimentally measured. We introduce f_r*A as an optimization criterion for piezofans. Optimization according to this criterion has been carried out for some piezofan configurations, such as the length and the location of the piezo patch, as well as the thickness ratio between the elastic and piezoelectric layers among a few available variations. Results show this optimisation approach to be promising when compared to previously defined piezofan performance parameters such as the energy transmission coefficient and electromechanical coupling coefficient.

Keywords: piezoelectric fan, cantilever, optimization, resonance, FEM, MAV

1 Introduction

Piezoelectric materials especially lead zircornate titanate (PZT) are widely used in smart structure as sensors (e.g. accelerometers, microphones, etc.) and actuators (e.g. micropumps, micromotors, etc.) due to their high bandwidth, high output force, compact size, and high power density [1]. However, piezoelectric effect is intrinsically very small, only a small deflection can be expected directly from the bending piezoelectric unimorph/bimorph, therefore some kind of motion amplification mechanism is required to achieve large deflection. One of the simple motion amplification mechanisms is a piezoelectric fan (piezofan) which couples a piezoelectric unimorph to an attached flexible blade and is competent to produce large deflection especially at resonance. Piezofans were first investigated in the late seventies [2]. In the last a few years the popularity of portable electronics devices has resulted in an interest to use piezofans as a compact, low power, noiseless air cooling technology for the applications such as laptop computer, mobile phones or DVD players for example [3, 4].

The optimization of the piezofan configuration however is complex since the optimization criterion is application dependent and can vary among optimal mode shape and frequency, tip deflection, and maximal electromechanical coupling factor (EMCF), etc. A closely related subject is the optimization of piezoelectric unimorph/bimorph structures since these have been extensively studied for the static and dynamic operations [5-13]. Smits and Cooney discussed the effectiveness of piezoelectric bimorph actuator to perform mechanical work under varies constant loading conditions using constituent equations for quasi-static operation [5-7]. Wang et al. investigated the electromechanical coupling and output efficiency of piezoelectric bimorph and unimorph actuators in terms of maximization of three actuator characteristic parameters, namely electromechanical coupling coefficient, energy transmission coefficient and mechanical output energy for quasi-static

operation [8, 9]. Dynamic and topology optimization of the piezofan structures without load (free vibration) for the cooling application based on the maximizing EMCF using analytical solution and finite element modelling (FEM) have been reported recently [14-16]. Optimal design of the piezofan configuration in practical operation is difficult because it requires an accurate knowledge of the fan damping model which is lacking at present. A form of a piezofan mechanism has been proposed for flapping wing micro-aerial-vehicle (MAV) application [17-19]. The main purpose of using piezofan as actuators is to facilitate this simple actuation mechanism to realise two degree of freedom motion (2DOF), namely the flapping and twisting, of the wing and to develop methods for the control of its 2DOF motion [17].

The Strouhal Number is often used in the analyzing of oscillating, unsteady fluid flow dynamics [20]. It is an important dimensionless number and can be expressed as St=fA/U, which divides stroke frequency (f) and amplitude (A) by forward speed (U). St is known to govern a well-defined series of vortex growth and shedding regimes and propulsive efficiency is high over a narrow range of St and usually peaks within the interval $0.2<St<0.4$. Most swimming and flying animals when cruising operate at $0.2<St<0.4$ [21]. This can be used for the prediction of cruising flight and swimming speed for animals as U=fA/St, and can also be used as design guide fA=U*St for wing morphology and kinematics in MAV application, where $St\approx0.3$ [21]. In this report we introduce an optimization criterion fA for the design of the flapping wing actuators where f is the vibration frequency and A the amplitude. Since piezofan is usually operated at its first resonant frequency and its vibration amplitude is largest at this frequency, f_rA can also be used as an optimization criterion for piezofan where f_r is its fundamental resonant frequency and A its vibration amplitude. In this paper, analytical solution and finite element modelling (FEM) will be used to analyse the performance of piezoelectric unimorph and piezofan structures at quasi-static and dynamic operations, and these theoretical results are compared with experimental measured ones. From this

aerodynamic approach we propose a form of design optimization using the Strouhal number and a limited numbers of materials parameters.

2 Experimental

Piezoelectric unimorphs and piezofans were prepared by bonding together a stainless steel metal shim with a piezoelectric PZT patch using epoxy glue EPOTEK 301-2 (Epoxy Technology, US). The PZT wafers (PSI-5H4E) were purchased from Piezo Systems, Inc, USA and there were three thicknesses available, namely 127, 191 and 267 μm. The stainless steel foils (Fe/Cr15/Ni7/Mo2.25) were purchased from Goodfellow Cambridge Ltd, UK and three thicknesses, 50, 125 and 250 μm were available. The effects of bonding conditions such as the curing temperature and time…, on the bonding strength of the ceramic/elastic lamina have been investigated to optimise the bonding strength. The static displacement and blocking force of the piezoelectric fans were characterized with a setup consisted of a signal generator, a high voltage amplifier, an optical fibre sensor (PHILTEC Ltd, model D20) and its power supply unit; a load cell strain gauge (Omega, model LCL-113G) with capacity up to 113 gram adopted for measuring the blocking force. A square wave at 0.5 Hz frequency was used for the quasi-static measurements.

A high speed camera (Photron APX) with frame rate of 2000 frames/s was used to record the dynamic motion of the piezofans. The camera was controlled by a computer system to record images of the vibration continuously for about one second, collecting just over 2000 images, which covered several full cycles of the vibration (the frequency was usually between 10 to 100 Hz). The displacement data were obtained by comparing images over a full cycle and directly measuring the images showing the largest displacement. ANSYS finite element modelling (FEM) was used to modelling the displacement amplitude of the piezofans at quasi-static operation, and to obtain the resonant frequencies.

3 Results and Discussion

3.1 Optimization criterions for piezoelectric unimorph cantilever structures

When a piezoelectric unimorph cantilever is used as an actuator, part of the input electric energy U_{el} is stored as electric energy due to the capacitive nature of the piezo-layer, and the other part stored as mechanical energy U_m. Under a fixed external voltage V, the free-tip deflection δ_0 is the maximum tip deflection and the blocking force F_{bl} is the maximum generative force (opposite in direction though). Generally [8],

$$\delta_0 = \frac{3L^2}{t_p^2} \cdot \frac{ab(1+b)}{a^2b^4 + 2a(2b+3b^2+2b^3)+1} \cdot d_{31}V \tag{1}$$

$$F_{bl} = \frac{3wt_p E_p}{4L} \cdot \frac{ab(1+b)}{(ab+1)} \cdot d_{31}V \tag{2}$$

$$f_{ra} = \frac{3.52t_p}{4\pi L^2}\sqrt{\frac{E_p}{3\rho_p}}\left[\frac{a^2b^4 + 2a(2b+3b^2+2b^3)+1}{(1+bc)(ab+1)}\right]^{1/2} \tag{3}$$

Where $a = E_m / E_p$, $b = t_m / t_p$, $c = \rho_m / \rho_p$, L and w are the length and width of the cantilever respectively. E_m and E_p Young's modulus, t_m and t_p thickness, ρ_m and ρ_p density, for the elastic layer and piezoelectric layer, respectively; d_{31} the transverse piezoelectric coefficient for the piezoelectric layer, and f_{ra} the fundamental bending resonant frequency.

If the actuator displaced δ at an external load F, then the work carried out is – δF. This work reaches maximum $U_{m\text{-}max}$ when the load F is half of the maximum generative force $-0.5F_{bl}$. The ratio between this maximum mechanical output energy and the input electric energy is defined as the energy transmission coefficient λ [9],

$$\lambda = \frac{U_{m-\max}}{U_{el}} = [-1 + \frac{8}{9k_{31}^2}\frac{[a^2b^4 + 2a(2b+3b^2+2b^3)+1-k_{31}^2(1+ab^3)](1+ab)}{a^2b^2(1+b)^2}]^{-1} \tag{4}$$

Here k_{31} is the piezoelectric coupling coefficient. Wang et al. used λ as a criterion for actuator design—the best actuators are those have the largest energy transmission coefficient. [9] The optimal thickness ratio obtained using this optimization criterion agrees with the results obtained

based on the optimization of the EMCF. [14] However, λ is not a directly measurable quantity therefore is difficult to be compared with measurement results.

Figure 1 shows the calculated λ as a function of the thickness ratio b for the PZT/Stainless-steel unimorph cantilevers, the materials parameters used in the calculation are summarised in Table I. Also shown in figure 1 is the value $f_{ra}*\delta_0$ as a function of the thickness ratio. The remarkable similarity between the shapes of the two curves suggests that $f_{ra}*\delta_0$ can also be used as a criterion for the unimorph design for actuator application. Indeed the ratio of $\lambda/f_{ra}*\delta_0$ is almost a constant when b>1 and reduces gradually until b<0.4. There is a slight difference at the peak positions though between the two curves: the λ peaks at the thickness ratio $\approx$ 0.9 but $f_{ra}*\delta_0$ peaks at about thickness ratio $\approx$ 0.6. Another point worth point out is the fact that $f_{ra}*\delta_0$ does not depend on the length of the cantilever, which is clear from the equations (1) and (3).

It should be noted that strictly speaking $f_{ra}*\delta_0$ is not a "fA" since δ_0 is the quasi-static displacement amplitude, not the vibration amplitude at the resonant frequency f_{ra}. The optimization of "fA" is equivalent to the optimization of $f_{ra}*\delta_0$ only when the vibration amplitude A is proportional to the free-tip deflection δ_0. Also, λ is a dimensionless value but $f_{ra}*\delta_0$ has a dimension of m/s and its value depends on the external voltage V. When V changes, the numerical value of $f_{ra}*\delta_0$ changes as well, but not the shape of the $f_{ra}*\delta_0$ curve in figure 1. The "A" can also be used as the amplitude per volt without affecting the results and discussion provided the external voltage V is kept a constant and within the linear range. The total amplitude "A" is used in this work in order to be directly connected to the Strouhal Number St.

Table II summarise the calculated performance parameters using the equations (1)-(4) for all possible thickness ratios from the three available PZT and three stainless steel thicknesses. It can be seen that the combinations t_m=50 μm, t_p=127 μm, and t_m=125 μm, t_p=127 μm have clearly the highest $f_{ra}*\delta_0$ values, and λ is the highest for the combination t_m=125 μm, t_p=127 μm. Although the

unimorph cantilever with t_m=250 μm, t_p=267 μm also has a very high λ, its 1st resonant frequency 189.7 Hz is too high for applications based on mechanical vibration.

3.2 Optimization of piezoelectric fan at quasi-static operation

In a piezofan configuration, unlike in the unimorph structures, the piezoelectric active layer is shorter than the passive elastic layer. In practice, a length at the foot of the piezofan is always needed for clamping and also needed is a gap between the clamping and the start of the piezoelectric patch, in order to prevent the piezo patch being broken during vibration. For these reasons our piezofans always have a 10 mm bare elastic length at the foot: 7 mm for clamping and 3 mm as the gap between the clamping and the start of the piezoelectric layer, as shown in figure 2. For these piezofan structures, there are no analytical formulae similar to equations (1) to (4) available in the literature for the calculation of the free tip displacement and 1st resonant frequency, so finite element modelling (FEM) was used to calculate the δ_0, f_{rm} and other performance parameters for varies fan configurations.

For the fixed PZT patch and elastic layer dimensions, change the location of the PZT patch leads to the change of the piezofan performances. Figure 2 shows the FEM results for the free-tip displacement and the 1st resonant frequency with the PZT patch location. The PZT patch was 30 mm in length and the stainless steel shim was 50 mm long (7 mm for clamping, so 43 mm is the full length outside). It can be seen that for the location of the PZT patch (as represented by the left of the PZT patch), further away from the clamping position leads to a smaller free tip displacement under a certain driving voltage and lower 1st resonant frequency of the fan. So, if a larger $f_{rm}*\delta_0$ is required, the PZT patch should be placed as close to the clamping position as possible (in this case, 3 mm).

FEM investigation on the effect of the length of the PZT patch was also carried out. The results showed that for the fixed stainless steel length, the longer the PZT patch, the larger the free-tip displacement and higher the resonant frequency, therefore larger the $f_{rm}*\delta_0$ value. So, ideally the PZT patch should cover the full length of the elastic layer. However, in practice, an extra length of the elastic layer at the tip is always needed in order to be able to attach the load for flapping wing applications.

Another variation of the configuration investigated is that the active part is consisted of two or more discrete PZT patches. Figure 3(a) shows schematically a piezofan consisted of two discrete PZT patches with a total length 30 mm, so each one is 15 mm long. The width of the piezofan was 10 mm. As discussed above there is always a 3 mm gap between the clamping and the left of the first PZT patch. The gap between the two PZT patches was varied from zero to 9 mm. Figure 3 (b) shows the dependence of the tip displacement and the 1st resonant frequency on the gap size between the two PZT patches. It can be seen that the larger gap between the two PZT patch leads to smaller tip displacement δ_0 and the lower first resonant frequency f_{rm} of the piezofan. Hence, if a large $f_{rm}*\delta_0$ is required, the PZT patches should be bonded as close as possible.

A piezoelectric fan with the PZT patch 30 mm and the metal shim 40 mm in lengths (and both were 10 mm in width) was prepared. The PZT patch was placed at the foot of the metal shim and there was almost no gap between the clamping and the left of the PZT patch, therefore leaving 10 mm stainless steel layer at the tip of the piezofan. Fig. 4 shows its quasi-static tip displacement as a function of the driving voltage between 0 and 70 V. The quasi-static tip displacement was 401 μm under 70 V, and it was nearly a linear relationship between the tip displacement and the driving voltage. Also observed was the good agreement between the measured and the FEM values (Fig. 4).

Table III summaries FEM results of the first resonant frequencies f_{rm} and the quasi-static free-tip displacements δ_0 for varies piezofan configurations. All the piezofans have 30 mm PZT patch and

43 mm stainless steel, with the PZT placed 3 mm from the clamping position, therefore leaving 10 mm stainless at the top. The calculated $f_{rm}*\delta_0$ are listed in the last column. It can be seen that the combination t_m=125 μm, t_p=127 μm has clearly the highest $f_{rm}*\delta_0$ value. Although the piezofan with t_m=250 μm, t_p=127 μm also has a high $f_{rm}*\delta_0$, its 1st resonant frequency 130.1 Hz is too high for the reason mentioned above.

3.3 Characterization of piezoelectric fan at dynamic operation

So far we have defined a criterion for the optimization of piezofan structure and discussed the optimization accordingly in terms of the patch location and the thickness ratio of the two layers, at quasi-static operation. However, piezofans are often operated at or close to their 1st resonant frequency, it is desirable to investigate their dynamic behaviours. Without the detailed knowledge of the fan damping which includes the mechanical damping and air damping, it is not possible to calculate or model the vibration amplitude at its resonant frequency although the resonant frequencies could be calculated by FEM and analytical solutions. In the following the fundamental resonant frequency of the piezofan structures will be calculated by the FEM and analytical methods and these values compared with the measured values. The vibration amplitudes were obtained from high speed camera measurements.

For the piezofan structure, as shown in Figure 5, there are three sections. Section I is from the origin (clamping) to length L_1; section II is from the length L_1 to L_2, and section III is from the length L_2 to L_3. The PZT layer has the same length with the substrate in the section two; however, there are no piezoelectric materials in section I and III.

The equation of motion in section I and III is

$$E_b I_b y'''' - \rho_b A_b \ddot{y} = 0 \qquad L_1 \le x \le L_2,\ L_2 \le x \le L_3 \qquad (5)$$

The equation of motion in the section II is [14-16]

$$\left(E_b I_{bN} + 2a_2 I_{pN} + 2a_3 A_P\right) y'''' - \left(\rho_b A_b + \rho_p A_p\right) \ddot{y} = 0 \quad L_1 \le x \le L_2 \tag{6}$$

Where E_b and E_p are the Young's modulus for the elastic layer and the piezolayer respectively, ρ_b and ρ_p the mass density, A_b and A_p the cross section area (product of width and thickness) and I_b the moment of inertia of the elastic layer. Also,

$$a_2 = \frac{1}{2}\left(E_p + \frac{{e_{31}}^2}{\varepsilon_{33}^s}\right) = \frac{1}{2}E_p\left(1 + \frac{E_p {d_{31}}^2}{\varepsilon_{33}^s}\right) = \frac{1}{2}E_p\left(1 + \frac{E_p {d_{31}}^2}{\varepsilon_{33}^T\left(1-k_{31}^2\right)}\right) \tag{7}$$

$$a_3 = -\frac{{e_{31}}^2}{8\varepsilon_{33}^s}\left(t_p - 2t_N\right)^2 = -\frac{E_p^2 d_{31}^2}{8\varepsilon_{33}^T\left(1-k_{31}^2\right)}\left(t_p - 2t_N\right)^2 \tag{8}$$

Where ε_{33}^s, ε_{33}^T are the dielectric constants at constant strain and constant stress respectively, with $\varepsilon_{33}^s = \varepsilon_{33}^T(1-k_{31}^2)$, and $e_{31} = E_p d_{31}$. And,

$t_N = \frac{1}{2}\cdot\frac{E_p {t_p}^2 - E_b {t_b}^2}{E_b t_b + t_p E_p}$ is the position of the neutral axis (assuming within the piezo layer),

$I_{bN} = \int dy \int_{-t_b - t_N}^{-t_N} z^2 dz$ is the moment of inertia relative to the neutral axis for the substrate layer,

$I_{pN} = \int dy \int_{-t_N}^{t_p - t_N} z^2 dz$ is the moment of inertia of the piezo layer relative to the neutral axis.

Assuming the solutions are:

$y_i = u_i e^{i\omega t}$ i=1,2,3. (9)

$u_1 = c_1 \cos\alpha x + c_2 \sin\alpha x + c_3 \cosh\alpha x + c_4 \sinh\alpha x,\ 0 \le x \le L_1$ (10)

$u_2 = c_5 \cos\beta x + c_6 \sin\beta x + c_7 \cosh\beta x + c_8 \sinh\beta x),\ L_1 \le x \le L_2$ (11)

$u_3 = c_9 \cos\alpha x + c_{10} \sin\alpha x + c_{11} \cosh\alpha x + c_{12} \sinh\alpha x),\ L_2 \le x \le L_3$ (12)

where

$$\beta = \left[\frac{\left(\rho_b A_b + \rho_p A_p\right)\omega^2}{2a_2 I_{PN} + 2a_3 A_p + E_b I_{bN}} \right]^{1/4} \tag{13}$$

$$\alpha = \left(\frac{\rho_b A_b \omega^2}{E_b I_b} \right)^{1/4} \tag{14}$$

In section I, there are four constants to be determined, C_1, C_2, C_3, and C_4, and the boundary conditions are

$$u_1(0) = 0,$$

$$u_1'(0) = 0 \tag{15}$$

In section III, there are four constants to be determined, C_9, C_{10}, C_{11}, and C_{12}, and the boundary conditions are

$$u_3''(L_3) = 0,$$

$$u_3'''(L_3) = 0. \tag{16}$$

In section II, there are four constants to be determined, C_5, C_6, C_7, and C_8.

At free-vibrations, i.e., short circuit condition or the external voltage equals zero, the boundary conditions are natural boundary conditions at L_1:

$$\begin{aligned} &u_1(L_1) = u_2(L_1), \\ &u_1'(L_1) = u_2'(L_1), \\ &Y_1 u_1''(L_1) = Y_2 u_2''(L_1), \\ &Y_1 u_1'''(L_1) = Y_2 u_2'''(L_1). \end{aligned} \tag{17}$$

Where $Y_1 = E_b I_b$ (18)

and $Y_2 = \left(E_b I_{bN} + 2a_2 I_{pN} + 2a_3 A_P\right)$ (19)

And the natural boundary conditions at L_2:

$$
\begin{aligned}
&u_2(L_2) = u_3(L_2),\\
&u_2^{'}(L_2) = u_3^{'}(L_2),\\
&Y_2 u_2^{''}(L_2) = Y_1 u_3^{''}(L_2),\\
&Y_2 u_2^{'''}(L_2) = Y_1 u_3^{'''}(L_2).
\end{aligned}
\qquad (20)
$$

So there are 12 unknown constants and 12 equations. In matrix form, these equations can be written as $M_{12x12}\, C_{1x12} = 0$ (21)

To have meaningful $c_1 \ldots c_{12}$, the determinant of the matrix M_{12x12} must be 0, which yields the natural frequencies and mode shapes of the structure. MatLab® programme was used to find the zeros of the determinant, therefore the natural frequencies.

The calculations were carried out for a number of piezofan configurations, Table IV summaries the calculated first resonant frequencies f_{ra}. It also summarises the 1st mode frequencies f_{rm} as obtained from FEM and the experimental measured 1st resonant frequencies f_r. From this table, it is clear that for thick metal shims, the FEM and the analytical results agrees with each other very well. However, for the thinnest metal shim (50 μm), discrepancy exists between the FEM and the analytical values. This was probably due to the not dense enough meshing for the thin layers and also the fact that the epoxy bonding layer was ignored in the FEM. From the table we can also see that the measured resonant frequencies (with the nominal gap distance being 3 mm) matched those theoretical ones (FEM or analytical) with the gap distances range from 3 to 7 mm, depending on the individual piezofan. This is understandable considering the variable conditions of the clamping therefore the deviation of the actual clamping length from its nominal value. The nominal clamping lengths for all the measured samples were 7 mm and there was a nominal 3 mm distance from the clamping edge to the start of the piezoelectric ceramics. If the clamping was perfect, the whole length of the clamping (7 mm) was clamped firmly, then the actual distance from the clamping edge

to the start of the ceramics equals to its nominal value (3 mm). However, if the clamping was not perfect, part of the clamping length was still movable when the piezofan vibrates, then the effective distance from the clamping to the start of the ceramics will be larger than its nominal value 3 mm.

The dynamic performances of four actuators Ba2, Ab1, Bb1, and Ab2 were investigated by using a high-speed camera system. Figure 6 (b) shows the measured vibration amplitude at the tip as a function of frequency for the bending mode under a sinusoidal voltage of 170 V_{pp} for the piezofan Bb1. It shows that the vibration amplitudes of the piezofans increased with the increasing frequency at first and peaked at their respective first resonant frequency, after that it decreased with the increasing frequency. The mechanical quality factor of the system, as defined by $f_r/\Delta f$, where Δf is the frequency difference between the two half maximum points, can be obtained from this profile and found to be equal to 19.8. Table IV summaries the properties of these four piezofans as well. From this table, it can be seen that longer PZT length (comparing Bb1 with Ab1), thicker PZT thickness (comparing Ba2 with Ab2) and thicker metal shim (comparing Ab1 with Ab2) leads to higher quality factor.

The first resonant frequency of these piezoefans were 28.2 Hz, 48.1 Hz, 50.8 Hz, and 23.8 Hz for Ab1, Ab2, Ba2, and Bb1, respectively; the corresponding measured vibration amplitudes were 7.2 mm, 8.3 mm, 13.2 mm and 22.1 mm, respectively. The $f_{r*}A$ values were then 203.1, 399, 670.6, 526 respectively. These are also summarised in the Table IV. According to the $f_{r*}A$ criteria, the Ba2 had the best performance among these four piezofans. This agrees with the conclusion obtained at the quasi-static operation. It also agrees with the conclusion obtained from the EMCF optimization that the optimized PZT/steel thickness ratio is around one. [14]

It is worth to point out that the effect of air damping on the performance of piezofans are not considered in this work. This is because for the piezofans discussed in this work, their projected

surface areas are small, the induced aerodynamic forces are expected to be small as well comparing with their elastic and inertia forces. However, for other configurations with a purpose designed aerodynamic surface, air damping may have a significant influence on their performances, which will be reported in a separate paper. [17] Yao and Uchino discussed these effects using a lumped-mass model and concluded that air damping played a dominant role on the vibration of their piezofans. [13]

4 Conclusions

We have introduced f_r*A as an optimization criterion for piezofans where f_r is its fundamental resonant frequency and A the vibration amplitude at the resonant frequency, or the free tip deflection at quasi-static operation. This criterion can be used to obtain the piezofans with the best energy transmission coefficient, and is a measurable quantity therefore can be compared with experimental results. Optimization according to this criterion has been carried out for a number of piezofan configurations, such as the length and the location of the piezo patch, as well as the thickness ratio between the elastic and piezoelectric layers.

The fundamental resonant frequencies of the piezoelectric fan structures have been calculated by analytical method and finite element modelling, and these were compared with measurement results. Good agreements have been obtained between them. The free tip deflection at quasi-static operation and the vibration amplitude at dynamic operation of the piezofans have been measured by experiments and the experimental f_r*A values have been used to select the best piezofans for flapping wing MAV applications [17]. Overall the results suggest this approach to provide a promising method to optimise piezofans.

Acknowledgements

This work was financially supported by the UK EPSRC Grant Flapping Wing MAV EP/C511190/1 and Platform Grant EP/D506638/1. We thank Drs. E. Liani and G. Leighton of Cranfield University for their helps on MatLab calculation and ANSYS finite element modelling.

References

[1] C. Niezrecki, D. Brei, S. Balakrishnan, and A. Moskalik, Piezoelectric actuation: state of the art, The shock and vibration digest. 33 (2001) 269-280.

[2] M. Toda, Voltage-induced large amplitude bending device-PVF2 bimorph-its properties and applications, Ferroelectrics. 32 (1981) 911.

[3] J. Yoo, J. Hong, and W. Cao, Piezoelectric ceramic bimorph coupled to thin metal plate as cooling fan for electronic devices, Sensors &Actuators A 79 (2000) 8-12

[4] T. Wu, P. Ro, A. Kingon, and J. Mulling, Piezoelectric resonating structures for microelectronic cooling, Smart. Mater. Struct. 12 (2003) 181-187.

[5] J. G. Smits, S. I Dalke, T.K. Cooney, The constituent equations of piezoelectric bimorphs, Sensors and Actuators, A**28** (1991) 41-61.

[6] J.G. Smits, W. Choi, and A. Ballato, Resonance and anti-resonance of symmetric and asymmetric cantilevered piezoelectric flexors, IEEE Trans. Ultrason. Ferroelectr. Freq. Control, **44 (1997)** 250-258.

[7] J. G. Smits and T. K. Cooney, The effectiveness of a piezoelectric bimorph actuator to perform mechanical work under various constant loading conditions, Ferroelectrics, 119 (1991) 89-105.

[8] Q. Wang and L.E. Cross, Performance analysis of piezoelectric cantilever bending actuators, Ferroelectrics, 215 (1998) 187-213.

[9] Q. Wang, X. Du, B. Xu and L.E. Cross, Electromechanical coupling and output efficiency of piezoelectric bending actuators, IEEE Trans. On Ultroson. Ferro. Freq. Contr., **46**, (1999) 638-646.

[10] G. Gibbs and C. Fuller, Excitation of thin beams using asymmetric piezoelectric actuators, J. Acoust. Soc. Am., 92 (1992) 3221-3227.

[11] E. F. Crawley, and J. de Luis, Use of piezoelectric actuators as elements of intelligent structures, AIAA Journal, 25 (1987) 1373-1385.

[12] M. J. Brennan, S.J. Elliott, and R. J. Pinnington, The dynamic coupling between piezoceramic actuators and a beam, J. Acoust. Soc. Am., 102 (1997) 1931-1942.

[13] K. Yao and K. Uchino, Analysis on a composite cantilever beam coupling a piezoelectric bimorph to an elastic blade, Sensors and Actuators, A**89** (2001) 215-221.

[14] K. Wolf, "Electromechanical energy conversion in asymmetric piezoelectric bending actuators", PhD thesis, Technische Universität Darmstadt, Germany, 2000.

[15] P. Burman, A. Raman, and S.V. Garimella**,** Dynamic and topology optimization of piezoelectric fans, IEEE Trans. Components and Packaging Technology, 25 (2002) 592-600.

[16] S. Basak, A. Raman, and S. V. Garimella, Dynamic response optimization of piezoelectrically excited thin resonant beams, Trans. of ASME, 127 (2005) 18-26.

[17] Hsien-Chun Chung, K. Lal Kummari, S. J.Croucher, N. J.Lawson, S. Guo, Z. Huang, Coupled Piezoelectric Fans with Two Degree of Freedom Motion for the Application of Flapping Wing Micro Aerial Vehicles, Sensors and Actuators A, in press.

[18] W. Shyy, M. Berg and D. Ljungqvist, Flapping and flexible wings for biological and micro air vehicles, Prog. in Aerospace Sci. 35 (1999) 455-505.

[19] D. L. Raney and E. C. Slominski, Mechanization and control concepts for biologically inspired micro aerial vehicles, AIAA 2003-5354, AIAA Guidance, Navigation and Control Conference, Austin, Texas, Aug. 2003.

[20] R. M. Alexander, Principles of Animal Locomotion, Princeton Uni. Press, Princeton, 2003.

[21] G. Taylor, R. Nudds and A. Thomas, Flying and swimming animals cruise at a Strouhal number tuned for higher power efficiency, Nature, **425** (2003) 707-711.

Figure Captions

Fig. 1 The calculated energy transmission coefficient λ, $f_{ra}*\delta_0$ and the ratio of $\lambda/f_{ra}*\delta_0$ as functions of the thickness ratio for the PZT/Stainless-steel unimorph cantilevers. The remarkable similarity between the shapes of the λ and $f_{ra}*\delta_0$ curves suggests that $f_{ra}*\delta_0$ can also be used as an optimization criterion for the unimorph for actuator application. The ratio of $\lambda/f_{ra}*\delta_0$ is almost a constant when the thickness ratio is larger than 0.4.

Fig. 2 FEM results of the effect of the PZT patch location: (a) Scheme; (b) on the free tip displacement and the 1st resonant frequency. The piezofans have the effective length L= 43 mm and width w=10 mm.

Fig. 3 (a) Schematic of piezofan with two discrete PZT patches. (b) FEM results on the effect of the distance between the two PZT patch on the tip displacement and the 1st resonant frequency. The piezofans have a total length of 43 mm and width of 10 mm.

Fig. 4 The FEM and measured tip displacement under the applied voltages from 0 to 70 V at quasi-static frequency for a piezofan with a length of 40 mm and width of 10 mm.

Fig. 5 The scheme of a piezoelectric fan consisting of three sections. The piezoelectric material exists in the section two only.

Fig. 6 The measured bending displacement amplitude of a piezofan as a function of the operating frequency under 170 Vpp.

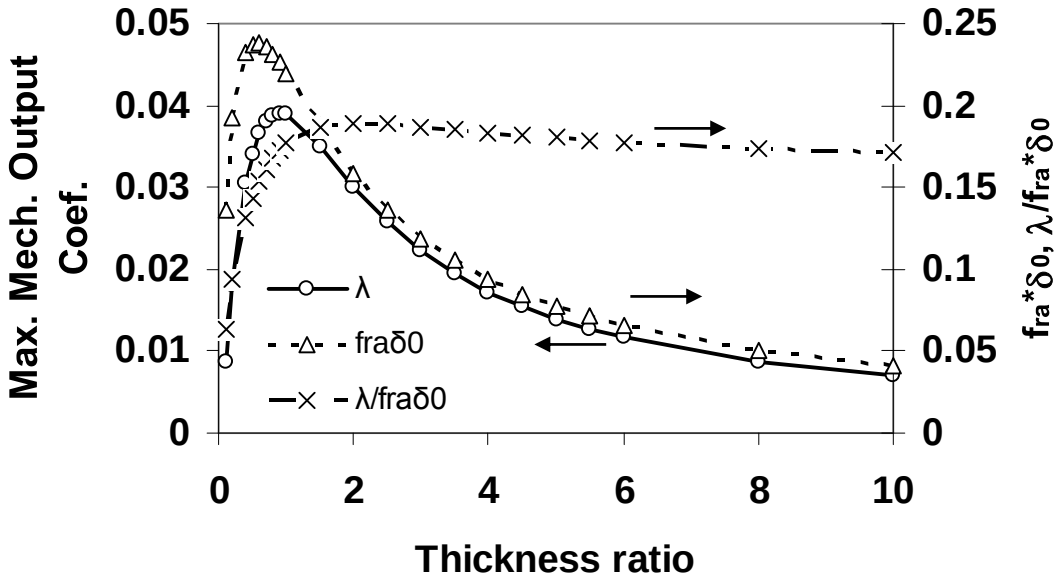

Figure 1

Chung et al.

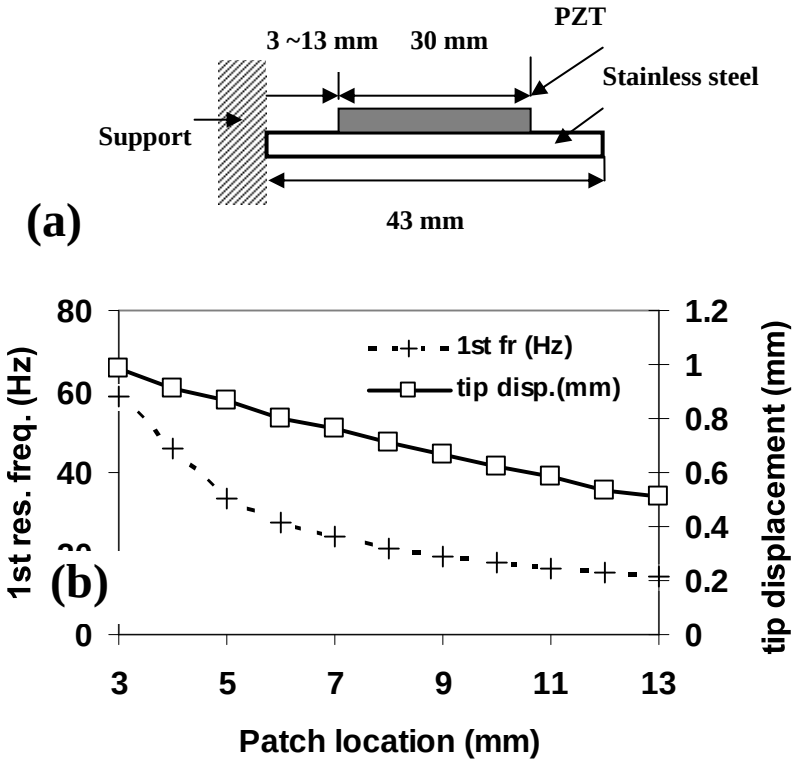

Figure 2

Chung et al.

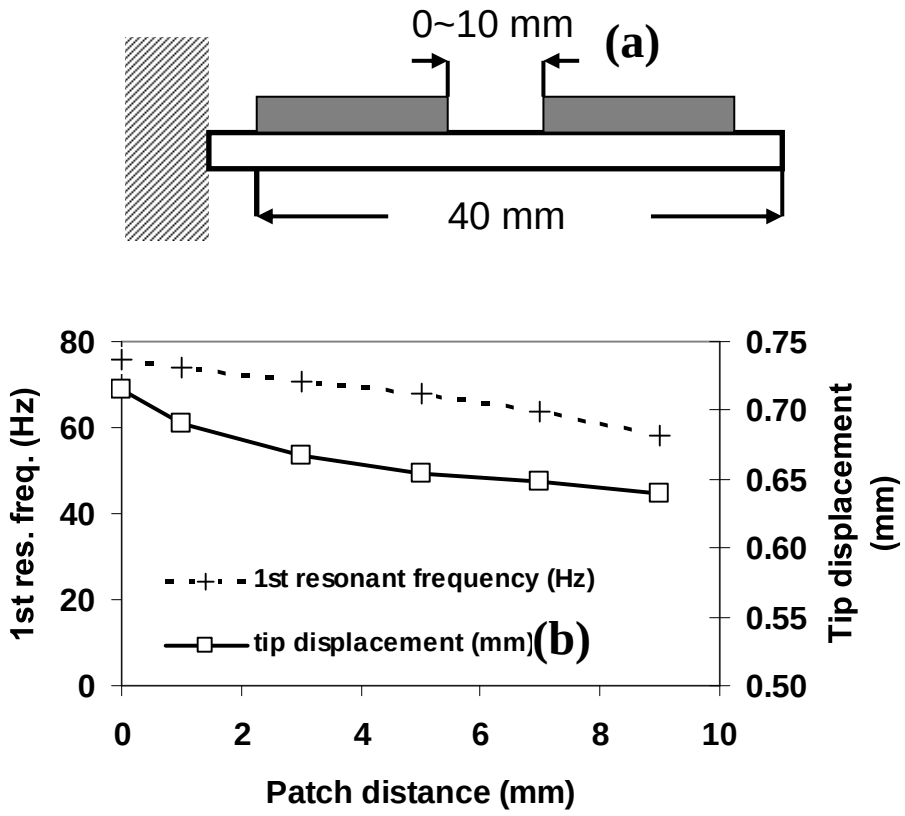

Figure 3

Chung et al.

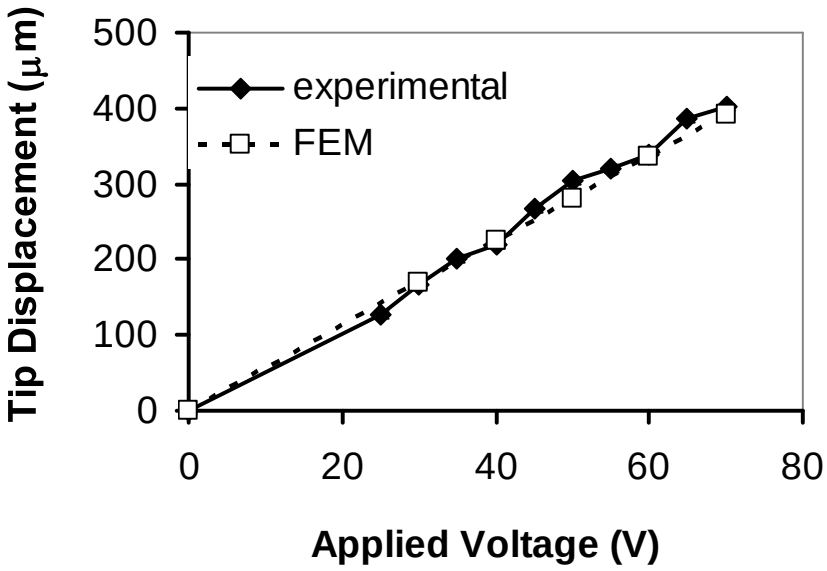

Figure 4

Chung et al.

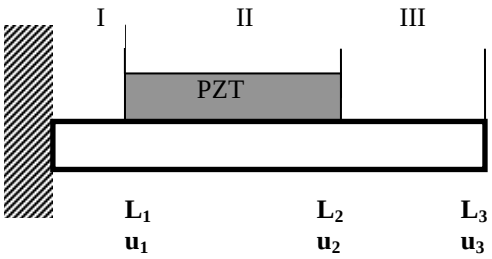

Figure 5

Chung et al.

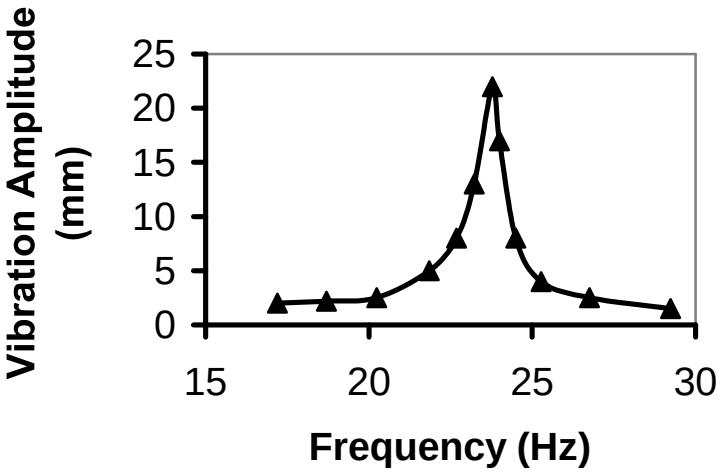

Figure 6

Chung et al.

Table I: Material property parameters used for the finite element modelling and the analytical calculations.

	PZT 5H	**Stainless Steel**
Young's Modulus (GPa)	62	200
Density (Kg/ m^3)	7800	7900
Poisson's ratio	—	0.28
$d_{31}(10^{-12}m/V)$	-320	—
ε_{33}	3400	—
e_{31}	-12	—
e_{33}	22.22	—
e_{15}	19.39	—
$c_{11}(10^9N/m^2)$	126	255.7
$c_{12}(10^9N/m^2)$	79.5	99.4
$c_{13}(10^9N/m^2)$	84.1	—
$c_{33}(10^9N/m^2)$	117	—
$c_{44}(10^9N/m^2)$	23.0	78.1

Table II: Summary of the calculated performance parameters for a number of piezoelectric unimorph cantilevers with the length L = 40 mm and width w=10 mm.

T_m (μm)	T_p (μm)	free tip displacement (δ_0)	Blocking force (F_{bl})	1st resonant frequency (f_{ra})	$\delta_0 * f_{ra}$	Max. mech. output coef. λ
50	127	2.83	0.063	64.6	182.8	0.0301
50	191	1.27	0.07	87.2	110.7	0.0227
50	267	0.63	0.075	112.8	71.1	0.017
125	127	1.87	0.121	92.6	173.2	0.039
125	191	1.07	0.136	115.5	123.6	0.037
125	267	0.62	0.149	143.3	88.8	0.033
250	127	0.86	0.206	145.7	125.3	0.03
250	191	0.63	0.225	164.3	103.5	0.037
250	267	0.44	0.246	189.7	83.5	0.039

Table III: Summary of the first resonant frequencies, the quasi-static free-tip deflections, and the product of these two for a number of piezofans with different thickness ratios as obtained from FEM. All the piezofans have 30 mm PZT patch and 43 mm stainless steel, with the PZT placed 3 mm from the clamping position, leaving 10 mm stainless at the top.

PZT Thickness (t_p, μm)	**Metal Thickness (t_m, μm)**	**FEM f_{rm} (Hz)**	**free tip displacement (δ_0, mm)**	**$\delta_0 * f_{rm}$**
127	50	29.4	2.13	62.6
191	50	26.7	0.92	24.6
267	50	24.5	0.44	10.8
127	125	67.1	1.54	103.3
191	125	71.6	0.85	60.9
267	125	74.8	0.48	35.9
127	250	130.1	0.73	95
191	250	139.6	0.53	74
267	250	146.5	0.36	52.7

Table IV: Summary of the analytical, finite element modelling and experimental measured 1st resonant frequencies, the measured vibration amplitude and quality factors for a few piezofan configurations.

Sample	Distance from Clamping (L_1, mm)	PZT Length (L_2-L_1, mm)	Metal Length (L_3-L_1, mm)	PZT Thickness (t_p, μm)	Metal Thickness (t_m, μm)	FEM f_{rm} (Hz)	Analytical f_{ra} (Hz)	Measured f_r (Hz)	Measured amp. (A, mm)	f_rA	Δf at 3 db (Hz)	Q Factor ($f_r/\Delta f$)
Ba2	3	30	40	127	125	67.1	70.9	50.8	13.2	670.6	4.9	10.4
	5	30	40	127	125	56.3	57.8					
	7	30	40	127	125	48.6	49					
Ab1	3	30	40	191	50	26.7	32	28.2	7.2	203.1	4	7
	4	30	40	191	50		27.3					
Bb1	3	40	40	191	50	20	23.7	23.8	22.1	526	1.2	19.8
Ab2	3	30	40	191	125	71.6	73.5	48.1	8.3	399	4	12
	5	30	40	191	125	57.5	57.6					
	7	30	40	191	125	48.4	47.9					